POLITECNICO DI MILANO
DEPARTMENT OF PHYSICS
DOCTORAL PROGRAMME IN PHYSICS

ULTRAFAST SCANNING ELECTRON MICROSCOPY

CHARGE DYNAMICS AT SEMICONDUCTOR AND INSULATOR SURFACES

Doctoral Dissertation of:
Vittorio Sala
838243

Supervisor:
Prof. Alberto Tagliaferri

Co-Supervisors:
Prof. Silvia Maria Pietralunga
Prof. Maurizio Zani

Tutor:
Prof. Marco Finazzi

The Chair of the Doctoral Program:
Prof. Paola Taroni

2018 – XXX cycle

Contents

1 Introduction ... **6**

2 State of the art ... 9

2.1 Scanning Electron Microscope ... 9

2.1.1 SEs and spatial resolution ... 10

2.1.2 Auger emission ... 11

2.2 Time resolution in electron microscopy ... 12

2.2.1 Optical pump probe on semiconductors ... 14

2.2.2 Ultrafast Electron Microscopy ... 17

2.2.3 Ultrafast electron sources ... 19

2.3 Ultrafast Scanning Electron Microscopy ... 20

2.3.1 Experimental setup ... 20

2.3.2 Spatial resolution ... 22

2.3.3 Sensitivity to excited carriers and temporal resolution ... 23

2.4 USEM on semiconductors ... 24

2.4.1 Sensitivity to doping ... 24

2.4.2 Excited carrier dynamics in nanostructured materials ... 26

2.4.2 Effect of PE energy on the pump-probe differential SE contrast ... 27

2.4.3 Importance of the surface ... 28

2.4.4 Charge transport in pn junction ... 30

2.4.5 Diffusion of optically excited carriers on silicon ... 31

2.5 Other techniques for semiconductors ... 31

2.5.1 Cathodoluminescence ... 32

2.5.2 Time-resolved cathodoluminescence ... 32

2.5.3 Time-resolved PEEM ... 35

2.6 Diffraction contrast ... 37

2.6.1 Time-resolved electron diffraction ... 38

2.6.2 Time-resolved electron diffraction in USEM ... 39

2.7 Transmission electron microscopy ... 39

2.7.1 Ultrafast Transmission Electron Microscopy ... 40

2.8 Objectives and motivations of this work - Surface sensitive USEM ... 42

2.8.1 The development of the UHV USEM apparatus ... 43

2.8.2 The choice of the scientific cases ... 45

3 Experimental setup ... 47

3.1 Scanning Auger Microscope ... 48

3.1.1 Electronic column ... 49

3.1.2 Secondary Electrons detector ... 52

3.1.3 Cylindrical Mirror Analyzer ... 55

3.1.4 Sample management ... 56

3.2 Ultrafast electron source ... 56

3.2.1 Description and operation 57
3.2.2 Source performances and limitations 59
3.2.3 Resolution limit 60

3.3 Optical setup 61
3.3.1 Ultrafast laser 61
3.3.2 Beam splitting and harmonic generator 62
3.3.3 Optical layout: path to the sample 64
3.3.4 Optical layout: path to the ultrafast electron source 67

3.4 Pulsed emission 68
3.4.1 Alignment of the laser beam on the tip 69
3.4.2 Fluence dependence 69
3.4.3 SEM imaging with pulsed current 70

3.5 Spatial alignment 71
3.5.1 Spatial alignment on a phosphor reference 71
3.5.2 Damage fluences 74

3.6 Temporal alignment 76
3.6.1 Time-resolved SEM images 76
3.6.2 Contrast enhancement and coarse temporal alignment 77
3.6.3 Data acquisition and analysis 80
3.6.4 Discussion of the horizontal stripe noise in the SE images 82
3.6.5 Fine temporal alignment 85

3.7 Time resolution 87
3.7.1 Linearity of the differential SE contrast versus PE current 89
3.7.2 Estimation of rise time 90

3.8 Conclusions 91

4 USEM investigation of the surface charge dynamics at the Si(001) surface as a function of doping 92

4.1 *Ultrafast dynamics at the surface of Si(001) 92*

4.2 *Sample set and preparation 94*

4.3 Experimental setup 96
4.3.1 Measurement procedure 97

4.4 Measurement results on silicon 97
4.4.1 Results on silicon exposed to air 98
4.4.2 Results on silicon exposed to nitrogen 99
4.4.3 Optically induced SE contrast step and recovery dynamics 100

4.5 Data analysis 102
4.5.1 Effect of the exposure of the surface to environmental gases 103
4.5.2 Trends of the amplitude of the step and of the recovery time 106

4.6 Conclusions 107

5 USEM investigation of the color center charge dynamics at the surface of aluminum oxide 108

5.1 Aluminum oxide on silicon 108
5.1.1 Lattice defects in aluminum oxide 110

5.1.2 F-color centers dynamics 112
5.1.3 Objectives of the present work 112

5.2 Sample and experimental setup 113
5.2.1 Pump wavelength 113
5.2.2 Sample 113
5.2.3 Charging effects 114
5.2.4 Chopper and lock-in 114

5.3 Experimental data 116

5.4 Data analysis 117
5.4.1 Analytical model 117
5.4.2 Fitting 118
5.4.4 Fitting error 119

5.5 Theoretical model 121
5.5.1 Enhancement at positive delays [134] 121
5.5.2 Enhancement at negative delays [134] 121
5.5.3 Stationary background [134] 121
5.5.4 Depletion at positive delays [134] 122

5.6 Conclusions 122

Conclusions 123

Appendix A: UED investigation of Verwey transition dynamics in magnetite 125

A.1 Ultrafast Electron Diffraction 126

A.2 Magnetite and Verwey transition 128

A.3 Results at room temperature 130

A.4 Results at temperature below Verwey threshold 131

A.5 Conclusions 132

Appendix B: Data on silicon 133

Appendix C: fitting results 142

Appendix D: paper on aluminum oxide [134] 144

***Abstract* 144**

***Keywords* 144**

***2. Experimental setup and measurement technique* 146**

***3. Results and discussion* 150**

***4. Conclusions* 155**

***Acknowledgments* 155**

***References* 156**

Appendix E: Convolution of an exponential and a Gaussian 160

Appendix F: other works [162] **162**

The Role of Higher Lying Electronic States in Charge Photogeneration in Organic Solar Cells *162*

Abstract *162*

Introduction *162*

Results *164*

Discussion *168*

Conclusion *170*

Experimental Section *170*

Acknowledgements *171*

References *171*

References **173**

List of figures **182**

List of tables **189**

Acknowledgements **190**

1 Introduction

Electron microscopy was first developed by Ernest Ruska and Max Knoll [1] to overcome the diffraction limit that affected the lateral resolution in optical microscopes. They managed, through electric and magnetic fields, to focus an electron beam obtaining a magnified image of a sample. Nowadays, electron microscopy is a widely used tool, and many different kinds of electronic microscopes were developed. The advantage brought by electron microscopy is not only the improved spatial resolution with respect to optical microscopes, but also the stronger imaging contrast and surface sensitivity due to the fact that electrons interact with matter more than photons do. The cross section of interaction is up to five order of magnitude larger for electrons than for photons.

Electron imaging has been associated up to few years ago to static objects and did not allow to obtain direct information on dynamics. Nonetheless, advanced electronics and photonics require to control, at the same time, dimensions at the nanoscale and dynamics in the fast and ultrafast regime (GHz or faster). The physics of the ultrafast phenomena is today typically accessed by laser-based optical experiments, where the spatial resolution is limited to hundreds of nanometers by diffraction in a far field approach. Breaking this space scale limit is today possible following several pioneering approaches that join the ultrafast time resolution of lasers to the high spatial resolution of modern microscopes. This set of techniques includes table-top apparatuses like electron microscopes, scanning probe microscopes, and specialized beamlines at large-scale facilities, like synchrotron and free electron lasers.

Time-resolved electron microscopy was first proposed with the aim of investigating charge trapping in Si devices in the early ‘90s of the last century [2]. The proposers intend to use electron beam induced charge (EBIC) and cathodoluminescence (CL) [3] as probes. The access to ultrafast dynamics was then proposed and pursued in the new millennium by the group of the Nobel prize A. H. Zewail and by few others [4–10],[11], with the goal of combining the advantages of pulsed lasers with electron microscopy and, ultimately, accessing the physics of ultrafast phenomena at the nanoscale. Different kinds of time-resolved electron microscopes were developed for different applications:

- Ultrafast Transmission Electron Microscopy (UTEM) [4,12–14] to study mechanical oscillations of cantilevers [15] , plasmonic effects [16–19] and quantum interference [20,21];
- Ultrafast Electron Diffraction (UED) [22] to study lattice dynamics [23], phonons [24] and phase transitions [8,25];
- Ultrafast Scanning Electron Microscopy (USEM) [26,27] to study time-resolved dynamics at the surface of the samples [9] like electric charges generation, transport and recombination in semiconductors [28–34].

Results already reported by USEM experiments confirm the sensitivity of the technique to detect carriers dynamics in semiconductors, with a time resolution below the picosecond [9]. This work focuses on the development of ultra-high vacuum (UHV) ultrafast scanning electron microscopy at the Physics Department of Politecnico di Milano. The ability of scanning electron microscopy (SEM) of accessing large field of view and of attaining nanoscale resolution by secondary electron (SE) emission is joined to the ultrafast time resolution of a pulsed laser. The sample environment is maintained under UHV conditions, which preserve surface from contamination, with the aim at investigating the dynamics of charge carriers at surfaces of semiconductor and insulator materials and devices.

In chapter “2 State of the art”, Ultrafast Scanning Electron Microscopy is introduced, and the literature on charge carrier dynamics in semiconductors will be presented. Alternative and complementary techniques are also discussed.

The commissioning of the USEM apparatus is described in chapter “3 Experimental setup”, with particular emphasis on the realization of the pulsed electron source and its characterization. The operating parameters, the measurement technique, and the spatial and time resolution obtained is discussed.

Chap. 4 and 5 deal with the experimental results obtained on prototypical semiconductor and insulating systems. Chapter “4 USEM investigation of the surface charge dynamics at the Si(001) surface as a function of doping” is dedicated to the investigation of charge dynamics at the Si(001) surface as a function of the material doping (*n* and *p*, from intrinsic to degenerate at 10^{19} cm^{-3}). In our pump-probe setup, an UV femtosecond laser excitation pulse and a delayed picosecond electron probe pulse are spatially overlapped on the sample, triggering secondary electrons (SE) emission to the detector. The delay time between the pump and the probe is spanned over a range of 4 ns. The use of near ultraviolet (NUV) pump pulses allows optimizing the surface sensitivity of the experiment, as the photon absorption length in Si (about 10 nm) approaches the nm escape depth of the SE probe. The time evolution of the SE imaging contrast is attributed to the superposition of bulk and surface mechanisms. A strong, nearly monotonic dependence on the doping level of the SE emission was found, which suggest a leading role of the carrier population in the contrast generation mechanism. The experimental results also show a strong dependence on the surface preparation, supporting the surface sensitivity of the technique. The dynamics evolves over several timescales ranging from tens of picoseconds up to tens of nanoseconds. A preliminary interpretation of the physics behind the contrast formation involves as main actors the dynamics of charge carriers and of trap states at the surface [35,36], which determines a change of the vacuum barrier for the emitted electrons by a band flattening mechanism. These evidences highlight the potential of USEM to image ultrafast dynamics at surfaces of semiconductor materials and devices.

The case of insulator surfaces was investigated by point measurements, using signal frequency modulation to filter out the continuous-wave component due to sample charging. A fast dynamics was measured on a 100 nm film of aluminum oxide on a silicon substrate, with components ranging from tens of picoseconds to few nanoseconds, that fits within the timescales typical of the ultraviolet color center evolution. The surface sensitivity of SE detection confirms the presence of active color centers at large gap insulator surfaces and broadens the field of application of USEM in todays nano-devices.

Chapter 5 USEM investigation of the color center charge dynamics at the surface of aluminum oxide” deals with the study of charge dynamics in aluminum oxide, taken as a prototypical insulator[37]. Aluminum oxide, thanks to its excellent mechanical and insulating properties, has applications ranging from aerospace to electronics [38]. Although being an insulator, aluminum oxide absorbs subgap photons thanks to charges trapped in lattice defects, known as color centers[39]. Color centers excitation and recombination has been fully studied by optical techniques[40–42]. Electrons trapped in defects in insulators may be excited both optically and by an electron beam as reported by cathodoluminescence experiments[43]. In the USEM experiment, an UV femtosecond laser pulse and a delayed picosecond electron probe pulse are spatially overlapped on a sample made by 100 nm film

of aluminum oxide on silicon, triggering SE emission to the detector. In order to enhance the contributions of the defects with ultrafast dynamics, the intensity of the electron pulses was modulated, and the SE signal was demodulated synchronously with a lock-in. The SE intensity, over a 4 ns range, shows ultrafast dynamics components ranging from tens of picoseconds to few nanoseconds. A model is proposed to describe the SE dynamics observed in terms of the color centers evolution. According to the knowledge of the author, this is the first application of USEM to insulating materials, showing the potential of the technique over a large range of systems and applications from Electronics and Photonics to Quantum computing.

“Appendix A: UED investigation of Verwey transition dynamics in magnetite” is devoted to the dynamics of the Verwey transition in magnetite, studied by ultrafast electron diffraction at the Laboratory for Ultrafast Electron Microscopy and Spectroscopy at Ecole Polytechnique Federale de Lausanne where I attended a three month stage.

2 State of the art

This chapter introduces the problem of attaining ultrafast time resolution in electron techniques, with the main focus on microscopy. After recalling the relevant features of scanning electron microscopy, the present implementations of Ultrafast Scanning Electron Microscopy and of alternative approaches will be compared on the ground of their results and technical limits for the study of carrier dynamics in semiconductors. At the end of the chapter, the goal specifications for this thesis will be reported.

2.1 Scanning Electron Microscope

Scanning electron microscopy (SEM) allows to map the morphology and, with the support of energy-resolved probes, chemical composition, with spatial resolution and surface sensitivity down to few nanometers [44]. The result is obtained by focusing an electron beam, called primary beam, on the surface of a bulk sample. The electrons of the beam lose their energy by scattering with other electrons in the sample and with the ions of the lattice. When the sample thickness exceeds few micrometers, the incident beam is completely attenuated, and the primary electrons (PE) emitted by the source do not pass through the sample. Nonetheless, some photons and electrons are emitted from the same side of the incident beam. The energy of the emitted particles is lower than the one of the primary electrons that may range from hundreds of eV up to 30 keV. A sketch comparing the depth at which different kind of radiation are generated, and a plot of the energy spectrum of the emitted electrons are reported in Figure 1.

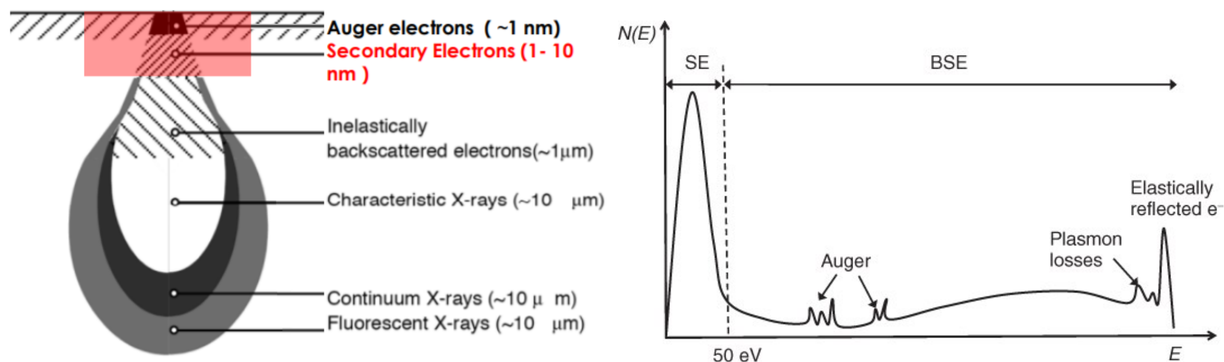

FIGURE 1 - VOLUME EXCITED BY THE PRIMARY BEAM AND THE DIFFERENT DEPTH PROBED BY X-RAYS AND BY ELECTRONS ON THE LEFT. ON THE RIGHT ENERGY SPECTRUM OF EMITTED ELECTRONS AFTER THE INTERACTION OF A BEAM OF ELECTRONS WITH ENERGY E WITH A BULK SAMPLE

In the plot, it is possible to distinguish the peak corresponding to elastically reflected PE called backscattered electron, BSE. PE may propagate for few micrometers in the sample, in all directions. BSE, therefore, could be reach a depth of few micrometers and being emitted few micrometers away from the impact point of PE, independently on the size of the PE beam at the surface[44]. When PE are not elastically scattered, they undergo energy losses due to scattering with electrons of the material determining deep core hole excitations or lower energy excitations like the creation of electron-hole pairs. Deep core hole excitation may decay radiatively,

emitting X-rays [45], or by Auger decay, emitting electrons[46]. The volume of the sample excited may extend to a depth of a tenth of micrometers. The width may also reach few micrometers even if the size of the PE beam at the surface is smaller. While X-rays may be collected from the entire excited volume, only the Auger electrons emitted from few atomic layer below the surface could be emitted without undergoing inelastic scattering. Lower energy excitations may bring to radiative decays, with emission in the optical region known as cathodoluminescence [47], or to the emission of low energy electrons from the material. Electrons, initially belonging to the sample that are emitted following the collision with PE are known as SE and have energy generally below 50 eV [48]. SE are generated in the entire volume excited by PE, but only the ones created few nanometers below the surface could be emitted [48]. Different detectors may be used according to the interest in photons or electrons and to the energy region involved. In the scanning electron microscope, imaging is obtained by recording the intensity of the desired signal, (the most common is SE emission) at each pixel position on the sample by moving there the primary beam spot. Usually, pixels are distributed on a matrix of equally spaced points on the surface. The intensity is reported in grayscale maps called SEM micrographs. The acquisition process is called raster scanning and involves to set the pointing of the PE beam thanks to deflection plates and to record the detector signal acquired over the so-called 'dwell time'. It is possible to map several signals like the intensity of SE, BSE, the energy-resolved Auger electron emission, the cathodoluminescence or X-ray emission. In the following, the most relevant for this thesis will be discussed in detail, with particular emphasis on SE.

2.1.1 SEs and spatial resolution

Most of the SEs have an energy below 50 eV. They are electrons coming from the sample excited by inelastic scattering. SEs are generated in all the volume of the sample excited by the PE beam, but only the ones nearest to the surface may be emitted. Emission depth is generally considered of the order of few or even less than a nanometers[49], depending on the PE energy and on the material. Therefore, the emission is localized to the area directly under the surface at the PE beam spot as shown in Figure 1. Nowadays, PE beam focusing below 1 nm of diameter can be reached. This is the ultimate spatial resolution limit when imaging by SE. SEM micrographs showing SE intensity have to be considered strongly sensitive to the surface because the emitted SEs are generated only a few nanometers below the surface. The intensity of SE current emitted depends mainly on the material, on the local work function and on the effective area of interaction of the PE beam with the surface of the sample. The latter depends on the angle between the propagation direction of the PE beam and the normal of the surface in the footprint ot the beam. The larger the angle, the bigger the area of interaction and the emission of SE current: strongly dependent on the local morphology of the sample. The collecting angle of the SE detector, usually quite off-axis in case of side-mounted detectors, also determines shadowing effects on SE intensity maps. These factors made the success of the SEM as a simple and affordable tool to have an insight on the morphology of micro and nanostructures. A comparison of SEM micrograph acquired with SE and BSE is shown in Figure 2.

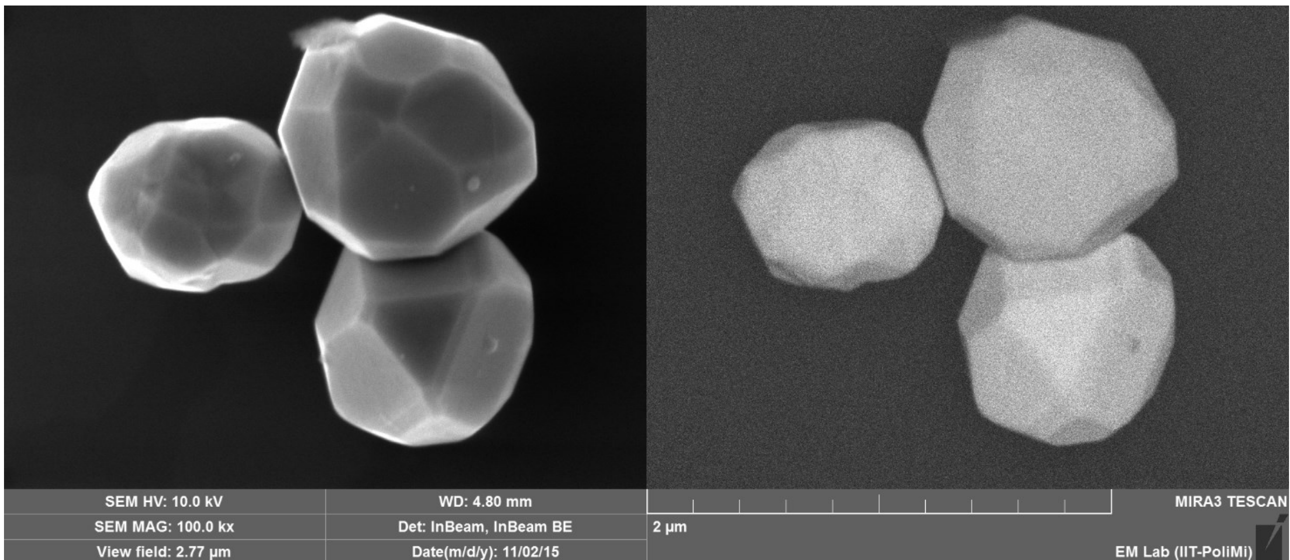

FIGURE 2 – GOLD MICROSTRUCTURES ON SILICON: SE IMAGE ON THE LEFT AND BSE IMAGE ON THE RIGHT

SEM micrograph shown confirm that SE contrast depends both on material and morphology, while BSE contrast is more related to the chemical composition. The lateral spatial resolution appears better in the image representing SE intensity with respect to BSE, thanks to the smaller area of emission. Small details that appears only in the SE images confirms not only the better spatial lateral resolution but also the surface sensitivity of SEM images representing SE intensity. Regarding emitted electrons, SE, therefore, appear the best compromise between resolution and contrast. SEM images are 2D projections of the sample surface along the PE beam direction. It is eventually possible to reconstruct a 3D model measuring the actual height of each point through a geometrical reconstruction process using two or more images of the same surface, taken at different angles of incidence of the PE beam like, i.e., in stereophotogrammetry [50].

2.1.2 Auger emission

The excitation of core electrons brings to the formations of core holes that could be filled by a radiative decay, leading to the emission of x-rays with energies typical of the materials involved or by Auger decay leading to the emission of electrons [46]. Both the analysis of the energies of emitted photons and electrons give information about the chemical composition. Only Auger electrons generated within a depth of few atomic layers from the impact point of the PE beam are detected: since the others have a high probability to undergo inelastic scattering. On the contrary, X-rays, thanks to the much lower cross section of interaction with matter, comes from the entire excited volume. Therefore, the analysis of characteristic X-rays allows to get information on the elemental concentration in the bulk of the material at a depth of up to few micrometers below the sample surface, while Auger spectroscopy is extremely surface-sensitive and gives information about the elemental composition of the first atomic layers. A comparison of Auger and X-ray spectra for carbon is reported in Figure 3.

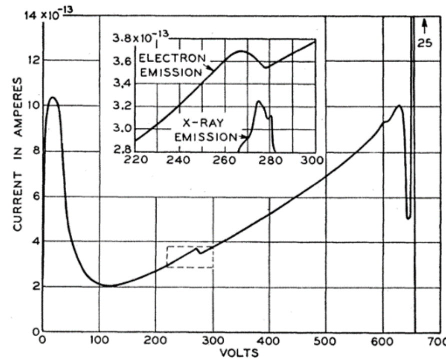

Figure 3 – Energy spectrum of emitted electrons from a carbon sample, in the inset the comparison between the Auger peak and the X-ray peak of carbon. Reprinted with permission from [46]

Due to its surface sensitivity, Auger spectroscopy requires an ultra-high vacuum (UHV) environment at the sample position in order to avoid surface contamination. Auger spectroscopy may be relevant to study surface coatings or surface contamination [51][51]. Scanning Auger microscopy combines the Auger energy analysis with the spatial resolution of the SEM in UHV conditions; this approach will be used to characterize the sample surface of Si in chapter 4 USEM investigation of the surface charge dynamics at the Si(001) surface as a function of doping.

2.2 Time resolution in electron microscopy

The temporal resolution of commercial SEMs is limited to milliseconds by the process of image acquisition. The time required for the acquisition of an image in SEM it is roughly the product of the dwell time, and the number of pixels summed to the time required to move the electron beam. The acquisition of sequence of images in real time allows studying phenomena that involves a dynamical evolution of the sample. The technique, called real-time acquisition, is the best choice for phenomena slower than few milliseconds. Figure 4 shows a sequence of SEM images acquired on a carrot while applying tensile loading. First, the structure deforms elastically, and then a crack appears [52].

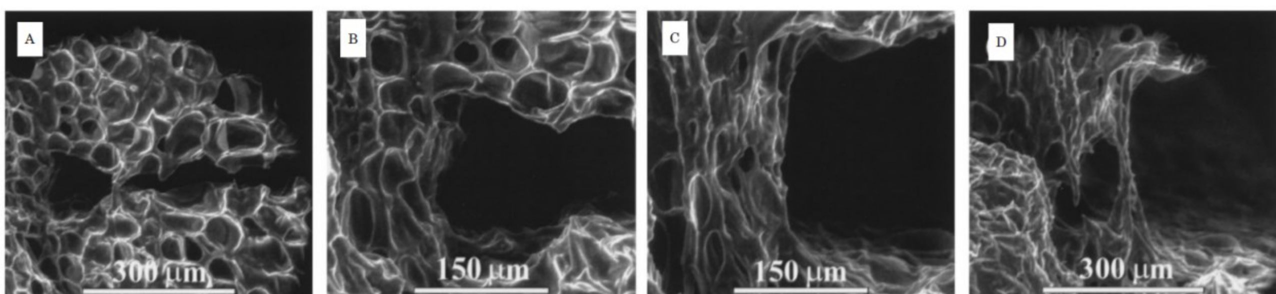

Figure 4 – Sequence of SEM images showing opening of a crack in a carrot due to tensile loading. Reprinted with permission from [52]

Faster sequence may be obtained in optical imaging or in transmission electron microscopy (TEM), thanks to the parallel acquisition. In optical cameras gating systems of the optical channel allows temporal resolution in microsecond range. To improve the resolution of electron microscopy, the continuous electron beam was substituted with a pulsed one. One of the first implementations was proposed by Bostanjolo and coworkers [53,54]. Dynamic TEM, proposed by Thomas LaGrange triggers a dynamic on the sample with a laser pulse and acquires an image with a delayed electron pulse [55]. He reported a temporal resolution of 30 ns and a spatial resolution of 20 nm. Dynamic TEM is the only option for phenomena that changes the sample without any possibility of recovering the initial condition. Examples are laser ablation that breaks atomic bonds or phenomena that introduce mechanical stress overpassing the elastic deformation limit of the material. Nonetheless, repeatable phenomena exist that do not permanently change the samples, like excitations by laser or electron pulses, weak enough to impact on the sample's phonon or electron population without displacing the atoms. Once the excitation stops, the time required for the sample to recover its initial condition is called recovery time. Only under the hypothesis of repeatable phenomena, it is possible to go beyond the time resolution of real-time acquisition in SEM with the pump-probe (P-p) approach. Both pump and probe are pulses that interact with the sample. The pump pulse triggers the excitation of interest in the system, while the probe excites a less perturbing excitation that is used to investigate the state of the system at a chosen time delay. By scanning the delay of the probe with respect to the pump, it is possible to build a movie of the time evolution of the phenomenon. The excitation and test cycle is usually repeated many times using low energy pulses, allowing to avoid permanent changes at the sample and to improve statistics. The time interval between two consecutive pump pulses has to be larger than the recovery time of the sample back to the initial state of interest. Many implementations of the P-p technique have been proposed with electrical and optical pulses [56]. Since the convolution of the two pulses determines the experimental time resolution, they have to be as short as possible. In optical pump-probe, also known as time-resolved spectroscopy, both pulses are optical and generated by a mode-locked laser. Examples of the optical properties measured by an optical probe are absorption, used for transparent materials [57] [58], and reflectivity, used for opaque materials like metals [59]. Optical pump-probe found wide range of applications: from measuring carrier lifetime in semiconductors [60] to study chemical reaction like the isomerization of the rhodopsin molecule, at the base of the human vision, both with a time resolution better than 50 fs [61]. The plot of relative transmission versus delay for the rhodopsin is shown in Figure 5.

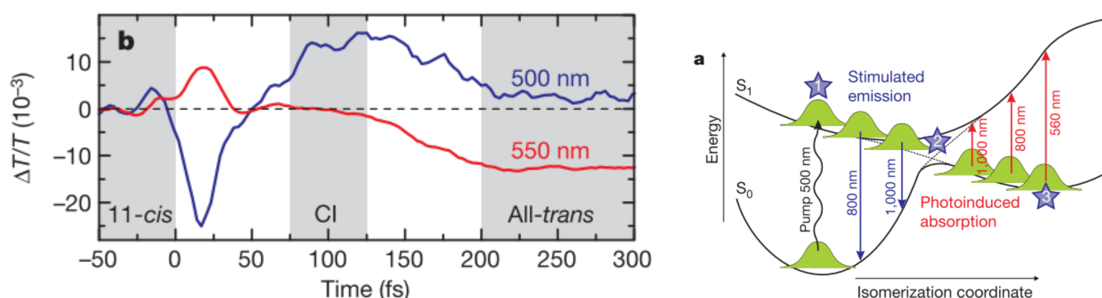

FIGURE 5 – RELATIVE TRANSMISSION OF RHODOPSIN MOLECULE VERSUS PROBE TO PUMP DELAY FOR TWO DIFFERENT PROBE WAVELENGTHS AND SCHEME OF THE REACTION. REPRINTED WITH PERMISSION FROM [61]

An experimental setup for optical pump-probe is reported in Figure 6. The train of optical pulses generated by the laser is beam split to generate the pump and probe pulses. They follow different optical paths and are superimposed on the sample. The wavelength of the two beams may be chosen separately by using crystal for

harmonic generation to obtain submultiples of the fundamental wavelength generated by the laser or Optical Parametric Generator for a continuous regulation. The pump pulse passes through a delay line made of a back reflector installed on a linear motorized stage. By moving the back reflector, the length of the optical path is changed and the delay with respect to the probe tuned. The pump beam is stopped after the sample while the probe is directed toward a detector that measures the intensity of reflected or transmitted probe light in dependence of the delay.

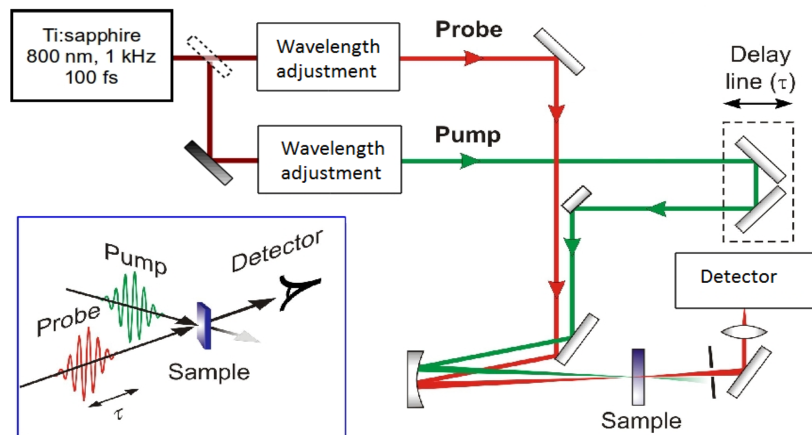

FIGURE 6 – EXPERIMENTAL SETUP FOR OPTICAL PUMP-PROBE

2.2.1 Optical pump probe on semiconductors

Two selected work are presented here to highlight the potentials and the limits of optical pump-probe techniques applied to study the topic of charge carrier dynamics in inorganic semiconductors. In both works, an optical pump pulse of photon energy larger than the optical bandgap excites electron-hole pairs in silicon. Sabbah and Riffe measured the transient reflectivity of the optically-excited area of silicon (001) with the goal to study excitation dynamics and carrier recombination [60]. Their results are reported in Figure 7.

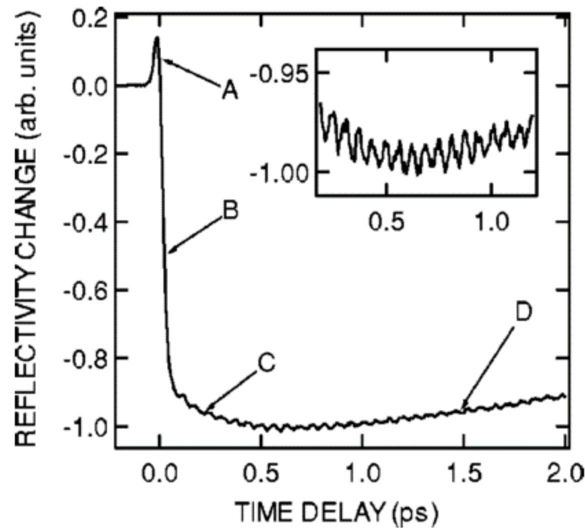

FIGURE 7 - OPTICAL PUMP-PROBE ON BULK SILICON (001) WITH 28 FS RESOLUTION. REPRINTED WITH PERMISSION FROM [60]

Plot reported in Figure 7 left represents transient reflectivity measured on silicon (001) covered with native oxide with a time resolution of 28 fs versus the delay of the probe with respect to the pump. The dynamics shows a positive spike at zero delay, followed by a decrease in reflectivity and a recovery in picosecond range. The positive spike in the reflectivity change is attributed to a nonlinear process. The decrease was fitted by the authors with a double exponential: time constants found are equal to 32 fs and 260 fs. The phenomenon describe by an exponential with time constant equal to 32 fs has a duration comparable with the length of the exciting pulse and is attributed to the generation of hot electrons. The second one, with time constant of 20 fs, is attributed to the thermalization of hot electrons with the lattice. Hot electrons are conduction band electrons with an energy higher than the minimum allowed by conduction band. They come from the valence band and are excited by the optical pump at 800 nm. Since photon energy is higher than the silicon bandgap, hot electrons have some kinetic energy. Hot electrons thermalize with the lattice releasing the kinetic energy by inelastic scattering inducing lattice oscillations called phonons. Oscillations observed in reflectivity are attributed to coherent phonons. The recovery with time constant in picosecond range is attributed to interband recombination mediated by surface defects [60]. Gabriel and co-workers built a pump-probe setup with an optical microscope to measure excited carrier transport and recombination with spatial resolution. The pump was kept fixed while probe was scanned on the surface of the sample [62]. Plot reported in Figure 8 reports the decay dynamics of transmitted light through nanowires. NW1 and NW2 are intrinsic, while NW3 is n-doped.

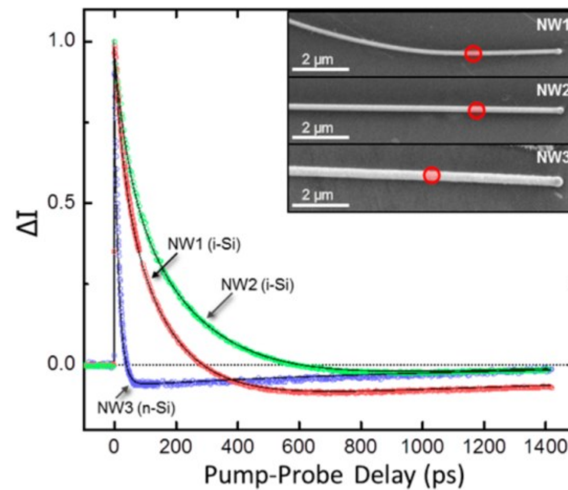

FIGURE 8 - OPTICAL PUMP-PROBE ON SILICON NANOWIRES WITH 500 FS TIME RESOLUTION. REPRINTED WITH PERMISSION FROM [62]

The experiment uses pump at 425 nm and probe at 850 nm that is raster scanned on the sample. The effect observed on all the nanowires is an increase of the intensity of transmitted light just after zero delay followed by exponential recovery. This is attributed by the authors to a bleaching of the absorption, due to the fact that electrons, already excited to conduction band by the pump, show reduced capability of absorbing light. Recovery, attributed to surface recombination, has a time constant of tens of picosecond for the intrinsic nanowires while appears to be an order of magnitude faster for the n-doped nanowire NW3, due to higher concentration of surface defects or to Auger recombination. Once recovered the positive component the intensity of transmitted light goes below zero, the steady-state values for large negative delays, showing that probe light is absorbed by the material. The absorption is attributed to carriers excited by the pump and then trapped. The recovery time constant, attributed to trapped carriers recombination, ranges from hundreds of picoseconds to few nanoseconds. To study diffusion of excited electrons along the nanowire time-resolved images were also acquired by scanning the probe on the sample while keeping fixed both the pump position and the probe to pump delay [62]. The images are reported in Figure 9.

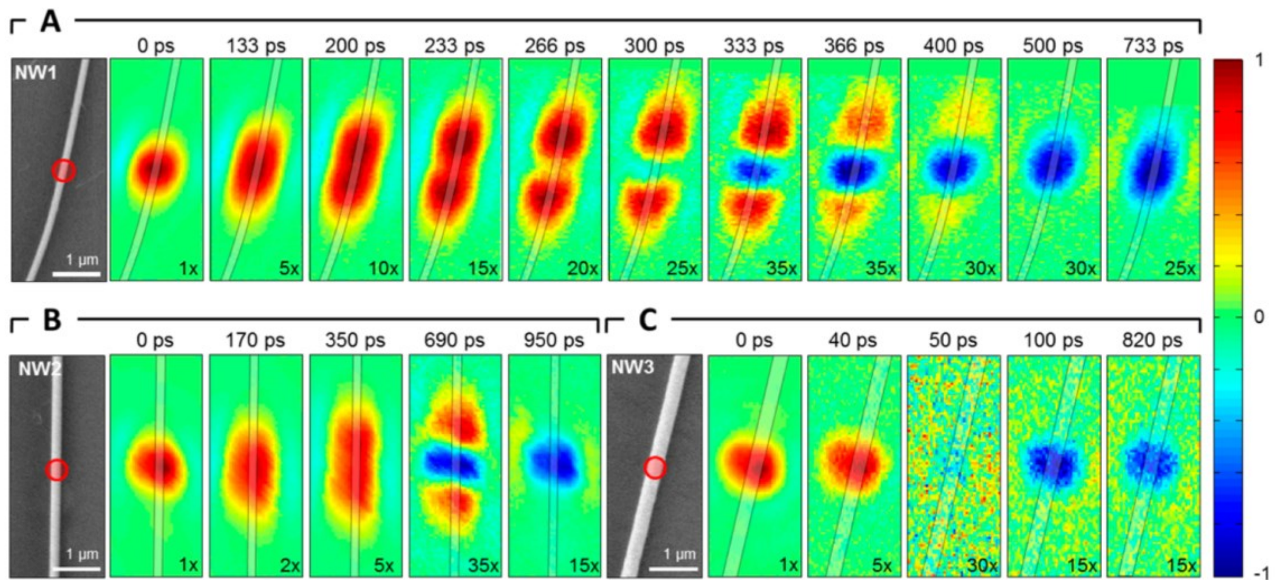

FIGURE 9 – OPTICAL PUMP-PROBE IMAGES ACQUIRED AT CONSTANT TIME DELAY IN SILICON NANOWIRES. THE MEASUREMENTS REFER TO THREE DIFFERENT NANOWIRES: FOR EACH ONE, A SEM IMAGE SHOWS THE MORPHOLOGY OF THE SAMPLE AND THE POSITION OF THE PUMP. REPRINTED WITH PERMISSION FROM [62]

The time-resolved images show the diffusion of the optically induced free carriers along the nanowires and their recombination. The positive signal, in red, spreads along the nanowires and is attributed to free carriers, while the negative signal, in blue, is localized and is attributed to trapped carriers. The nanowire called NW3 has a faster recombination speed than the other two, confirming what was reported in the comment to figure Figure 8. The spatial resolution appears of few hundreds of nanometers. The Abbe diffraction limit on the minimum radius of the probe spot size is equal to $d = \frac{\lambda}{2NA} = 530\,nm$ for the parameters used: numerical aperture NA equal to 0.8 and wavelength λ equal to 850 nm. The experimental results reported by the authors [62] not only are fully compatible with the light diffraction limits for the far field optics used in the experiment but also shows that the authors were able to reach that limit. Higher spatial resolutions could be obtained only by near field optical technique or by using shorter wavelength far field microscopes, like X-ray or electron microscopy.

2.2.2 Ultrafast Electron Microscopy

Many approaches have been proposed to combine optical pump-probe with electron microscopy. It is possible to substitute either the pump or the probe with an electron pulse or to generate electrons by photoemission at the sample by the optical probe pulse[63]. Except for the last method, introduced in paragraph 2.5.3 Time-resolved PEEM, the others require to generate electron pulses with the shortest duration at the sample surface. The first proposal to obtain electron pulses was to chop the electron beam. By synchronously opening and closing a beam blanker, it is possible to slice the electron beam into pulses that were delayed with respect to the pump excitation. In the first implementations, the beam blanker was made by electrostatic deflecting plates, and the clocking signal was electrical. The experimental setup was used for example to study oscillation of voltage onto the surface of a microdevice with a time resolution of 10 ns [64]. New beam blanking design allows today to obtain electron pulses of less than 90 ps [65], at the cost of reducing the electron beam current by the duty factor of the chopping cycle. The number of electrons per pulse may be estimated in 0.01 by multiplying the

length of the pulse (90 ps) for the PE current (20 pA) and dividing by the electron charge. This approach has the advantage of simplicity and versatility in accessing long time delay ranges up to the single shot. To overcome the brightness limitation of methods based on beam chopping, reaching one electron per pulse, and improving time resolution laser stimulated ultrafast electron sources were developed. Miller[66], Zewail [26] [67], Merano[3], and others [56] proposed and implemented time-resolved electronic microscopes based on ultrafast electron sources. The approach patented by Ahmed Zewail, awarded with Nobel Prize in 1999 for his studies about femtochemistry [68], is derived from optical pump-probe. Pump is an optical pulse while an ultrafast electron source allows to convert the probe from an optical pulse to an electron pulse[69].

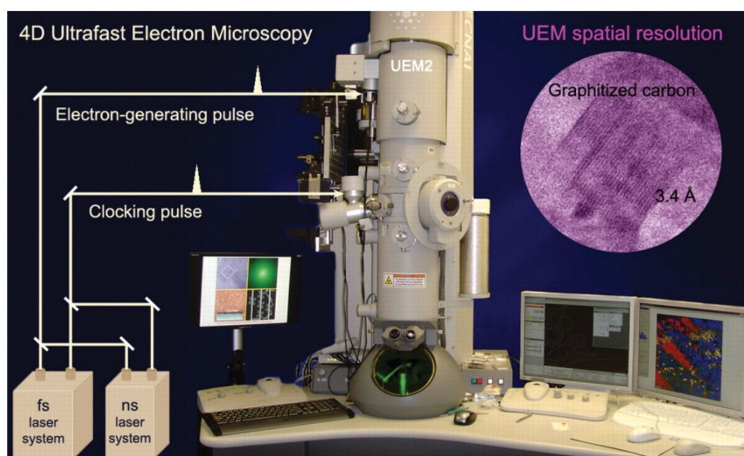

FIGURE 10 – EXPERIMENTAL SETUP FOR A TIME-RESOLVED TRANSMISSION ELECTRON MICROSCOPE. REPRINTED WITH PERMISSION FROM [69]

The experimental setup developed by Zewail is reported in Figure 10: the setup was also patented [67]. Both the pump and the probe are obtained by splitting the output of a single mode-locked laser with a semi-reflective mirror. Therefore pump and probe pulses are coherent. Pump and probe follow a different path from the beam splitter to the sample. The pump passes through a delay stage and then reaches the sample. The probe is converted from an optical pulse to an electron pulse by an ultrafast electron source and substitutes the continuous electron beam of the microscope. The delay stage allows to scan the delay between the pump and the probe by changing the length of the optical path of the pump. The approach proposed allows to use the not time-resolved detectors of commercial microscopes to get time-resolved measurement. The general scheme was applied to all the main categories of electronic microscopes:

- Transmission Electron Microscope (TEM) becomes Ultrafast TEM (UTEM or UEM) [70];
- Electron Diffractions becomes Ultrafast Electron Diffraction (UED) [71];
- Scanning Electron Microscope (SEM) becomes Ultrafast SEM (USEM or SUEM) [26] [9];
- Scanning Electron Microscope (STEM) becomes Ultrafast STEM (STUEM) [72];

All the techniques have the goal to study electron and structural dynamics [12] [16]. Other groups joined the field of ultrafast electron microscopy, and many works have been published until today [73], mainly by using transmission electron microscopy. Ultrafast Scanning Electron Microscope, subject of this thesis, will be described in detail in the next paragraph 2.3 Ultrafast Scanning Electron Microscopy2.3 Ultrafast Scanning Electron , while UTEM and UED will be introduced in paragraphs 2.6.1 Time-resolved electron diffraction and 2.7.1 Ultrafast Transmission Electron Microscopy respectively for comparison with USEM.

2.2.3 Ultrafast electron sources

The development of sources of ultrafast electron pulses and the study of propagation of ultrafast electron pulses was done by Miller[66], Zewail [26], Merano[3], Baum [74] and others [75]. Ultrafast electron sources are low work function materials that photoemit electrons when excited by light pulses. There are different types of ultrafast electron sources that differ in the geometry of optical excitation and configuration of the electric fields. The many models available are presented in the review by Baum about electron pulses [74]. The most used in ultrafast electron microscopy are thin film photocathodes [75] and needles [14]: a sketch of both is reported in Figure 11.

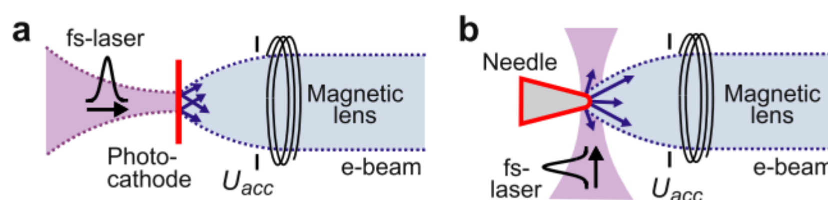

FIGURE 11 – LASER POWERED ULTRAFAST ELECTRON SOURCES. REPRINTED WITH PERMISSION FROM [74]

In Figure 11, panel a, a photocathode is represented: it is made by a thin layer of low work function metal deposited on the down-beam side of a transparent material. The laser beam crosses the transparent material and determine photoemission by the active layer. In Figure 11 panel b a needle is represented. Needle may be made by LaB_6 or by tungsten, usually covered by a thin film of zirconium oxide to reduce work function. Laser arrives on the tip perpendicularly to the symmetry axis and determines photoemission of electrons from the tip of the needle. The main parameters to evaluate an ultrafast electron source are the brightness and the product of temporal spread and energy spread because both quantities stay constant during the propagation along the electron optics of the beam line. Brightness is defined as the current emitted divided by the area of the source and the solid angle of emission. Brightness conservation during electron propagation along the beamline is related to the Liouville's theorem and the minimum achievable is described by the Abbe diffraction limit, also related for a single particle to the uncertainty principle on momentum and position. The higher the brightness the lower the minimum size of the beam achievable on the sample. Photocathodes have a minimum source size of few hundreds of nanometers, limited by optical diffraction, and limited emission divergence. Needles have source size ranging from ten to hundreds of nanometer, therefore two order of magnitude less than the photocathodes. Nonetheless, the lower size is compensated by a higher divergence[74]. Average brightness of $10^6 - 10^7\ A\ cm^{-2} sr^{-1}$ have been reported for both photocathodes [3] and needles[14]. This result is different from what obtained in the case of continuous emission where the needles reach the highest brilliance [76]. Photocathodes are implemented in UED thanks to the wide source area [22]. Ultrafast TEM has been implemented both with needle [14] and with photocathodes [4]. All the implementations of Ultrafast Scanning Electron Microscopy reported in the following use a needle [26] [27]. An ultrafast electron source based on a needle may be obtained by modifying the operating conditions of a field emission gun, therefore the system allows imaging both with pulsed and continuous electron beam. Furthermore, the needle, thanks to the lower beam size requires a lower demagnification factor. The use of photocathode is reported in previous implementations of time resolved SEM's [3] [56]. Once created, the electron pulse behaves like a space-charge region so it broadens due to coulomb repulsion among the electrons of the pulse [66]. The broadening in the

direction of propagation turns into different arrivals time of the electron on the sample and therefore determines a loss in the time resolution of the system [77]. To avoid limitations on the time resolution it is necessary to adopt longitudinal focusing lenses like RF cavities [22,78] or to operate with single electron pulses[9]. Nonetheless, Liouville's theorem, states that the product of the energy spread and the temporal spread of the pulse should be constant setting a limit to the compression of the electron pulse. The minimum limit in case of a single particle is set by the uncertainty principle [74].

2.3 Ultrafast Scanning Electron Microscopy

Ultrafast scanning electron microscopy (USEM) is a time-resolved technique sensitive to the surface [9]. A first attempt to build a time-resolved microscope was done in the '80s with the goal to measured electrical signals in integrated circuits. The experimental setup developed is a modified optical pump-probe where optical pump is converted into an electrical signal by a photoconductive switch and the optical probe control the PE beam through an ultrafast electron source[56]. In this pioneering work, the spatial and temporal resolution obtained were 0.1 µm and 5 ps respectively[79]. Later, Merano built a time-resolved SEM with the goal to study charge transport in nanostructures: the pulsed PE beam was used to trigger cathodoluminescence measured by a time-resolved detector[3]. The setup and the results will be discussed in paragraph 2.5.2 Time-resolved cathodoluminescence. The latest configuration of the time-resolved SEM, called Ultrafast Scanning Electron Microscope (USEM), was proposed and built by the group of Zewail at Caltech [26], while an updated version is now operated by Omar Mohammed at KAUST [27]. In USEM an optical pulse triggers the dynamic in a semiconductor sample, by exciting electrons from valence to conduction band, while a delayed electron pulse, generated by an ultrafast electron source, act as probe determining the emission of SE to the detector. This paragraph deals with the experimental USEM setup, and the characterization of the spatial and temporal resolution. The results reported by the group of Zewail (Yang, Mohammed, Cho, Najafi, and others), proves that the SE intensity recorded in pump-probe mode is sensitive to optically induced carriers in semiconductor [9,28]. In principle, USEM - thanks to the chemical contrast given by electron or X-rays spectroscopy or to the structural contrast provided by Electron Back Scatter Diffraction (EBSD)- allows to study others ultrafast phenomena like optically induced chemical reactions or lattice dynamics. Some preliminary results were reported by the group of Zewail about time-resolved EBSD and will be discussed in the paragraph 2.6.2 Time-resolved electron diffraction in USEM. Finally, a different approach to study charge dynamics in semiconductors, with combined spatial and temporal resolution, based on time-resolved photoemission[63], will be presented in paragraph 2.5.3 Time-resolved PEEM.

2.3.1 Experimental setup

The typical experimental setup in pump-probe mode reported in Figure 12 panel a from ref. [26], includes a femtosecond laser and a SEM with needle emission gun. The Schottky field emission gun is often chosen for the high brightness and can be adapted as ultrafast electron source by opening an optical access to the tip of the needle. A more detailed view of the excitation geometry is reported in Figure 12 panel b.

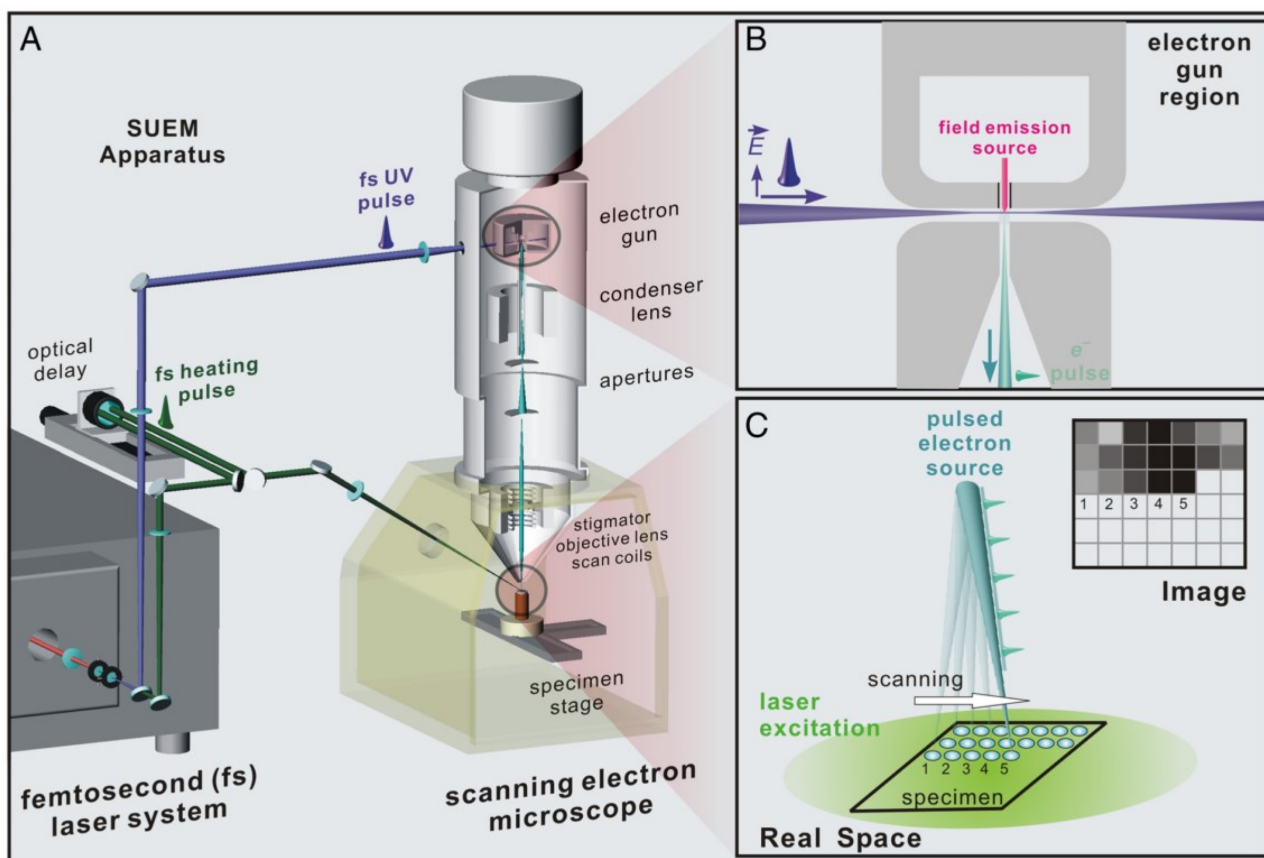

FIGURE 12 – EXPERIMENTAL SETUP OF THE ULTRAFAST SCANNING ELECTRON MICROSCOPE. REPRINTED WITH PERMISSION FROM *[26]*

As shown in the general scheme of ultrafast electron microscopy the output of the laser is beam splitted: a part of the beam passes through a delay stage and reaches the sample while the other reaches the ultrafast electron field emission source [26]. A practical choice for the wavelength of the laser is 1030 nm, due to the ready availability of powerful fiber lasers with hundreds of femtosecond pulse duration and repetition rates from kHz to tens of MHz. Harmonic generators are installed on the optical path to the sample, providing excitation wavelengths of 515 nm, 343 nm, and 257 nm, for the second, third and fourth harmonic respectively. The operating parameters of the source have been modified in order to prevent continuous emission. This result was obtained by cooling the tip below thermal emission threshold. Therefore Yang and coworkers in ref. [26] state that the electron emission is due only to photoemission and that the resulting PE beam is fully pulsed. Time-resolved images are acquired by scanning the PE beam on the sample and recording SE emission for each point as in classical SEM [80]. Yang and coworkers regulated the field of view of the image to include in the image the area excited by the pump laser beam as shown in Figure 12 panel c [26]. The position of the optical beam on the sample and the delay of the electronic pulse with respect to the optical pulse are kept fixed during the acquisition of the entire image. Yang and coworkers estimated that the SE signal from a single pixel is the result of the average of $\sim$ 5000 pump-probe cycles [26]. A test image acquired with pulsed PE beam is reported in Figure 13.

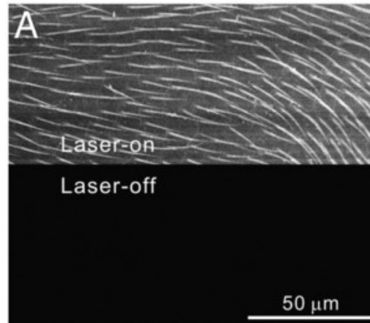

FIGURE 13 – USEM IMAGE ACQUIRED WITH PULSED PE BEAM. DURING THE ACQUISITION OF THE IMAGE, THE LASER TO THE ULTRAFAST ELECTRON SOURCE WAS STOPPED. REPRINTED WITH PERMISSION FROM [26]

According to the authors, the image reported in Figure 13 confirms that the emission from the source is due only to the laser. In fact when the laser to the ultrafast electron source was stopped no SE emission was detected [26].

2.3.2 Spatial resolution

Authors evaluated spatial resolution on images acquired with pulsed electron beam [26] without the pump laser beam on the sample. A comparison was proposed among images acquired with continuous electron beam, as in classical SEM, and with pulsed electron beam, in USEM. Images are reported in Figure 14.

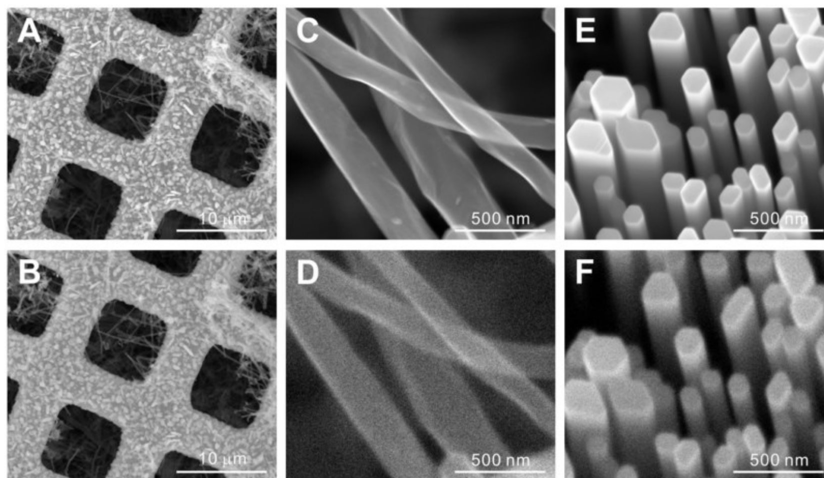

FIGURE 14 – SEM IMAGES (UPPER A,C,E) AND USEM (LOWER B,D,F) IMAGES OF NANOSTRUCTURES. CARBON NANOTUBES ON A COPPER GRID (A,B), CARBON NANOTUBES (C,D) AND ZINC OXIDE NANOWIRES (E,F). REPRINTED WITH PERMISSION FROM *[26]*

In USEM images, acquired with pulsed PE beam, the spatial resolution was evaluated equal to 10 nm [26].

2.3.3 Sensitivity to excited carriers and temporal resolution

Mohammed and coworkers showed that SE emission from the surface of silicon (100) is sensitive to optical excitation of the sample [9]. The result was obtained by acquiring two time-resolved USEM images: one at negative delay and the other at positive delay. In each pump-probe cycle of the image acquired at negative delay, the probe arrives before the pump. This means the PE pulse reaches the sample before the optical pulse. The opposite happens at positive delay. Authors reported an increase in SE emission from the optically excited area of the surface of silicon after the optical excitation, as shown in Figure 15 [9]. The pump wavelength used is 515 nm, and the fluence is $0.5\ mJcm^{-2}$. The images are acquired in single electron pulse regime [9] to avoid loss of resolution due to Coulombian broadening of the electronic pulse while travelling trough the electronic column [81][27] .

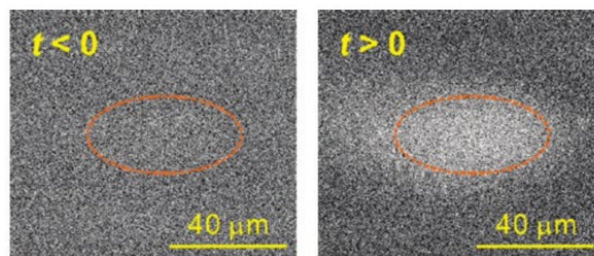

FIGURE 15 – TIME-RESOLVED USEM IMAGES ACQUIRED ON SILICON (UNDECLARED SURFACE ORIENTATION) AT NEGATIVE DELAY (T<0) AND POSITIVE DELAY (T>0). DASHED ORANGE ELLIPSE HIGHLIGHTS LASER FOOTPRINT. REPRINTED WITH PERMISSION FROM *[9]*

Authors evaluated the dynamics of the SE emission by acquiring a sequence of time-resolved images at different delays [9]. The average gray level, corresponding to the SE emission intensity within the area of the laser footprint, was plotted against the delay (Figure 16).

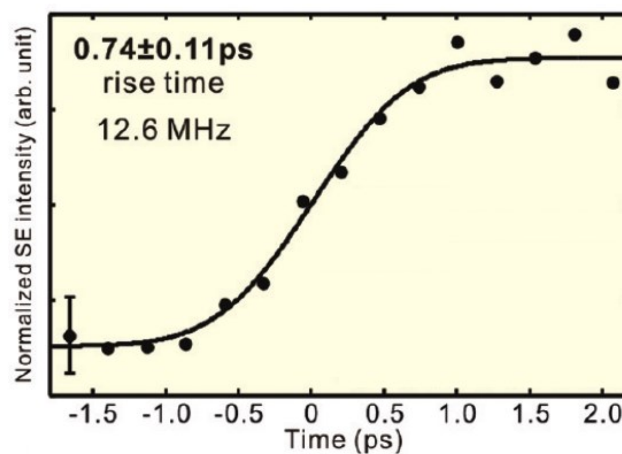

FIGURE 16 – NORMALIZED SE INTENSITY FROM OPTICALLY EXCITED AREA OF SILICON VERSUS PROBE TO PUMP DELAY. REPRINTED WITH PERMISSION FROM *[9]*

Mohammed and coworkers fitted the dynamics with an error function with rise time of $0.74 \pm 0.11\ ps$. The rise time is considered as a measurement of the system resolution, and is attributed to the energy spread of the electrons emitted by the ultrafast electron source. Mohammed and coworkers attribute the contrast observed to the increase of average electron energy, following the excitation of electron-hole pairs across the Si bandgap by the pump pulse (photon energy 2.4 eV, larger than the optical bandgap). A model was proposed and is described in detail in the following [9].

2.4 USEM on semiconductors

A brief overview of the results available in literature on imaging charge dynamics in semiconductors by USEM is presented in this chapter. Study of SE contrast were done on Si, GaAs, CdSe, and InGaN nanowires in dependence on doping, PE energy, and surface quality.

2.4.1 Sensitivity to doping

Cho and coworkers reported an USEM study of the SE emission from surface (110) of Gallium Arsenide in dependence on the doping [28]. Time-resolved images and plot of the SE intensities from optically excited area versus delay are reported in Figure 17.

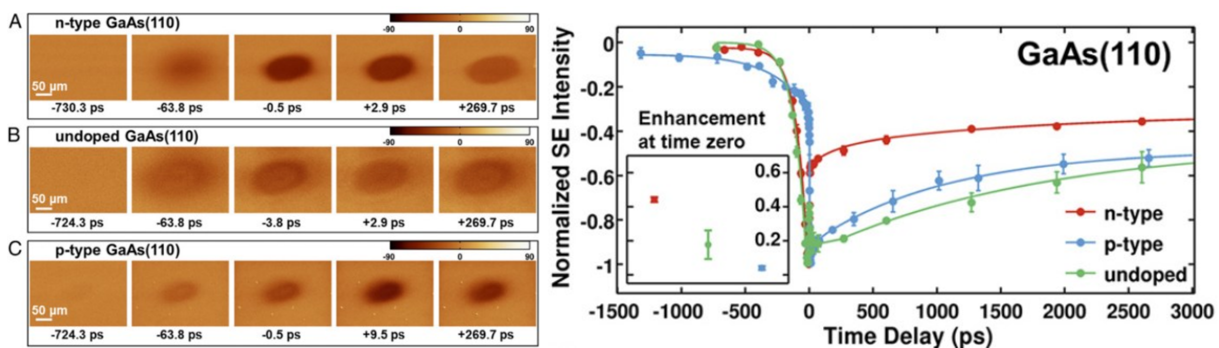

FIGURE 17 – TIME-RESOLVED DYNAMICS OF SE EMISSION FROM GALLIUM ARSENIDE AND SILICON AFTER OPTICAL EXCITATION. REPRINTED WITH PERMISSION FROM *[28]*

In the time-resolved images reported in Figure 17, the optical excitation determines a depletion of the secondary emission from the optically excited area, independently on the doping [28]. The differential SE contrast shown is defined as the SE average intensity from the optically excited area at a given delay minus SE average intensity from the same area at a large negative delay of reference (730 ps). A depletion corresponds to dark contrast. The graphs of the differential SE intensity versus delay show that the effect of the optical excitation recovers when increasing the delay. Has also to be observed that the depletion do not start its growth at the optical excitation, but tens of picoseconds before. This effect is identified in the following as contrast at negative delays, to distinguish it from what happens after optical excitation. Furthermore, reported intensity of

time-resolved SE emission in GaAs shows a dependence on the doping [28]. Cho and coworkers proposed a model; their picture is reported in Figure 18.

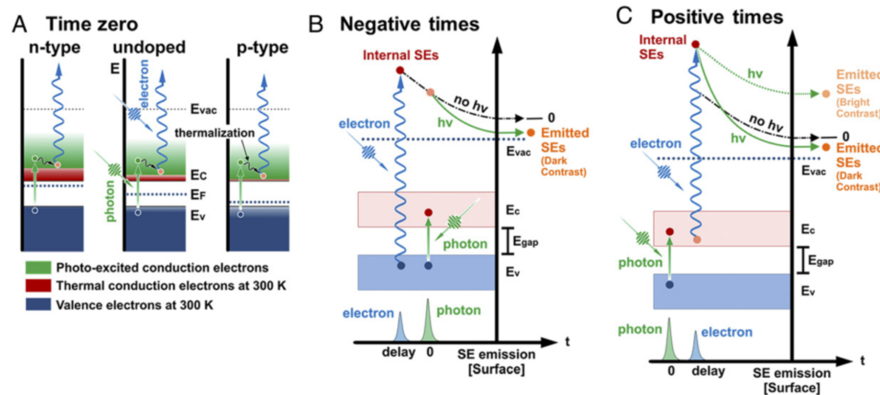

FIGURE 18 – FLAT BAND ENERGY DIAGRAM SHOWING THE CONTRIBUTIONS OF THE PHOTON PULSE AND THE ELECTRON PULSE IN DEPENDENCE ON THE DOPING (A), AT NEGATIVE DELAYS (B), AND AT POSITIVE DELAYS (C). REPRINTED WITH PERMISSION FROM *[28]*

In the model proposed by Cho and coworkers, the optical pulse excites electrons from the valence to the conduction band. Electrons and holes generated by the photon pulse are called optically excited carriers. Two competing mechanism are proposed to describe the effect of optically excited carriers on probability of SE emission [28]. The first mechanism is the increase in average electron energy: optically excited electrons have higher energy with respect to non-excited ones and therefore may be emitted with higher probability. This mechanism, labeled in Figure 18 panel c as "bright contrast", acts only at positive delays after optical excitation and determines an enhancement of the intensity of emitted electrons [28]. Mohammed and coworkers proposed the mechanism called "bright contrast" to explain the enhancement of SE emission after optical excitation observed on silicon [9]. Cho and coworkers also states that a second mechanism plays a relevant role: optically excited carriers reduce SE emission by inelastic scattering. In fact, SEs, before being emitted, propagate inside the material. If they lose energy due to scattering, then the probability of emission is reduced. This second effect depletes SE emission, corresponding to a dark contrast, and acts both at positive and at negative delays. The mechanism labeled as dark contrast is therefore reported both in Figure 18 panel b and in Figure 18 panel c. Dark contrast at negative delays is explained by the scattering mechanism, while the trade-off of the two mechanisms is invoked to explain contrast at positive delays. The rise of the contrast observed just after zero delay is attributed to the bright contrast mechanism, although the overall sign of the contrast keeps negative also at positive delays due to the stronger intensity of the dark contrast mechanism. Both mechanisms have an intensity that is dependent on the doping. According to Cho and coworkers, the intensity of the bright mechanism depends on the concentration of the electrons in the conduction band, due to the fact that when concentration is higher states with higher energy are filled and therefore the energy available for SE emission. The optically excited electrons sums to the electrons already in conduction band in the ground state. Concentration of conduction band electrons in the ground state increases from p-doped to intrinsic to n-doped as represented in Figure 18 panel a explaining the doping dependence of the enhancement at time zero measured experimentally and reported in Figure 17 [28]. The scattering mechanism is also doping dependent since both the electron penetration depth and the scattering rate depends on the type and the concentration of the dopant atoms: Si for n-type and Zn for p-type. Electron penetration depth is lower, and the scattering rate is stronger in Zn-doped with respect to Si-doped explaining the faster dynamics at negative delays observed in Zn-doped (p) with respect to Si-doped (n) [28].

2.4.2 Excited carrier dynamics in nanostructured materials

Nanowires made of alloys of Indium Gallium and Nitrogen have been proposed to replace the bulk semiconductor in light emitting diodes thanks to the low defect density and the tunable bandgap. Nonetheless, the excessive surface recombination reduces the carrier density and the device efficiency with respect to bulk materials, and passivation methods have been proposed to limit this effect. One of the most effective passivation method uses octadecyl thiol (ODT) [82]. An USEM measurement on InGaN nanowires with the goal of measuring the effect of ODT passivation has been reported [31]. A sequence of time-resolved SEM images have been acquired on InGaN nanowires in dependence on the probe to pump delay, as shown in Figure 19. Two samples were compared: in the first sample, the nanowires were left as grown, while in the other they were covered with a passivating layer. Although the scanning electron microscope could spatially resolve the single nanowires, an ensemble average at low magnification is presented [31], and the effective spatial resolution of the time-resolved measurement is of the order of tens of micrometers.

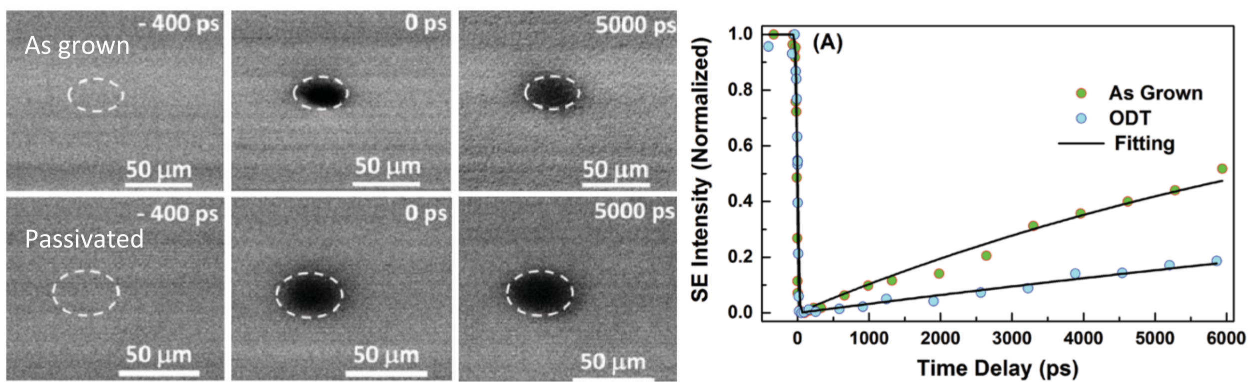

FIGURE 19 – TIME-RESOLVED SE IMAGES OF INGAN NANOWIRES AS-GROWN AND PASSIVATED WITH OCTADECYL THIOL (ODT) ON THE LEFT, INTENSITY OF THE EMISSION FROM THE LASER-EXCITED AREA IN DEPENDENCE ON THE PROBE TO PUMP DELAY ON THE RIGHT. REPRINTED WITH PERMISSION FROM *[31]*

The SE emission intensity from the area excited by the spot was averaged and plotted versus the delay, both for nanowires as grown and passivated. The effect of the optical excitation induces a depletion in SE emission with the same intensity for both samples. SE emission recovery is of the order of few nanoseconds. The recovery appears slower for the passivated sample. Khan and coworkers attributes the negative contrast to the fact that optical excitation creates energy-loss pathways for SE depending on the concentration of the excited carrier [31] as already reported for gallium arsenide [28]. The recovery of the differential SE contrast is attributed to recombination of optically excited carriers. According to the Khan and coworkers, the slower recovery of the contrast in the passivated sample confirms that the passivation layer reduces the rate of the recombination at the surface[31]. Authors observed a similar effect when comparing powder and crystalline CdSe [27]. SE emission intensity from the optically excited area of both specimen is reported in Figure 20.

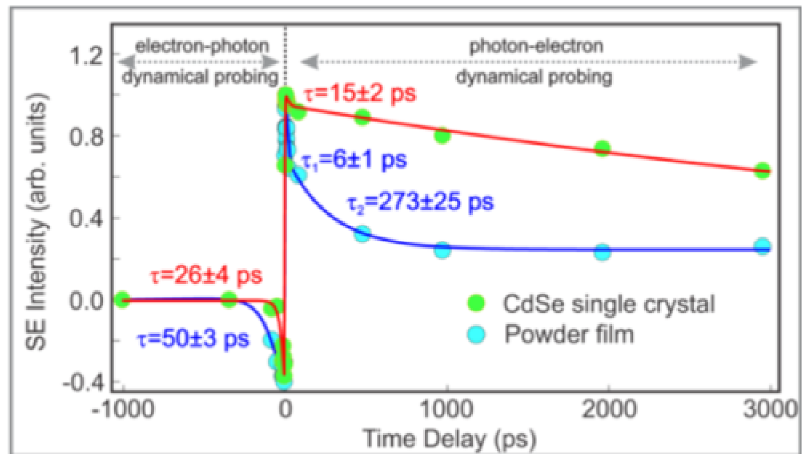

FIGURE 20 – TIME-RESOLVED SE EMISSION FROM OPTICALLY EXCITED AREA OF CADMIUM SELENIDE. REPRINTED WITH PERMISSION FROM *[27]*

On CdSe the optical excitation determines an enhancement of SE emission. Authors explains this contrast with the same model used for silicon: optically excited carriers increase average energy of electrons and therefore probability of SE emission [9]. At positive delays, powder sample shows a faster recovery of the contrast. This was attributed to the fastest recombination of optically excited carriers in powder sample with respect to the crystalline one. Since the powder sample has a wider surface are authors concluded that recombination was mediated by defects on the surface[27]. Nonetheless, on CdSe a depletion of SE emission is observed at negative delays. This is explained as an exchange of the role of the pump and the probe [9] as shown in Figure 21.

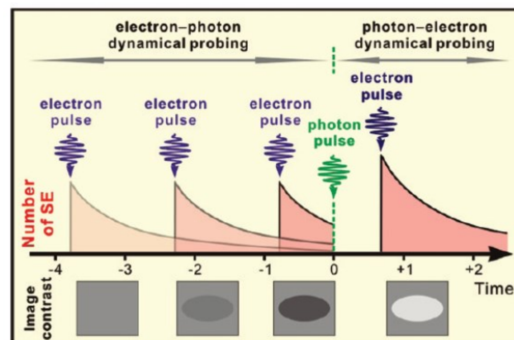

FIGURE 21 – REGIME OF PUMPING AND PROBING OF SEMICONDUCTOR SAMPLE BY ULTRAFAST SCANNING ELECTRON MICROSCOPY. REPRINTED WITH PERMISSION FROM *[9]*

Depletion of SE emission at negative delays is attributed to the same effects proposed in the case of gallium arsenide [28], already introduced in paragraph 2.4.1 Sensitivity to doping.

2.4.2 Effect of PE energy on the pump-probe differential SE contrast

Further studies were done to determine the effect of PE energy on time-resolved SE emission from CdSe by Mohammed and coworkers [83]. Reported time-resolved images, acquired with PE energy of 30 keV and 1 keV respectively, are reported in Figure 22.

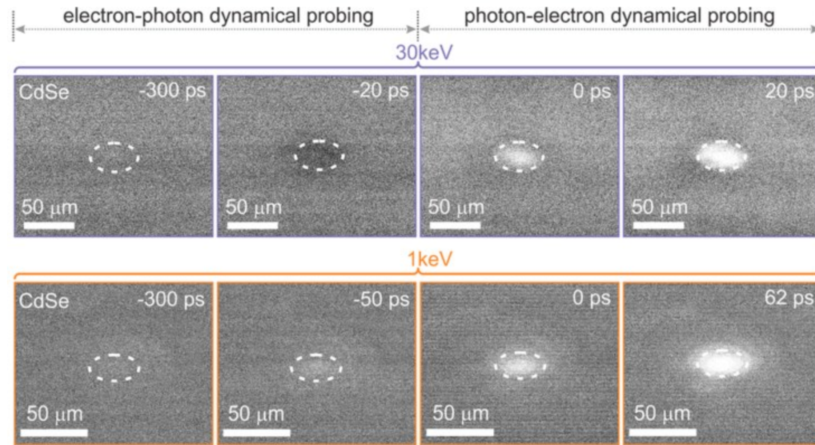

FIGURE 22 – COMPARISON OF TIME-RESOLVED IMAGES ACQUIRED ON CADMIUM SELENIDE WITH PE ENERGY OF 30 KEV AND 1 KEV. REPRINTED WITH PERMISSION FROM [83]

Results shows that PE energy affects the intensity of SE emission only at negative delays. The optically excited area of the time-resolved USEM image acquired with a delay of -50 ps appears bright for a PE energy of 1 keV and dark for 30 keV. Authors attributes the inversion to two opposite effects acting on the internal SE's:

- Energy gain due to interaction with photons determining an increase in SE emission[32];
- Energy loss due to scattering against electron-hole pairs created by the photon pulse determining a depletion of SE emission [32];

According to Mohammed and coworkers, the energy gain mechanism involves only the SEs that are nearer to the surface than the absorption depth of the pump pulse, equal to 100 nm[32]. To exchange energy with photons SEs have to be within the absorption depth exactly when the optical pulse arrives. On the contrary, energy loss mechanism is driven by scattering against the electron-hole pairs that survive for longer than the optical pulse. Therefore, scattering happens within the pump absorption depth but may involve SEs that comes from a higher depth and arrives later on surface. According to Mohammed and coworkers, the relative intensity of the gain and loss mechanism depends on the depth at which SEs are generated, that increases when increasing the energy of PE[32]. When PE energy is 1 keV, SEs are generated within the absorption depth of the optical pump and gain energy by interacting with photons: energy gain mechanism prevails and more SE are emitted. On the contrary, when PE energy is 30 keV, most SEs are generated at a depth higher than the absorption depth of the optical pump. They cannot interact with the photons and the scattering mechanism prevails: less SE are emitted. The model proposed by Mohammed and coauthors appears compatible with the experimental results that they report [32].

2.4.3 Importance of the surface

Yang and coworkers studied the time-resolved SE contrast on different surfaces of the CdSe crystal [29]. They also tested the effect of exposing the surface to different gases. The surface studied were the (0001)-oriented one, terminated by cadmium atoms and, and the $(10\bar{1}0) - \mathrm{terminated}$ one, where the same number of cadmium and selenide atoms are present. The surface (0001) is perpendicular to the permanent crystal dipole moment while $(10\bar{1}0)$ is parallel. The measurements was repeated after inserting water vapor in the SEM chamber, at a pressure of hundreds of Pa. The exposure dose is not declared. SE detector was updated to work at such pressure according to the well-known technology of environmental SEM. Image acquired are reported in Figure 23.

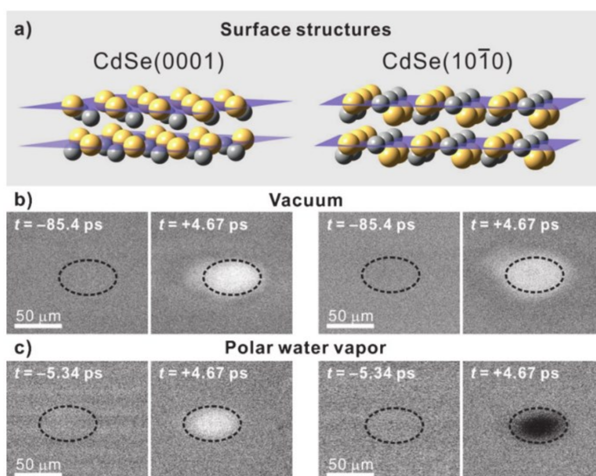

FIGURE 23 – TIME-RESOLVED USEM IMAGES ACQUIRED ON SURFACES (0001) AND $(10\bar{1}0)$ IN VACUUM AND EXPOSED TO WATER VAPOR. REPRINTED WITH PERMISSION FROM *[29]*

An enhancement of SE emission from the optically excited area 4.67 ps after laser excitation was reported both on (0001) and on $(10\bar{1}0)$ surfaces in vacuum. When the sample is exposed to water vapor, in the same conditions as in vacuum, surface (0001) still shows an enhancement of SE emission while surface $(10\bar{1}0)$ show a depletion [29]. Full dynamic of the intensity of SE emission from the optically excited areas of surfaces (0001) and $(10\bar{1}0)$ versus delay is reported in Figure 24.

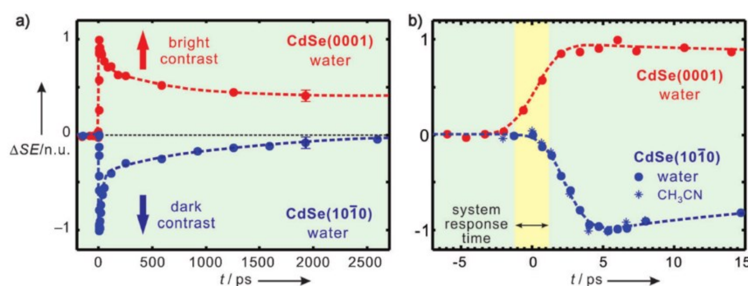

FIGURE 24 – TIME-RESOLVED INTENSITY SE EMISSION FROM OPTICALLY EXCITED AREA OF ON SURFACES (0001) AND $(10\bar{1}0)$ SURFACES OF CADMIUM SELENIDE EXPOSED TO WATER VAPOR. REPRINTED WITH PERMISSION FROM *[29]*

The comparison of time-resolved intensity of SE emission from surfaces (0001) and $(10\bar{1}0)$ exposed to water vapor is reported in Figure 24. After optical excitation SE emission is enhanced on surface (0001) and depleted on surface $(10\bar{1}0)$. The effect on surface $(10\bar{1}0)$ appears delayed by 2 ps with respect to the other surface [29]. Yang and coworkers explains the enhancement with increased probability of SE emission due to generation of excited carriers by the optical pulse [29], as already explained for silicon [9]. The depletion is attributed to the fact that optically excited carriers screens the crystal dipole permanent momentum, this makes the adsorbate molecule to rearrange affecting the work function in order to reduce the probability of SE emission [29]. The effect is considered less relevant on surface (0001), parallel to the axis of crystal momentum, where the gain mechanism prevails [29]. Recovery of SE emission happens for both surfaces; Yang and coworkers attribute that to interband recombination [29]. Nonetheless, a recovery component may be observed in the dynamic with time constant of tens of picoseconds, that is not explained by Yang and coworkers.

2.4.4 Charge transport in pn junction

Najafi and coworkers made further USEM measurements on p-doped and n-doped silicon [84] and on a pn silicon junction [33]. The latter is composed of phosphorous doped n-type silicon ($1.4 \times 10^{14} cm^{-3}$) epitaxially grown on boron doped p-type silicon ($9.4 \times 10^{18} cm^{-3}$) on crystal surface (111). The sample has been cleaved and observed in cross section. Reported surface roughness is less than 100 nm [33], far from an atomically flat sample. Measuring conditions are the ones used in other USEM experiments already reported: optical pump with a wavelength of 515 nm and PE beam energy of 30 keV. USEM images on p silicon, n silicon and pn junction are reported in Figure 25. The spatial resolution was estimated by the authors in 200 nm [33].

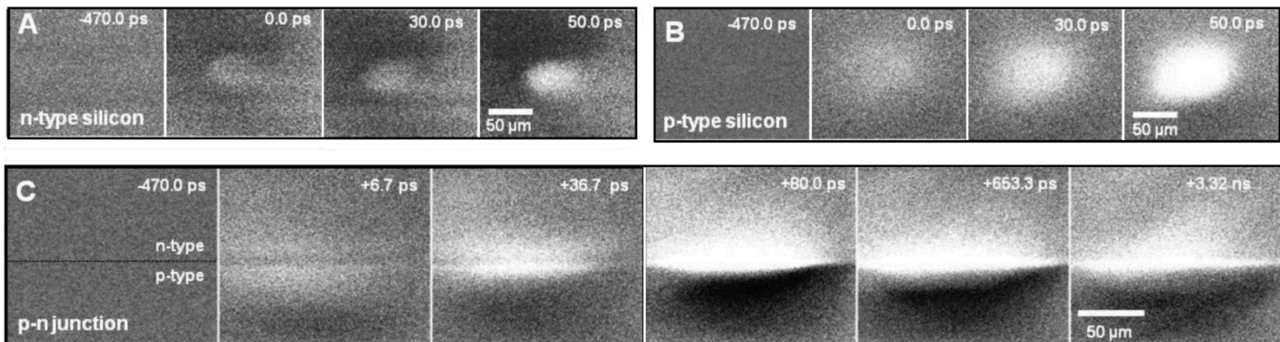

FIGURE 25 – TIME-RESOLVED SEM IMAGES OF SILICON P AND N DOPED AND OF A PN JUNCTION. REPRINTED WITH PERMISSION FROM *[33]*

Far away from the junction both on p and on n-doped silicon, an enhancement of the SE emission is observed as a consequence of optical excitation, although the contrast is stronger in p-doped silicon. Superimposing the laser on the junction the contrast is positive on both sides 6.7 ps after excitation while becomes negative in the p-doped region after 80 ps. According to the Najafi and coworkers, this is attributed to the drift of the excited carriers through the junction that determines a strong concentration both of electrons in the n-doped silicon and of holes at the opposite side of the junction. Therefore the presence of excited electrons enhances the probability of emission of SEs while the extra holes determine a depletion [33]. The dynamics influence a region

that extends 50 μm away from the junction, while the space charge region due to the junction is only few micrometers thick. According to Najafi and coworkers, the effect may be described by a diffusion speed of the carrier orders of magnitude higher than the estimate reported in literature for silicon [85].

2.4.5 Diffusion of optically excited carriers on silicon

Measurement of diffusion of optically excited from time-resolved USEM images have been reported by Najafi and coworkers [34]. The result was obtained by measuring the size of the region of the sample where SE contrast was affected by optical excitation in dependence on the delay [34]. Time-resolved images and plots of the size of the region of the sample where SE emission is perturbed versus delay are reported in Figure 26.

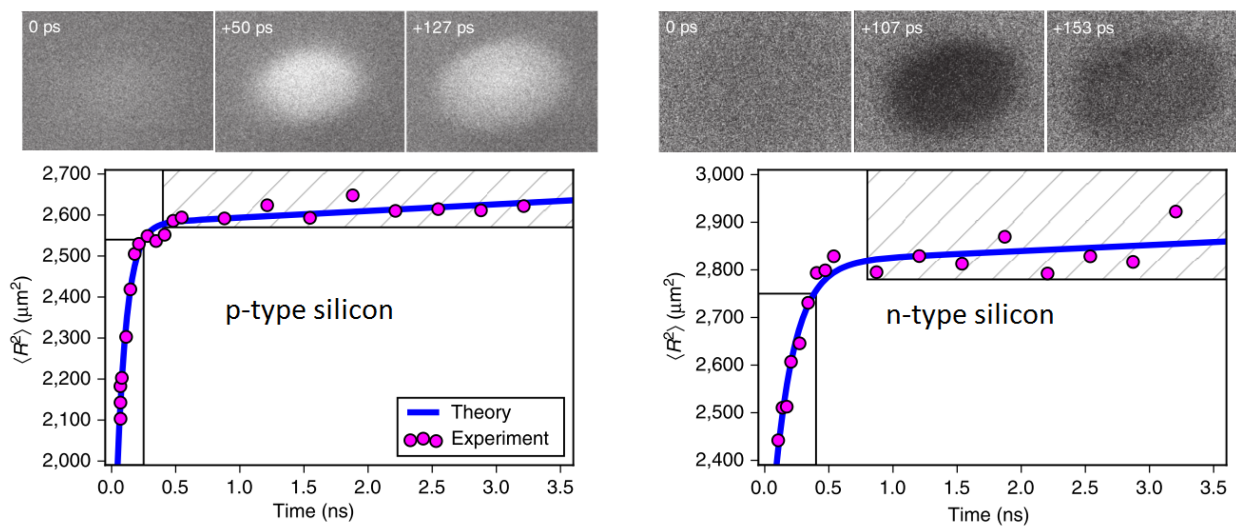

FIGURE 26 – EXCITATION DYNAMICS OF ELECTRONS IN P-TYPE SILICON (ON THE LEFT) AND OF HOLES ON N-TYPE SILICON (ON THE RIGHT). REPRINTED WITH PERMISSION FROM [34]

The contrast is attributed to the density of excited carriers: bright for the extra electrons added by the optical excitation to p-type silicon and dark for the extra holes in n-type. Two regimes of diffusion have been found: in the first few hundred of picosecond the diffusivity coefficient is estimated as $10'000\ cm^2s^{-1}$ and then decreases to $20\ cm^2s^{-1}$, that is comparable to values previously measured for silicon at ambient temperature. The transient diffusivity observed, strongly dependent on optical pumping fluence, is attributed to the high concentration of laser induced carriers that enhance the diffusion coefficient [34]. Enhanced diffusion was already observed in semiconductors by Young and Driel and explained in term of manybody effects [86].

2.5 Other techniques for semiconductors

This paragraph introduces some techniques that combine optical pump-probe and electron microscopy developed with the goal of studying charge carrier dynamics in semiconductors with temporal and lateral spatial resolution comparable with the goal of the Ultrafast Scanning Electron Microscope.

2.5.1 Cathodoluminescence

Cathodoluminescence refers to light emission from the area of the sample excited by an electron beam. In semiconductors, it is attributed mainly to radiative decay due to interband recombination of electron-hole pair excited by the PE beam [4]. The wavelength of emitted light depends on the optical band of the semiconductor, therefore allowing to test the effective bandgap of semiconductor alloys. It has been shown that the cathodoluminescence is sensitive to drift of carrier through a p-n junction since that determines a reduction in the concentration of carriers in the neighbor of the junction and a reduced intensity of emitted light [7]. The emission may also be due to radiative decay of excited electron from traps like color center in oxides [8] or defects in semiconductors both in the bulk and at the surface [9]. Cathodoluminescence has been applied to the study of buried interfaces, the emission depth of the signal, in fact, may be tuned by the PE energy [87].

2.5.2 Time-resolved cathodoluminescence

Michele Merano and co-workers built and tested an experimental setup for time-resolved cathodoluminescence [3]. They modified an SEM by substituting the electron gun with a transmission photocathode. Laser pulses with a wavelength of 266 nm, a duration of 100 fs and a repetition rate of 80 MHz determines photoemission of electron pulses from a thin layer of gold deposited on quartz. The electrons pulses are accelerated and focused on the sample by the SEM electronic column. The system allows to obtain a maximum pulsed PE current at the sample of 100 pA, enough to excite SE emission and cathodoluminescence. The SE signal was measured by the original detector of the SEM, while cathodoluminescence was collected by a parabolic mirror, monochromated and revealed by a streak camera, a 2D time-resolved detector with a resolution of 10 ps. A sketch of the setup is reported in Figure 27 panel a.

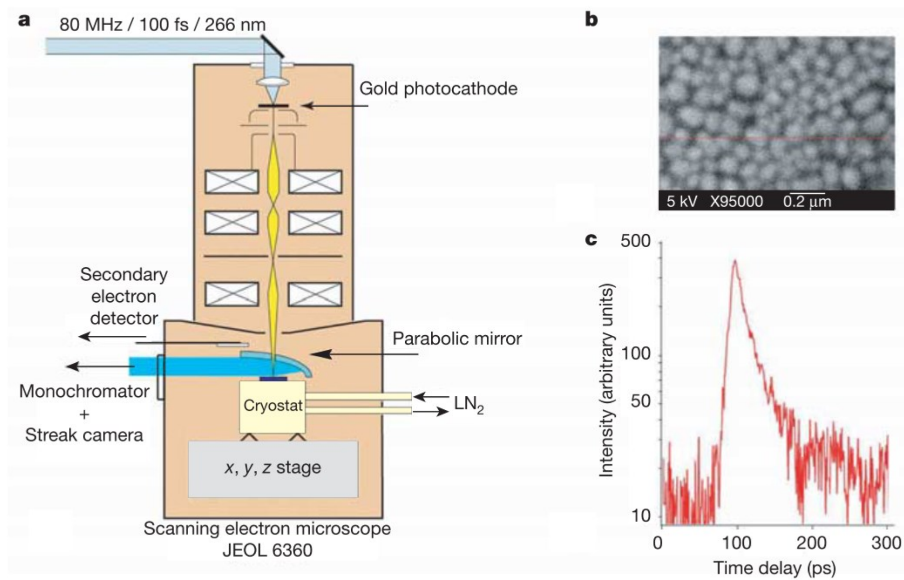

FIGURE 27 – PANEL A SHOWS A SKETCH OF THE EXPERIMENTAL SETUP OF TIME-RESOLVED CATHODOLUMINESCENCE, PANEL B AN SEM IMAGE WHERE GRAY LEVELS REPRESENTS INTENSITY OF SES OF A SAMPLE OF GOLD NANOPARTICLES ON CARBON, AND PANEL C SHOWS A TIME-RESOLVED MEASUREMENT OF THE CATHODOLUMINESCENCE SIGNAL FROM GAN. REPRINTED WITH PERMISSION FROM *[3]*

Merano and coworkers evaluated the spatial resolution of the setup by acquiring a non-time resolved SEM image of a sample of gold nanoparticles on carbon. The image is reported in Figure 27 panel b, and spatial resolution is estimated to be better than 50 nm [3]. The time resolution was estimated by looking at the rise time of the cathodoluminescence signal in Gallium Nitride. The result of the time-resolved measurement is reported in Figure 27 panel c and rise time is equal to 10 ps [3]. The time-resolved cathodoluminescence setup was used to study charge transport in low dimensional system that were obtained by growing layers of III-V semiconductor pyramidal nanostructures [3]. All the structures were grown with a gallium arsenide alloy in a matrix of indium gallium arsenide; they show a bandgap dependent on the impact point of the PE beam, due to the different confinement level of the electrons. Therefore, Merano and coworkers associated the spectral features found to well defined geometrical sub-parts of the micrometer-sized pyramids, as shown in Figure 28: the vertex were identified as responsible of a quantum dot-like spectral feature, the lateral edges of a quantum wires like while the lateral faces of a quantum wells like. The intensity of the spectral features found were mapped in dependence on the impact point of the PE beam on the sample. The energy resolved cathodoluminescence images show the intensity of monochromated cathodoluminescence signal on a grayscale

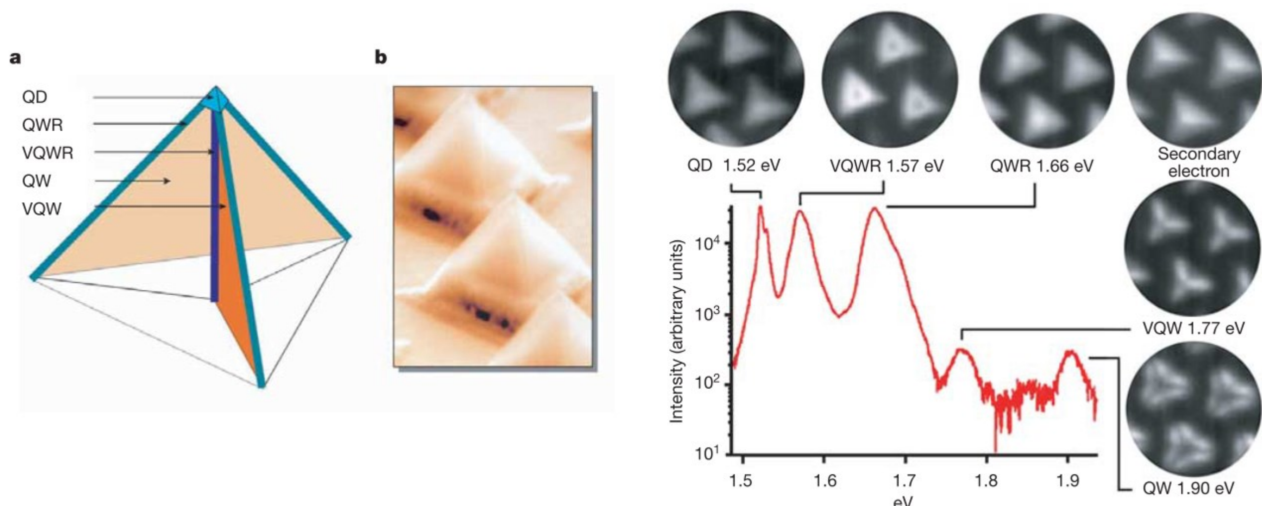

FIGURE 28 - FROM THE LEFT TO THE RIGHT: A MODEL OF THE SAMPLE WITH THE LOW DIMENSIONAL STRUCTURES, SEM IMAGE OF THE MICRO PYRAMIDS IN A PERSPECTIVE VIEW AND CATHODOLUMINESCENCE ENERGY SPECTRUM. FOR EACH PEAK OF THE ENERGY SPECTRUM, THE CORRESPONDING ENERGY RESOLVED CATHODOLUMINESCENCE IMAGE IS REPORTED, TO BE COMPARED TO THE SE IMAGE IN THE CORNER. QD MEANS QUANTUM DOT, QWR QUANTUM WIRE, VQWR VERTICAL QUANTUM WIRE, QW QUANTUM WELL AND VQW VERTICAL QUANTUM WELL. REPRINTED WITH PERMISSION FROM *[3]*

According to Merano and coworkers, in cathodoluminescence, the electron beam acts as a pump determining the generation of electron-hole pairs in the excited volume. Energy-resolved images show that there are preferred regions of the sample related to each different structures. Therefore, by regulating the electron beam position on the sample, it is possible to populate only selected structures with electron-hole pairs.

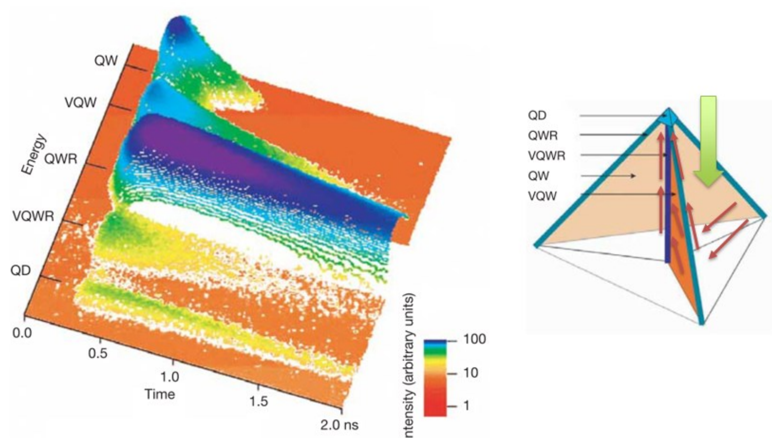

FIGURE 29 - ON THE RIGHT, ENERGY AND TIME-RESOLVED CATHODOLUMINESCENCE SPECTRUM OBTAINED BY PUMPING A LATERAL FACE WITH THE ELECTRON BEAM. ON THE LEFT, SKETCH OF THE PROPAGATION OF THE CHARGES FROM THE LATERAL FACE TOWARDS THE QUANTUM DOT, THE STRUCTURE WITH THE SMALLER BANDGAP. REPRINTED WITH PERMISSION FROM *[3]*

The time and energy resolved cathodoluminescence spectrum obtained by pumping a lateral face shows that charges diffuse towards the quantum dot placed at the top of the pyramid. This last one has a low signal since it can host only a few electrons and a very slow decay showing saturation. Once charges in the quantum dot

recombine, they are refilled from the quantum wires and the quantum well, up to saturation. Therefore, the faster decay of the quantum well and vertical quantum well is attributed not only to recombination but also to diffusion toward lower bandgap structure [3]. Time-resolved cathodoluminescence (TR-CL) shows a spatial resolution of 50 nm, slightly worse than the 10 nm reported for USEM [26] although in principle the two systems needs to fulfill the same goal: delivering on the sample a PE beam using an SEM column equipped with an ultrafast electron source. Regarding the experimental results reported TR-CL proved to be sensitive to charge transport in nanostructures with a spatial resolution better than what has been reported for USEM. Time resolution of TR-CL is equal to 10 ps, an order of magnitude worse with respect to USEM [27] although the temporal resolution of USEM has not been fully exploited yet. USEM has the advantage of energy resolution on excitation. By tuning the pump laser wavelength it would be possible to selectively excite different processes, like for color centers in aluminum oxide, but this possibility has not been exploited yet. TR-CL excites with an electron pulse that provides broadband excitation but give the possibility to analyze the spectrum of the emitted light. This could give particularly relevant information to untangle the contributions of the different nanostructures as reported by Merano and coauthors [3]. Finally, cathodoluminescence is due to radiative recombination that is not efficient in indirect bandgap semiconductors like silicon and germanium, the ones most used in today electronic. Thus, USEM appears to be more suited to study transport and recombination of optically generated charges at the surface of indirect bandgap semiconductors, while TR-CL proved to be optimum to study charge transport in nanostructures made by direct gap semiconductors. Therefore USEM and TR-CL has to be considered complementary techniques.

2.5.3 Time-resolved PEEM

Time-resolved Photoemission Electron Microscopy has the goal to study dynamics of optically excited electrons on ultra-small and ultrafast scale. In semiconductors, an optical pump excites electrons from valence to conduction band. An optical probe determines photoemission of electrons from the sample. The emitted electrons are collected by electron optics and reconstructed by a CCD [63]. The spatial resolution of the image is better than 100 nm while excitation is obtained by far-field optical and therefore limited by diffraction to few micrometers. The experimental setup and an energy diagram with the effect of pump and probe are reported in Figure 30.

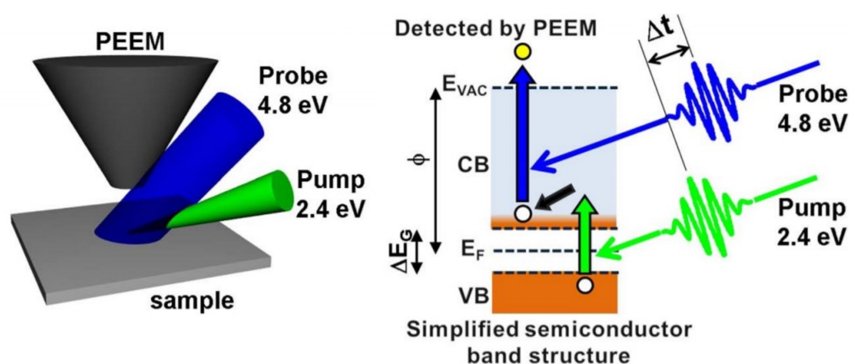

FIGURE 30 – BASIC PRINCIPLES OF TIME-RESOLVED PHOTOEMISSION ELECTRON MICROSCOPY TR-PEEM. REPRINTED WITH PERMISSION FROM [63]

Photoemission of electrons determines a positive charging of the surface of the sample. Charging effects in PEEM are particularly severe because the electrons emitted kinetic energies below few eV and are strongly influenced by the local charge left on the emission volume of the sample. To limit charging effects the repetition rate of the pulses has to be optimized [63].

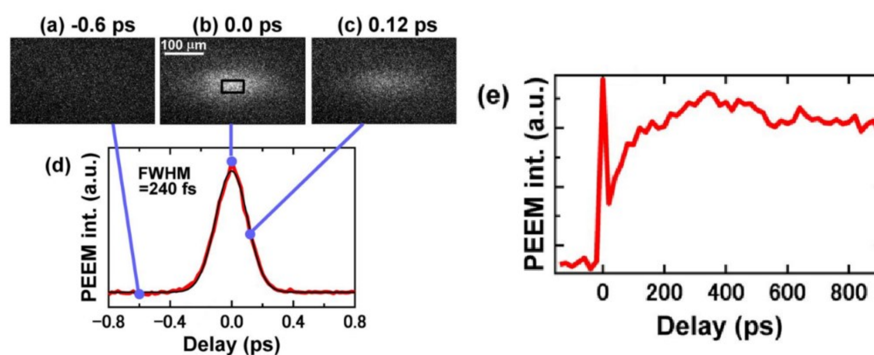

FIGURE 31 – TIME-RESOLVED PEEM IMAGES, PLOT D, AND E SHOWS THE INTENSITY OF THE SIGNAL OVER THE RECTANGULAR AREA HIGHLIGHTED IN THE IMAGE ACQUIRED FOR A DELAY EQUAL TO 0.0 PS. REPRINTED WITH PERMISSION FROM [63]

The time-resolved images of photoemitted electrons reported in Figure 31 have been acquired on a sample made by a thin layer of silica on silicon. A bright spot appears when pump and probe pulses are overlapped on the sample confirming that pump excitations determines an increase in the intensity of photoemitted electrons. The plot reported in Figure 31, panel d, shows the average intensity of emitted current from the rectangular area shown in the image acquired at 0.0 ps centered on the spot versus delay. The Gaussian peak is attributed to non-resonant two-photon photoemission, and the full width at half maximum of 240 fs gives an upper limit of the time resolution of the setup. The increase from few ps to 300 ps is attributed to surface photovoltage and the following decrease to optically excited carrier recombination [63]. Time-resolved PEEM (TR-PEEM) shows a spatial resolution of 100 nm, between the best resolution presently achievable for time-resolved measurements on bulk samples and comparable with the reported USEM measurements. Time resolution of TR-PEEM, equal to 240 fs, is slightly less with respect to USEM [27] thanks to the full optical pump-probe. Both in USEM and in TR-PEEM an optical pulse on the sample triggers the electron-hole generation in a semiconductor. In both techniques, the probe pulse determines the emission of low energy electrons from the sample, and therefore both are surface sensitive. In TR-PEEM electrons are emitted by photoemission induced by an optical pulse. All the emitted electrons receive the same amount of energy by the probe photons. Measuring the energy of emitted electrons and subtracting the contribution of the probe photons it is possible to determine electron energy before emission for each electron. TR-PEEM allows, therefore, to reconstruct the energy distribution of electrons in the sample on the energy scale typical of valence and conduction band. This is an advantage over USEM, where electron emission happens by multiple scattering events, and it is not possible to reconstruct the energy of an emitted electron before emission. The only relevant information in USEM is intensity of emitted electrons, influenced by morphology and local charging. Nonetheless, also in TR-PEEM the intensity and the energy of emitted electrons appear extremely sensitive to local charging effects and to morphology, and therefore the advantage of energy resolution has to be tested in real experiments. In conclusion, by now USEM and TR-PEEM has to be considered complementary pioneering techniques.

2.6 Diffraction contrast

Diffraction pattern allows to study the periodicity of the lattice. It may be obtained by elastic scattering of X-rays or electrons with wavelength comparable to the lattice. In this paragraph, the focus is on electron diffraction because X-rays are definitely not sensitive to the surface. In the machines designed for electron diffraction, the goal is the resolution in the reciprocal space with the goal to determine lattice structure, more than spatial resolution in direct space. Time-resolved electron diffraction setup has been developed by the group of Zewail[23], Miller[8] and others [22,24,88] with the goal to study the dynamics of lattice structure with temporal resolution [73]. The solutions proposed were to develop a custom setup or to integrate electron diffraction in an electron microscope like Ultrafast Transmission Microscope, introduced in paragraph "2.7.1 Ultrafast Transmission Electron Microscopy", or Time-Resolved Electron Backscattered Diffraction integrated in USEM. Concerning time-integrated electron diffraction, it is possible to operate both in reflection mode, recording the diffraction pattern at the same side of the sample with respect to incident beam, or in transmission mode, where the electrons pass across the sample. There are two main groups of machine that differ in design and energy of the primary beam:

- Low Energy Electron Diffraction or LEED;
- Reflection High Energy Electron Diffraction or RHEED.

LEED has a strong surface sensitivity thanks to the low energy of the primary beam, usually hundreds of volt. The primary beam is perpendicular to the sample while the diffracted electrons are collected, after accelerating grids, on a hemisphere centered on the sample. LEED is used to characterize the quality of the crystalline surface of samples [89].

RHEED has a PE beam with an energy of tens of keV and a grazing incidence. The main advantage, with respect to LEED, is that the experimental setup does not occupy the volume of space above the surface of the sample and does not prevent to a flux of precursor to reach the surface of the sample. This property makes RHEED useful for in situ characterization of growth of crystalline samples. It is possible to measure the crystallinity of the surface of samples [90] and the rate of growth [91]. The intensity of Bragg diffraction spots depends on the number of atoms contributing to the considered reflection, therefore is maximum when the surface is perfectly crystalline and atomically flat. If the growth proceed monolayer by monolayer, the maximum intensity of the peaks is reached when a monolayer is completed while it reduces when the next one is growing because atoms attaches in random position to the surface reducing the periodicity. RHEED was also used to characterize phase transitions that imply a change in the crystalline structure of the sample, as for the Pt 110 surface from 1x1 to 2x1 order[92].

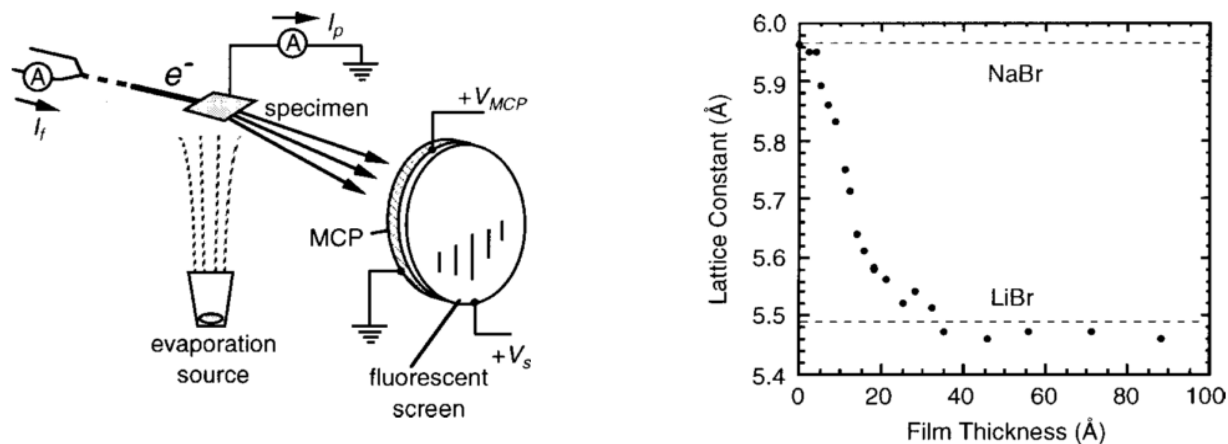

FIGURE 32 - EXPERIMENTAL SETUP OF RHEED (ON THE LEFT) AND CHANGE IN LATTICE CONSTANT DURING GROWTH OF LITHIUM BROMIDE ON SODIUM BROMIDE (ON THE RIGHT). REPRINTED WITH PERMISSION FROM [93]

Diffraction pattern may be obtained in SEM with a technique known as BackScattered Electron Diffraction (EBSD). The pattern obtained by EBSD gives complementary information with respect to RHEED and may be used to study crystallinity [94], defects [95] and deformations [96].

2.6.1 Time-resolved electron diffraction

Time-resolved electron diffraction gives information about structural dynamics [73]. An optical pulse act as a pump and clocks the ultrafast dynamics in the sample while an electron beam act as a probe and creates the diffraction pattern by interacting with the atoms of the lattice. The first prototypes of time-resolved machine for diffraction operating in pump-probe were developed by Ahmed Zewail [23] and Dwayne Miller [8]. Nowadays other groups joined the research field [22]. Transmission configuration is usually implemented in UTEM machines, that will be introduced in paragraph 2.7.1 Ultrafast Transmission Electron Microscopy, and allows to study nanoparticles [97], nanotubes and free-standing layers [73]. Grazing incidence may be implemented only in specifically designed machines [22] known as time-resolved RHEED. Grazing incidence is the main option for bulk samples except for Ultrafast Electron BackScattered Diffraction that will be introduced in paragraph 2.6.2 Time-resolved electron diffraction in USEM . Relevant scientific cases are adsorbates on crystal surfaces [98] and epitaxial nanostructures [24]. Time-resolved diffraction pattern gives information about transient electric fields at the surface of the sample [99] or lattice constant dynamic due to thermal dilatation, phonon excitations or changes in the crystalline structure [23]. Thanks to the theory of Debye-Waller factor diffraction pattern allows to study atomic disorder that may be due to thermal heating or phase transitions [5].

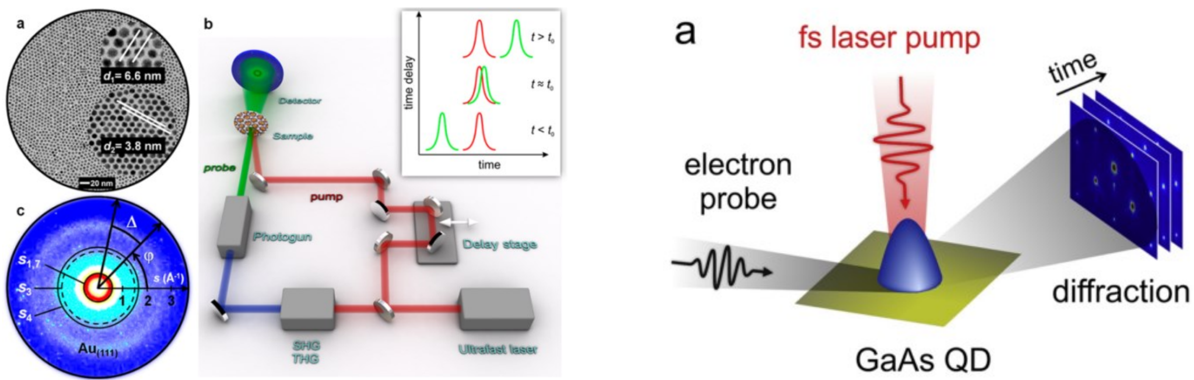

FIGURE 33 – SKETCH OF THE ULTRAFAST ELECTRON DIFFRACTION SETUP: ON THE LEFT DIFFRACTION FROM GOLD NANOPARTICLES IN TRANSMISSION MODE AND ON THE RIGHT DIFFRACTION FROM GALLIUM ARSENIDE QUANTUM DOTS IN REFLECTION MODE. REPRINTED WITH PERMISSION FROM [97] AND [24]

2.6.2 Time-resolved electron diffraction in USEM

Ultrafast SEM was demonstrated to be sensitive to optical excitation of indium arsenide thanks to Electron BackScattered Diffraction (EBSD) [9]. Results are reported in Figure 34.

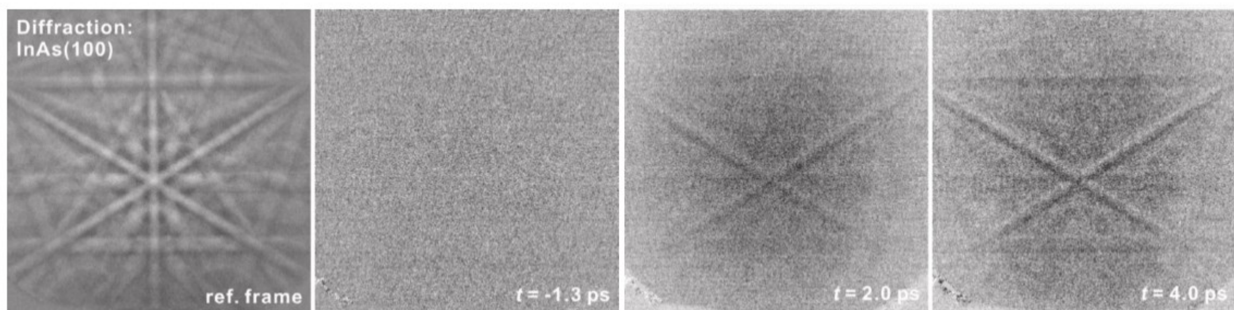

FIGURE 34 – EBSD DIFFRACTION PATTERN ON INAS: REFERENCE FRAME AND TIME-RESOLVED DIFFERENTIAL SPECTRA. REPRINTED WITH PERMISSION FROM [9]

The change in the EBSD diffraction pattern of the surface (100) of InAs crystal was attributed to an expansion of 0,16% of the lattice in the direction normal to the surface. The cause is not attributed to the thermal expansion of the lattice due to laser heating but related to the population of antibonding orbitals as a consequence of the optical excitation [9]. Time-resolved EBSD allows studying lattice dynamics in an Ultrafast Scanning Electron Microscope. The advantage with respect to dedicated setup for time-resolved electron diffraction setup could be the spatial resolution, demonstrated up to tens of nanometers in a not time-resolved implementation [100].

2.7 Transmission electron microscopy

The first working electronic microscope operated in transmission: focusing a beam of electrons onto a sample and analyzing the electrons that were able to pass through. The electrons that are deviated below a limit angle due to the interaction with the atoms of the solid are projected onto a screen. This type of microscopes, called Transmission Electron Microscope (TEM), allows today to image samples with sub-atomic spatial resolution. It is possible to reconstruct 3D models with subatomic resolution thanks to high-resolution electron microscopes and tomography [101]. The 3D model of a gold nanoparticle was reconstructed with a resolution of 240 pm showing individual atoms [102]. More recently, a tungsten needle was reconstructed with a resolution of 19 pm: it was possible to measure the displacement of atoms from ideal crystalline lattice position and evaluate the strain tensor [103]. Electron microscopes work in high vacuum to prevent sample contamination and allow propagation of electron beam: organic samples cannot withstand vacuum at room temperature but are imaged thanks to cryo-TEM techniques [104]. The technique involves freezing the sample by liquid nitrogen cooling and keeping it in that condition for the entire measurement. Since electrons used in TEM have a wavelength comparable to the distance between atomic planes in solids, they also diffract. TEM allows to easily switch from the direct magnified image of the sample to the diffraction pattern; it is also possible to reconstruct an image after filtering the electron according on the scattering angle. The flexibility to change from direct to reciprocal space made TEM a crucial tool in the development of material science. Thanks to the diffraction pattern it allowed to reconstruct the structure of many crystals, also the one too small to be analyzed by conventional x-ray diffraction. An example is the discovery of quasicrystals [105]. Although having a size of few micrometers and being immersed in an amorphous matrix, Dan Shechtman with TEM managed to observe the five-fold symmetry in their diffraction pattern, incompatible with translational symmetry. The main limitations of TEM are the sample thickness and the time resolution.

2.7.1 Ultrafast Transmission Electron Microscopy

The first working prototype of Ultrafast Transmission Electron Microscopy was developed by Ahmed Zewail at Caltech [12]. It operates in pump-probe mode, with a scheme similar to the one already presented for Ultrafast Scanning Electron Microscopy in paragraph 2.2.2 Ultrafast Electron Microscopy. The machine offers all the capabilities of a commercial TEM like imaging, diffraction, and energy loss plus the temporal resolution. With the latest implementation that uses a field emission gun as an ultrafast electron source, it is possible to reach a spatial resolution of 0.2 nm when imaging with an electron beam generated by Schottky field emission (TEM mode) and of 0.9 nm when the electron beam is generated by laser-driven photoemission (Ultrafast TEM mode) [14].

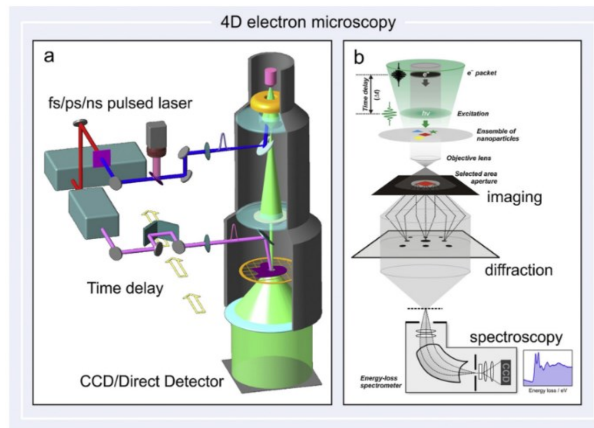

FIGURE 35 - SKETCH OF THE EXPERIMENTAL SETUP OF ULTRAFAST TRANSMISSION MICROSCOPE. IT IS POSSIBLE TO COLLECT THE MAGNIFIED ELECTRON BEAM ON A DETECTOR (ON THE LEFT) OR THE DIFFRACTED ELECTRONS AND THE ENERGY-LOSS SPECTRUM (ON THE RIGHT). REPRINTED WITH PERMISSION FROM [73]

Ultrafast imaging is effective to study mechanical phenomena like oscillation of a nanomechanical resonator at a few MHz up to several GHz that were filmed with a time resolution of 10 ns [15] or the observation of the mechanical drumming of a 75 nm thick membrane [106]. The possibility to analyze the energy of the transmitted electron allows studying plasmonic effects and light-matter interaction. Sidebands equally spaced appear in the energy spectrum near to the zero loss peak when the PE beam crosses a near-field optical induced electric field. This phenomenon is known as Photo-Induced Near field Electron Microscopy (PINEM) and is attributed to the quantized interactions between the electron of the beam and the photons [20]. The PINEM effect is observable only when the optical beam and the electron beam are temporally overlapped on a sample close to the zero delay condition[18].

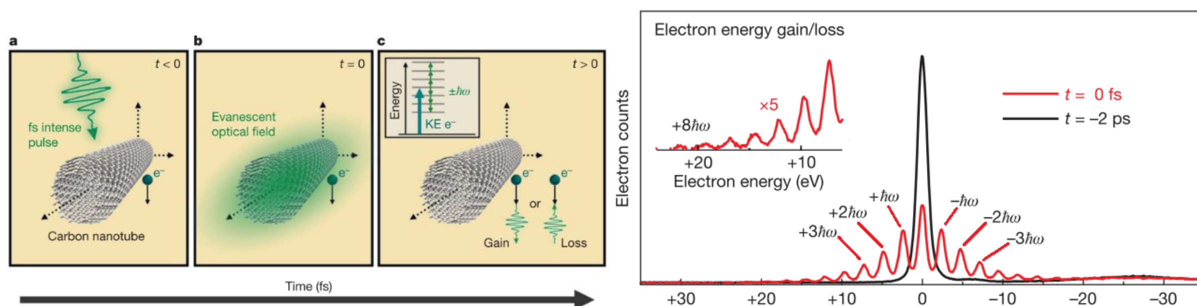

FIGURE 36 - ENERGY SPECTRUM OF THE PE BEAM AFTER INTERACTING WITH THE NEAR ELECTRIC FIELD INDUCED BY AN OPTICAL PULSE ON A CARBON NANOTUBE. IF THE ELECTRON AND OPTICAL BEAM OVERLAP TEMPORALLY ON THE NANOTUBE (RED PLOT) THE ELECTRON EXCHANGE QUANTA OF ENERGY WITH THE ELECTRIC FIELD. REPRINTED WITH PERMISSION FROM *[18]*

By PINEM it was possible to map the intensity of the near field in plasmonic structures like silver nanowires that show a peak of intensity in the region where the standing wave induced by the optical excitation interfere constructively [20]. Furthermore, on a gold nanotip, it was observed that the intensity of the sidebands was related to the intensity of the optical excitation beam. The appearance and disappearance of some excitation bands were attributed to Rabi oscillations of the population of the excited levels and interpreted of a proof of

the quantum superposition between the electron and the photon beam [21]. Optically induced ultrafast magnetization phenomena are also studied by Lorentz-microscopy like vortex was induced by laser pulses on the iron surface [10].

2.8 Objectives and motivations of this work - Surface sensitive USEM

The state of the art described above shows that few research groups have already demonstrated Ultrafast Scanning Electron Microscopy [26]. Temporal resolutions of less than 1 ps [9] were shown. Concerning the lateral spatial resolution, 10 nm [26] were demonstrated from a pulsed electron beam, although the best resolution reported in time-resolved differential imaging is not well defined and is in the range of few micrometers. It has been proven that SE contrast is sensitive to optically induced carriers in semiconductors [9], while no results were reported so far on insulators. In semiconductors, the optically induced SE contrast was studied in dependence on doping on GaAs, and a model with two competing effects was proposed [28]. Both the effects happens in the bulk of the sample, although it has also been reported that surface states, for example, the ones deriving from contamination, can play a crucial role, up to reversing the sign of the differential SE contrast [29] and changing dramatically the recombination speed of optically excited carriers [31]. Others time-resolved electron microscopies were also presented that compete with and/or complement the information that USEM could provide. The competing techniques on optically carrier dynamics in semiconductors are optical pump-probe, USEM, TR-CL, and TR-PEEM, while UTEM and UED study different topics but may give relevant and comparable information in selected cases. A summary of the resolution capabilities of the different techniques is reported in Table 1. The techniques are compared on the fields of time resolution, lateral spatial resolution, surface sensitivity, and energy resolution. Except for time resolution the other are divided in excitation, or pump, and detection, or probe. Optical pump-probe, TR-PEEM, and USEM use an optical pulse as a pump limiting lateral spatial resolution to few μm according to Abbè diffraction theory. Surface sensitivity on excitation depends on the absorption depth ranging from 1 to 0.1 μm and energy resolution is less than 1 meV. In the proposed USEM the wavelength would be optimized to minimize absorption depth to 10 nm. TR-CL excites the sample with electron pulses: the spatial resolution may be of the order of nanometers, while the energy resolution is wide because electron beam does determines broadband excitation. TR-CL detects cathodoluminescence signal from the whole sample, therefore, has no spatial resolution on detection. Analysis of the spectrum of emitted light gives TR-CL energy resolution on detection while surface sensitivity depends strongly on the energy of the exciting electrons and on the absorption depth of light inside the material, nonetheless is of the order of tens of nanometers. Optical pump-probe uses an optical pulse also for probing and therefore has the same spatial resolution, surface sensitivity, and energy resolution both in excitation and in detection. TR-PEEM uses an optical pulse to determine photoemission: this increase surface sensitivity to 1-10 nm because deeper electrons cannot be photoemitted and pushes spatial resolution down to nanometer scale while keeping the energy resolution typical of the optical probe. Finally, USEM probes the sample with an electron pulse triggering SE emission to the detector. SE emission may be localized in a radius of few nanometers; surface sensitivity is related to SE emission depth and equal to few nanometers.

		Spatial resolution		Surface sensitivity		Energy resolution	
	Time resolution	excitation	detection	excitation	detection	excitation	detection
Optical	500 fs [62]	few μm	few μm	1-0.1 μm	1-0.1 μm	< 1 meV	< 1 meV

TR-CL	10 ps [3]	< 50 nm	All sample	5 nm-50 nm [87]		Tens of eV	0.2 meV
TR-PEEM	240 fs [63]	few μm	100 nm [63]	1-0.1 μm	1-10 nm	< 1 meV	(< 1 meV)
USEM	< 1 ps [9]	few μm	10 nm	1-0.1 μm	1-10 nm	< 1 meV	Tens of eV
Proposed USEM	**1 ps**	**few μm**	**10 nm**	**10 nm**	**1-10 nm**	**< 1 meV**	**Tens of eV**

TABLE 1 – COMPARISON OF TIME-RESOLVED TECHNIQUES FOR TIME-RESOLVED DYNAMICS OF OPTICALLY EXCITED CARRIERS IN SEMICONDUCTORS

Summing up the results optical pump-probe, TR-CL, TR-PEEM and USEM may give information about charge generation, transport and recombination in semiconductors with temporal, lateral spatial and depth resolution. All of them have similar temporal resolution around hundreds of femtoseconds except for cathodoluminescence that reached 10 ps [3] and optical pump-probe that could reach the tens of femtoseconds. Spatial resolution of optical pump-probe is limited to few micrometers or hundreds of nanometers by Abbè diffraction limit also using UV light. TR-CL proved a spatial resolution of 10 nm and a measurement of charge transport in semiconductor was reported [3]. TR-PEEM proved a spatial resolution of 100 nm [63]. By the state of the knowledge, spatial resolution in USEM should be limited to few nanometers by the SE emission area. This resolution has been proved in static SEM images obtained with pulsed electron beam but all the systems studied had typical size on the microscale. Further experiments could allow evaluating the spatial resolution limit of USEM in a time-resolved measurement to exploit the full potential of the technique. Other complementary techniques based on electron transmission and electron diffraction exist that could provide helpful information in addition to the USEM measurement in selected cases. Ultrafast TEM has better spatial resolution than USEM but does not apply to thin samples. It has been proven that time-resolved EBSD may be combined with USEM, but potentiality of the technique has not been fully exploited yet.

The objective of this thesis is to present

1) the development of an Ultra High Vacuum Ultrafast Scanning Electron Microscopy apparatus, optimized to investigate the dynamics of charges at sample surface, and
2) the first results obtained on prototypical samples of semiconductors and insulators, namely the (001) surface of silicon, as a function of its doping level, and a alumina polycrystalline film on Si.

2.8.1 The development of the UHV USEM apparatus

To reach the goal, we focused on three main parameters in order to optimize the technique with respect to the status-of-the-art:

- the residual gas pressure within the USEM chamber;
- the pump excitation wavelength;
- the primary beam voltage.

Our choices are briefly outlined in the following.

The use of an ultra-high vacuum (pressure lower than 10^{-7} Pa) is justified by

- the evidences [29] [31] on the role of the surface on charge dynamics and specifically on the differential SE contrast adopted in most of the USEM setups, and
- the role of the environmental pressure within the USEM apparatus on the surface properties, due to electron beam enhanced deposition of contaminants [51] [107] [108].

It is common wisdom that residual gases, and particularly hydrocarbons, are effectively dissociated by electron impact and deposit at the sample surface [107]. The process is purposely exploited in electron beam deposition setups where precursor gases are introduced in the SEM chamber [108]; when not pursued, the effect can be evident up to residual gas pressures down to 10^{-11} Pa at the electron kinetic energies and fluences typical of SEM and USEM imaging. Thus, quantitative measurements of surface dependent quantities require UHV conditions, as well known to the electron spectroscopy community. This approach makes our apparatus a unique in the present scenario of the USEM measurements and is aimed at providing quantitative and reproducible results on the dynamics on controlled sample surfaces.

The operating pressure was in the range of $10^{-8} Pa$. At such a pressure, a monolayer of contaminant needs few hours to deposit in the worst scenario, where each molecule hitting the sample surface stiches on it. Our experience on the Si and Aluminum oxide surfaces, demonstrate that few acquisitions in the USEM conditions do not alter significantly our results.

We chose to use an optical excitation wavelength for the pump pulses of 343 nm, third harmonic of an ytterbium doped fiber laser, corresponding to a photon energy of 3.6 eV. The corresponding extinction length in silicon is 10 nanometers [109], less than one order of magnitude larger with respect to the emission depth of SEs, estimated in a few nm. The choice of the wavelength is different from the one reported in state-of-the-art experiments on USEM, which employ the second harmonic of an ytterbium doped fiber laser at 515 nm. Figure 37 presents a comparison of the absorption length at the different wavelengths, showing a difference of more than one order of magnitude for the two harmonics, in favor of an enhanced surface sensitivity for the pump at 343 nm.

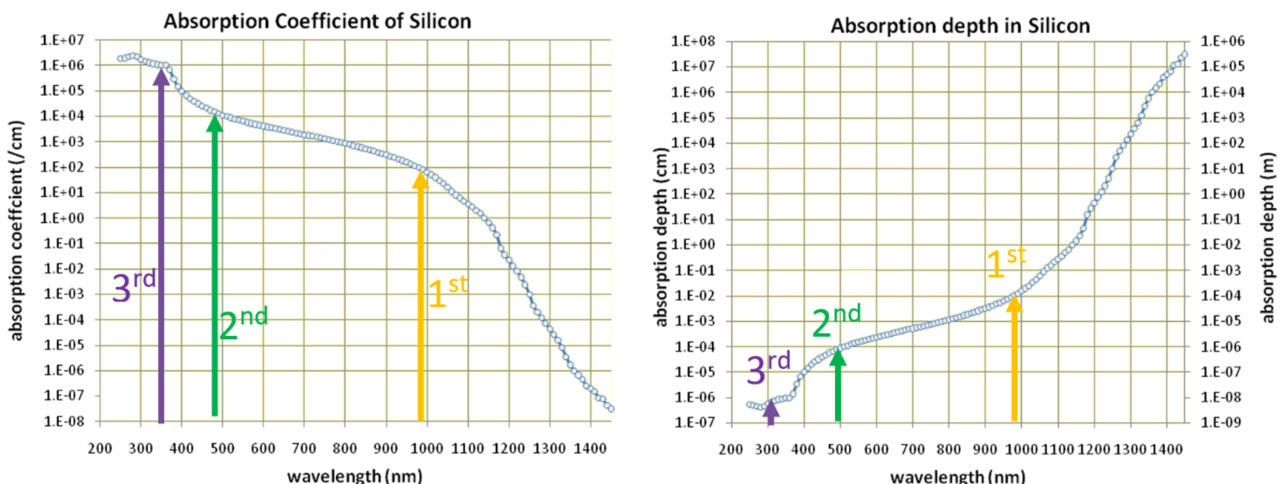

FIGURE 37 – ABSORPTION COEFFICIENT (ON THE LEFT) AND ABSORPTION DEPTH (ON THE RIGHT) FOR THE 1ST, 2ND AND 3RD HARMONICS OF THE LASER. DATA FROM [110]

Aluminum oxide the gap has a gap equal to ~8 eV and valence to conduction band excitation would have required a harmonic generator operating in vacuum to prevent optical absorption from nitrogen. Third harmonic photons have energy equal to 3.6 eV, definitely lower than the bandgap. Nonetheless, also for sub-bandgap photons, optical absorption is non-zero thanks to crystalline defects like oxygen vacancies, known as color centers because they give optical properties in the visible and UV part of the spectrum to wide band gap crystals. The extinction length for the third harmonic in aluminum oxide ranges is equal to few millimeters [111], strongly depending on the concentration of defects and considerably larger than in the case of Si. Valence to conduction band excitations in aluminum oxide may be obtained as an effect of the PE beam, as already shown for cathodoluminescence. Since in aluminum oxide the concentration of electrons in conduction band is negligible this effect is relevant, much more than what could be expected for silicon.

The USEM results on electron dynamics of oxygen vacancy in aluminum oxide are reported in chapter 5 USEM investigation of the color center charge dynamics at the surface of aluminum oxide.

Most of the previous experiments reported on USEM used PE beam energy of 30 keV [9]. Nonetheless, it was shown that on CdSe SE contrast at positive delays was independent on PE energy in the range 1-30 keV [83]. The operating energy of 10 keV, chosen for the USEM in this work, is a compromise between surface sensitivity and temporal resolution. Lower voltages have better surface sensitivity and low penetration depth of the PE. However, the longer travel time of electron pulses along the electronic column of the microscope brings to the deterioration of the time resolution. The present trade-off results in a time resolution of about 60ps at the pulse charges used in the measurements, as discussed in paragraph 3.7 Time resolution.

2.8.2 The choice of the scientific cases

The sample choice relies on both their well-known properties and availability and on their importance for electronics and energy harvesting industry.

Silicon plays a unique role in electronics that doesn't need commenting; we selected the Si(001) surface that is mostly used in technological applications, to be investigated versus doping, in a set of samples ranging from *n* degenerate (electron carrier density, about 10^{19} $1/cm^3$) to *p* degenerate (electron carrier density, about 10 $1/cm^3$) passing through the intrinsic material. This choice turns out to highlight the role of doping and of the surface in charge carrier dynamics and its contribution to the formation of the differential SE contrast in USEM. The results and their discussion, including a model for the surface contribution, complementing the bulk model proposed by A. H. Zewail and coworkers are presented in chapter 4 USEM investigation of the surface charge dynamics at the Si(001) surface as a function of doping.

Alumina is widely adopted as insulator in a variety of semiconductor devices and is nowadays an important transparent support for photovoltaic devices. Alumina and its defects are deeply characterized in the literature, where optical pump-probe provide a reliable and close comparison for our results. This makes it an optimal test bed for the USEM capabilities on insulators, as Si is for the semiconductors.

Finally, a short section will be devoted to the time-resolved EBSD investigation of ultrafast dynamics of the Verwey transition in magnetite, that was performed at the state-of-the-art UED setup of EPFL, Lausanne. This

research was done at the Laboratory for Ultrafast Electron Microscopy and Spectroscopy directed by prof. Fabrizio Carbone, in view of the future implementation of the EBSD technique in time-resolved mode.

3 Experimental setup

The goal of the thesis is the development and characterization of an UHV USEM. The experimental setup of an USEM has been introduced in paragraph “2.3 Ultrafast Scanning Electron Microscopy” and is made by a SEM equipped with an ultrafast electron source, a mode-locked ultrafast laser, and an optical setup that generates two optical pulses, synchronized and delayed. One, the pump, excites the ultrafast dynamic on the sample while the other, the probe, triggers the emission of an electron pulse from the ultrafast electron source. The electronic column of the SEM drives the electron pulse to the sample, and a detector records SEs emitted. Comparison of SEM and Ultrafast SEM (USEM) is reported in Figure 38. The SEM chosen for the thesis is the Scanning Auger Microscope model 660 by Physical Electronics that will be introduced in paragraph 3.1 Scanning Auger Microscope. With respect to other SEM’s the chosen one operates in UHV and is designed for surface sensitive elemental analysis based on Auger electron energy spectrum, helpful in characterizing surface quality. To obtain a pulsed PE beam and increase the performance, the original lanthanum hexaboride electron gun was substituted with an ultrafast electron source based on a Schottky field emission tip. In this way, it is possible to switch from high brightness continuous electron beam – in case standard SEM imaging operation is needed- to pulsed electron beam for time-resolved measurements, by simply changing the tip operating conditions. The upgrade of the electron source will be discussed in paragraph “3.2 Ultrafast electron source”, where the spatial resolution obtained will also be discussed. The ultrafast electron source is driven by a pulsed laser beam, while another laser beam is required to trigger the ultrafast dynamic on the sample. The laser source, an, Ytterbium-doped fiber laser model Satsuma manufactured by Amplitude Systémes, provides high power femtosecond pulses at a tunable repetition rate in the range of MHz. Stability, reliability and low maintenance were also key points for the choice. The laser system and the optical setup, including harmonic generators and a delay stage, are described in paragraph “3.3 Optical setup”. To overcome limitations due to low signal to noise ratio a detection scheme based on probe modulation and lock-in detection was implemented and tested. The modulation was obtained by an optical chopper on the path of the laser beam driving the electron source while the signal to demodulate was collected at the output of the SE detector. The comparison of classical SEM, ultrafast SEM and Ultrafast SEM with lock-in detection is shown in Figure 38.

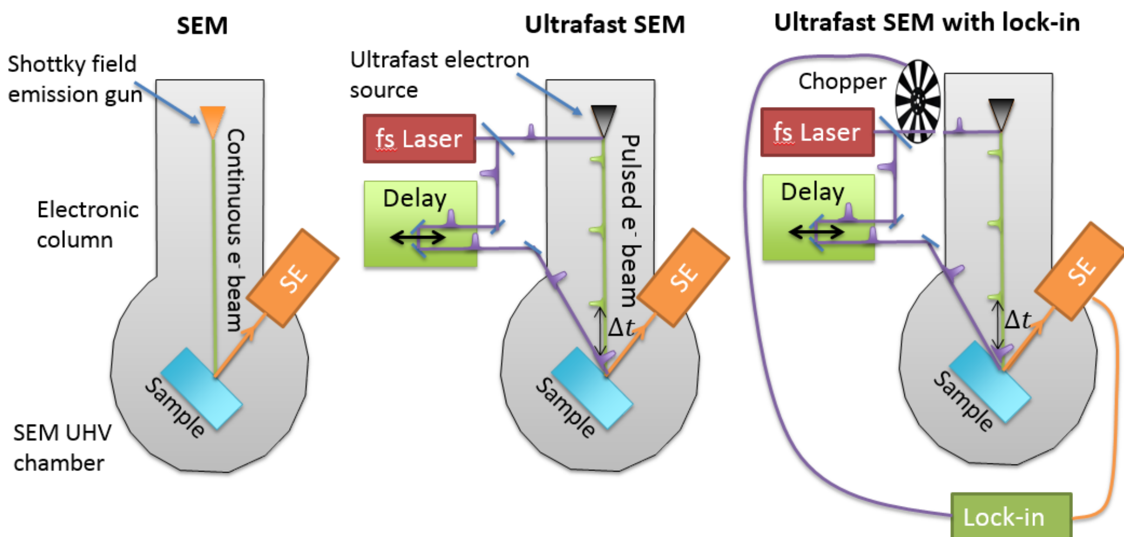

FIGURE 38 – COMPARISON OF EXPERIMENTAL SETUPS OF SEM AND ULTRAFAST SEM

Classical SEM was used for non-time-resolved imaging, USEM was used for time-resolved imaging, and USEM for lock-in detection was used for time-resolved SE measurement when signal to noise ratio was low. The alignment operations required to switch from continuous electron beam to pulsed electron beam and the quality of SEM images acquired with pulsed electron beam will be discussed in paragraph “3.4 Pulsed emission”. Both USEM and USEM with lock-in configuration required spatial superposition of the laser beam and the electron beam on the sample. The techniques and the operations done with the goal to reach spatial alignment will be presented in paragraph “3.5 Spatial alignment”. Paragraph “3.6 Temporal alignment” introduces the procedure used to acquire and analyze the USEM images in the dependence on the delay of the electron pulse with respect to the laser pulse. The time zero, corresponding to the temporal overlap of the electron and laser pulse on the sample, was identified by an abrupt change in contrast in dependence on delay observed on highly doped p-silicon. Temporal resolution, strongly influenced by the Boersh effect that spreads the electron pulses while traveling along the SEM column, was characterized in dependence on the number of electrons per pulse. Results are presented in paragraph “3.7 Time resolution”. The USEM with lock-in detection was developed for the measurements on aluminum oxide and will be presented in paragraph “5.2.4 Chopper and lock-in” of chapter “5 USEM investigation of the color center charge dynamics at the surface of aluminum oxide”.

3.1 Scanning Auger Microscope

The SEM used is a Scanning Auger Microscope model Phi660. It was chosen because it allows both SEM imaging and surface sensitive elemental analysis in Ultra High Vacuum. Elemental analysis is done by the analysis of the energy spectrum of the Auger electrons, introduced in paragraph “2.1.2 Auger emission”. Energy resolved detector is a Cylindrical Mirror Analyzer integrated in the electronic column of the microscope. To get a good signal to noise ratio in the energy-resolved Auger spectra the electronic column was originally designed to operate with a PE beam current ranging from nA to μA. The original lanthanum hexaboride electron gun was substituted with a Shottky field emission gun with optical access. The new source will be presented in the paragraph “3.2 Ultrafast electron source”. A picture of the microscope before the upgrade is reported in Figure 39.

FIGURE 39 – THE SCANNING AUGER MICROSCOPE MODEL 660 BY PHYSICAL ELECTRONICS BEFORE THE UPGRADE

This chapter will introduce the electronic column, the SE detector and the procedure for SE SEM image acquisition. Since the description given in this paragraph corresponds to a scanning electron microscope, a reader who already knows about SEM could skip the chapter and jump to paragraph "3.2 Ultrafast electron source".

3.1.1 Electronic column

The electronic column has the goal to convey the PE beam from the electron source to the sample. Sample, excited by PE beam emits SEs that are collected by external SE detector, and Auger electrons, energy filtered by a Cylindrical Mirror Analyzer and measured by the collector. A picture and a cross-section of the electronic column of the Phi 660 microscope before the upgrade of the electron source is reported in Figure 40.

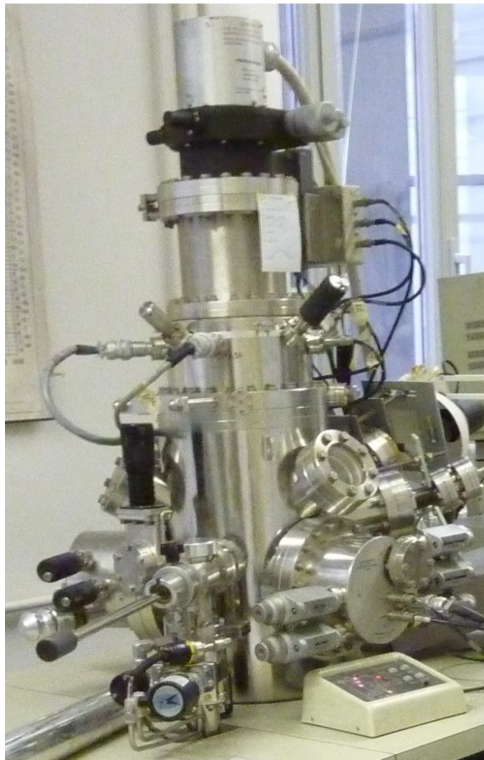

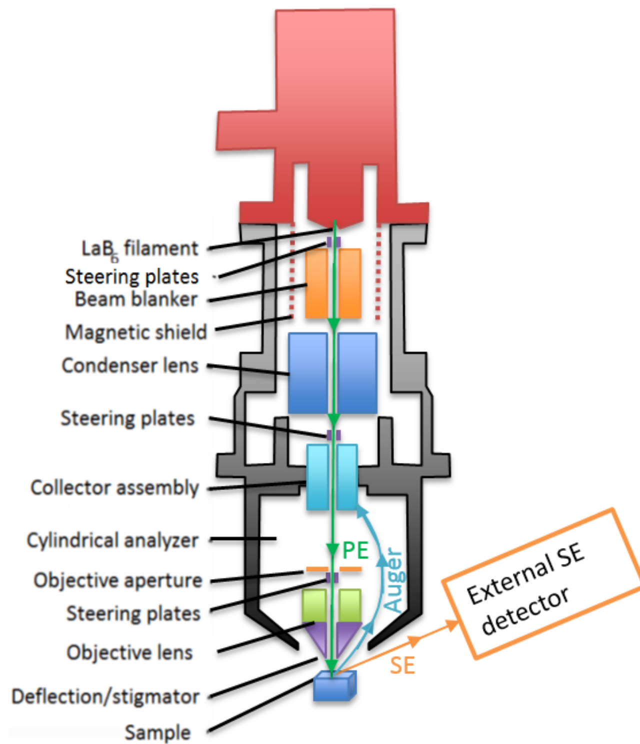

FIGURE 40 – PICTURE OF THE ELECTRONIC COLUMN BEFORE THE UPGRADE (ON THE LEFT) AND CROSS-SECTION SKETCH (ON THE RIGHT)

From the source to the sample the electrons meet deflecting plates, beam blanker, condenser lens, objective aperture, objective lens and a scanning octupole. Deflecting plates have the goal to finely compensate alignment mismatch between the electron source and the column. Condenser and objective are magnetic lenses that regulates intensity, magnification and angular divergence of the electron beam on the sample. The focal length of the condenser and of the objective may be regulated by a current regulated power supply. The aperture act as a spatial filters on the electron beam, reducing the current. The size of the aperture cannot be continuously regulated. Nonetheless thanks to a manipulator it is possible to switch among different apertures with four sizes. By the aperture and the lenses, it is possible to optimize the electron beam parameters as a trade-off between maximum current and minimum spot size. Maximum current helps to improve signal to noise ratio while minimum spot size improves lateral spatial resolution. The operating parameters of the electronic column may be regulated continuously by acting on the current to the lenses and on the size of the aperture. A sketch of the electron beam in the extreme conditions is reported in Figure 41. Maximum current is obtained by choosing the widest aperture and regulating the focal length of the condenser in order to minimize the size of the electron beam at the aperture plane. In this condition the full electron beam passes through the aperture and current reaching the sample is the maximum possible. Once set the focal length of the condenser, objective is regulated to adjust the focus on the sample. Electronic column was optimized for maximum current both during Auger and USEM measurements, to improve the signal to noise ratio. It is possible to reduce intensity of the PE beam at the sample by choosing a smaller aperture or by changing the setting of the condenser lens. In fact, when reducing the focal length of the condenser, the image plane becomes nearer to the lens and the size of the electron beam at the aperture plane increases. A portion of the electron beam hits the aperture and current is reduced. In addition, the magnification of the condenser lens is reduced since the object plane is nearer. As a consequence, the objective focal length has to be reduced to keep focus on the sample because the image plane distance has increased while the object is still the sample, in the same place. Also, the magnification of the objective lens is

therefore reduced. The total magnification is the product of the magnification of the objective and the condenser and then is reduced when reducing the current. The image of the source is demagnified, and the size of the electron beam on the sample is reduced. Reducing current allows to improve spatial resolution and to reduce electron beam induced contamination. The limit to the spot size is the intensity of the beam at the sample and the corresponding signal to noise ratio.

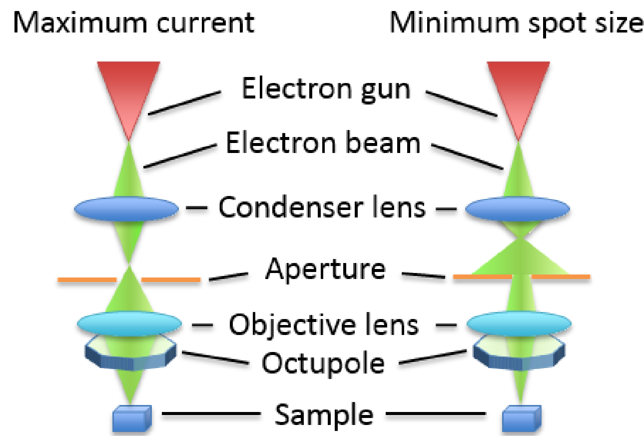

FIGURE 41 – FROM THE LEFT TO THE RIGHT: SKETCH OF PATH OF THE ELECTRON BEAM IN MAXIMUM CURRENT MODE, PATH OF THE ELECTRON BEAM IN THE MINIMUM SPOT SIZE MODE

The electrostatic octupole, installed after the objective lens, has the function of both raster scanning the electron beam on the sample and to correct astigmatism as shown in Figure 42.

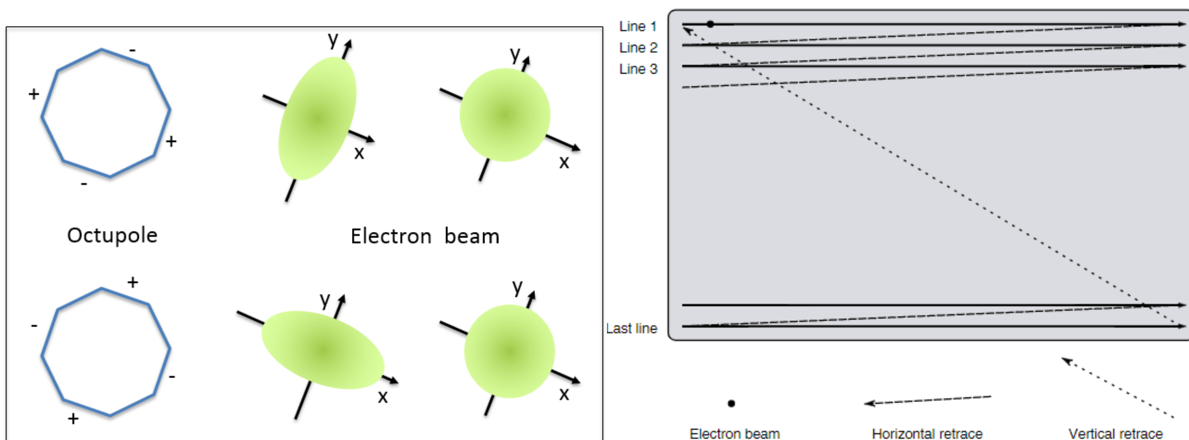

FIGURE 42– ASTIGMATISM COMPENSATION WITH AN ELECTROSTATIC OCTUPOLE ON THE LEFT AND RASTER SCAN PATH ON THE RIGHT

The raster scan is a process that allows scanning a beam on a rectangular area. The full path is sketched in Figure 42. The scan starts from one corner of the image, and then the beam is shifted horizontally by discrete step. After the beam has reached the desired position, the signal from desired detector is integrated for the dwell time, is acquired, is digitized and finally is assigned to the corresponding pixel. The displacement of the electron

beam for each step corresponds to pixel size. After completing the first line, the beam is brought back to the beginning of the line and displaced vertically by a pixel size. The process is called horizontal retrace. The second line is acquired pixel by pixel as the first, and then all the other lines. When the beam reaches the last point of the last line, the scan is completed. The beam is brought back to the initial position following a path called vertical retrace. The entire scanning process is controlled by a dedicated microprocessor. In the PHI 660 SAM, the raster is able to scan a grid of 512 pixels x 512 pixels. The result of a single raster scan is a frame: up to 16 frames could be averaged to obtain an image. The acquisition time per frame may be regulated from 0.2 s to 6.7 s. USEM images were acquired by averaging 8 frames: each of the frame was integrated for 6.7 s. The scanning microprocessors calculates for each pixel the voltage for the octupole. For each plate, the control electronics is a chain of a 16-bit analog to digital converter followed by a high voltage amplifier. Voltage supply ranges from +200 V to -200 V. The deviation of the electron beam is dependent on the PE current. At a PE energy of 10 keV, the diagonal of the maximum view field that could be obtained is equal to 1009 μm. Precision on the positioning is therefore equal to diagonal size divided by number of steps equal to 15 nm. USEM images were acquired with a view field of horizontal size equal to 393 μm with a size ratio of 4:3. Length of the diagonal is therefore 491 μm. The added path when the electron beam hits the extremum of the image with respect to the center may be calculated with the Pythagorean Theorem in the hypothesis of sample surface perpendicular to the electron beam, setting d as diagonal and d_w as the working distance. The distance from the octupole to the sample for the beam that hits in the center of the raster scanned area is d_w, while it is $\sqrt{\frac{d^2}{4}+d_w^2}$ for a beam hitting in the edge. The difference is $\sqrt{\frac{d^2}{4}+d_w^2}-d_w=d_w\left(1-\sqrt{\frac{d^2}{d_w^2 4}+1}\right)\sim d_w\left(\frac{d^2}{2d_w^2}\right)=\frac{d^2}{2d_w}$ equal to 4.5 μm for the working distance used in USEM measurements, $d_w=27\ mm$. In the conditions used for acquisition of USEM images, the raster scan may add a systematic uncertainty on the travelling time of the electron beam equal to 7 fs. The effect is fully negligible with respect to the temporal broadening introduced by the expansion of the electron pulse while it is travelling along the electronic column reported in paragraph “3.7 Time resolution”.

3.1.2 Secondary Electrons detector

Detection of SEs is a key factor for the success of the USEM experiment. The most common detector is the Everhart-Thornley [112]. The scheme of an Everhart Thornley detector is reported in Figure 43.

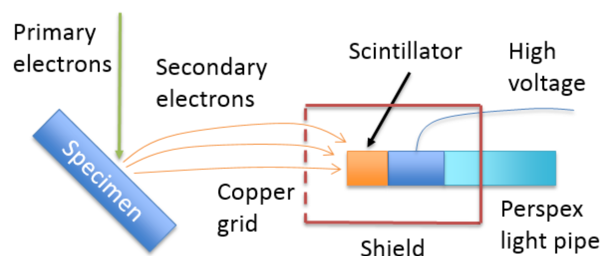

FIGURE 43 – SCHEME OF AN EVERHART-THORNLEY SE DETECTOR

The Everhart-Thornley detector is made by a scintillator covered with a thin layer of metal. SEs are attracted by a positively biased grid and accelerated towards the scintillator. The electrons cross the metal layer determining

emission of light from the scintillator. Emitted light is conveyed to a photomultiplier by a light pipe [112]. The main advantages of Everhart-Thornley detector are sensitivity, wide bandwidth and optical insulation. Sensitivity is limited by the dark current of the photomultiplier to SE currents of the order of fA. Bandwith is limited to hundreds of MHz by photomultiplier transit time and by scintillator decay time. Finally, the electron to light conversion allows to decouple the high voltage used to accelerate SEs from the electronics that process the output signal [112]. The limits of Everhart- Thornley are the low compatibility with Ultra High Vacuum and the sensitivity to light, not fully screened by the metal that covers the scintillator. The microscope chosen for USEM experiment is equipped with a channeltron based SE detector, insensitive to light and UHV compatible. A scheme of the detector is reported in Figure 44. With respect to the Everhart-Thornley has the advantage of being fully compatible with UHV and totally insensitive to light. Light rejection is particularly relevant in an ultra-high vacuum chamber where the filament of the Bayard-Alpert vacuometer [113] and the ionic pump generate wide spectrum light. Furthermore, in the experimental setup of USEM, the laser beam that reaches the sample is partially scattered adding diffused light into the chamber. Another advantage is the reproducibility of the gain, particularly relevant to compare measurement acquired in the same nominal conditions but in different days with different lab temperature and relative humidity. The main disadvantage are a lower sensitivity with respect to Everhart-Thornley. Sensitivity was not an issue in the original microscope since the machine was optimized to work with larger PE beam current than a common SEM to improve the signal to noise ratio of the Auger energy-resolved measurements, but appears critical for the development of USEM.

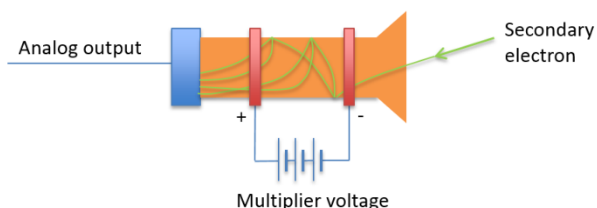

FIGURE 44 – SKETCH OF THE SE DETECTOR INSTALLED ON THE PHI 660 SCANNING ELECTRON MICROSCOPE

The SE detector has multiplier voltage as input and generates an analog output as shown in Figure 44. The detector has the shape of a pipe with a funnel at the end. Electrons are attracted inside the pipe by the positive bias placed at the end. Once an electron hits the surface, it generates SEs. They are newly accelerated and hit the surface once again. The process brought to an amplification of the SE current. The multiplier voltage, ranging from 0 V to 4000 V, determines the gain of the amplification of SE current by the channeltron. It is supplied by the control electronics and may set by the user. Values commonly used in SEM imaging ranges from 1300 V to 1700 V. Increasing the multiplier voltage allows to increase the gain of the amplification system. Once amplified electrons are collected at the end of the pipe that is connected to the analog output. The analog output is connected to a preamplifier. The output of the preamplifier is an analog voltage signal ranging from 2V to -1V proportional to the SE current. The full sketch of the control electronics is reported in Figure 45.

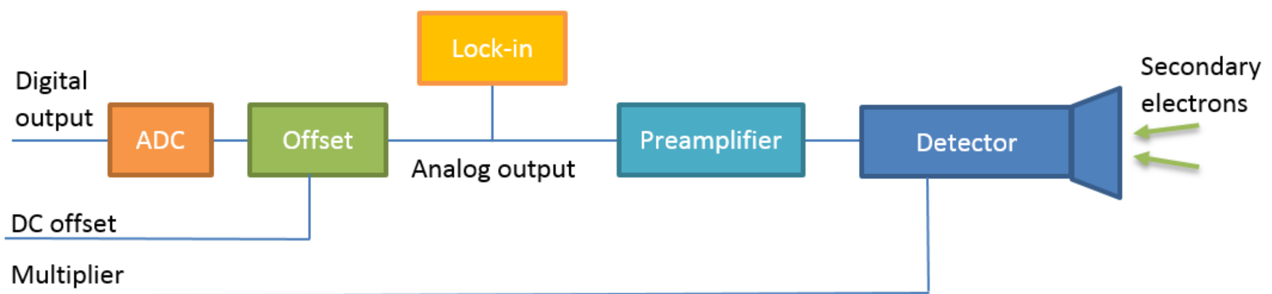

FIGURE 45 – SKETCH OF THE AMPLIFICATION AND PROCESSING CHAIN OF THE SE CURRENT SIGNAL. INPUT PARAMETERS DEFINED BY THE USER ARE MULTIPLIER, AND DC OFFSET AND OUTPUT IS A DIGITAL SIGNAL

The analog output of the preamplifier is shifted in voltage by adding a constant offset defined by the user and then is converted into a digital signal by an 8 bit Analog to Digital converter. After digital processing of the signal is done before associating the SE intensity measurement to a pixel and saving the data on the disk. To compare different images, it is necessary to be sure that the processing of the signal is the same. This was obtained by choosing a set of parameters and keeping them constant for all the USEM images. The choice was done in order to keep the detector working in the linear region far from saturation, that grants that the value measured is linearly proportional to the SE current. For measurement on aluminum oxide, the signal to noise ratio appeared too low, and the SE acquisition chain was modified by adding a lock-in. The signal for the lock-in was collected at the output of the preamplifier. The only relevant parameter affecting the output of the preamplifier is the multiplier voltage that was kept constant. acquisition parameter constant. Since the minimum integration time of the lock-in was much longer than the maximum dwell time allowed by the acquisition electronic, it was not possible to acquire images of demodulated SE signal. The demodulated signal is, therefore, an average over the entire raster scanned area of 38 μm x 41 μm. A new detector, based on Everhart-Thornley technology, but optimized for ultra-high vacuum and modified to be insensitive to light has been designed and is being built. A sketch of the detector is shown in Figure 46

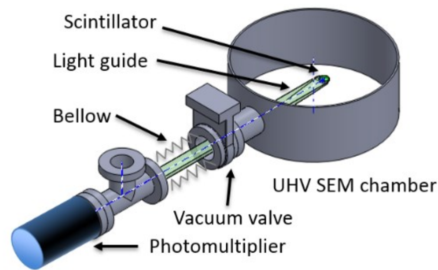

FIGURE 46 – SKETCH OF THE PROJECT OF AN UHV COMPATIBLE EVERHART- THORNLEY DETECTOR

3.1.3 Cylindrical Mirror Analyzer

CMA has the goal to energy filter the electron backscattered from the sample. It covers the energy range from 0 to 3200 eV with an energy resolution $\frac{\Delta E}{E}$ that may be regulated from 0.3% and 2%. A better resolution determines a lower signal to noise ratio. Cylindrical mirror analyzer is concentric with the column and accepts electrons from the full 360° around the axis of the analyzer. The capture angle is 42° ± 6° from the axis. When passing through the analyzer electrons are deviated by a radial electric field. At the end of the cylinder, there is an aperture. The electric field may be regulated in order to choose the energy of the electron that cross the aperture. By scanning the energy range it is possible to obtain an energy resolved measurement of the intensity of backscattered electrons. Auger peaks corresponding to elements at the surface of the sample, already introduced in paragraph 2.1.2 Auger emission, are resolved [51].

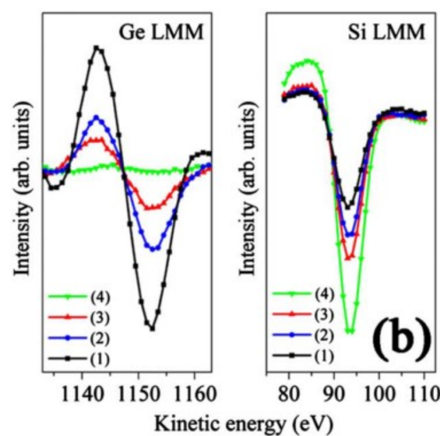

FIGURE 47 – PEAKS OF GERMANIUM AND SILICON IN DIFFERENT POSITION ON THE SURFACE OF THE SAMPLE. REPRINTED WITH PERMISSION FROM [51]

The intensity of the Auger peaks allows to determine the concentration of the corresponding element in the first monolayers of the surface of the sample.

3.1.4 Sample management

The Phi660 microscope has a load lock to allow the insertion of the samples into the main chamber without breaking the vacuum. While the main chamber is pumped by ionic and titanium pump, the load lock is pumped by a chain of turbo pump and forepump. The load lock chamber takes half an hour to reach high vacuum from air pressure and few minutes to vent. The sample holder with the sample attached on the top surface is inserted first into the load lock, pumped to high vacuum and then transferred into the main chamber onto the sample stage installed on a 5 axis manipulator. The axis are the three spatial translation direction X, Y and Z and the angular tilting and rotation. The Z always moves parallel to the electronic column independently on the angles while X and Y work on the tilted plane but affects the rotation axis.

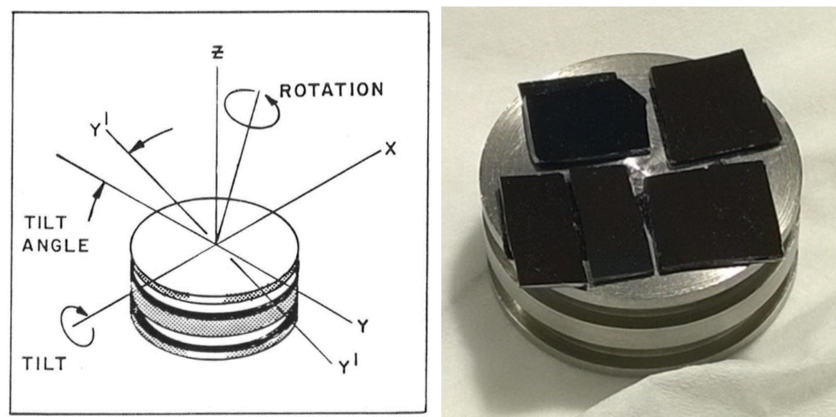

FIGURE 48 – SCHEME OF THE MOVEMENT ALLOWED BY THE SAMPLE STAGE (FROM USER MANUAL OF PHI660) AND A SAMPLE HOLDER READY TO BE INSTALLED INTO THE SEM CHAMBER

In the main chamber, there is a carousel able to store up to six circular sample holders with a diameter of 25 mm. Before installation, the sample has to pass two steps of ultrasonic cleaning, the first using acetone as a solvent to remove organic contaminants and the second using ethanol to remove acetone from the sample, which may be dangerous for the chamber. This is the standard procedure given by the user manual that was applied for aluminum oxide samples, that is not damaged when exposed to organic solvents. Further cleaning steps, including etching in Hydrofluoric acid, were added to control the surface quality of silicon samples and remove the native oxide layer. The full procedure is presented in paragraph **4.2** Sample set and preparation.

3.2 Ultrafast electron source

The ultrafast electron source is a Schottky field emission gun excited by photoemission through 300 fs laser pulses at 257 nm of wavelength (fourth harmonic of the laser fundamental at 1030 nm). It was installed on top of the Phi660 electronic column as a replacement of the original lanthanum hexaboride electron gun. A picture of the parts removed and of the parts installed is reported in Figure 49.

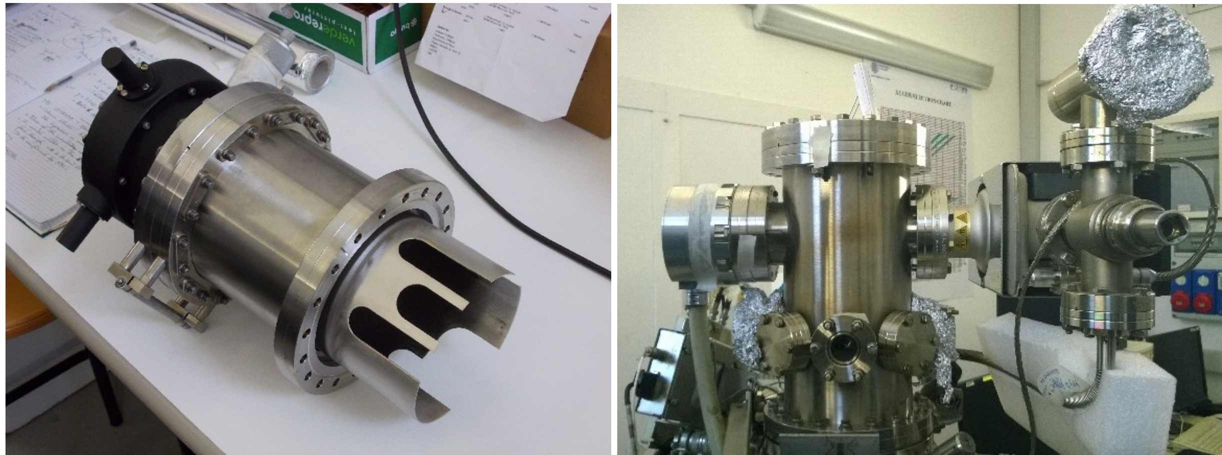

FIGURE 49– THE LANTHANUM HEXABORIDE SOURCE REMOVED (ON THE LEFT) AND THE NEW SCHOTTKY FIELD EMISSION GUN WITH OPTICAL ACCESS INSTALLED (ON THE RIGHT)

3.2.1 Description and operation

The source, developed by YPS Ltd, is a Schottky field emission source with optical access. A sketch of the source is shown in Figure 50. The core is a needle made by tungsten and covered with zirconium oxide to reduce the work function. Emission happens from the tip of the needle that has a radius of 300 nm [114]. In front of the tip, there is an electrode positively biased called 'extractor' that generates an electric field parallel to the axis of the needle. Vacuum creates a potential barrier from the tip to the extractor electrode. Thermal energy is given to electrons in the needle to help them overcome the potential energy barrier [115]. This is obtained by heating the needle to the desired temperature by a dedicated heater, made by an electrical resistor. A cylindrical electrode called suppressor helps to reduce the divergence of the emitted electrons. Emitted electrons are spatially filtered by an aperture in the extractor electrode. The ones emitted with lower divergence are accelerated by the anode to a desired voltage ranging from 1 to 30 kV. The accelerating field is obtained by setting the anode at the same potential of the SEM chamber while raising the needle to negative high voltage. An intermediate electrode between the anode and the extractor, called 'lens' that improves collimation of the electron beam [76]. Four holes were drilled in extractors and suppressor electrodes, and viewports were installed in the electron source chamber to allow a UV laser beam to reach the tip of the needle. The light not absorbed by the needle passes by and may be collected at the opposite side of the chamber.

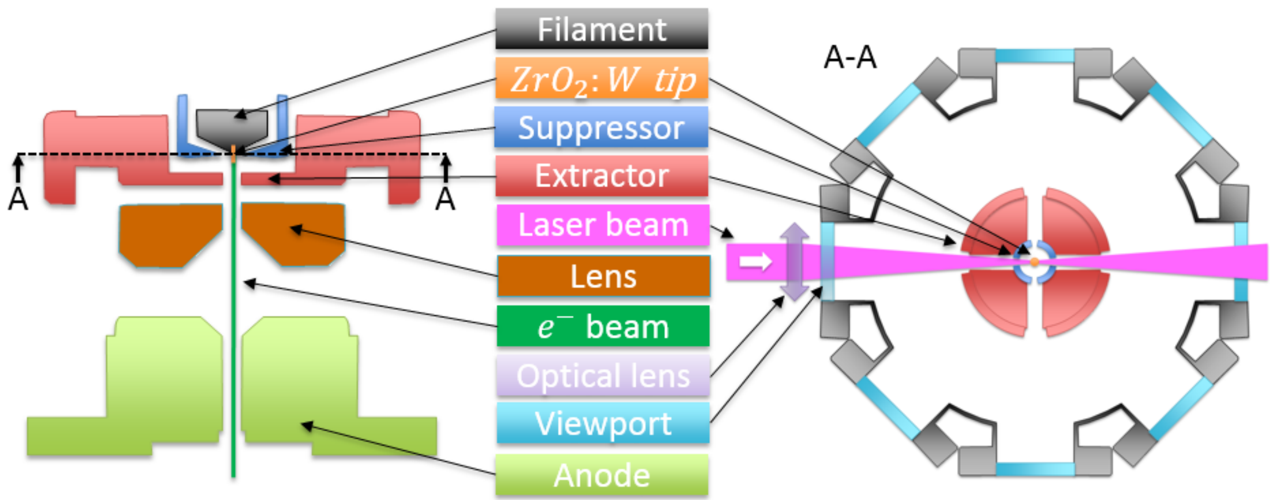

FIGURE 50 – CROSS-SECTION VIEW OF THE SCHOTTKY FIELD EMISSION ELECTRON GUN ON THE PLANE OF THE ELECTRON BEAM (ON THE LEFT) AND ON THE PLANE OF THE LASER BEAM (ON THE RIGHT)

The electron source has two operating regimes [26]:

- Continuous electron emission;
- Pulsed electron emission.

Continuous emission is a combined effect of the heating and the extracting electric field. In standard operating conditions for continuous emission, the needle is heated to 1800 K by applying a current equal to 2.4 A to the heater. The extractor electrode is positively biased at 2540 V with respect to the needle, while the suppressor is negatively biased at 300 V. In standard operating conditions, the maximum emitted current collected by the extractor electrode is 100 μA. The intensity of emitted current is dependent both on the extracting voltage and on the tip temperature that may be controlled by the heater current.

Pulsed emission is obtained by laser-induced photoemission from the tip. The suppression of continuous emission is obtained by cooling the tip until no current is emitted. Reducing the temperature was preferred to changing extracting voltage in order not to minimally perturb the configuration of electric fields around the needle and therefore keep, as far as possible, the same emission geometry. The experimentally measured emission threshold corresponds to a heater current equal to 2 A. The trade-off between the necessity to avoid continuous emission and to minimize surface contamination brought to the choice to keep the temperature of the tip just below continuous emission threshold. Tip temperature in pulsed emission mode may be estimated in the hypothesis that heater resistance is independent on temperature and that all the heat is dissipated by radiation according to Stefan-Boltzmann law. The dissipated power is:

$$P = Vi = i^2R = \sigma AT^4 \rightarrow \frac{T^4}{i^2} = \frac{R}{\sigma A} = const$$

The temperature of the tip in the condition of pulsed emission may be calculated comparing the case of continuous emission with pulsed emission:

$$\frac{T_{continuos}^4}{i_{continuos}^2} = \frac{T_{pulsed}^4}{i_{pulsed}^2} \rightarrow T_{pulsed} = \sqrt[4]{\frac{i_{pulsed}^2}{i_{continuos}^2} T_{continuos}^4} = \sqrt[2]{\frac{i_{pulsed}}{i_{continuos}}} T_{continuos} \sim 1600K$$

Therefore, the thermal energy spread of emitted electrons may be estimated as:

$$\Delta E = kT \sim 130\ meV$$

Independently on the operating regime, the voltage applied to the lens depends on the desired electron beam acceleration: at 10 kV the lens is biased at 1360 V.

3.2.2 Source performances and limitations

The new Schottky field emission gun was installed at the top of the electronic column of the Phi660 microscope as a replacement of the original lanthanum hexaboride electron gun. A comparison of the electronic column before and after the installation is reported in Figure 51. The installation of the source in the present setup required to remove parts of the electron column: the deflector plates immediately after the source, the beam blanker and part of the μ-metal screening of the electron column.

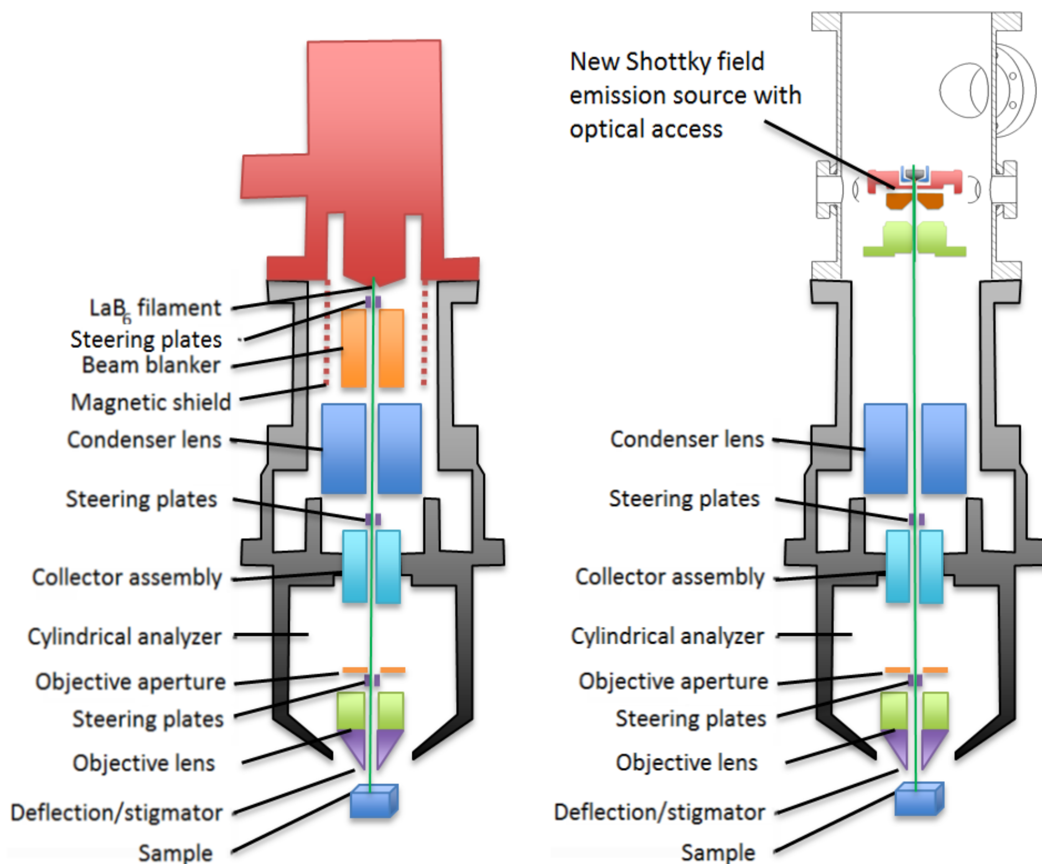

FIGURE 51 – CROSS-SECTION VIEW OF THE ORIGINAL ELECTRONIC COLUMN OF THE PHI660 ELECTRON MICROSCOPE (ON THE RIGHT) AND OF THE MODIFIED COLUMN (ON THE LEFT). THE LaB_6 FILAMENT, THE BEAM BLANKER, STEERING PLATES, AND PART OF THE MAGNETIC SHIELD WERE REMOVED TO INSTALL THE NEW SCHOTTKY FIELD EMISSION SOURCE WITH OPTICAL ACCESS

The present setup without those part is prone to a degradation of the microscope performances in terms of spatial resolution and stability, coming from a larger aberration within the condenser lens (due to a larger misalignment) and to a larger influence of the external electromagnetic fields, respectively. The performance

deterioration in the setup used in this work brings the spatial resolution up to about 80 nanometers, as discussed in detail in the paragraph 3.2.2 Source performances and limitations. Due to these resolution limitation, the experimental work has been focused on the depth and time resolution of the USEM technique, as described in chapters 4 USEM investigation of the surface charge dynamics at the Si(001) surface as a function of doping and 5 USEM investigation of the color center charge dynamics at the surface of aluminum oxide. A new mechanical mount of the source has been designed to allow the mechanical alignment of the electron gun with the electronic column. Other advantages would be the possibility to insert the removed parts of the magnetic field screen, restoring the full screening of the electronic column from magnetic noise, which allows the nominal lateral resolution of the PHI 660 SAM resolution of 25 nm. A view of the new mechanical support is reported in Figure 52.

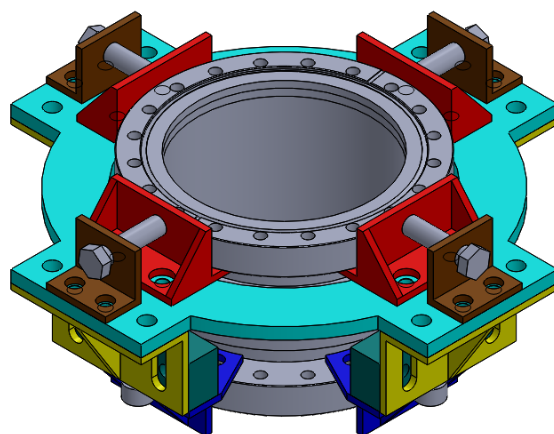

FIGURE 52 – THE NEW MECHANICAL 5 AXIS POSITIONING STAGE DESIGNED TO IMPROVE THE ALIGNMENT OF THE ELECTRON GUN AND TO ALLOW INSERTION OF A SCREEN FOR MAGNETIC NOISE

A further improvement in the lateral resolution performances is expected in the final configuration, thanks to the larger brightness of the Schottky field emission tip with respect to the LaB_6 source, commonly larger than 1 order of magnitude. Since the Phi 660 apparatus was already designed to work in ultrahigh vacuum no differential pumping was needed to separate the sample from the tip chamber, which are separated by a small hole for the electron beam; each chamber is equipped with an independent ionic pump. Therefore, variations in pressure in the main chamber in molecular regime does not significantly propagate to chamber of the electron source and do not affect the surface quality of the tip. A bypass was installed to connect the chamber of the tip to the main chamber to be used in case of venting.

3.2.3 Resolution limit

High magnification images have been acquired to test the resolution of the SEM microscope with the new source. Images were acquired by scanning on the surface of the sample a continuous PE beam generated by Schottky field emission.

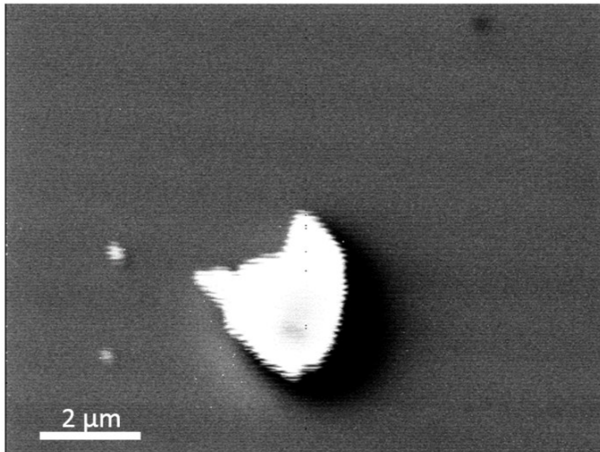

FIGURE 54 – HIGH MAGNIFICATION SEM IMAGES OF A GRAIN OF DUST

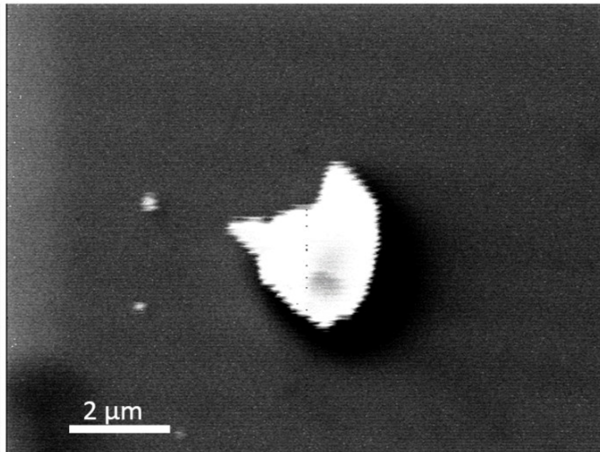

FIGURE 53 – HIGH MAGNIFICATION SEM IMAGES OF A GRAIN OF DUST

High magnification SEM image of a dust grain is reported in Figure 54. Consider the image on the left, acquired while the sample was installed on the sample holder. The edges of the particle appears zig-zagged. This is attributed to an oscillation of the electron beam spot on the sample. The frequency of the noise is comparable with the horizontal raster scan period of 76 Hz for the image. To check if the noise was caused by a mechanical oscillation the support of the sample was mechanically strengthened. The image acquired after strengthening the sample holder is reported in Figure 53. No difference was observed between images acquired while changing the mechanical stiffness of the sample holder support, which confirms that the contribution to the pointing oscillation due to mechanical oscillations is negligible. The pointing instability is therefore attributed to oscillations of the primary beam induced by electromagnetic noise, increased after the removal of a portion of the magnetic screen as discussed in paragraph 3.2.2 Source performances and limitations. The lateral resolution has been evaluated by fitting a luminosity profile perpendicular to luminosity gradients with an error function, therefore averaging the effect of the oscillations. The rise space from 20% to 80 % is the same for both images reported in Figure 53 and Figure 54 and equal to 80 nm. The results, worse than what could be expected considering the brilliance of the source installed, is affected by the electromagnetic noise.

3.3 Optical setup

The optical setup, introduced in this chapter, has the objective to deliver a pulsed optical beam on the sample and a second one, synchronized, coherent and delayed with respect to the first one, on the ultrafast electron source. The pulses are obtained by beam splitting the output of an ultrafast laser.

3.3.1 Ultrafast laser

The ultrafast fiber laser is an Amplitude Systèmes, model Satsuma. The emission wavelength is 1030 nm with a full width at half maximum of 7 nm. The pulses have a temporal length of 250 fs. The scheme of the laser is reported in Figure 55. Lasing happens in an optical fiber oscillator doped with ytterbium mode-locked at 40 MHz. A pulse picker allows to reduce the repetition rate by selecting only some of the pulses generated by the

oscillator. The repetition rate of the delivered beam needs to be a submultiple of the oscillator frequency but not less than 2 MHz. Selected pulses are amplified passing through a two-stage amplifier and a compressor that may be regulated to set the minimum length of the pulses. Finally, a modulator allows to reduce repetition rate below 2 MHz or to attenuate the intensity of the output beam when the repetition rate is higher than 2 MHz. The maximum available infrared power is 10 W when repetition rate is higher than 2 MHz, below the pulse energy is limited to 5 μJ. The repetition rate used for all the USEM measurement is 10 MHz.

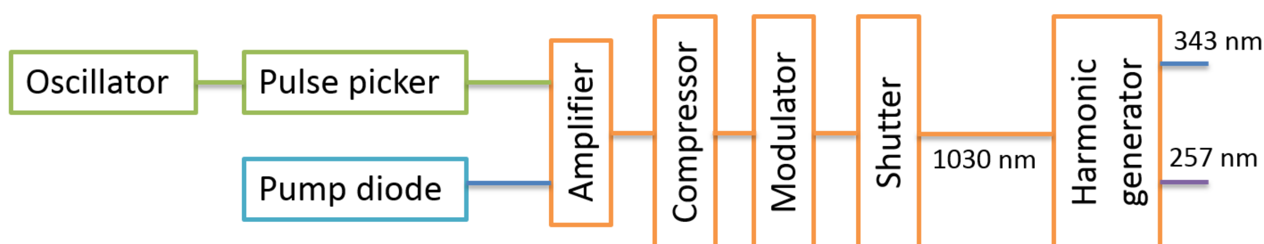

FIGURE 55 – DIAGRAM OF THE MAIN COMPONENTS OF THE LASER SYSTEM

The laser is followed by a beam splitter that generates both the beam used to excite the sample and the beam used to excite the ultrafast electron source. Harmonic generators are used to adjust the wavelength.

3.3.2 Beam splitting and harmonic generator

The wavelength of the optical beam that reaches the sample is 343 nm corresponding to an energy per photon of 3.6 eV. It is obtained by tripling the frequency of the laser beam. The ultrafast electron source is excited with a wavelength of 257 nm corresponding to an energy per photon equal to 4.8 eV. It is obtained by quadrupling the frequency of the laser output. First and second harmonic were excluded because the photons have an energy respectively equal to 1.2 eV and 2.4 eV, too low to excite photoemission. Both the third harmonic, 343 nm corresponding to 3.6 eV per photon, and the fourth, 257 nm corresponding to 4.8 eV per photon, are able to excite photoemission from the low work function materials of electron sources, such as LaB_6 and ZrO_2. The fourth harmonic beam was chosen to excite the photoemission of the electron pulses from the source tip in this work because it gives a higher emission efficiency and an output current that is more stable in time with respect to the third as reported in Figure 56 [26].

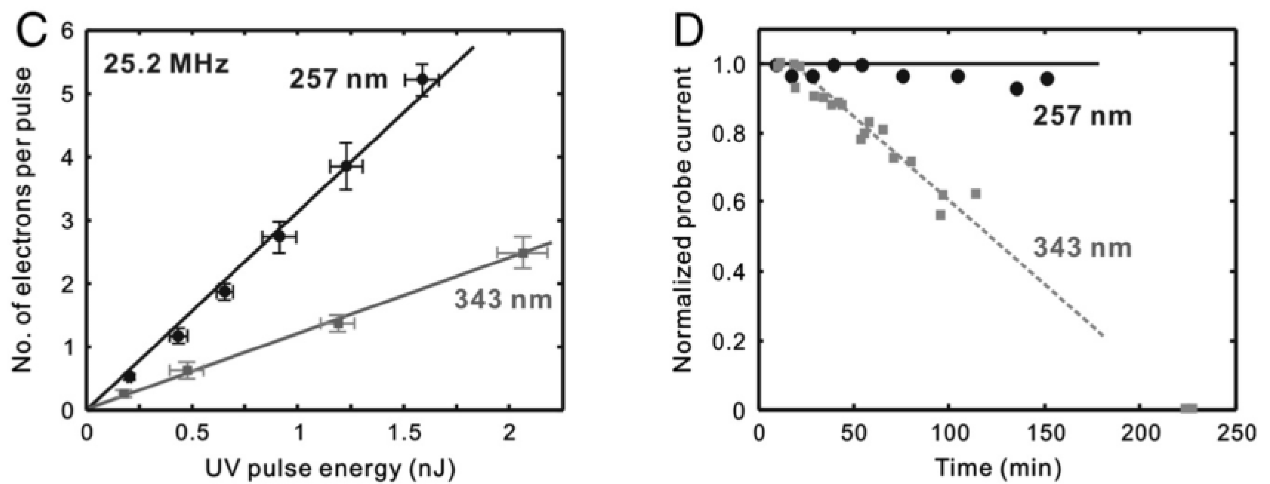

FIGURE 56 – COMPARISON BETWEEN ULTRAFAST SCHOTTKY FIELD EMISSION GUN POWERED BY A LASER OF WAVELENGTH 257 NM AND 343 NM IN EFFICIENCY (LEFT) AND STABILITY (RIGHT). IN PLOT C IT IS SHOWN THAT 257 NM IS ABLE TO CREATE MORE ELECTRONS PER PULSE WITH RESPECT TO 343 NM. IN PLOT D IT IS SHOWN THAT THE EMISSION OBTAINED WITH 257 NM IS CONSTANT OVER 3 HOURS WHILE 343 NM DECAYS LINEARLY AND BECOMES NEGLIGIBLE IN FEW HOURS. REPRINTED WITH PERMISSION FROM [26]

The harmonic generator, manufactured by Amplitude Systèmes, includes a beam splitter and the crystals for the harmonic generation. The optical sketch is reported in Figure 57. Third harmonic is obtained by summing infrared beam to its second harmonic. A quarter wavelength waveplate is used to align the polarization of the second harmonic with the one of the infrared beam. The fourth harmonic is generated by a sequence of two-second harmonic crystals. A magnifier, acting on the infrared beam, sets the proper size of the beam in order to make the crystals to operate at a good efficiency below the nonlinear crystals damage threshold. The magnifier used allows operating in a range of repetition rate from 2 MHz to 40 MHz. A motorized polarizer act as a switch and allows choosing whether to drive the infrared beam to the beam splitter and harmonic generators or to an output, used during alignment operation to check the power of the infrared beam. The power of the third harmonic (TH) and fourth harmonic (FH) may be optimized by aligning the crystal but also setting the optimum value for the compressor minimizing the length of the infrared pulses, as explained in paragraph 3.3.1 Ultrafast laser.

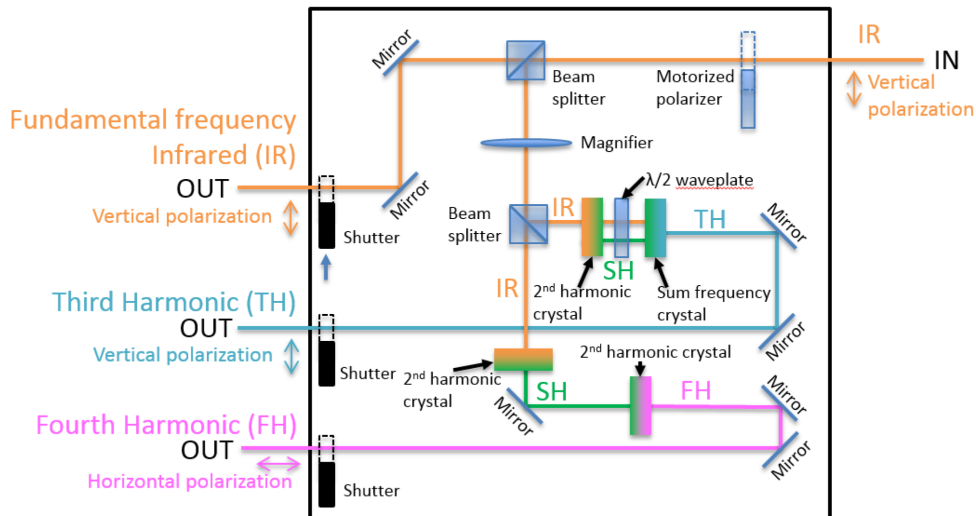

FIGURE 57 – OPTICAL SCHEME OF THE HARMONIC GENERATOR

At each output of the harmonic generator, a mechanical shutter allows independently switching on or off the corresponding beam

3.3.3 Optical layout: path to the sample

The complete path of the optical beam from the harmonic the laser to the sample is reported in Figure 58. After the harmonic generator, the third harmonic beam is sent on the sample through several steps where it can act as pump or probe depending on the experimental conditions as discussed in the experimental discussion in chapters 4 USEM investigation of the surface charge dynamics at the Si(001) surface as a function of doping and 5 USEM investigation of the color center charge dynamics at the surface of aluminum oxide. The laser beam passes through a beam expander, is reflected by a back reflector installed on a delay stage, and focused on sample by a focusing doublet of anti-reflective coated lenses. The available power at the output of the harmonic generator is 160 mW when the beam is delivered together with the fourth harmonic beam (used to generate the electron pulses at the electron source); the average beam power at the sample is 58 mW reaches the sample. The main losses are due to the beam expander and to the back reflector installed on the delay stage that are made by UV-enhanced aluminum mirrors with a reflectance of 92 %. All the other mirrors on the path of the pump are dielectric, with considerably lower power losses. An additional path was added to the beam that excites the sample with respect to the one that excites the electron source to compensate the traveling time of the electron beam in the electronic column of the microscope, from the source to the sample. The length of the compensation path depends on the energy of the PE beam.

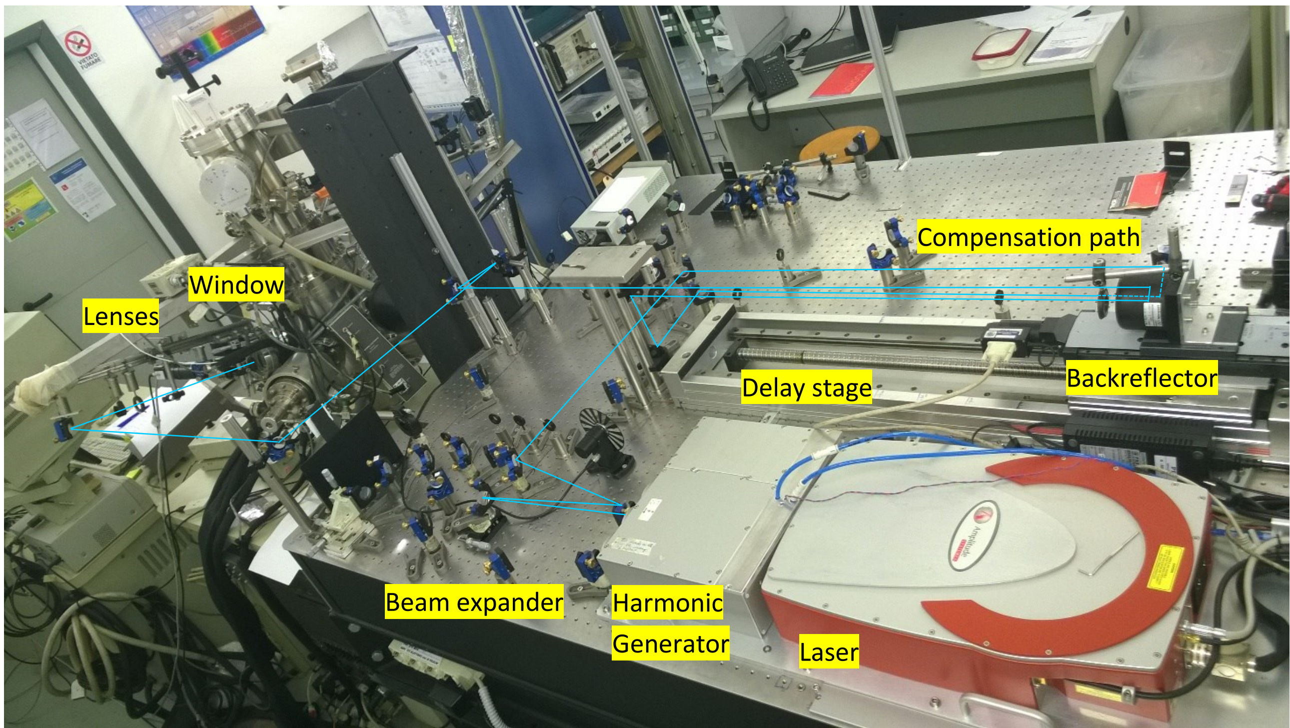

FIGURE 58 – OPTICAL PATH FROM THE LASER TO SAMPLE

The delay stage is 600 mm long and light pass through it two times. Therefore, the relative delay time of the electron pulses with respect to the photon pulses at the sample position may be regulated over a range of 4 ns. All over this work, the sign convention for the delay times is that positive delays indicate electron pulses arriving later than the photon pulses. The stage position is controlled by a SmartMotor: a brushless motor working in closed loop with an encoder. The entire length of the delay stage corresponds to 480’000 steps of the encoder meaning that 1 step corresponds to 1.25 μm and about 4 fs of sensitivity in the delay time selection. A detailed view of the optical beam passing through the delay stage is shown in Figure 59. The optical beam is lifted by a periscope and then is pointed towards the back reflector installed on a moving slit that runs on the linear stage. It is of paramount importance that the pointing direction of the optical beam, is parallel to the direction of movement of the linear stage; this is obtained by acting on the positioning stage of the last mirror before the back reflector.

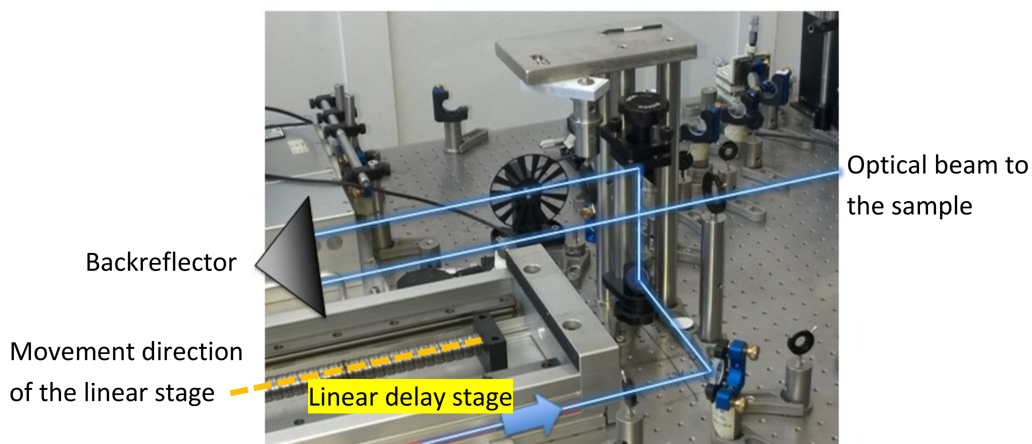

FIGURE 59 – DETAIL OF THE DELAY STAGE

The alignment condition allows that the laser hits the back reflector in the same place independently on the position of the stage, makes the same path and prevents displacement of the reflected beam because of a movement of the stage. A sketch of the optical path of the beam through the delay stage is reported in Figure 60. The alignment condition, propagation direction of the optical beam parallel to the movement direction of the linear stage mechanically joined with the back reflector, is shown in the bottom panel. For a perfect alignment, the direction of the reflected beam at the output of the stage is the same, independently on the position of the back reflector. On the contrary, when an angle between the propagation direction of the optical beam and the movement direction of the linear stage is present (2° for the example in figure), the output direction is not independent on the position of the back reflector on the stage as shown in the top panel.

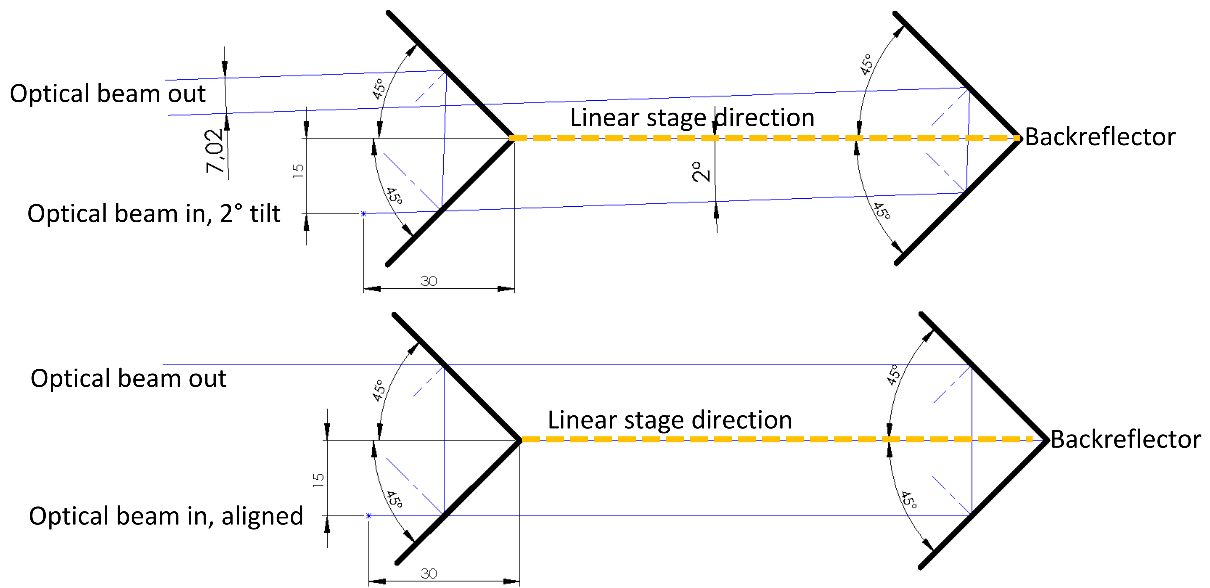

FIGURE 60 – PATH OF THE OPTICAL BEAM THROUGH THE DELAY STAGE WITH OPTICAL BEAM PARALLEL TO THE MOVEMENT DIRECTION OF THE LINEAR STAGE AND WITH THE OPTICAL BEAM TILTED BY 2°

The path of the laser beam from the last mirror before the focusing doublet and the window of the SEM chamber is shown in Figure 61. The beam is attenuated by a neutral attenuator, then passes through an iris, the focusing doublet of lenses and enters the chamber through a window made by fused silica. The optics are installed on a rail, aligned in order to allow the laser beam to reach the sample with the minimum aberration. The tilting stage of the last mirror before the doublet allows to finely displacing the position of the laser footprint on the sample with a precision of few micrometers. Controlling the position of the laser footprint is important to obtain spatial superposition of the optically excited area with the area raster scanned by the electron beam. The alignment procedure is described in paragraph 3.5 Spatial alignment.

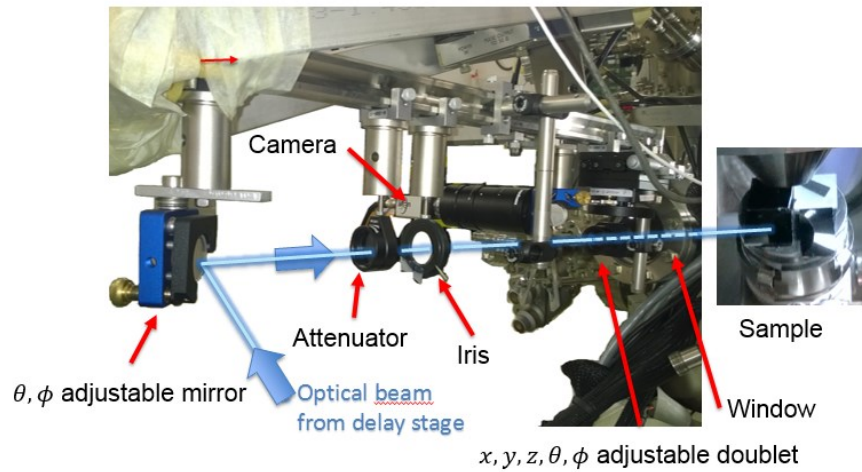

FIGURE 61 – PATH OF THE OPTICAL BEAM FROM THE LAST MIRROR TO THE SAMPLE. ON THE RIGHT AN OPTICAL VIEW OF THE SAMPLE FROM THE WINDOW.

3.3.4 Optical layout: path to the ultrafast electron source

The optical path of the beam that is used to excite the ultrafast electron source is shown in Figure 62. After the Harmonic Generator, the fourth harmonic passes through a beam expander then is lifted by a periscope and is focused on the tip of the ultrafast electron source by a lens placed outside the UHV chamber.

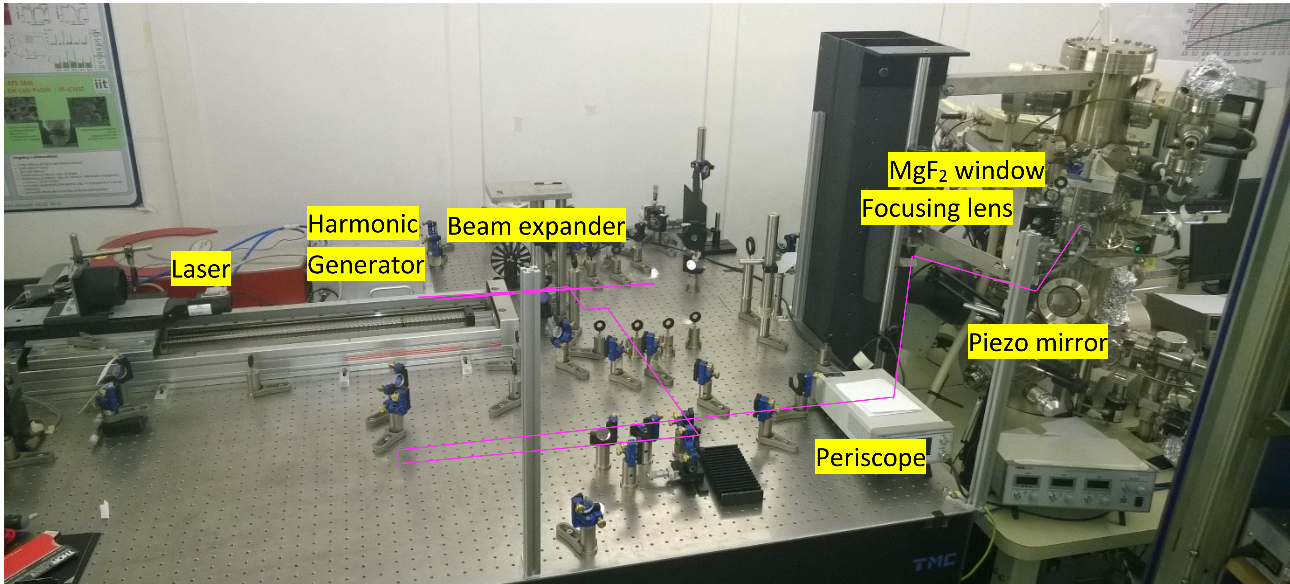

FIGURE 62 – OPTICAL PATH FROM THE LASER TO THE ULTRAFAST ELECTRON SOURCE

The optical path of the beam from the last mirror to the tip is shown in Figure 63. The optical beam, coming from the periscope, is pointed to the source by a mirror, passes through two irises, is focused by a lens, enters the UHV chamber thanks to a viewport , and throughout an optical aperture in the source, assembly reaches the tip where it is diffracted. The diffraction pattern, useful for the alignment procedure described in paragraph 3.4.1 Alignment of the laser beam on the tip, is projected on a screen at the opposite side of the chamber

through an optical aperture in the tip assembly opposite to the preceding one and then through a second viewport.

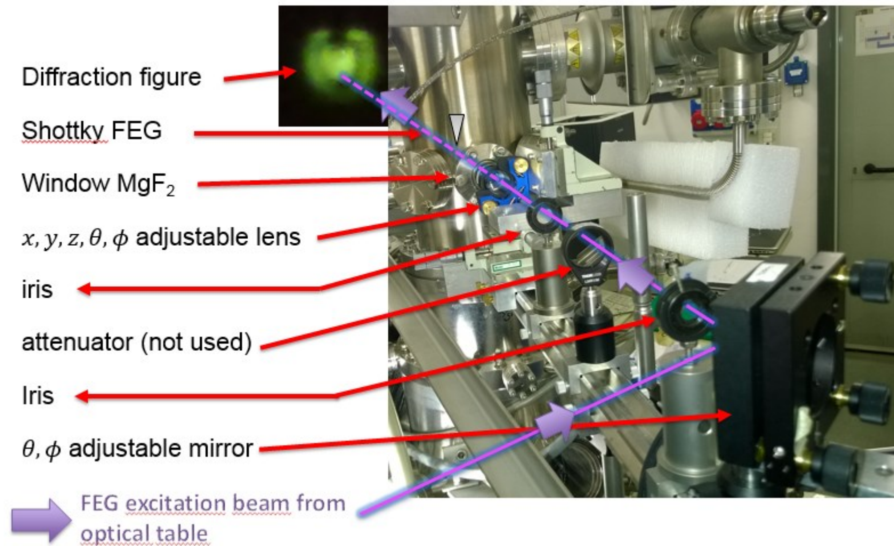

FIGURE 63 – PATH OF THE OPTICAL BEAM FROM THE LAST MIRROR TO THE ULTRAFAST ELECTRON SOURCE. IN THE INSET ON THE LEFT THE DIFFRACTION FIGURE GENERATED BY THE TIP

The mirror is installed on a piezoelectric tilting stage in order to allow fine correction of the beam alignment. After the mirror, the beam passes through two irises: the first one is used during alignment operation while the second is used both for alignment and for intensity attenuation. An iris is used to attenuate the beam intensity because it allows continuous regulation and helps in compensating the effect of mechanical pointing instabilities. After the iris, a fused silica lens with anti-reflective coating focuses the beam on the tip inside the ultrahigh vacuum chamber. The entrance viewport is made in magnesium fluoride that transmit 92% of incident light at the laser wavelength of 257 nm with reduced dispersion with respect to the more common fused silica. At the opposite side of the chamber, there is a second window in fused silica.

3.4 Pulsed emission

This paragraph describes the operation necessary to obtain a pulsed PE beam will be introduced. First of all the temperature of the tungsten tip of the ultrafast electron source has to be reduced to prevent thermal aided field emission as discussed in paragraphs “3.2 Ultrafast electron source” and “3.2.1 Description and operation”. Then the path of the laser beam from the laser to the ultrafast electron source, described in paragraph “3.3.4 Optical layout: path to the ultrafast electron source”, has to be aligned and the beam focused on the tip. Finally, the pulsed emission was characterized in dependence on the optical power and SEM images acquired with time-resolved PE current have been acquired. A comparison of the experimental setup of SEM with pulsed emission with a classical SEM and a USEM is reported in Figure 64.

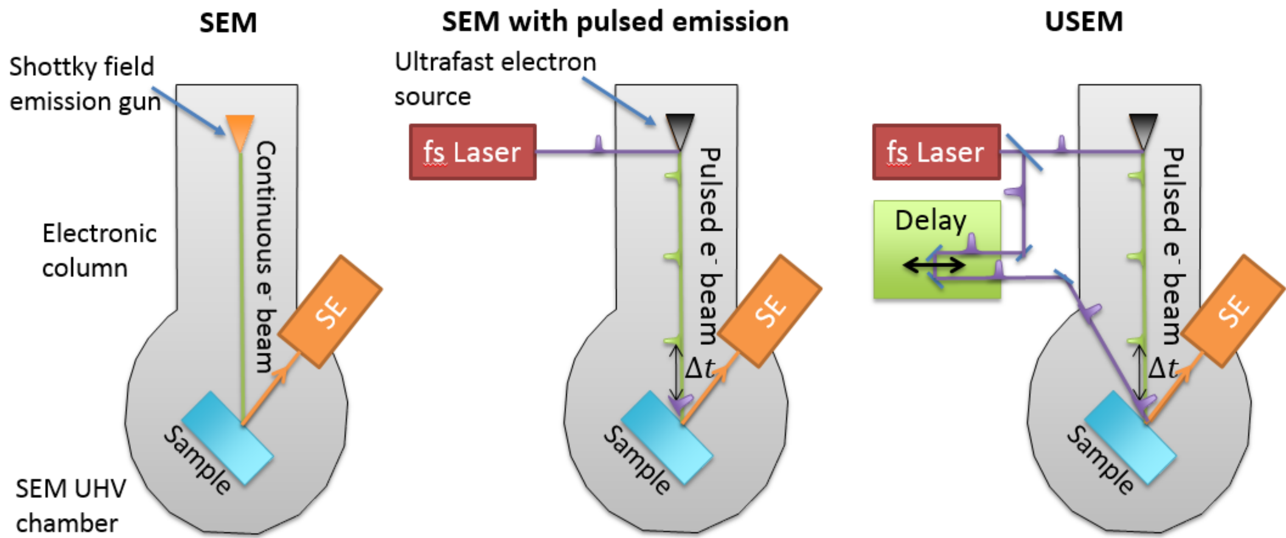

FIGURE 64 - COMPARISON OF THE EXPERIMENTAL SETUP USED FOR TESTING PULSED BEAM EMISSION WITH SEM AND USEM

3.4.1 Alignment of the laser beam on the tip

The alignment of the laser beam on the tip was obtained by a two-step process. A coarse optimization is obtained by moving the focusing lens with an XYZ stage and using the diffraction pattern of the laser by the tip as a feedback signal both for the lateral centering and the longitudinal focusing. A comparison of the diffraction pattern obtained with tip on the focal point, before and after is sketched in Figure 65. When the tip is before the focal point a shadow appears on the bottom when the tip is after shadow is on the top. When the tip is in the focal point no shadow is observed, only diffraction.

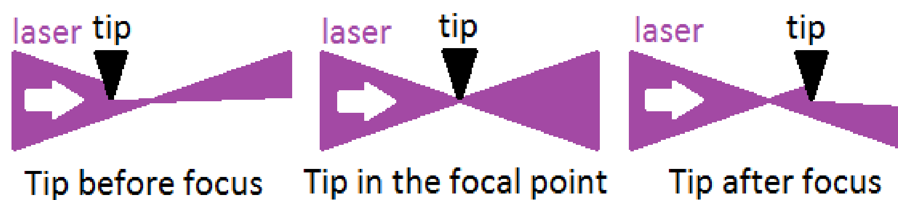

FIGURE 65 – SHADOW OF THE TIP IN DEPENDENCE ON THE POSITION WITH RESPECT TO THE FOCAL POINT

The fine optimization was obtained by acting on the piezo-actuated tilting and maximizing the PE current at the sample used as the feedback signal.

3.4.2 Fluence dependence

The 4.8 eV photon energy of the fourth harmonic beam is definitely enough to emit electrons with a single photon process. A characterization measurement was done by measuring the extractor current in dependence

on the power of the laser at the output of the fourth harmonic generator with a repetition rate of 10 MHz. The laser power was set by the modulator: that allows introducing a variable attenuation without changing the profile of the beam. The results, reported in Figure 66, show a linear dependence of current emitted and collected at the extractor on the input laser power. The measurement was repeated twice: during the first measurement, called 'Power increased,' the laser power is increased monotonically by step from 0 to the maximum while during the second, called 'Power decreased,' is decreased. Both scans confirm the linear dependence of the current at the extractor versus laser power, supporting that single photon photoemission is the leading process in that regime.

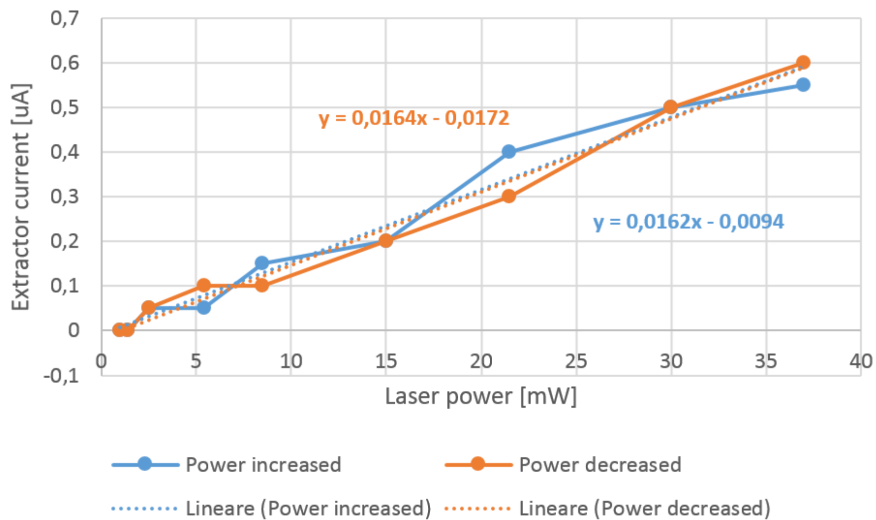

FIGURE 66 – PLOT OF THE EXTRACTOR CURRENT VERSUS THE POWER ABSORBED BY THE CHAMBER

The laser power absorbed by the tip is a small fraction of the power sent. It was measured that 36 % of the power is absorbed by the optics between the Harmonic Generator and the last focusing lens while the 38% is available at the opposite side of the chamber of the ultrafast electron source. The losses are attributed to the geometrical mismatch between the tip, with a final radius of 300 nm, and the focus of the laser beam with size of more than one micrometer. The full system generates 16 pA per mW of laser power absorbed by the chamber. The current delivered to the sample in pulsed mode depends on the settings of the electronic column.

3.4.3 SEM imaging with pulsed current

From the comparison of the SEM micrographs acquired at low magnification with a continuous electron beam and a pulsed electron beam reported in Figure 67, no difference in SE contrast is evident. The signal to noise ratio in the image acquired with 40 pA pulsed current is lower with respect to the one acquired with 8 nA of continuous current. The limited sensitivity of the detector discussed in paragraph 3.1.2 Secondary Electrons detector is one of the main limiting factor for the sensitivity of the measurement in pulsed mode, in the present configuration. No characterization at larger magnification was done due to the lateral resolution limits discussed above.

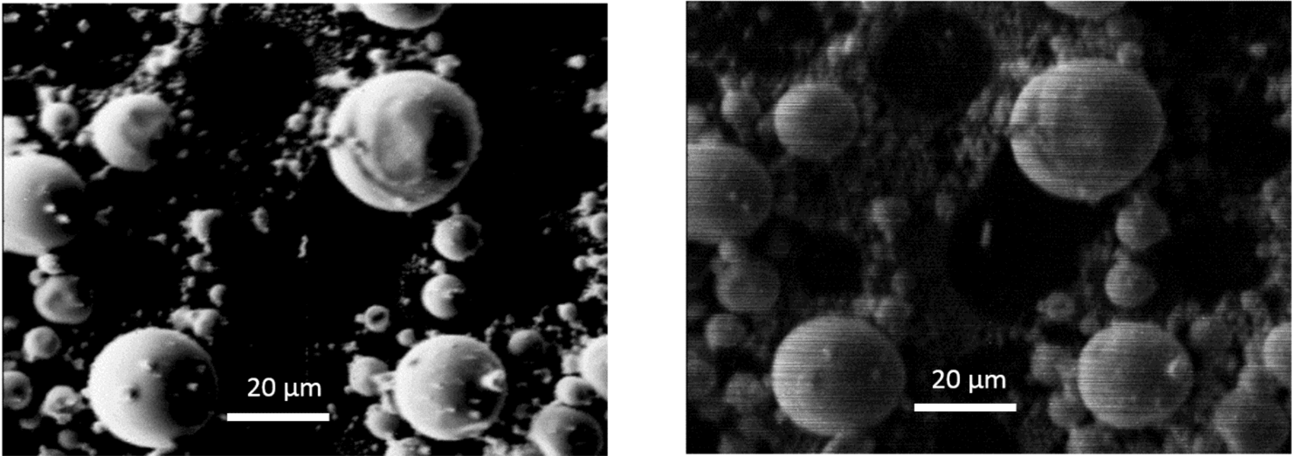

FIGURE 67 – SEM IMAGES OF THE SAME AREA OF A RESOLUTION TEST SAMPLE, MADE BY TIN SPHERES OVER CARBON, WITH CONTINUOUS ELECTRON BEAM (8 NA) ON THE LEFT AND WITH PULSED ELECTRON BEAM (40 PA) ON THE RIGHT

3.5 Spatial alignment

This paragraph presents the procedure used to spatially superimpose the pump laser beam and probe electron beam on the surface of the sample. The operation was done by keeping laser path to the sample open and using continuous PE beam that has higher average current and grants a better contrast with respect to the pulsed electron beam. The configuration used may be called optically pumped SEM. A comparison of optically pumped SEM with a classical SEM and a USEM is reported in Figure 68.

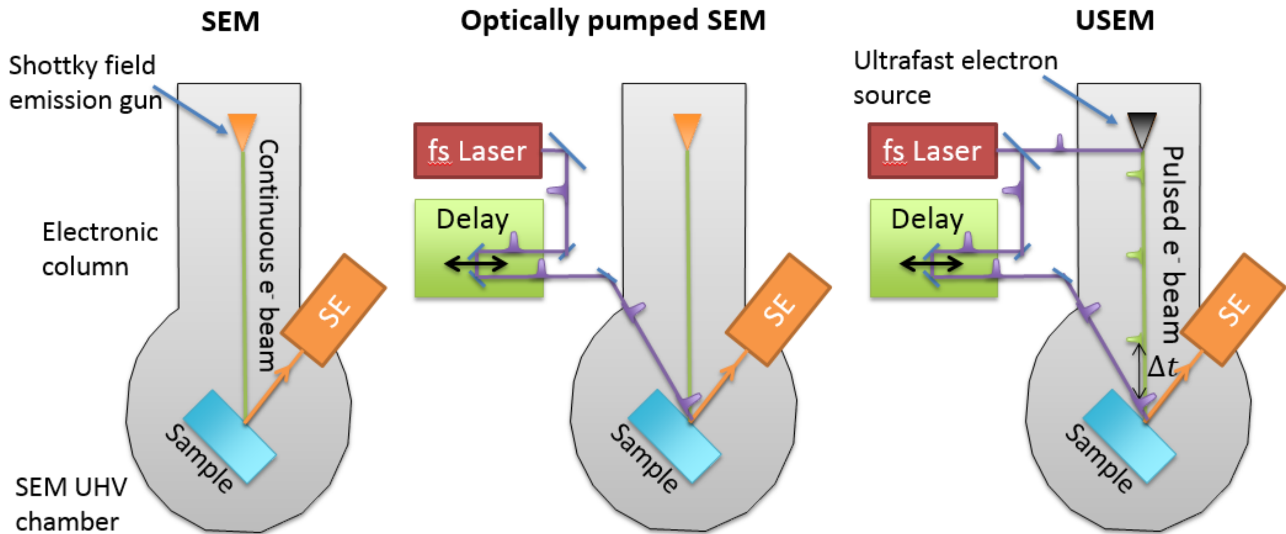

FIGURE 68 - COMPARISON OF THE EXPERIMENTAL SETUP OF SEM WITH OPTICALLY EXCITED SAMPLE WITH SEM AND USEM

3.5.1 Spatial alignment on a phosphor reference

The use of a fluorescent material is an effective way of observing the photon and the electron beam at the same time. This allows to superpose of their spots at the position where the sample surface will be moved at the measurement time. The fluorescent screen was prepared by deposing phosphor powder on carbon tape. The phosphors emits green light both as a consequence of electron excitation and of optical excitation. Low magnification is set on the SEM in order to have electron beam raster scanned on an area of the surface of the sample few millimeters wide. The area of the surface of the sample excited by the electron beam will appear bright. The laser beam is focused in a spot much smaller than the area excited by the electrons and is aligned, acting on the last mirror in the optical path, in the center of the rectangular area scanned by the electrons. An optical camera was installed outside the chamber to look at the sample and help in the alignment operations. This method allows for a coarse alignment, due to the low magnification that is delivered by the optical camera. A pictorial image of the luminescence induced by laser beam on phosphor sample is shown in Figure 69.

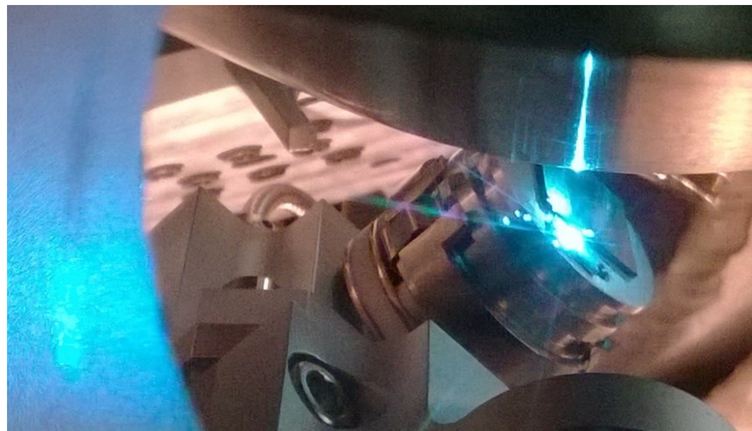

FIGURE 69 - PHOSPHORESCENCE DUE TO THE LASER BEAM ON THE SAMPLE OF PHOSPHORS POWDER DETECTED BY AN OPTICAL CAMERA

For the fine alignment, SEM images of the surface of the sample were acquired both with laser on and with laser off to determine the effect whether the laser excitation affects the intensity of SE emission. Continuous PE beam with energy was reduced to 3 keV to increase the size of the view field and correspondingly, of the footprint of the scanned area on the phosphors sample. The PE current measured at the sample was 1.2 nA and laser power outside at the entrance window into the vacuum chamber was set to 3 mW.

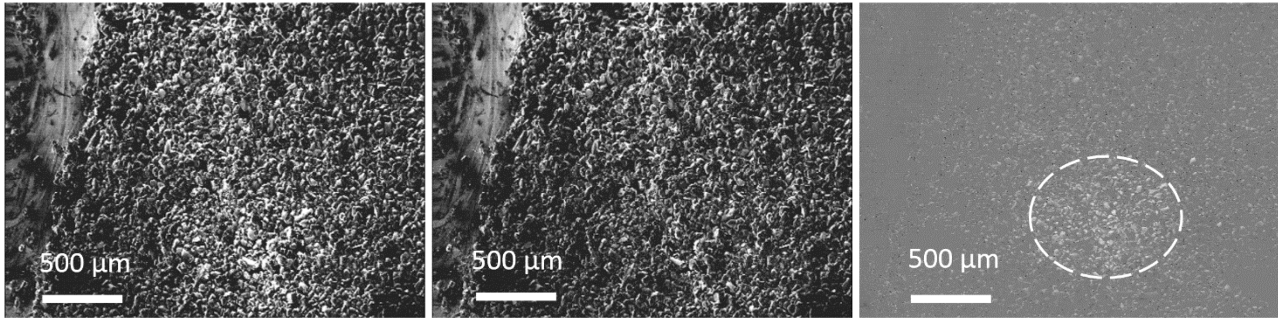

FIGURE 70 - SEM IMAGES OF THE PHOSPHORS: FROM THE RIGHT TO THE LEFT LASER ON, LASER OFF AND DIFFERENCE IMAGE. THE WHITE DASHED ELLIPSE INDICATE THE FOOTPRINT OF THE LASER SPOT ON THE SAMPLE

The comparison of SEM images of the phosphors sample reported in Figure 70 shows that laser excitation affects SE emission intensity. An SEM image was acquired with the photon beam off and the other with the photon beam on, whit the same experimental conditions. The contribution due to the optical excitation is enhanced by the SE difference image, obtained by pixel by pixel subtraction. The maximum positive difference is set to white and maximum negative difference to black. Zero difference is represented as 50% gray. The difference image helps to recognize the optically induced contrast. It is important to notice that subtraction does not completely cancel the contribution of morphological contrast, which is relevant in a powder sample. The issue was solved by substituting the phosphors powder with a phosphorescent flat sample made by a layer of 100 nm of aluminum oxide grown on silicon. SEM images of the cross-section and the surface of the aluminum oxide sample are reported in Figure 71

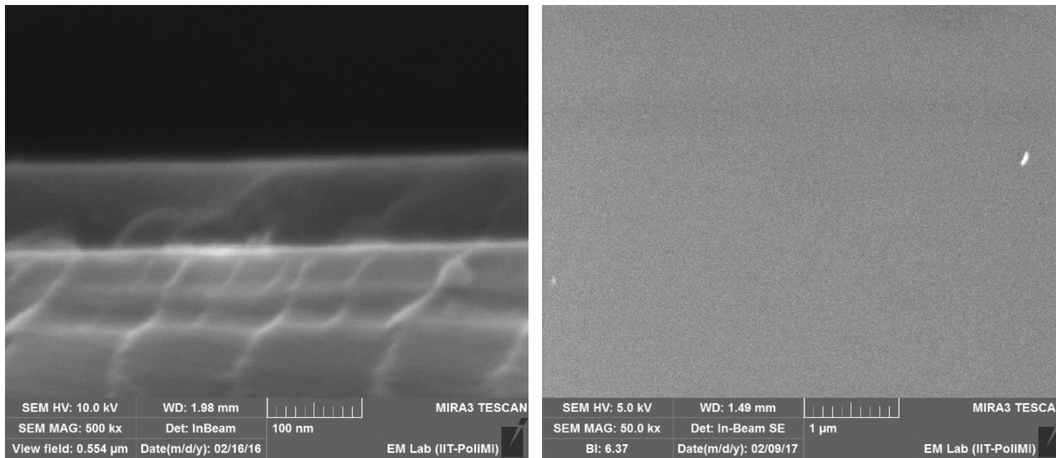

FIGURE 71 – CROSS-SECTION SEM IMAGE OF THE ALUMINUM OXIDE THIN FILM ON SILICON (ON THE LEFT) AND TOP IMAGE OF THE SURFACE, UNIFORM AND FLAT EXCEPT FOR CONTAMINATION

As already explained the electron source of the modified Phi660 can be operated either as a Schottky field emission gun, generating a continuous electron beam, or as an ultrafast electron source, generating a pulsed electron beam. When the emitted electron beam is continuous, the apparatus works as a classical scanning electron microscope. In this operating mode, the surface of the alumina sample appears flat and uniform. The

optical pump laser beam is focused on the sample in the SEM chamber. On alumina, the laser pump (fluence per pulse 400 μJ/cm^2) enhances SE emission in the area of the laser fingerprint as shown in Figure 72 (right).

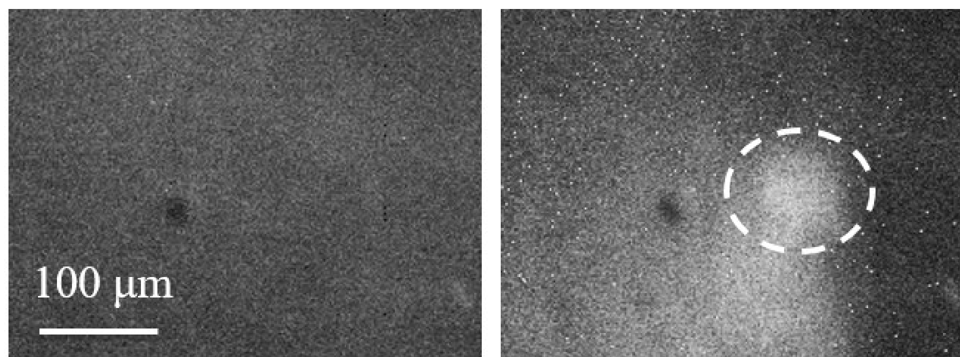

FIGURE 72 - CLASSICAL SEM IMAGE OF THE MORPHOLOGY OF ALUMINA (LEFT) AND EFFECT OF THE LASER PUMP ON THE SEM IMAGE OF ALUMINA, SHOWING A BRIGHT ZONE MAINLY IN THE LASER SPOT AREA (RIGHT)

The enhancement is localized in the area of the surface of the sample excited by the laser beam. There are three contribution affecting the SE emission:

- The PE beam alone;
- The laser beam alone;
- The combined effect of the electron and laser beam.

The PE beam alone determines the effect that is observed in the image acquired without the laser beam shown in Figure 72 (left), showing a uniform contrast (apart the defect in the dark spot, which provides a localization reference). The laser beam alone may determine photoemission by multiple photon absorption. Nonetheless, this emission is not related to the position of the PE beam on the sample and therefore is the same for each pixel in the SE SEM image. Thus the effect of the laser beam alone is a uniform background. The bright spot visible in the SEM image shown in Figure 72 (right) is therefore due to a combined effect of the electron and the photon beam confirming their spatial superposition. The nonuniform contrast outside the area excited by the laser spot might be due to photons diffused in the aluminum oxide film by multiple reflections. Further information of the laser-induced SE contrast on silicon will be provided in chapter 5 USEM investigation of the color center charge dynamics at the surface of aluminum oxide.

3.5.2 Damage fluences

Gallais and coworkers reported in literature a laser-induced damage threshold of $4\ mJ/cm^2$ for silicon exposed to a 100 fs laser pulse of wavelength equal to 357 nm [116]. They considered a damage any change observed in the differential interference contrast microscopy image of the surface of the sample after irradiation [116]. A test has been done to verify that the absence of damage for an exposure time of half-an-hour, comparable with the acquisition of a sequence of time resolved SEM images. SEM images have been acquired before and after exposing the surface of the sample to laser radiation. Difference images were then obtained as discussed above. The maximum fluence provided by the experimental setup with optimal focus of the laser beam is equal to $1\ mJ/cm^2$, lower than the damage threshold reported by Gallais and coworkers. Nonetheless, a change in the SEM image was observed after few minutes of exposure to the laser beam, with fluence per pulse equal to

1 $mJ/cm^2$and repetition rate of 10 MHz, as shown in Figure 73. The persistent effect might be due to a change, induced by the laser beam on the local work-function and therefore on the SE emission intensity, or to a local perturbation on the concentration of the dopants induced by the laser affecting the surface potential [117].

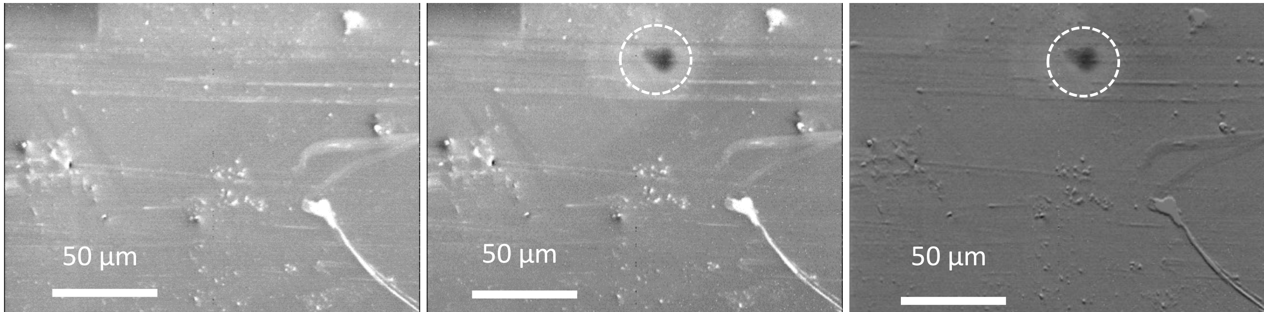

FIGURE 73 – FROM LEFT TO RIGHT SURFACE OF SILICON, SURFACE OF SILICON AFTER 12 MINUTES OF LASER EXPOSURE AT A FLUENCE OF 1 mJ/cm^2 PER PULSE, AND DIFFERENCE IMAGE. THE WHITE DASHED ELLIPSE INDICATES LASER FOOTPRINT

Fluence was reduced to 0.5 mJ/cm^2 to avoid the persistent effect on the surface. The reduction was obtained by inserting along the optical path a 50% neutral attenuator. A neutral attenuator allows to reduce the fluence on the sample without changing the properties of the beam. The exposure was repeated on a fresh area of the sample but, after 15 minutes of exposure a persistent effect was observed after turning off the laser as shown in Figure 74.

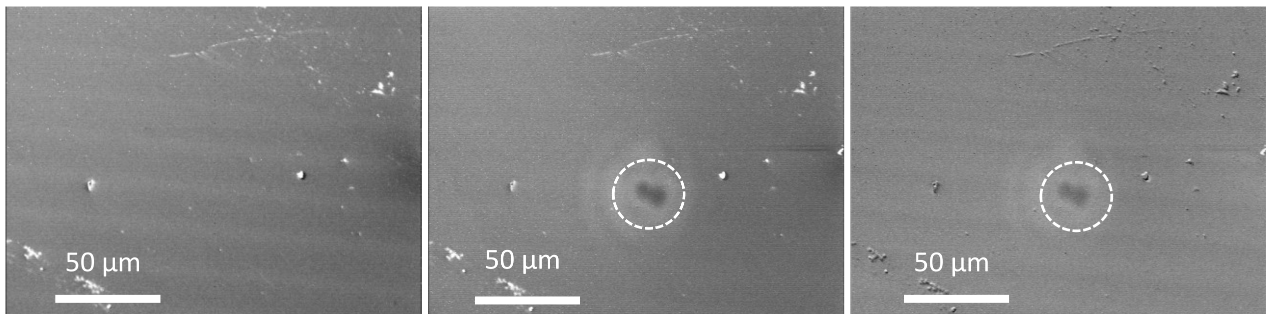

FIGURE 74 - FROM LEFT TO RIGHT SURFACE OF SILICON, SURFACE OF SILICON AFTER 15 MINUTES OF LASER EXPOSURE AT A FLUENCE OF 0.5 mJ/cm^2 PER PULSE, AND DIFFERENCE IMAGE. THE WHITE DASHED ELLIPSE INDICATES LASER FOOTPRINT

To avoid the persistent effect the 50% neutral attenuator was substituted with a new one with 10% transmission at the wavelength used. The exposure was repeated on a fresh area of the sample. No persistent laser effect was observed at a fluence of 0.1 mJ/cm^2 after 30 minutes exposure as shown in Figure 75.

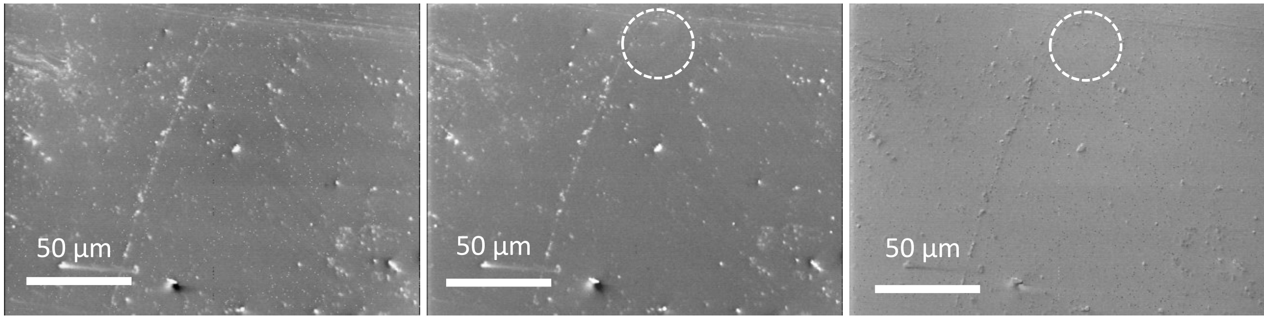

FIGURE 75 - FROM LEFT TO RIGHT SURFACE OF SILICON, SURFACE OF SILICON AFTER 30 MINUTES OF LASER EXPOSURE AT A FLUENCE OF 0.1 mJ/cm^2 PER PULSE, AND DIFFERENCE IMAGE. THE WHITE DASHED ELLIPSE INDICATES LASER FOOTPRINT

The laser spot was also defocused, and the operating fluence for measurements on silicon was chosen equal to $30\ \mu J/cm^2$, two order of magnitudes below the for a single pulse laser induced damage threshold reported by Gallais and coworkers after looking at the Differential interference contrast microscopy image after irradiation [116].

3.6 Temporal alignment

The temporal alignment of the USEM apparatus consists in tuning the position of delay stage to overlap temporally the optical and electron pulses, generated by the same fundamental harmonic pulse, at their arrival on the same position at the sample surface. The alignment is done by measuring SE emission from the laser footprint of the surface of highly p-doped silicon ($10^{19}\ cm^{-3}$) in the full USEM configuration, where both the PE beam and the optical beam are pulsed.

3.6.1 Time-resolved SEM images

Time-resolved SE images are acquired scanning the pulsed electron beam while exciting the surface of the sample with the pulsed optical beam. Each image is labeled by the delay between the two pulses on the sample, kept fixed during the acquisition. The delay may be tuned by operating on the position of the delay stage. The evolution of the SE contrast against delay is measured by acquiring a sequence of time-resolved images: one for each delay. Further detail on the acquisition of sequence of time-resolved images will be provided in paragraph 3.6.3 Data acquisition and analysis. Before studying the evolution of SE contrast, the delay stage was calibrate to determine the mechanical position of the back reflector mirror corresponding to temporal overlap of the electron and photon pulses on the surface of the sample. For this measurement, highly p-doped ($10^{19}\ cm^{-3}$) silicon was chosen because, with respect to other silicon samples with different level an type of doping, it shows the strongest optically induced effect on SE emission. Further details will be provided in chapter 4 USEM investigation of the surface charge dynamics at the Si(001) surface as a function of doping. First, a coarse matching of the photon optical path and the hybrid path of the mixed beam generating the electron pulses was done. This matching takes into account the kinetic energy dependent travel time of the electrons. In our USEM apparatus the electron column length is about 50 cm; the corresponding travel time of an electron pulse with a kinetic energy of 10 keV, the value used for our USEM measurements, is about 8.5 ns. After a sequence of time

resolved SE images were acquired over evenly spaced positions of the delay stage. Selected example images are reported in Figure 76. Each image is the average of 8 frames of 512x464 pixels. The acquisition of a frame requires 6.7 s corresponding to a dwell time per pixel equal to 25 µs. The fluence used corresponds to $30\,\mu J/cm^2$ as determined to avoid sample damaging in paragraph "3.5.2 Damage fluences". The average intensity of pulsed PE current used, measured by biasing the sample at +100 V, is 130 pA. The sample was kept fixed during the acquisition of the entire scan.

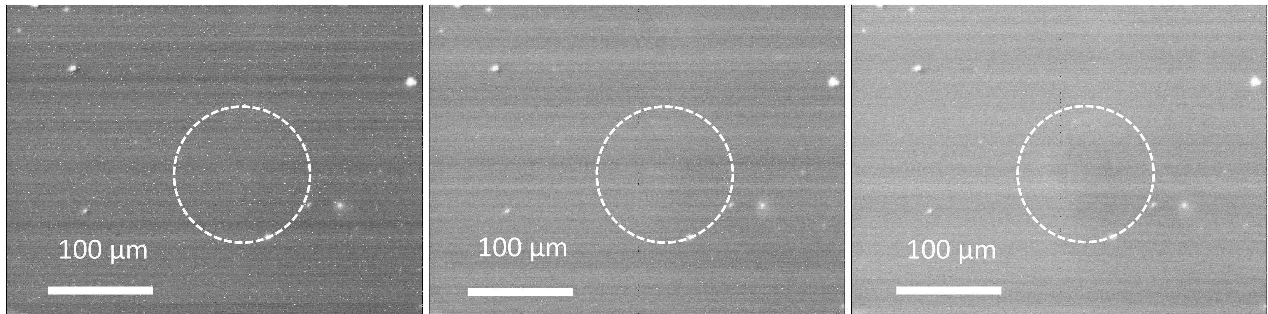

FIGURE 76– TIME-RESOLVED SEM IMAGES ACQUIRED ON HIGHLY P-DOPED 001 SILICON. FROM LEFT TO RIGHT THE EXTRA PATH ADDED BY THE DELAY STAGE IS EQUAL TO 562.50 MM, 581.25 MM AND 600.00 MM. DASHED ELLIPSE IS CENTERED ON THE LASER-INDUCED CONTRAST, WITH DOUBLE SIZE. THE ZERO IS SET AT THE EXTREMUM OF THE DELAY STAGE.

The time-resolved images reported in Figure 76 show a strong noise determined by a low signal to noise ratio due to the limited sensitivity of the detector as explained in paragraph 3.1.2 Secondary Electrons detector. There randomly occurring white and black pixels, horizontal stripes, and the average mean intensity is not uniform. Nonetheless, it is possible to notice on the image on the right a dark area corresponding to the laser footprint. In the following, a procedure will be shown to compensate the noise and extract reproducible and robust information from the area of the laser footprint, as a function of the delay. The middle of the rise ramp of the SE contrast in the spot area, when plotted against the delay stage position, is then defined as the "zero delay position," as shown in the following.

3.6.2 Contrast enhancement and coarse temporal alignment

Images are digitally treated according to the following procedure using the software ImageJ. The first step was to remove randomly occurring white and black pixels, by the "Remove outliers" function, with a threshold of 50 gray levels: gray level scale ranges from 0 to 255. The value of the pixel is considered an outlier if it differs from the median of the neighbors more than the threshold. The second step is the removal of the horizontal noise stripes by Fast Fourier Transform filtering. The part of the spectrum corresponding to horizontal bars with tolerance of 5% on the tilt was removed and the imaged reconstructed. The results of the single steps of processing for the image of Figure 76 are reported respectively in Figure 77, Figure 78 and Figure 79.

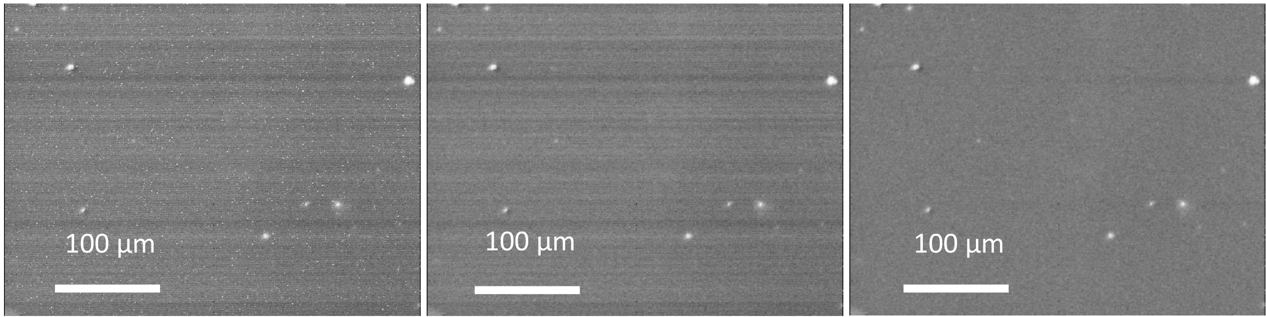

FIGURE 77 – PROCESSING OF TIME-RESOLVED IMAGE ACQUIRED WITH EXTRA PATH ADDED BY THE DELAY STAGE IS EQUAL TO 562.50 MM. FROM LEFT TO RIGHT: RAW IMAGE, OUTLIER REMOVAL, OUTLIER AND HORIZONTAL BAR REMOVAL

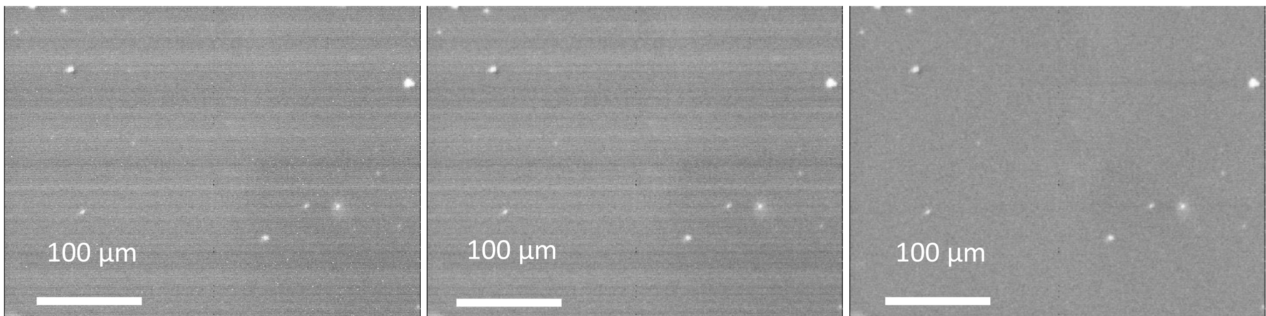

FIGURE 78 – PROCESSING OF TIME-RESOLVED IMAGE ACQUIRED WITH EXTRA PATH ADDED BY THE DELAY STAGE EQUAL TO 581.25 MM. FROM LEFT TO RIGHT: RAW IMAGE, OUTLIER REMOVAL, OUTLIER AND HORIZONTAL BAR REMOVAL

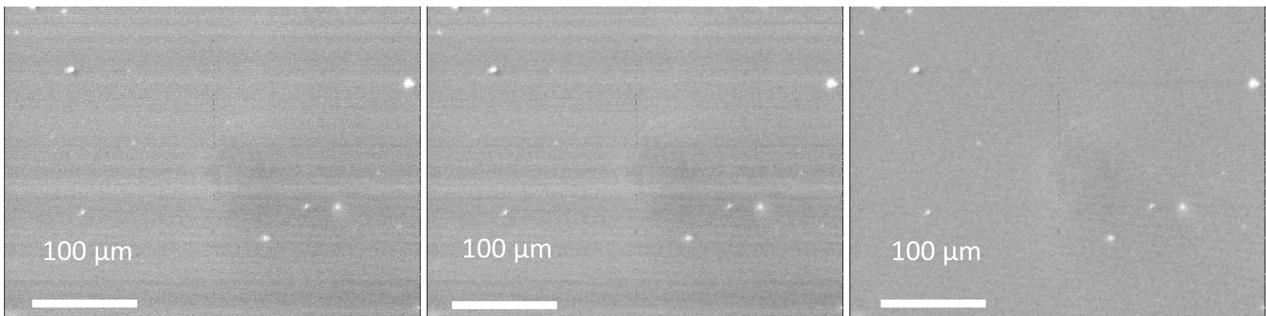

FIGURE 79 – PROCESSING OF TIME-RESOLVED IMAGE ACQUIRED WITH EXTRA PATH ADDED BY THE DELAY STAGE EQUAL TO 600.00 MM. FROM LEFT TO RIGHT: RAW IMAGE, OUTLIER REMOVAL, OUTLIER AND HORIZONTAL BAR REMOVAL

The last step of the elaboration aims at enhancing the representation dynamics by a common factor and at compensating for the difference in mean luminosity. This is done by acting on the gray levels of the image in a linear way. An offset is summed in order to set the mean of the image equal to average gray. The difference from the mean are expanded in order to set the entire scale from black to white equal to 8 times the standard deviation of the ensemble distribution of levels of the processed images. Results of the equalization is reported in Figure 80.

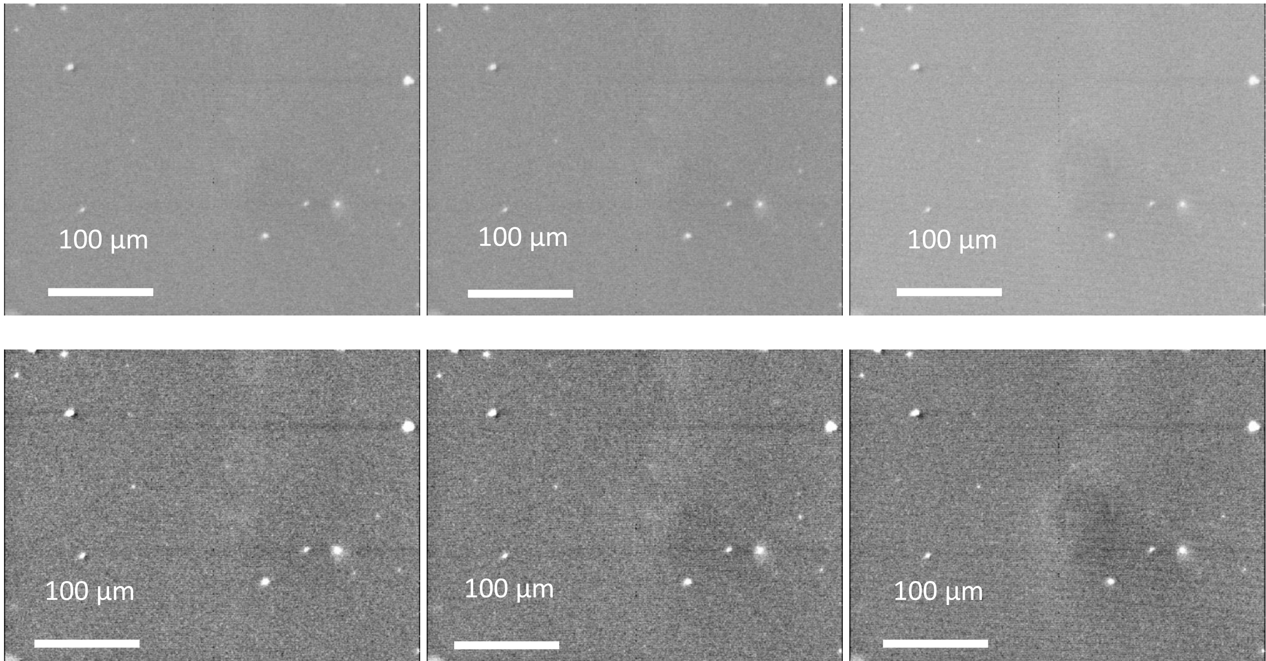

FIGURE 80 – EQUALIZATION OF CONTRAST OF TIME-RESOLVED SEM IMAGES. IN THE FIRST LINE FROM LEFT TO RIGHT IMAGES ACQUIRED WITH AN EXTRA PATH ADDED BY THE DELAY STAGE EQUAL TO 562.50 MM, 581.25 MM AND 600.00 MM AFTER REMOVAL OF OUTLIERS AND HORIZONTAL BARS. IN THE SECOND LINE THE CORRESPONDING IMAGES AFTER HISTOGRAM EQUALIZATION.

After the operations of contrast enhancement and noise compensation, the area excited by the laser appears as a dark spot in time-resolved images as reported in Figure 81.

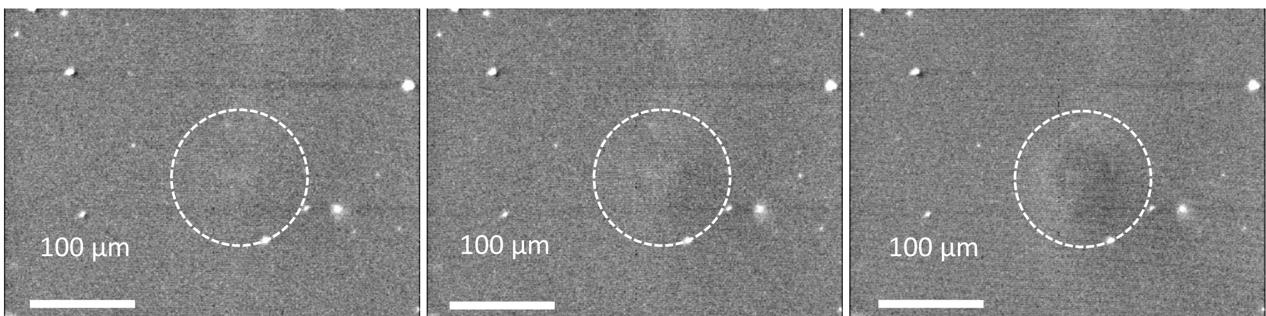

FIGURE 81 - FROM LEFT TO RIGHT IMAGES ACQUIRED WITH AN EXTRA PATH ADDED BY THE DELAY STAGE EQUAL TO 562.50 MM (0 PS), 581.25 MM (63 PS) AND 600.00 MM (125 PS) AFTER CONTRAST ENHANCEMENT AND NOISE COMPENSATION. THE WHITE DASHED ELLIPSE IS CENTERED ON THE OPTICALLY-EXCITED AREA, WITH DOUBLE SIZE

The intensity of SE emission from the excited area depends on the extra path added by the delay stage and therefore on the delay between the optical and the electron pulses. The spot becomes darker when passing from image acquired with an extra path of 581.25 mm to the one acquired with 600.00 mm while the signal from the same area in image acquired with an extra path of 562.50 mm is comparable with background and therefore negligible. Time zero is therefore set to the position of the delay stage corresponding to 581.25 mm. The other images are acquired respectively with a delay of -60 and +60 ps.

3.6.3 Data acquisition and analysis

The data analysis has the goal to evaluate the average gray level of the optically excited area. The goal is to operate on the image as acquired, in order to avoid the processing steps introduced in the previous paragraph 3.6.2 Contrast enhancement and coarse temporal alignment. The algorithm has to be robust against noise and should allow a consistent data treatment over sets of images acquired at different sessions. The noise that has to be compensated appears as:

- Randomly occurring white and black pixels;
- Horizontal luminosity bands;
- Instability of average gray level among different images.

The algorithm chosen to evaluate averages SE contrast within two areas in each acquired image: the optically excited area and another area, with the same shape, shifted horizontally to the left. The second area is the background. The area chosen are shown on a sample image in Figure 82. The algorithm applies to raw images acquired by the microscope without any further processing.

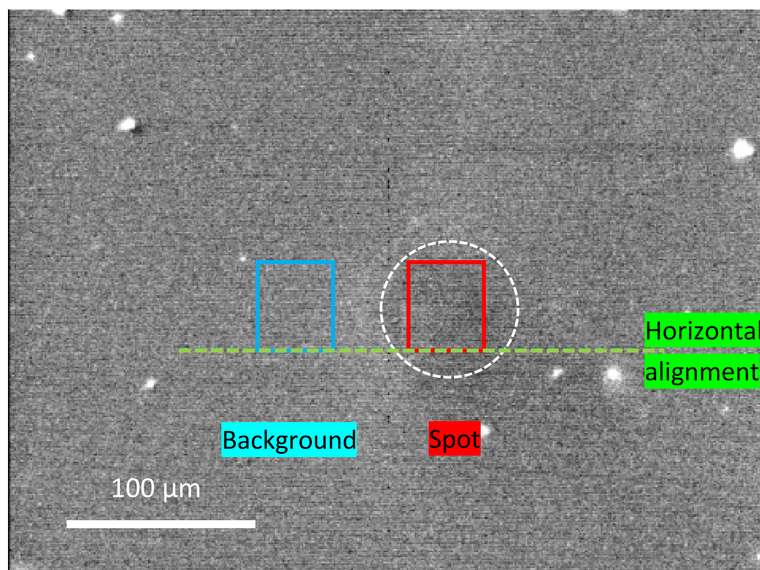

FIGURE 82 – POSITION OF THE AREA OF THE SPOT AND OF THE BACKGROUND

The area of the spot and of the background are rectangles with horizontal size of 38 µm and vertical size of 41 µm. The area of the background is obtained by shifting horizontally towards the left the area of the spot by 76 µm; this distance was carefully evaluated over several sets of data to minimize the instabilities from the external noise (giving rise to the horizontal stripes and other noise effects). Once evaluated average over the two areas the values are associated to the delay corresponding to the source image. The average SE signal from the areas of the spot and the background evaluated from a sequence of time-resolved SEM images is reported in Figure 83. Sequence of images was acquired spanning from negative delays (electron pulse arriving before the photon pulse) to positive delays (photon pulse arriving after the photon pulse). The scan was repeated twice with the

same measuring conditions: the first time the images were acquired starting from the most negative delay and increasing the delay value monotonically, the second time in the opposite versus of delay time variation. In the following, the first scan is called ‘forward’ and the second ‘backward.’

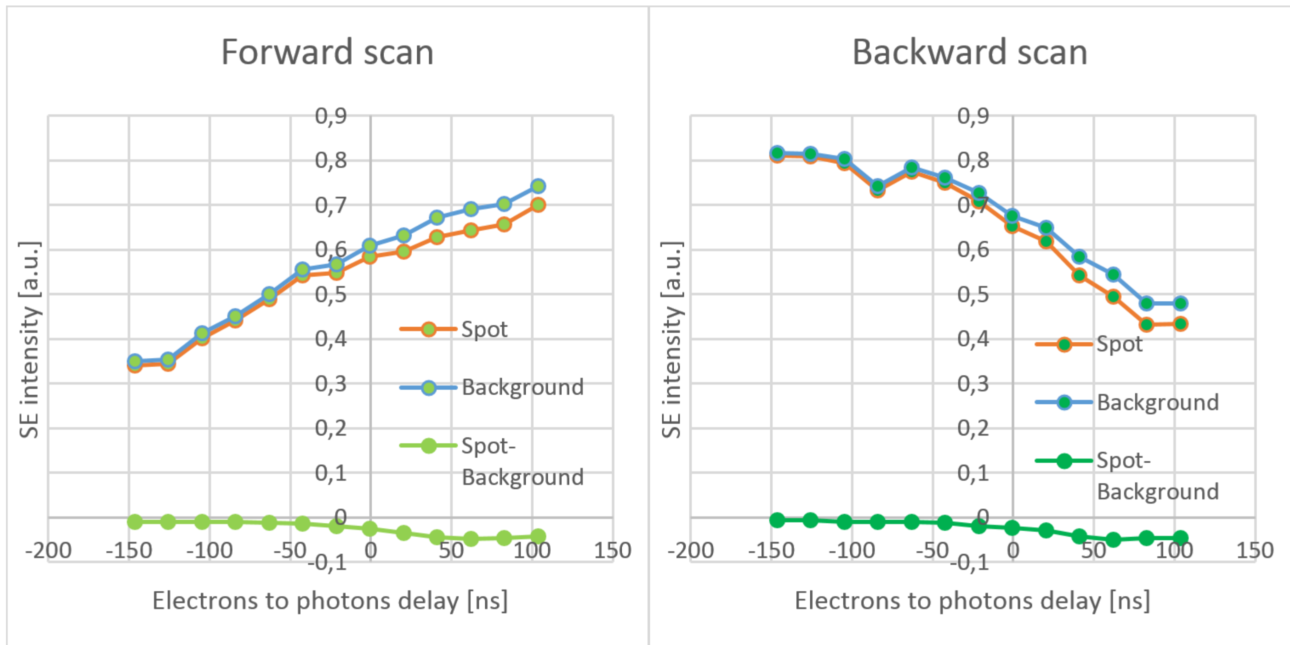

FIGURE 83 - PLOTS OF THE AVERAGE GRAY OVER THE AREA OF THE SPOT, ON A NEARBY AREA CALLED BACKGROUND, AND THE DIFFERENCE OF THE TWO SIGNAL VERSUS THE ELECTRONS TO PHOTONS DELAY. FORWARD SCAN ON THE LEFT AND BACKWARD SCAN ON THE RIGHT.

The average gray evaluated only on the area of the spot, shown in Figure 83, is not exactly the same in the forward and backward scan; the same happens for the background. This observation suggests that a systematic error contribution adds to the SE contrast while the acquisition time increases, independent on the delay time between pulses. This contribution may result from several drifts in the apparatus, probably more than one at the same time. The most probable cases include thermal and electronics drifts. The average gray of the spot and the background are very near to the corresponding value of the spot for each delay and in both scans and are almost equal for negative delays. The differential SE contrast, also reported in Figure 84, is defined as the difference between the average gray on the area on the spot and on the background. The adoption of the differential SE contrast is necessary to compensate unpredictable drifts in the average mean luminosity of the image. The choice of the position of the reference area on the background, which is horizontally aligned to the photon beam spot, allows to compensate the external electromagnetic noise visible as horizontal stripes, that will be discussed in paragraph 3.6.4 Discussion of the horizontal stripe noise in the SE images. A comparison of the differential contrast in the forward and backward scan is reported in Figure 85.

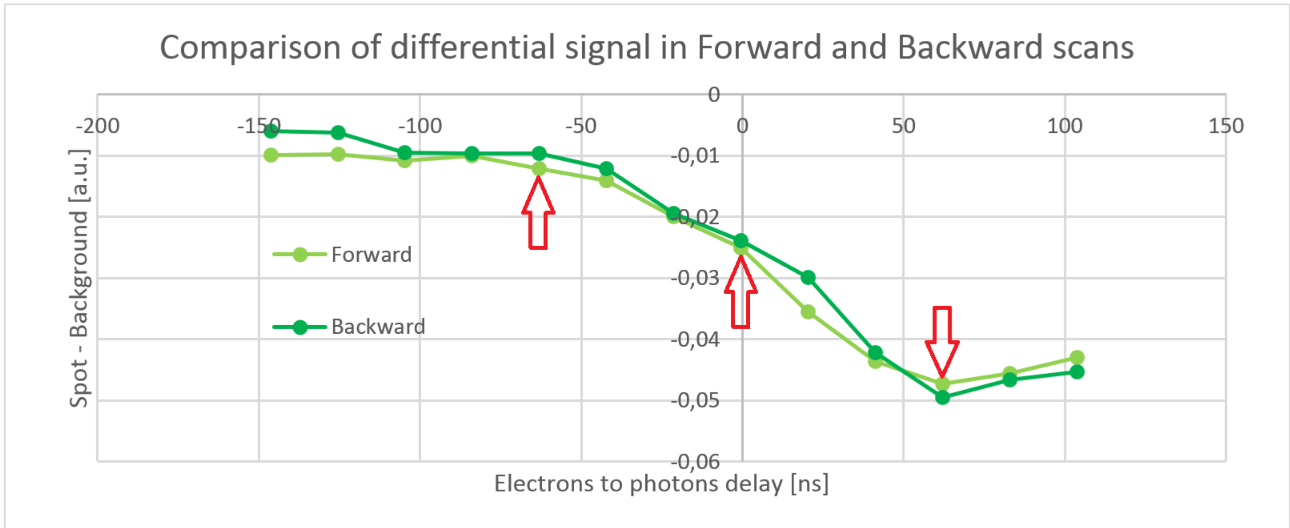

FIGURE 85 – CONTRAST, EVALUATED AS SPOT-BACKGROUND, VERSUS ELECTRONS TO PHOTONS DELAY. POINTS CORRESPONDING TO THE IMAGES SHOWN IN FIGURE 81 ARE HIGHLIGHTED BY RED ARROWS.

The differential SE contrast reported in Figure 85 is well superimposed in the forward and backward scans confirming that the algorithm chosen allows to compensate the effect of drifts. The laser-induced contrast is negative as it was possible to observe in the source images, reported in Figure 76, and in the same images after contrast enhancement and noise compensation, reported in Figure 81. The superposition of the forward and backward scan also confirms that the information provided by the differential SE contrast depends on the relative time delay between photon and electron pulses, while it does not depend on the absolute time at which images are actually acquired.

3.6.4 Discussion of the horizontal stripe noise in the SE images

A simulation was done to evaluate how the method chosen for data analysis was able to compensate a repetitive noise on the intensity of the PE current. This kind of noise may be generated by external electric and magnetic fields originated by electric and electronic devices and by the electrical power distribution, by instabilities on the intensity of the laser, amplified by the harmonic generation process, or by mechanical instabilities affecting the pointing of the laser on the tip. The goal of the test is to determine the rejection ration of the differential contrast algorithm versus the frequency of the noise. Test images were generated ranging from 0 to 1 with an average signal equal to ½. The images were affected by monochromatic sinusoidal noise on PE current n(t). The intensity of the noise was adjusted in order to span from 0, indicating zero PE current contribution at the sample, to 1 corresponding to maximum PE current contribution. Intensity of PE current is, therefore:

$$i_{PE}(t) = n(t) + \frac{1}{2} = \frac{1}{2} sen(2\pi f t + \phi) + \frac{1}{2}$$

The intensity of SE current is considered to be proportional to the PE beam current.

$$i_{SE}(t) = k\, i_{PE}(t)$$

The intensity is assigned to the pixels of the image following the path of the raster scan introduced in paragraph 3.1.1 Electronic column. The raster scan moves along horizontal lines when a line is completed pass to the next one. Given x as the horizontal coordinate of the pixel from the left side, X the number of pixel in a line, y the vertical coordinate of the pixel from the top, Y the number of pixel in a column and t_d the dwell time the time may be related to the position (x,y) of the raster scan on the image:

$$t(x,y) = xd + yXt_d$$

Summing and substituting the intensity of SE in dependence on the position may be related to the frequency and phase of the noise.

$$i_{SE}(t) = k\, i_{PE}(t) = \frac{k}{2}(sen(2\pi f t + \phi) + 1) = \frac{k}{2}(sen(2\pi f(xt_d + yXt_d) + \phi) + 1) = g(x,y,\phi)$$

Dwell time, number of vertical and horizontal lines were set equal to the typical parameters of acquisition of an USEM frame. Acquisition time for a frame is 6.7 s, at a resolution of 512 pixel x 512 pixel. Dwell time t_d is equal to 25 μs and acquisition time for a line 13 ms corresponding to an horizontal frequency of the raster scan $f_{horiz} = \frac{1}{Xt_d} = 76Hz$. An USEM image is the average of 8 frames. Phantom images are generated as a function of the frequency of the sine wave, setting the phase ϕ equal to 0, and reported in Figure 86.

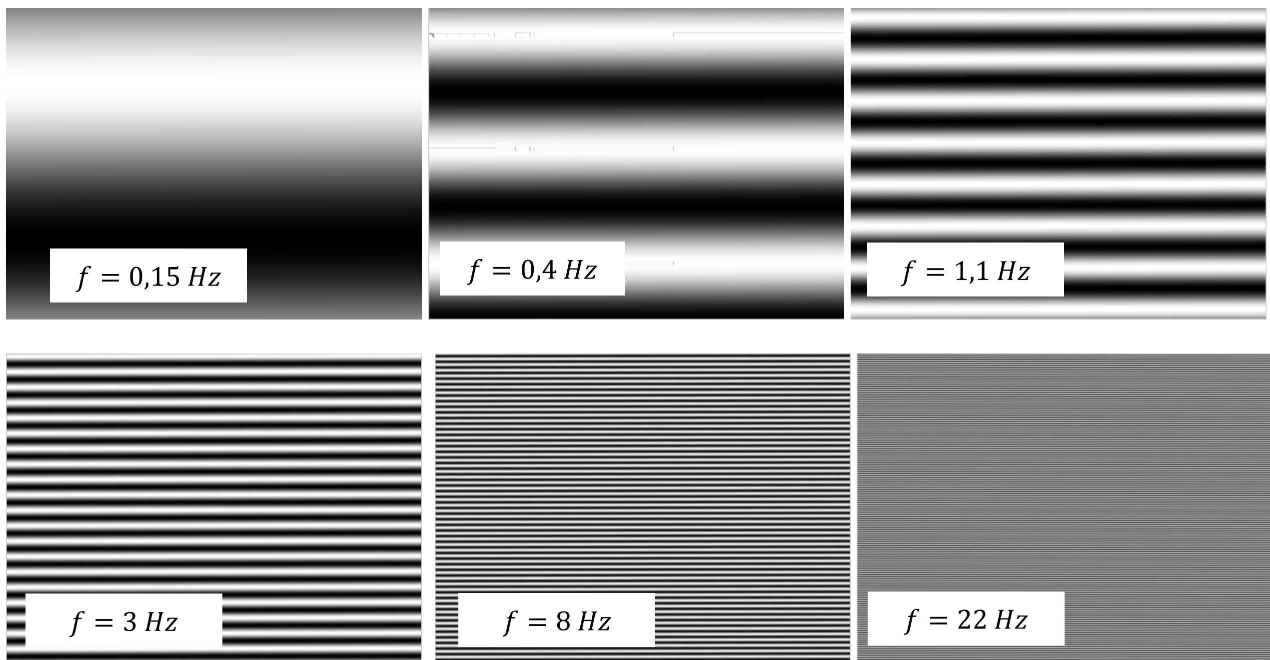

FIGURE 86 – PHANTOM IMAGES SHOWING THE EFFECT OF A SINUSOIDAL NOISE ON THE PE CURRENT

Phantom images, shown in Figure 86, shows that a noise on the PE current with components at a frequency below the one of the horizontal raster scan f_{horiz} =76 Hz, may generate horizontal bars on the SEM image. The effect may be understood by considering $f \ll \frac{1}{Xt_d} = f_{horiz} \rightarrow fXt_d \ll 1$ therefore the value along a line is almost constant and the term $fxt_d \leq fXt_d$ may be neglected:

$$i_{SE}(t) = \frac{k}{2}(sen(2\pi fxt_d + 2\pi fyXt_d + \phi) + 1) \approx \frac{k}{2}(sen(2\pi fyXt_d + \phi) + 1)$$

Therefore, the effect of a noise with a frequency much smaller than the horizontal scan frequency is almost negligible along a line while determines a modulation involving different lines. This is the condition observed in USEM images that are perturbed by horizontal luminosity bands. The choice to evaluate the background on an area horizontally aligned with the spot allows comparing points on the same line, compensating instabilities on the PE current at low frequency.

Simulations have been done to evaluate the reliability of the method in dependence on the frequency. Phantom images were created in dependence on frequency and phase of the noise. Signal has been evaluated on each image as the difference of two areas with the same size and positions of the ones used for the analysis of the time-resolved sequence reported in paragraph 3.6.3 Data acquisition and analysis. Zero signal is expected since the images are uniform, except for the noise. The difference measured on the phantom that is nonzero has to be completely attributed to the effect of the noise. The algorithm is useful if the differential signal, spot minus background, is lower than the spot alone. For each frequency the standard deviation of both parameters has been evaluated on a set of 20 phantom images, differing for the phase of the noise. The ratio of the standard deviation of the average on the area of the spot versus the standard deviation of the differential signal, called attenuation ratio, is reported in Figure 87. Attenuation ratio estimates the rejection ratio of the differential signal to a noise on PE current in dependence on the frequency of noise.

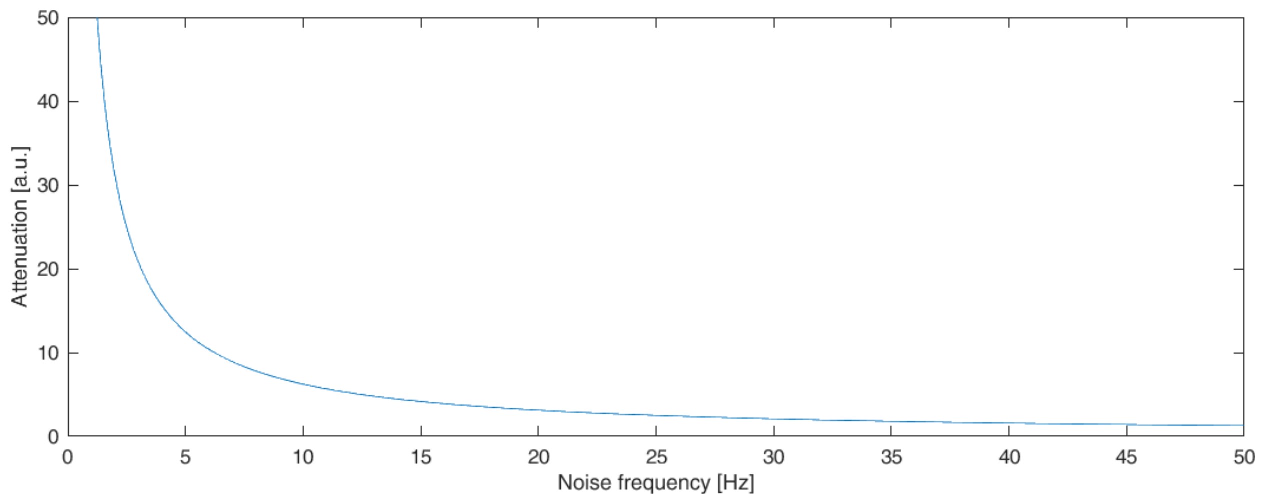

FIGURE 87 – ATTENUATION OF THE EFFECT OF A NOISE ON THE PE CURRENT OBTAINED WHEN COMPARING SPOT AND BACKGROUND AREAS, HORIZONTALLY ALIGNED, VERSUS THE FREQUENCY OF NOISE WITH RESPECT TO SPOT AREA ALONE

The algorithm chosen attenuates the effect of a noise on PE current intensity by a factor of 20 if the frequency is below 3 Hz and of a factor of 6 if it is below 10 Hz as shown in Figure 87. Attenuation reduces when frequency of the noise increases. The best attenuation is obtained for noise with frequencies comparable with the inverse of the period of acquisition of an image. The attenuation spectrum is adequate to compensate the horizontal bars observed in USEM images, that are related to noise with a frequency well below $f_{horiz} = 76Hz$. The choice of introducing a differential signal is therefore confirmed.

3.6.5 Fine temporal alignment

A scan on the entire delay stage was done to determine the position of the zero delay time with the best possible precision. Zero delay time corresponds on the temporal overlap of photon and electron pulse on the surface of the sample and may be determined by observing a rapid variation of the SE emission from the optically excited area. A rough procedure for finding time zero has been already presented in paragraph 3.6.2 Contrast enhancement and coarse temporal alignment. A forward and a backward scan were acquired with a step of 500 ps. The contrast, measured on the time-resolved SEM images with the algorithm introduced in paragraph 3.6.3 Data acquisition and analysis, is reported in Figure 88. For each delay, the average of the contrast measured in forward scan and backward scan is calculated.

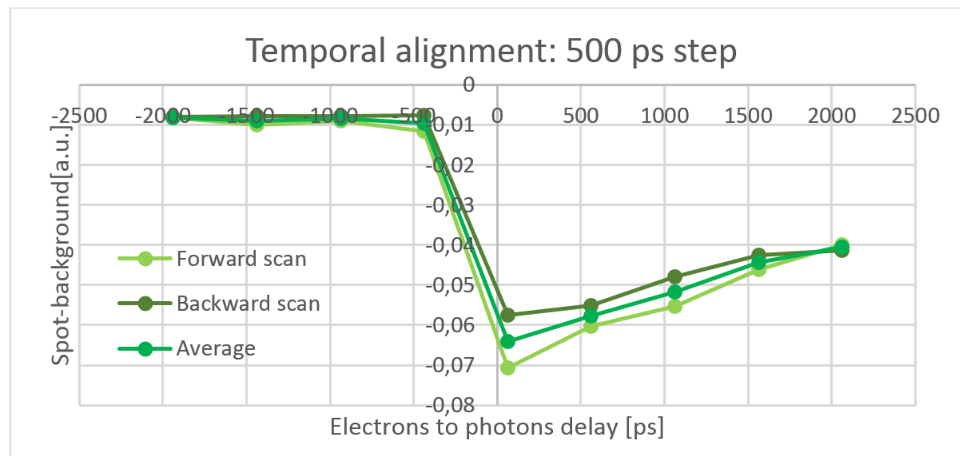

FIGURE 88 - CONTRAST, EVALUATED AS SPOT-BACKGROUND, VERSUS ELECTRONS TO PHOTONS DELAY ON (001) SURFACE P-DOPED (10^{19} CM^{-3}) SILICON. FORWARD AND BACKWARD SCANS ON THE ENTIRE DELAY STAGE WITH DELAY STEPS OF 500 PS WERE ACQUIRED

No difference appears between the forward and backward scan, confirming that long-term drifts do not affect the result of the measurement. Figure 88 shows negligible contrast for negative delay, then an abrupt negative drop followed by a recovery. The drop is attributed to the effect of the photon pulse, confirming in a coarse way the choice for time zero. A second scan with delay step of 83 ps, finer than the previous scan, was done on a fresh area of the same sample to identify with better precision the arrival of the photon pulse and therefore the temporal zero. Contrast measured is reported in Figure 89.

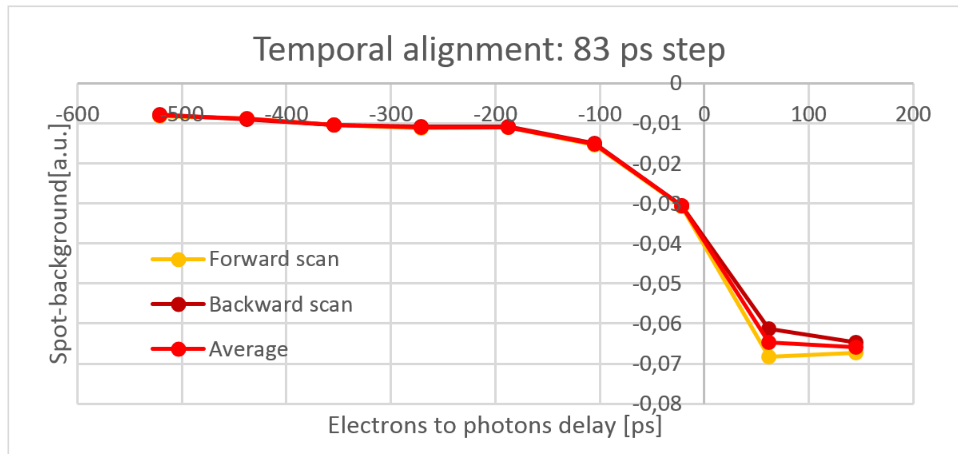

FIGURE 89 - CONTRAST, EVALUATED AS SPOT-BACKGROUND, VERSUS ELECTRONS TO PHOTONS DELAY ON (001) SURFACE P-DOPED (10^{19} CM^{-3}) SILICON. FORWARD AND BACKWARD SCANS IN THE DELAY REGION NEAR TIME ZERO WITH DELAY STEPS OF 83 PS WERE ACQUIRED

Forward and backward scan are superimposed confirming that the contrast observed depends only on delay on the electron pulse with respect to the photon pulse. Average signal was calculated for each delay. The plot shows negligible contrast for negative delay, then an abrupt negative drop. An even finer scan with steps of 20 ps was done on a fresh area of the sample. Contrast measured is reported in Figure 90.

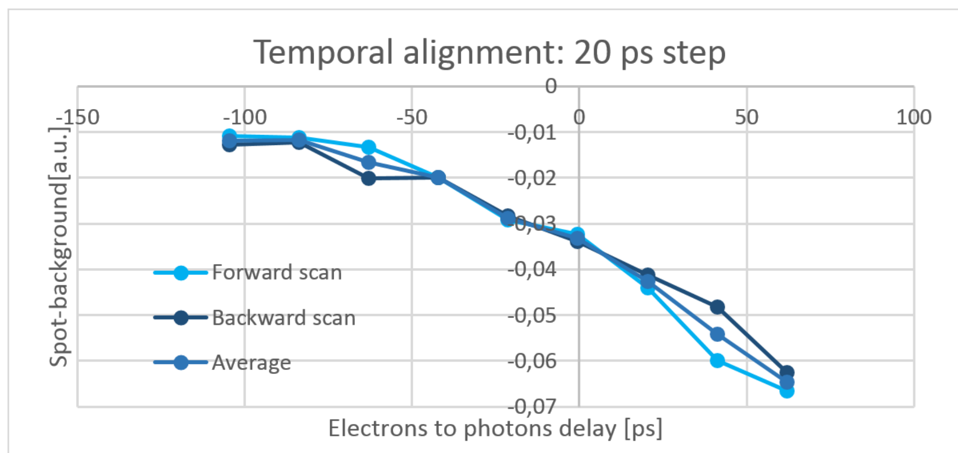

FIGURE 90 - CONTRAST, EVALUATED AS SPOT-BACKGROUND, VERSUS ELECTRONS TO PHOTONS DELAY ON (001) SURFACE P-DOPED (10^{19} CM^{-3}) SILICON. FORWARD AND BACKWARD SCANS IN THE DELAY REGION NEAR TIME ZERO WITH DELAY STEPS OF 20 PS WERE ACQUIRED.

Forward and backward scan are superimposed confirming that the contrast observed depends only on delay on the electron pulse with respect to the photon pulse. Average signal was calculated for each delay. Figure 90 shows negligible contrast for negative delays, then a negative drop that last for few tens of picoseconds. The temporal width of the drop is attributed to the temporal resolution of the machine, not to a dynamic of the sample as explained in the next paragraph 3.7 Time resolution. Therefore the zero was set at the half of the rise and not at the beginning of the dynamic. The coarse calibration of the zero, defined as the half of the rise of the

SE signal, is confirmed by the measurement acquired with delays spaced 20 ps. The position of the zero could be refined even better by fitting the data with an error function as described in the next paragraph 3.7.2 Estimation of rise time. The average of the different scans are superimposed for comparison.

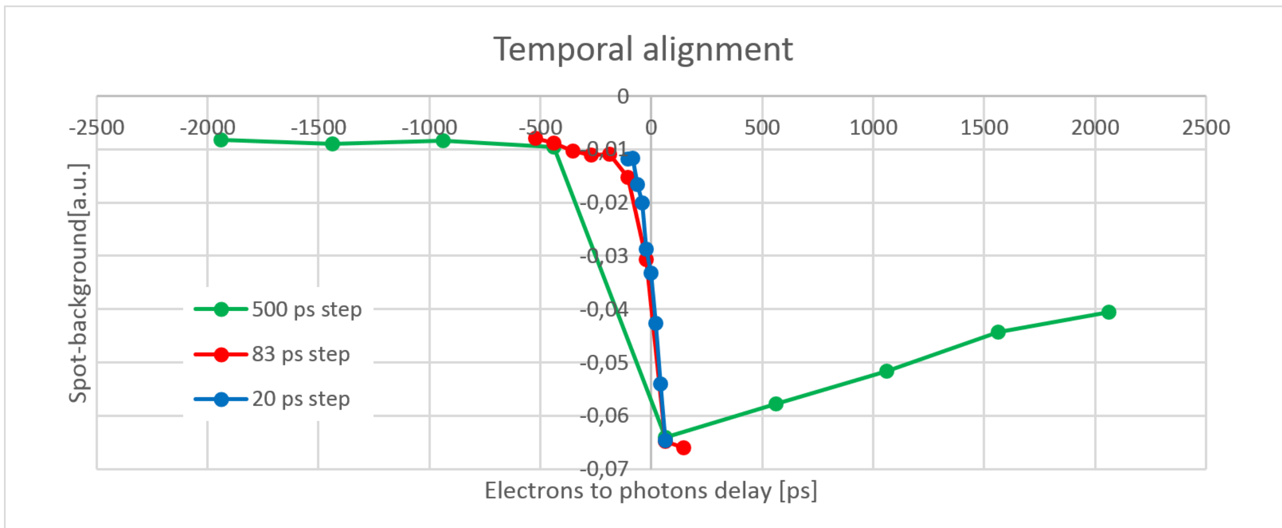

FIGURE 91 – COMPARISON OF AVERAGE CONTRAST OF FIGURE 88, FIGURE 89, AND FIGURE 90.

The superposition of scans, shown in Figure 91, acquired with the same conditions except for the region of the sample and the delay steps, confirms the repeatability of the measurement.

3.7 Time resolution

The time resolution of the apparatus was evaluated by measuring the rise time of contrast on the highly doped p-type Si(001) surface due to optical excitation as introduced above. The experimental conditions are the same used to determine the temporal zero of the pump-probe, namely the PE beam energy was 10 keV, the fluence 30 $\mu J/cm^2$ and the wavelength 343 nm. The probe current intensity was scanned from the maximum output allowed by the system to the lowest sensitivity limit allowed by the SE detector. For each level of current a forward and a backward scan were acquired. The delay steps were adjusted iteratively to have enough point density along the delay time axis to describe the evolution of the contrast. The PE current was controlled through the intensity of the photon beam impinging on the ultrafast electron source, which was regulated by the iris modulator following the method introduced in paragraph “3.3.4 Optical layout: path to the ultrafast electron source”. The PE current at the sample was measured with the picoammeter Keithley model 6485. A bias of +100 V was applied to the sample to prevent SE emission. Plot shown in Figure 92 represents the contrast on sequence of time resolved images acquired at different delay with PE current equal to 11, 30, 130, and 180 pA respectively. For each scan, the fitting function is also reported.

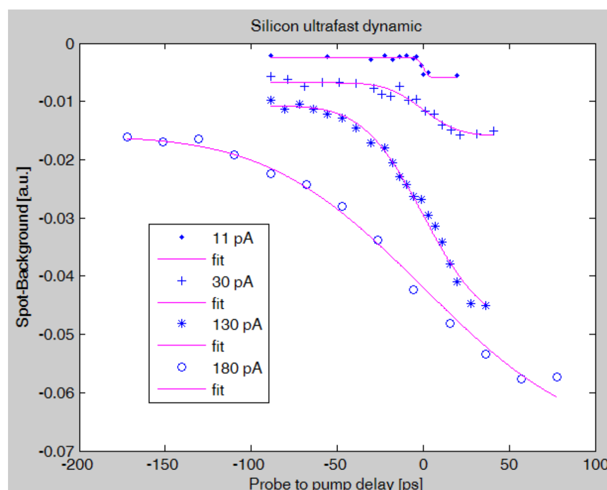

FIGURE 92 - SUPERPOSITION OF THE PLOT OF TIME-RESOLVED SCANS ACQUIRED ON SILICON P-DOPED WITH DIFFERENT PROBE CURRENT

The fitting of the data point was done in Matlab® with the following error function where t is the delay of the electron pulse with respect to the photon pulse:

$$y(t) = y_0 + g\,\mathrm{erf}\frac{t - t_0}{s}$$

The free parameters are the following:

- y_0: offset on the contrast;
- g: amplitude of the error function;
- t_0: offset on the delay, allows to keep into consideration uncertainty on time zero;
- s: smoothness of the error function, the relevant parameter to estimate the time resolution;

The result of the fitting is reported in Table 2.

Parameter\Current	180 pA	130 pA	30 pA	11 pA
y_0 [a.u.]	-0.038518	-0.033031	-0.011345	-0.003869
g [a.u.]	-0.021831	-0.022450	-0.004543	-0.001471
t_0 [ps]	73.122	96.659	88.811	87.516
s [ps]	76.483	46.919	23.939	0.890

TABLE 2 – RESULT OF THE FITTING ON THE SCANS IN DEPENDENCE ON PULSED PE BEAM CURRENT

The offset on the delay is almost the same for measurements done with PE current equal to 11 pA and 30 pA, while the values found for measurement done at 130 pA and 180 pA differs by few ps. The average value equal to 86.5 ps. The fitting was repeated, setting the offset on the delay equal to 88.81 ps, the estimated value from the data acquired with 30 pA, to reduce the uncertainty. The parameters estimated by the fitting are reported in

Table 3. The PE current may be expressed in term of number of electron per pulse considering the charge of the electron and the repetition rate.

Parameter\Current	180 pA	130 pA	30 pA	11 pA
Electrons per pulse	**112**	**81**	**19**	**7**
y_0 [a.u.]	-0.041896	-0.029522	-0.011355	-0.004184
g [a.u.]	-0.025939	-0.018766	-0.004554	-0.001772
t_0 [ps] - fixed	88.81	88.81	88.81	88.81
s [ps]	100.380	38.648	23.838	3.878

TABLE 3 - RESULT OF THE FITTING ON SE CONTRAST ON SILICON IN DEPENDENCE ON PULSED PE BEAM CURRENT, OFFSET ON THE DELAY WAS FIXED

3.7.1 Linearity of the differential SE contrast versus PE current

The parameters have been plotted versus PE current for comparison. Amplitude and offset of the contrast are plotted in Figure 93.

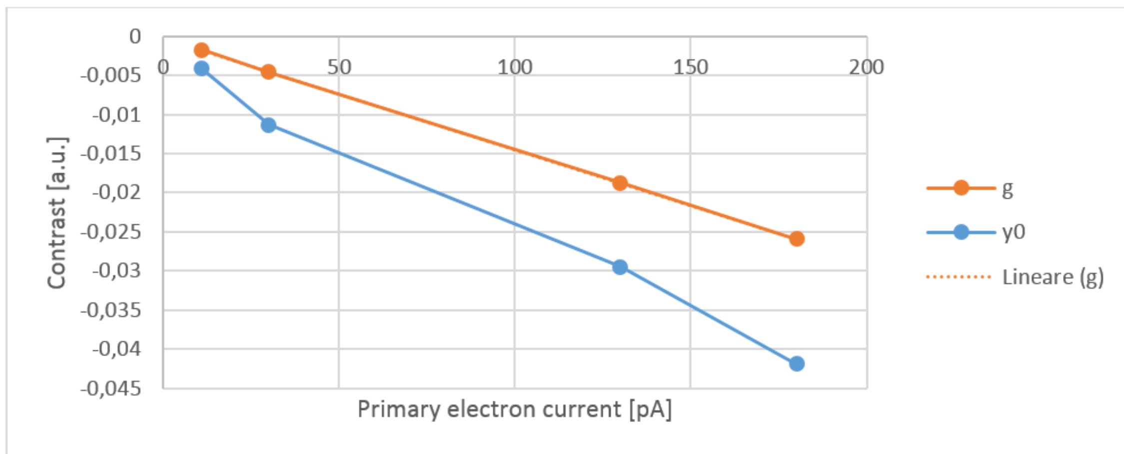

FIGURE 93 – AMPLITUDE AND OFFSET VERSUS PE CURRENT

The amplitude of the differential SE contrast g increases linearly with the PE beam current. As the PE current varied while keeping constant the repetition rate, this result means that the differential SE contrast is also linearly proportional to the number of electron per pulse. The offset y_0 increases almost linearly with PE current; this effect is attributed to the pile-up of the contribution of several succeeding pulses. It also has to be kept in consideration that the measurement of the offset may be affected by a nonzero difference between the area of the spot, s, and the area of the background, b. The signal may be expressed as a constant contribution $\eta = s_0 - b_0$ and a contribution $h(t) = s(t) - b(t)$ depending on the delay time t:

$$y(t) = s - b = s_0 + s(t) - b_0 - b(t) = (s_0 - b_0) + \big(s(t) - b(t)\big) = \eta + h(t)$$

The offset is a weighted sum of the signal at different delays:

$$y_0 = ay(t_1) + by(t_2) + \cdots = (a + b + \cdots)\eta + ah(t_1) + bh(t_2) +$$

And therefore is affected by the constant contribution η that may change while changing the region of the sample. Amplitude is related to a difference and therefore is not affected by the constant contribution and independent on the region on the sample and therefore is less noisy.

$$g = y(t_1) - y(t_2) = \eta + h(t_1) - \eta - h(t_2) = h(t_1) - h(t_2)$$

3.7.2 Estimation of rise time

The standard deviation of the Gaussian system response is bound to the smoothness parameter s of the fitting error function reported in Table 3 by a factor $1/\sqrt{2}$. The PE current may be expressed in term of number of electron per pulse considering the charge of the electron and the repetition rate. Results are reported in Table 4.

Current	Electrons per pulse	s	Sigma	Rise time 20-80%	Full Width at Half Maximum
[pA]		[ps]	[ps]	[ps]	[ps]
11	7	3.9	2.7	4.5	6.4
30	19	23.8	16.9	28.4	39.8
130	81	38.6	27.3	45.8	64.3
160	110	100.4	71.0	119.5	167.2

TABLE 4 – PROCESSING OF DATA TO OBTAIN RISE TIME VERSUS THE NUMBER OF ELECTRONS PER PULSE

The rise time is an estimation of the time resolution of the system. The dependence of time resolution on the number of electrons per pulse, shown in Figure 94, has already been reported by Sun and coauthors [83] and is attributed mainly to the Coulomb repulsion between the electrons in each pulse bunch, acting while it travels through the electronic column (Boersch effect) [66].

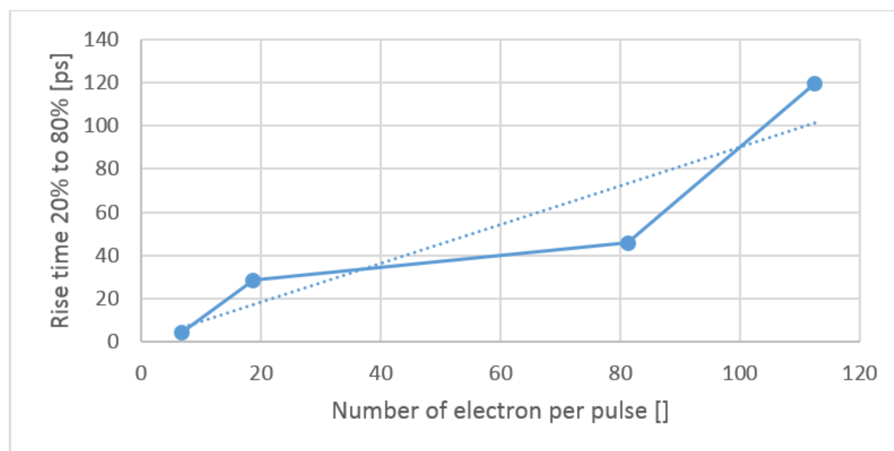

FIGURE 94 – RISE TIME FROM 20% TO 80% VERSUS THE NUMBER OF ELECTRONS PER PULSE

3.8 Conclusions

A time-resolved scanning electron microscope working in Ultra High Vacuum and operating in pump-probe has been implemented. Thanks to newly installed Schottky field emission source with optical access, it is possible to acquire SEM images with both a continuous and a pulsed PE beam. In SEM images acquired with continuous PE beam, the lateral spatial resolution was equal to 80 nm, evaluated as 20%-80% rise space of luminosity gradients. Dedicated samples have been chosen for the procedure of the spatial superposition of the optical and electron pulse on the sample. Phosphors allowed a coarse alignment that was refined by observing the footprint of the laser beam on the SEM image of a sample made by a thin film of aluminum oxide on silicon. The full system was tested on highly doped p-silicon, cleaned in hydrofluoric acid to remove the native oxide layer and passivated with hydrogen. Optimal fluence of the laser pump was determined for the silicon sample. The tests confirms the capability of the experimental setup of detecting in a reproducible and robust way the optically induced contribution on the emission of SE. The effect was characterized in dependence on the delay of the electron pulse to the photon pulse by acquiring sequences of time-resolved images. Dedicated measurement procedure and data analysis algorithm were developed for the acquisition of time-resolved SEM image with the goal to compensate drifts and instabilities and to improve the signal to noise ratio. Measured rise time and intensity of the optically induced contrast depends linearly on the PE current and, therefore of the number of electrons per pulse. The temporal resolution is limited by the Boersh effect to few picoseconds. The minimum rise time 20%-80% of the optically induced contrast measured on highly doped p-silicon was 5 ps with 7 electrons per pulse. Apparatus is now ready for time-resolved measurements on semiconductors and insulators. An improvement on the SE detection chain, implemented for measurements on aluminum oxide, will be presented in paragraph 5.2.4 Chopper and lock-in. Future perspectives for the development of the experimental setup includes the improvement of time and lateral spatial resolution. Time resolution could be improved by reducing the number of electrons per pulse to 1. This change requires an improvement of the sensitivity on SEs detection: that could be obtained by the new SE detector based on Everhart-Thornley technology introduced in paragraph “3.1.2 Secondary Electrons detector”. Spatial resolution may be improved by reducing the electromagnetic noise affecting the pointing of the electron beam on the sample. The result could be obtained by improving the mechanical mount of the electron source as explained in paragraph “3.2.2 Source performances and limitations”.

4 USEM investigation of the surface charge dynamics at the Si(001) surface as a function of doping

This chapter presents the first experimental investigation by UHV ultrafast scanning electron microscopy (USEM) of the surface charge dynamics at the Si(001) surface, as a function of doping of the bulk material. We investigated a set of six Si bulk specimens exposed on the (001) surface and doped in an interval ranging from *n*-type nearly degenerate (~10^{19} donors/cm^3) to the p-type nearly degenerate (~10^{19} acceptors/cm^3), passing through the intrinsic semiconductor. USEM imaging was performed in photon pump-electron probe mode at 10 MHz by differential secondary electron (SE) detection. The samples were investigated in an ultra-high vacuum (UHV) environment by repeated pump-probe cycles, where a 343 nm photon pulse, at a fluence of 30 µJ/cm^2, was followed at a controlled delay time by a pulse made of 80 electrons. The delay time was scanned in a range of 4 ns, with an overall time resolution of about 60 ps. The photon excitation at 3.6 eV largely exceeds the 1.12 eV optical bandgap of Si, so that a degenerate plasma of electron-hole pairs is created in a 10 nm thick layer adjacent to the surface.

The delay time series present features showing clear trends versus the doping. A sharp step in the differential SE contrast is observed at zero delay time, whose rise time is limited by the experimental time resolution; the amplitude of the step is monotonic with doping level and changes sign from negative to positive in passing from the *p*-type to the *n*-type suggesting a leading role of the carrier population in the contrast generation mechanism. Each sample was prepared in two different ways: with an exposure to ambient air of about 10 minutes after the cleaning procedure or by protecting it in a dry nitrogen atmosphere up to the upload in the measurement chamber. The experimental results show a strong dependence on the preparation, supporting the surface sensitivity of the technique. The signal dynamics evolves over several timescales ranging from tens of picoseconds up to tens of nanoseconds.

4.1 Ultrafast dynamics at the surface of Si(001)

The effect of a laser pump with photon energy of 3.6 eV is to excite electrons from valence to conduction band. Excited electrons have energy higher than the conduction band minimum. The dynamics of electrons excited by an optical pump at 3.44 eV were studied with 2 photon photoemission [118]. The result is that all the extra energy is rapidly dissipated and excited electrons thermalize to the conduction band minimum within few picoseconds [118]. The electron-hole plasma goes through interband recombination driven by both bulk and surface mechanism. Among the different processes:

- Radiative recombination with time constant τ_{rad};
- Shockley-Hall-Read recombination with time constant τ_{SRH};
- Auger recombination with time constant τ_{Auger};
- Recombination mediated by surface states (dangling bonds, defect states, adsorbed atoms states, etc) with time constant $\tau_{surf} = \frac{d}{s}$, where s is surface recombination velocity and d is the distance that the carrier have to travel to reach the surface (in our case, the few nanometers escape depth of SE);

The inverse of the overall time constant for recombination is the inverse of the time constant of different processes:

$$\tau^{-1} = \left(\tau_{rad}^{-1} + \tau_{SHR}^{-1} + \tau_{Auger}^{-1} + \tau_{surf}^{-1}\right)$$

The contribution of radiative recombination has to be considered negligible in silicon due to the indirect bandgap. Among the bulk mechanisms, the most relevant is Shockley-Hall-Read recombination [35,36]. In the SRH model, trapping and recombination of carriers are mediated by localized intragap energy states , related to bulk defects and impurities in the crystal. Mechanism is efficient because the trapping process allows to compensate the difference in momentum of the electron and the hole, typical of indirect bandgap semiconductors like silicon. Auger recombination is a three particles mechanism, where an electron-hole pair recombines by releasing the extra energy to a third carrier [119]. Auger recombination is relevant when excited carrier concentration is high. A summary of the optical excitation, thermalization and recombination processes is reported in Figure 95.

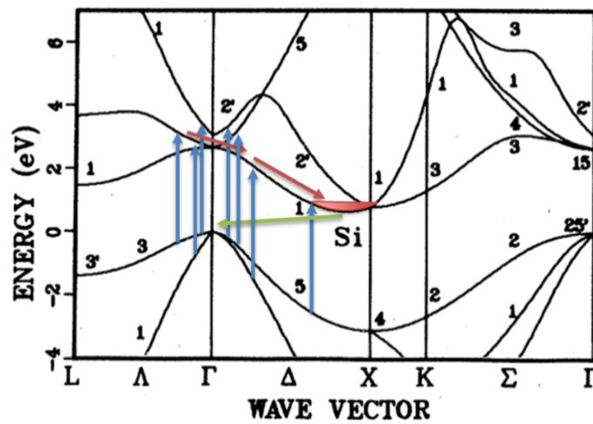

FIGURE 95 – ENERGY-MOMENTUM BAND DISPERSION FOR SILICON. ELECTRONS ARE OPTICALLY EXCITED (BLUE ARROWS), THEN THERMALIZE TO CONDUCTION BAND MINIMUM (RED ARROWS) AND FINALLY RECOMBINE (GREEN ARROW). ADAPTED FROM [120]

Recombination time constant depends on the concentration of the carriers and of the defects and may range from nanoseconds to milliseconds [121,122]. Surface defects play a key role in the temporal evolution of the optically excited electron-hole plasma. First, they may contribute as trapping and recombination sites [123]. Sabbah and Riffe measured the contribution of the surface to the recombination speed and found a strong dependence on the doping and on the oxidation [124]. Lower recombination speed was measured in p-doped silicon with respect to n-doped and even lower in p-doped silicon covered with native oxide [124]. The second effect is the pinning of the Fermi level [125]. For charge neutrality, a balanced double layer of charges is created near the surface: charges trapped by surface states are screened by a volume charge in the semiconductor. The depth of the volume charge layer depends on the doping of the semiconductor and may be described according to the Debye length[126]. The resulting space charge electric field creates a voltage barrier at the surface determining the curvature of the conduction and valence band. The optically induced electron-hole plasma screens the electric charges trapped in the defects flattening the energy bands and removing the potential barrier. The effect is known as surface photo-voltage[127]. The dynamics of surface photovoltages are driven by the recombination of the electron-hole plasma [128]. A comparison of energy bands of a p-doped semiconductor with and without light is reported in Figure 96.

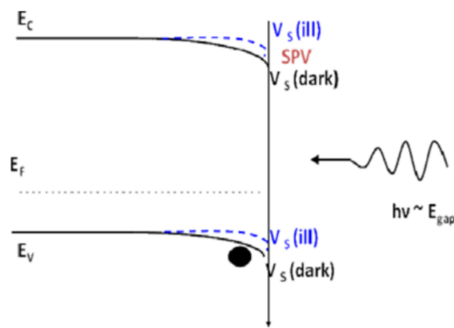

FIGURE 96 – ENERGY BANDS VERSUS DEPTH FOR A P-DOPED SEMICONDUCTOR. WITHOUT LIGHT (DARK) AND WITH LIGHT (ILL). REPRINTED WITH PERMISSION FROM [129]

Ultrafast scanning electron microscope measurements on semiconductors and in particular, on silicon, have been reported by Zewail and coworkers[9,33,34]. These results have been discussed in paragraph 2.4 USEM on semiconductors. The main result is that an optical excitation influence the rate of SE emission from the optically excited area of the semiconductor. Further studies were done to determine the sign, intensity and the temporal and spatial evolution dynamic of the effect in dependence on the doping and of the surface quality. According to Najafi and coworkers, optical excitation silicon determines an enhancement of SE emission both from phosphorous doped n-type silicon $(1.4\ 10^{14} cm^{-3})$ and from boron doped p-type silicon $(9.4\ 10^{18} cm^{-3})$ [33]. In a later work, Najafi and coworkers reported an enhancement on p-type silicon $(2.1\ 10^{19} cm^{-3})$ and a depletion on n-type silicon$(1.2\ 10^{19} cm^{-3})$ [34]. They attributed the effect to the optically induced minority carriers: the enhancement to optically induced extra electrons in p-type silicon and the depletion to optically induced extra holes in n-type silicon [34]. A depletion of SE emission was reported by Cho and coauthors on gallium arsenide: the intensity of the depletion appeared to be strongly doping dependent [28]. Other results reports the effect of the surface: Yang and coauthors reported an optical induce enhancement of SE emission from surface $(10\bar{1}0)$ when it is clean and a depletion in the same experimental condition after contaminating the surface with water vapor[29]. Finally, Bose and coauthors reported about a change in the evolution of the dynamic of the optically induced secondary emission from indium gallium nitride nanowires following surface passivation[30].

4.2 Sample set and preparation

The set of silicon samples cover an interval ranging from highly doped *p* to highly doped *n* passing through intrinsic silicon. The samples were factory polished over the (001) surface. Their doping level was evaluated from the declared resistivity, according to the results already reported in literature [130] [131]. The summary of the resistivity and doping measured set of samples is reported in Table 5. Samples with different doping are labeled by the concentration *n* of electron carriers in their conduction band in the ground state at room temperature. In fact, the electron and hole concentrations , labeled n and p respectively, in the ground state at a given temperature are related by a constant *np* product. In silicon, the *np* product is about $10^{20} cm^{-6}$. Doping the material increases the concentration of the electrons (*n* type) or of the holes (*p* type) by several order of magnitude above its value in the intrinsic material (around 10^{10} cm^{-6}), and their concentration is practically equal to the donor or acceptor concentration, respectively. The concentration of the minority carriers reduces accordingly to maintain the *np* product constant. Conduction band electron density for our set of samples is reported in Table 5.

Sample name	Doping type	Resistivity	Dopant concentration $[cm^{-3}]$		Conduction band electron concentration $n\ [cm^{-3}]$
			Interval	Average	
Si n++	n-type (arsenic)	5 mΩcm	$1.2\ 10^{19}$	10^{19}	10^{19}
Si n	n-type (phosphorus)	1-10 Ωcm	$4.4\ 10^{14} \div 4.8\ 10^{15}$	10^{15}	10^{15}
Si i	Intrinsic	1-10 kΩcm	$1.3\ 10^{13} \div 4.3\ 10^{11}$	10^{12}	10^{10}
Si p	p-type (boron)	1-10 Ωcm	$1.3\ 10^{15} \div 1.5\ 10^{16}$	10^{15}	10^{5}
Si p+	p-type (boron)	70-130 mΩcm	$1.7\ 10^{17} \div 4.0\ 10^{17}$	10^{17}	10^{3}
Si p++	p-type (boron)	1-10 mΩcm	$7.9\ 10^{18} \div 1.16\ 10^{20}$	10^{19}	10^{1}

TABLE 5 – RESISTIVITY AND DOPING CONCENTRATION OF THE SAMPLES MEASURED.

Native oxide on the surface of the sample was removed by hydrofluoric acid. The samples were kept in a box saturated with nitrogen to prevent oxide formation during the transport from the chemical lab to the load lock of the USEM. A second set of samples was cleaned with the same procedure and exposed few minutes to air before inserting them in the load lock. The full procedure to prepare the samples is the following:

- Ultrasound cleaning in acetone for 10’ at room temperature to remove organic contaminant;
- Ultrasound cleaning in ethanol for 10’ at room temperature to remove acetone;
- Immersion in 5% solution of HF in water for 45 seconds at room temperature;
- Immersion in deionized water at room temperature;
- Transport from chemical lab to load lock of USEM in nitrogen/air.

The exposure of silicon to air for few minutes may bring to the growth of one monolayer of silicon oxide, as reported by Morita and coworkers[132]. Concentration of oxygen and carbon at the surface of the samples cleaned and then exposed to nitrogen or to air has been characterized by an Auger measurement. Comparison of results on the energetic regions of the carbon and oxygen KLL peaks for highly doped silicon p++ are reported in Figure 97.

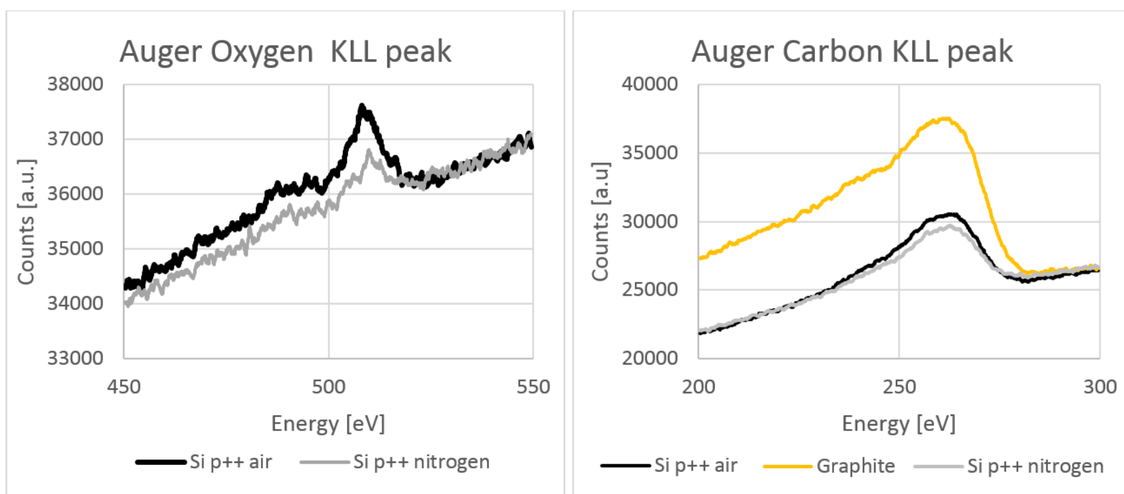

FIGURE 97 – OXYGEN AND CARBON AUGER KLL PEAKS ON SILICON P++ CLEANED IN HF EXPOSED OR TO AIR OR TO NITROGEN FOR FEW MINUTES

Auger energy spectra reported in Figure 97 confirms that keeping the sample into a nitrogen atmosphere reduce the contamination of the surface by oxygen while has minimum effect on carbon contamination. The carbon contamination may also be an effect of the Auger measurement itself since it has already been reported that exposition of silicon to PE beam determines deposition of carbon on the surface [133]. It is worth to remember that Auger measurements require a PE beam current of 40 nA while USEM images are acquired with a current of 130 pA, almost 300 times less. Since Auger and USEM measurements require approximately the same exposure time, the carbon contamination, proportional to the dose, induced by USEM has to be considered negligible.

4.3 Experimental setup

The experimental setup used to acquire time resolved SE images on silicon samples is the Ultrafast Scanning Electron Microscope described in chapter 3 Experimental setup. The configuration used is the same used for the temporal alignment of the system described in paragraph 3.6 Temporal alignment, and experimental conditions are the same. A sketch of the setup is reported from chap. 3 Experimental setup here in Figure 98 to simplify the consultation.

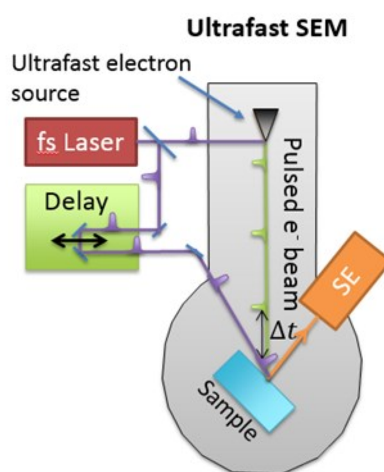

FIGURE 98 – EXPERIMENTAL SETUP FOR MEASUREMENTS ON SILICON

The optical pulse acts mainly as the pump and has a wavelength equal to 343 nm, third harmonic, with a fluence of 30 $\mu J/cm^2$. Repetition rate of the laser is set to 10 MHz. The electron pulse from the SEM column acts mainly as the probe. The role as pump or probe of the photon and electron pulses will be discussed thoroughly when commenting the results. The energy of primary electrons is kept fixed at 10 keV, while the typical average electron beam current, measured by biasing the sample at +100 V, is 130 pA that corresponds to a temporal resolution of 45.8 ps evaluated as a rise time 20-80% as reported in paragraph 3.7.2 Estimation of rise time. The pressure in the sample chamber was kept between $5\ 10^{-9}\ torr$ and $5\ 10^{-10}\ torr$ meaning that a monolayer of contaminants takes at least few hours to deposit on the surface, a time range larger than the acquisition time of one of the time series used in this work. The time resolved images were acquired at a magnification of 300 X,

corresponding to a view field of 393 μm. Such a view field is enough to include the footprint of the laser on the sample and a wide non-excited area around it. Measurements were done on area of the sample that appears uniform at the observation by SEM SE imaging, although some contaminant particles were included in the view field as spatial and focus reference.

4.3.1 Measurement procedure

A USEM time series consists of a sequence of time-resolved images, each acquired at a given delay time between the optical and the electron pulse; the values along the delay time axis were chosen with density roughly proportional to the gradient of the temporal evolution of the signal, with the highest density around the zero delay time. The experimental conditions outlined above, leading to the experimental resolution of 60 ps FWHM, are the optimal trade-off in terms of sensitivity and resolution of the apparatus at the present status. Taken the resolution into account, a delay time grid of 27 points was defined, with steps ranging from 25 ps in proximity of time zero to 500 ps at large positive and negative delay times. Each USEM image was acquired by averaging 8 frames, each one of the length of 6.7 s. Therefore the acquisition of an image requires almost one minute. Each image is associated not only to the delay time set during its acquisition but also to the time of its acquisition within a series. As described in paragraph "3.6.3 Data acquisition and analysis" a linear compensation method was chosen to remove at the first order the effect of the drifts of the apparatus. Each scan included two subsequences of images corresponding to the same time delays: during the first part of the scan the delay time is increased monotonically, while in the second part it is decreased. Each subsequence lasted about 30 minutes and included 27 images. For each image of the scan, the signal of the SE emission intensity from the optically excited area is evaluated with the procedure introduced in paragraph "3.6.3 Data acquisition and analysis". Then signal evaluated on the images corresponding to the same delay of the two subsequence acquired during a scan are averaged.

4.4 Measurement results on silicon

In this paragraph, the experimental results obtained on silicon will be presented. The data were obtained by averaging the data acquired in multiple scans made each by a forward and a backward subsequence of USEM images. Each scan has been acquired on a fresh area of the sample. The number of scans acquired for each sample are reported in Table 6.

Sample name	**Doping type**	**Doping concentration** $[cm^{-3}]$	**Conduction band electron concentration *n*** $[cm^{-3}]$	**Number of sequences**	
				Air	**Nitrogen**
Si n++	n-type	10^{19}	10^{19}	4	2
Si n	n-type	10^{15}	10^{15}	1	4
Si i	Intrinsic	10^{12}	10^{10}	5	6
Si p	p-type	10^{15}	10^{5}	4	16
Si p+	p-type	10^{17}	10^{3}	1	2
Si p++	p-type	10^{19}	10^{1}	11	6

TABLE 6 - STATISTIC OF THE EXPERIMENTAL DATA

4.4.1 Results on silicon exposed to air

Comparison of average time-resolved SE differential contrast versus electrons-to-photons delay acquired on differently doped silicon samples exposed to air are reported in Figure 99. Further details on data processing step are given in Appendix B: Data on silicon.

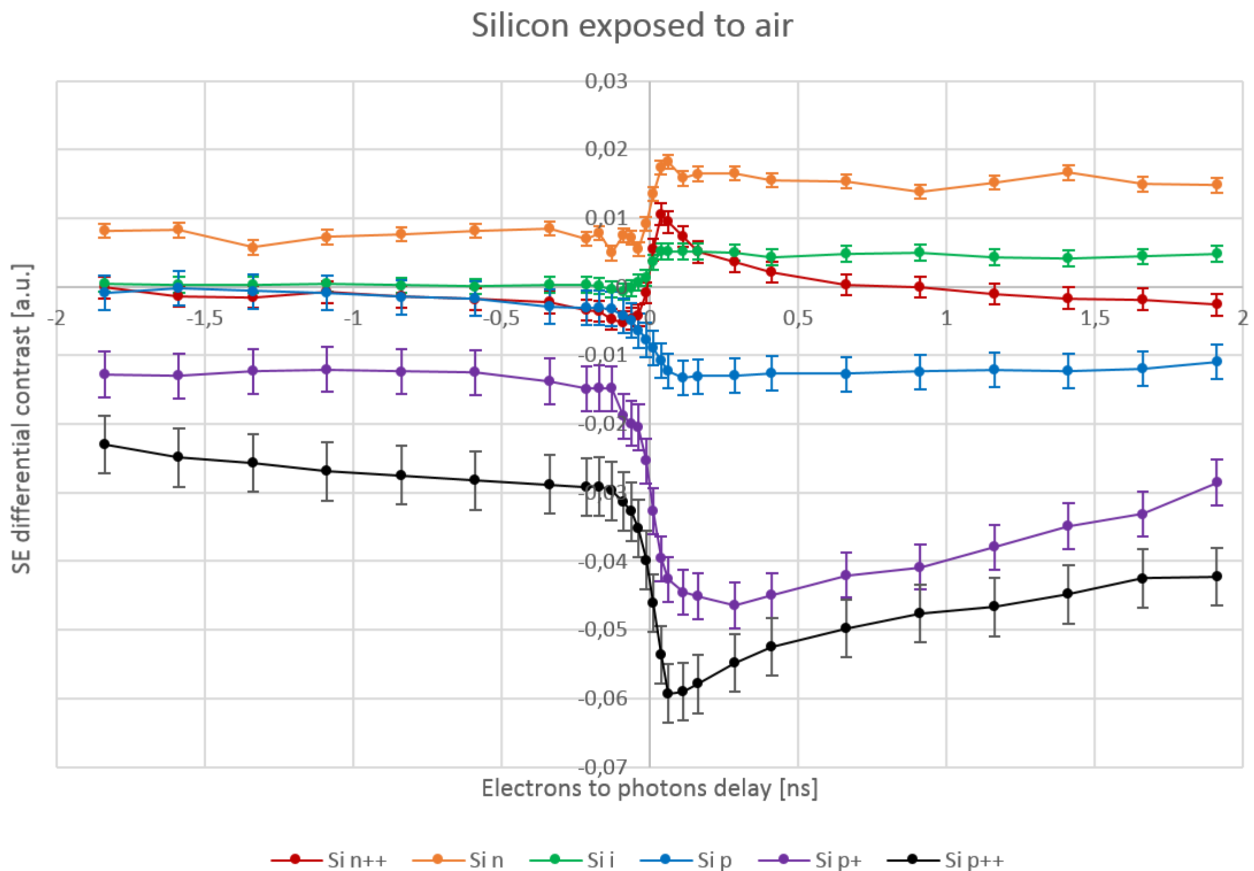

FIGURE 99 - COMPARISON OF DYNAMICS ON SILICON SAMPLES WITH DIFFERENT DOPING EXPOSED TO AIR VERSUS DELAY

The delay time series of the raw differential SE signal in Figure 99, silicon surfaces exposed to air, appear to be strongly doping dependent. Three main region of the delay time scale have to be considered:

- negative delays (electrons before photons);
- zero delay (electrons and photons superimposed);
- positive delays (electrons after photons);

At negative time delays, SE differential contrast appears constant or with a minimum linear dependence on the delay but not null as expected from a differential contrast signal. The effect may be attributed to an incomplete recovery of the effect of the optical excitation in the time interval between two consecutive optical pump pulses on the sample, equal to 100 ns .The pile-up of the effects of optical excitation over many pulses determines the observed onset at negative time delays. The maximum absolute value of the onset, negative, is recorded for the strongly p-doped silicon. The absolute values decreased monotonically with the dopant concentration. Silicon intrinsic do not shows any onset. A positive onset is recorded for the n-doped silicon sample, $n = 10^{19} cm^{-3}$. For

n-doped samples the amplitude the amplitude of the onset does not increase with the dopant concentration since highly n-doped, $n = 10^{19} cm^{-3}$, silicon sample shows an onset similar to the one of the p-doped sample, $p = 10^{15} cm^{-3} \rightarrow n = 10^{5} cm^{-3}$, and not maximum as expected. It has to be kept in consideration that the onset appears an unreliable source of information because its estimation may be affected by morphology as discussed in paragraph "3.7.1 Linearity of the differential SE contrast versus PE current". A linear background is subtracted from each delay time series to cancel out instabilities due to the onset.

At zero time delays, an abrupt change in SE differential contrast is observed. The step is attributed to the effect of the optical pump on the sample. Sign of the step appear positive for intrinsic and n-doped samples and negative for the p-doped sample. Positive sign corresponds to an enhancement in SE emission after optical excitation while negative sign corresponds to a depletion.

At positive delays, a recovery dynamic towards the level of the onset may be observed.

4.4.2 Results on silicon exposed to nitrogen

Comparison of average time-resolved SE differential contrast versus electrons to photons delay acquired on differently doped silicon samples exposed to nitrogen are reported in Figure 100. Further details on data processing step are given in Appendix B: Data on silicon.

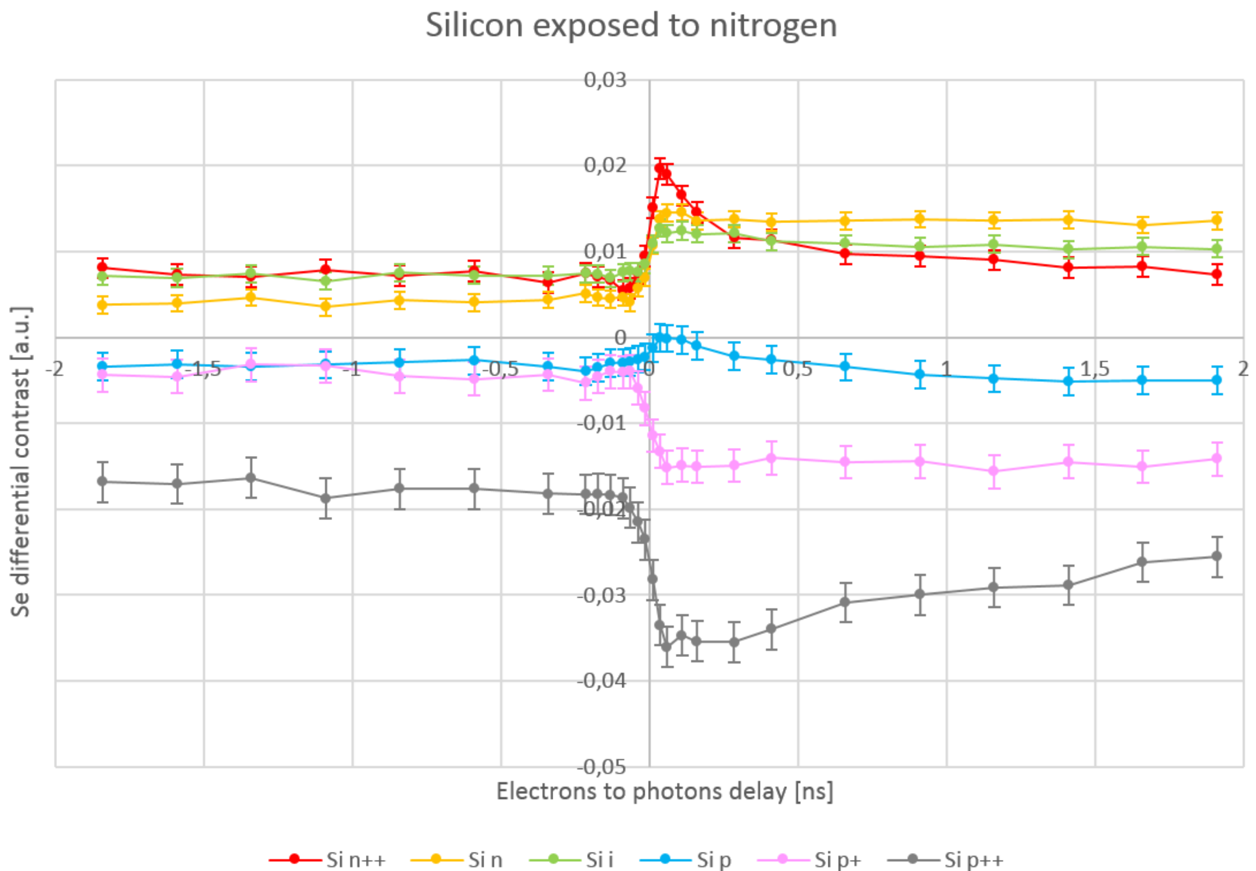

FIGURE 100 - COMPARISON OF DYNAMICS ON SILICON SAMPLES WITH DIFFERENT DOPING EXPOSED TO NITROGEN VERSUS DELAY

The delay time series of the raw differential SE signal in Figure 100, silicon surfaces exposed to nitrogen, appear to be strongly doping dependent. Three main region of the delay time scale have to be considered:

- negative delays (electrons before photons);
- zero delay (electrons and photons superimposed);
- positive delays (electrons after photons);

At negative time delays, an onset is observed, as it was already reported for data on silicon exposed to air. Similarly to what was reported for silicon exposed to air the amplitude of the onset appears maximum, negative, for the highly p-doped silicon sample. Then onset decreases with the dopant concentration. As in silicon exposed to air the onset values of the n-doped silicons samples are positive but in the case of silicon exposed to nitrogen the intensity is reversed. Onset increases with the concentration of n-dopant. The onset of intrinsic silicon sample appears positive and comparable with the one of the most n-doped silicon. This is a difference with respect to what was observed for silicon exposed to air and appears as an exception of the regularity of the value of the onset observed with the concentration of doping. It has to be kept in consideration that onset appears a critical parameter for the SE differential contrast algorithm because its estimation may be affected by morphology as discussed in paragraph “3.7.1 Linearity of the differential SE contrast versus PE current”.

At zero time delays, an abrupt change in SE differential contrast is observed. The step is attributed to the effect of the optical pump on the sample. Sign of the step appear positive for intrinsic and n-doped samples and negative for the strongly p-doped sample. Differently from what was reported for silicon exposed to air the sign of the step for lightly p-doped silicon, $p = 10^{15} cm^{-3}$, exposed to nitrogen appears positive. Except for lightly p-doped silicon, sign of the step measured on silicon exposed to air are confirmed.

Also for silicon exposed to nitrogen a recovery dynamic towards the level of the onset may be observed at positive delays.

4.4.3 Optically induced SE contrast step and recovery dynamics

A constant onset has been subtracted to improve the comparison of results obtained on silicon exposed to air and exposed to nitrogen. The comparison is reported in Figure 101

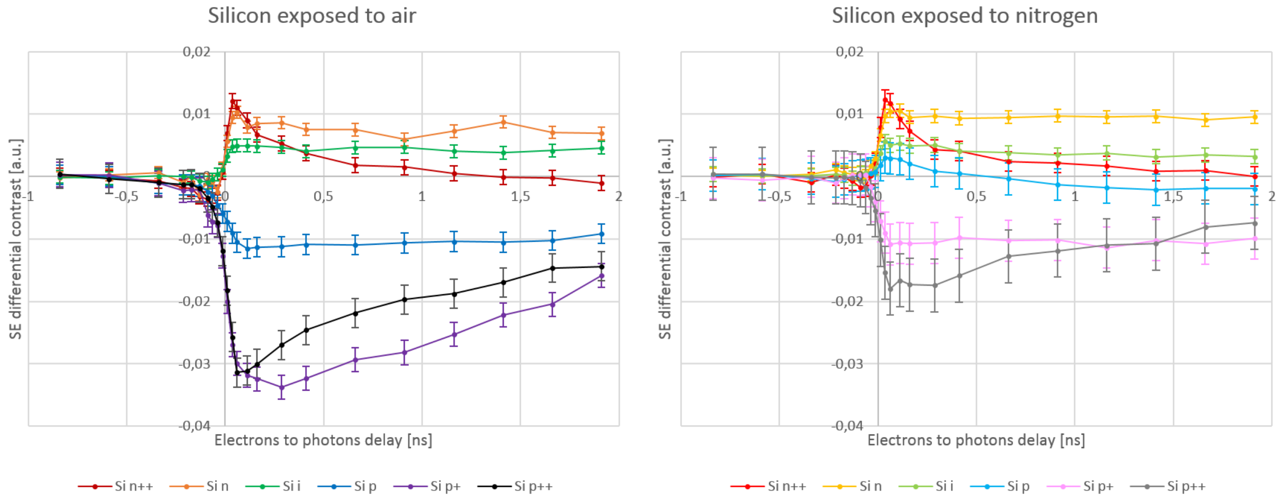

FIGURE 101 – SE DIFFERENTIAL CONTRAST ON SILICON EXPOSED TO AIR (ON THE LEFT) AND EXPOSED TO NITROGEN (ON THE RIGHT) AFTER CONSTANT OFFSET SUBTRACTION

The subtraction of the onset on the delay time series of the raw differential SE signal in Figure 101 allows to compare the amplitude of the step in the SE differential contrast due to optical excitation. Amplitude of the step appears monotonic with doping. The maximum step, positive, is recorded for highly n-doped silicon, $n = 10^{19}cm^{-3}$, both for silicon exposed to air and to nitrogen. Intensity of the step decreases when reducing concentration of n-dopant , $n = 10^{15}cm^{-3}$, and even more for intrinsic $n = 10^{10}cm^{-3}$. In silicon exposed to air the amplitude of the step is minimum in the intrinsic silicon, then it changes sign becoming negative and increasing again towards negative values when increasing the concentration of p-dopant. An exception is observed for intermediate p-doped sample $p = 10^{17}cm^{-3} \rightarrow n = 10^{3}cm^{-3}$ that shows a step with intensity higher than the highly p-doped one, $p = 10^{19}cm^{-3} \rightarrow n = 10^{1}cm^{-3}$. In silicon exposed to nitrogen, the amplitude of the step decreases from highly doped n to intrinsic and the minimum is reported for the lightly p-doped sample, $p = 10^{15}cm^{-3} \rightarrow n = 10^{5}cm^{-3}$. Increasing further the concentration of p-dopant the step change sign becoming negative, and increase its amplitude. The maximum is reported for the highly p-doped silicon $p = 10^{19}cm^{-3} \rightarrow n = 10^{1}cm^{-3}$. Apart from a single exception the amplitude with sign of the step appears correlated with the concentration of electrons in conduction band. Absolute value of the amplitude of negative steps for p-doped sample is higher than the absolute value of the amplitude of positive steps for n-doped samples, in both silicon exposed to air and silicon exposed to nitrogen. Absolute values of the steps observed on silicon exposed to air are generally larger than steps observed on silicon exposed to nitrogen with the same type and level of doping.

At positive delays, electron pulse after the optical pulse, the differential secondary electron contrast, perturbed by the optical exctitation, recovers towards the onset level. Recovery dynamic of the signal in dependence on the delay may be observed. The dynamics becomes faster when increasing the concentration of dopant, both p-type and n-type, and the highly n-doped silicon sample shows the fastest recovery. It has to be underlined that silicon p-doped, $p = 10^{15}cm^{-3}$ *and* $n = 10^{5}cm^{-3}$, exposed to nitrogen has a positive step than decreases to negative values of the contrast and finally recovers to the onset level from below. At least two recovery phenomena are necessary to explain its dynamics: one fast and positive, the second one slower and negative.

Finally, a constant onset subtraction does not fully describe the dynamics observed at negative delays and neither a linear background would do. An exponential deviation from the linear background is present on the scale of few tens up to few hundreds of ps.

4.5 Data analysis

From the inspection of the scans, it appears that some of them show a differential SE emission enhancement for positive delay time (electrons arriving after the optical excitations), while other show depletion. The rise time of the step is compatible with the time resolution of the machine, characterized in paragraph in paragraph 3.7 Time resolution. A rise time 20%-80% equal to 45.8 ps was measured with a current of 130 pA, the same used during the acquisition of time-resolved USEM images on silicon. Different time scales were identified in the evolution of the differential SE contrast over the time range investigated:

1. A recovery of the contrast for increasing positive delay time towards the value assumed in the onset at large positive delay time, with one or more time constants ranging from few hundreds of picosecond up to nanoseconds that is compatible with the timescales Shockley-Hall-Read recombination of optically excited carriers;
2. A fast evolution over a few tens up to few hundreds of picoseconds on the positive side of the zero of the delay time axis that might be due to Auger recombination of optically excited carriers or to the effect of the surface defects;
3. A fast evolution over a few tens up to few hundreds of picoseconds on the negative side of the zero of the delay time axis still unexplained.

These attributions are based over timescale and trends. For more robust statements, further experimental verification will be conducted.

Those contributions are kept into consideration by the following fitting model. Both phenomena 1 and 2 are described by an exponential decay: $A_1 e^{-\frac{t}{\tau_1}}$ for the first and $A_2 e^{-\frac{t}{\tau_2}}$ for the second, respectively. Each exponential is multiplied by a step function $H(t) = \{1 \forall\ t \geq 0;\ 0 \forall\ t < 0\}$ that sets signal to zero at negative delays. Phenomena 3 is described by an exponential decay at negative delays, $A_3 e^{-\frac{t}{\tau_3}}$, multiplied by a step function $H_3(t) = \{1 \forall\ t \leq 0;\ 0 \forall\ t > 0\}$ that sets signal to zero at positive delays. The three contributions are summed together and convoluted with a Gaussian bell G that accounts for the temporal resolution of the apparatus. Analytical solution of the convolution is reported in Appendix E: Convolution of an exponential and a Gaussian. Finally a linear term was added to describe the onset at negative delays. The full expression is:

$$f(t) = G(0, \sigma) \otimes \left(H(t) A_1 e^{-\frac{t}{\tau_1}} + H(t) A_2 e^{-\frac{t}{\tau_2}} + H_3(t) A_3 e^{\frac{t}{\tau_3}} \right) + m_0 t + y_0$$

Free parameters are:

- the coefficient of the linear offset m_0 and y_0;
- the amplitudes A_1, A_2 and A_3 and the time constant τ_1, τ_2 and τ_3 of the dynamics.

The FWHM of the Gaussian bell was first left as a free parameter, obtaining a standard error on the entire data set equal to 2 ps. The average value, equal to 60 ps, was set as a fixed parameter. The result found appears not far from the value of 64 ps found during the calibration measurements and reported in paragraph "3.7.2 Estimation of rise time". Conservation of the time resolution appears as a strong support about the long-term stability of the operation of the machine. Results of the fitting are reported in "Appendix C: fitting results".

4.5.1 Effect of the exposure of the surface to environmental gases

In the following, the comparison of samples exposed to air and to nitrogen is reported for each level of doping. Linear background has been subtracted.

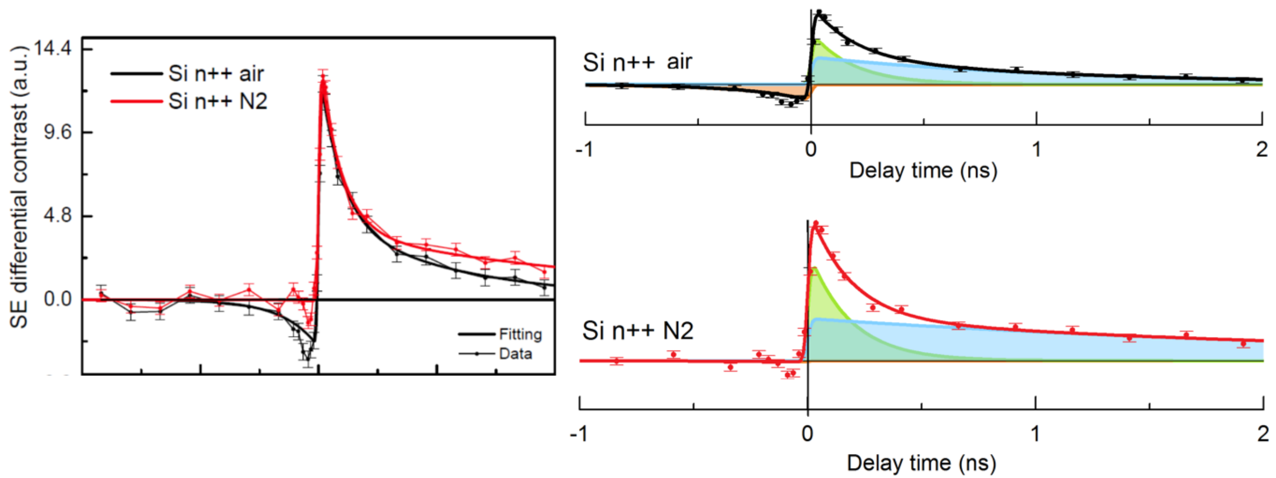

FIGURE 102 – FITTING OF THE DATA ON HIGHLY N-DOPED SILICON $n = 10^{19} cm^{-3}$

Comparison of SE differential contrast dynamics on highly n-doped silicon $n = 10^{19} cm^{-3}$ exposed to air and to nitrogen is reported in Figure 102. Amplitude of the step induced by laser is the same, recovery appears faster for the sample exposed to air. Recovery is fitted by a two time constant decay equal to 185 ps and 1.14 ns for air, and 183 ps and 2.67 ns for nitrogen. The slow recovery is compatible with SRH recombination while the fast might be due to Auger recombination. The surface affects recombination speed and the evolution at negative delays.

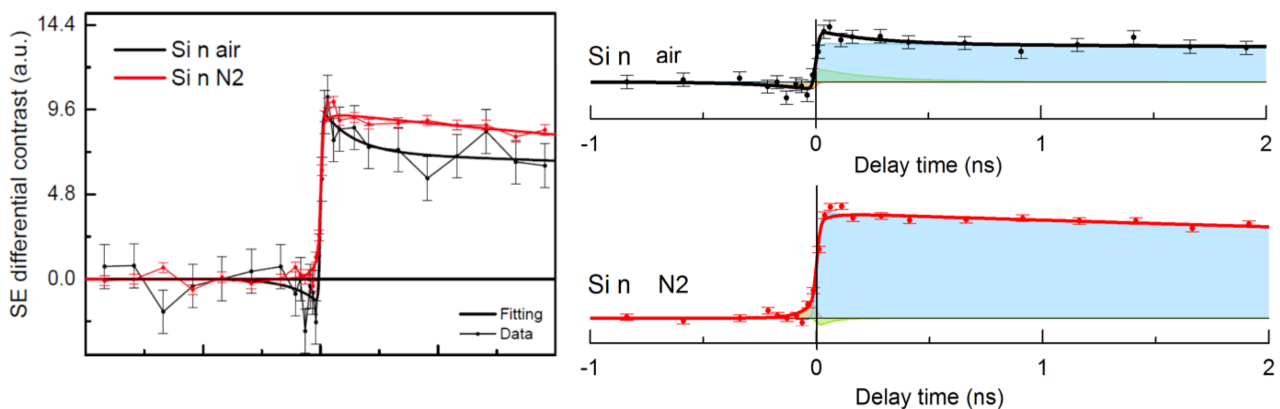

FIGURE 103 – FITTING OF THE DATA ON N-DOPED SILICON $n = 10^{15} cm^{-3}$

Comparison of SE differential contrast dynamics on n-doped silicon $n = 10^{15} cm^{-3}$ exposed to air and to nitrogen is reported in Figure 103. Amplitude of the step induced by laser is the same, recovery appears faster for the sample exposed to air. Recovery is fitted by a two time constant decay but most of the effect may be attributed to the slowest. Estimated time constant are equal to 30 ns for silicon exposed to air and 14 ns for nitrogen. The time constant estimated for the surface exposed to air reached the upper bound, indicating a decay too slow to be observed within the 4 ns observation window. The surface affects recombination speed and the evolution at negative delays.

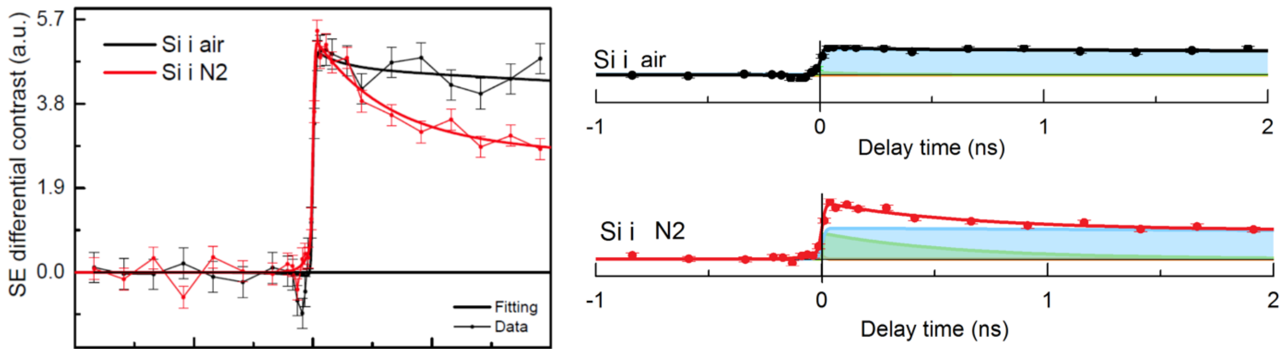

FIGURE 104 – FITTING OF THE DATA ON INTRINSIC SILICON $n = 10^{10} cm^{-3}$

Comparison of SE differential contrast dynamics on intrinsic silicon $n = 10^{10} cm^{-3}$ exposed to air and to nitrogen is reported in Figure 104. Amplitude of the step induced by laser is the same, recovery appears faster for the sample exposed to nitrogen. Recovery is fitted by a two time constant decay. Most of the effect may be attributed to the slowest, equal to 30 ns for silicon exposed to air. The time constant estimated for the surface exposed to nitrogen reached the upper bound, indicating a decay too slow to be observed within the 4 ns observation window. In silicon exposed to nitrogen both process are relevant, with time constant equal to 600 ps and 29 ns. The slow recovery is compatible with SRH recombination. The surface affects recombination speed.

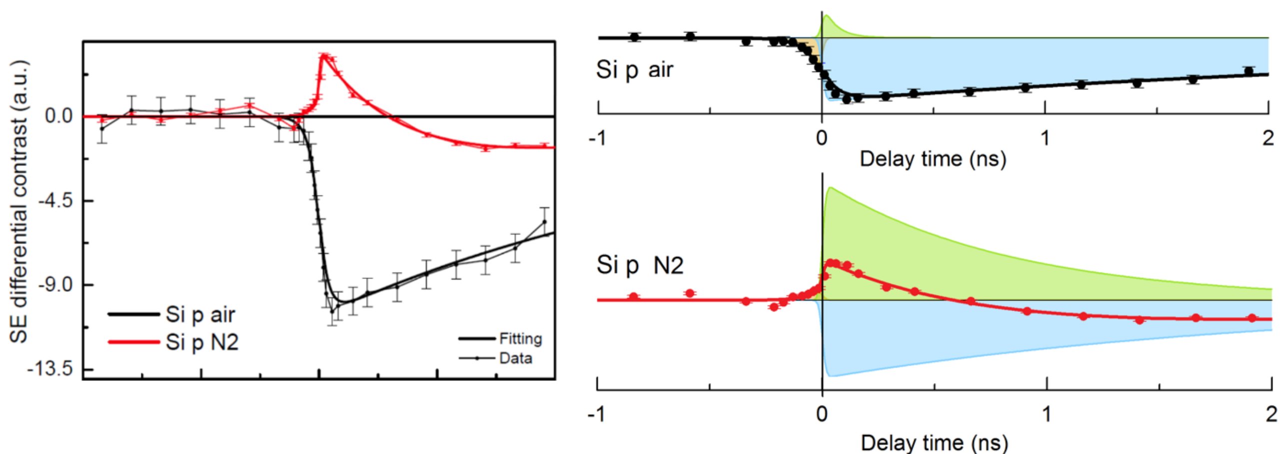

FIGURE 105 – FITTING OF THE DATA ON LIGHTLY P-DOPED SILICON $p = 10^{15} cm^{-3}$

Comparison of SE differential contrast dynamics on p-doped silicon $p = 10^{15} cm^{-3}$ exposed to air and to nitrogen is reported in Figure 105. Amplitude of the step induced by laser appears strongly influenced by the surface. Sample exposed to nitrogen shows the superposition of two phenomena that generates steps with different sign. The positive one recovers with a time constant equal to 834 ps while the second with a time constant of 2.07 ns. Sample exposed to air shows a negative step with a recovery time constant of 3.67 ns. A positive and fast component with a time constant equal to 60 ps is observed also on the sample exposed to air. Long term recombination observed on both sample may be attributed to SRH recombination. The positive and fast component, strongly dependent by the contamination of the surface, might be attributed to the effect of band flattening. Different surface defects could be associated to different energy levels. A slight change in the pinning level of the Fermi level may invert the curvature of the bands at the surface, inverting the effect of the optical excitation.

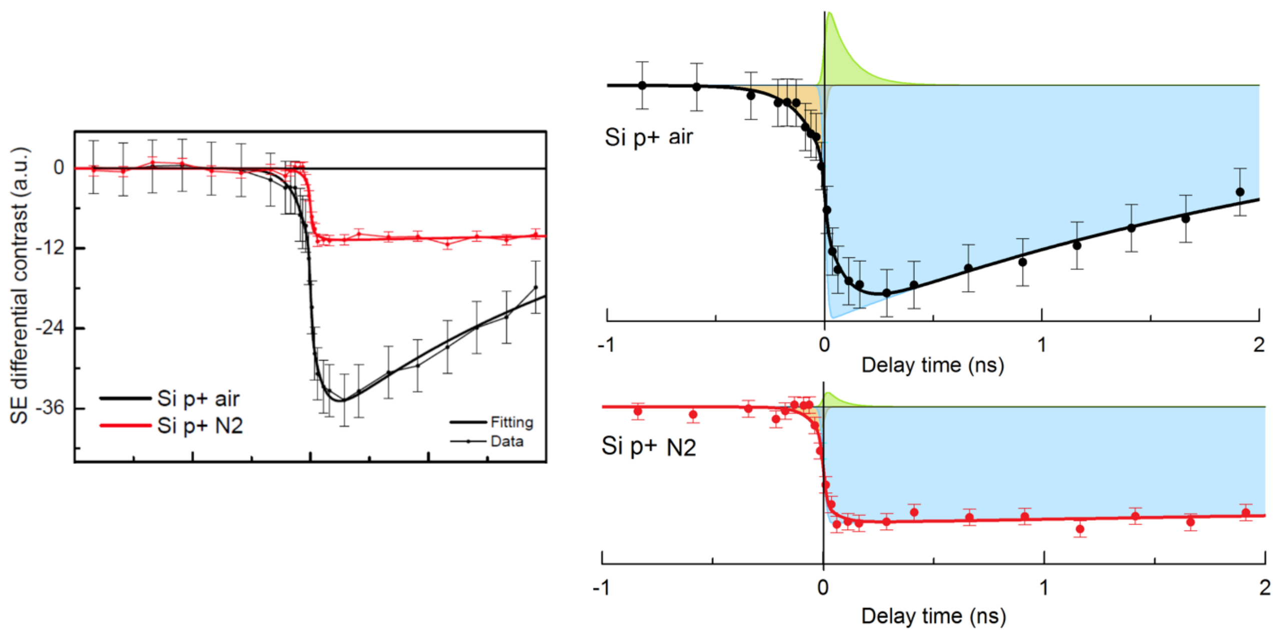

FIGURE 106 – FITTING OF THE DATA ON INTERMEDIATELY P-DOPED SILICON $p = 10^{17} cm^{-3}$

Comparison of SE differential contrast dynamics on p-doped silicon $p = 10^{17} cm^{-3}$ exposed to air and to nitrogen is reported in Figure 106. Optically induced step has the same negative sign but different amplitude. Silicon exposed to air shows a stronger amplitude and a faster recovery with time constant equal to 2.75 ns. Estimated time constant for silicon exposed to nitrogen is equal to 30 ns. In both cases, the recombination may be attributed to SRH recombination. The time constant estimated for the surface exposed to air reached the upper bound, indicating a decay too slow to be observed within the 4 ns observation window. Faster processes were detected on both dynamics, with time constant below 100 ps. The surface affects the amplitude of the step and recombination speed although has to be took into consideration that the data have low statistic, with a single sequence for silicon exposed to air and two sequences for silicon exposed to nitrogen.

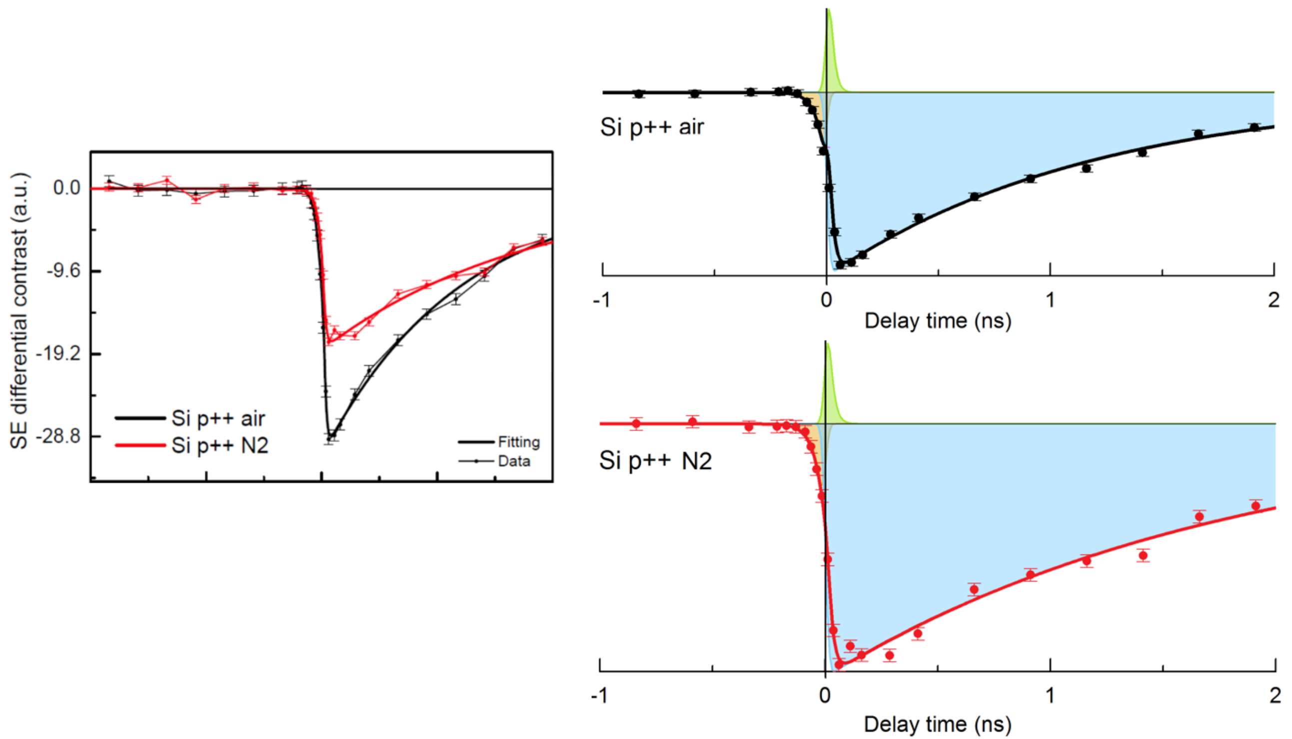

FIGURE 107 – FITTING OF THE DATA ON HIGHLY P-DOPED SILICON $p = 10^{19}cm^{-3}$

Comparison of SE differential contrast dynamics on highly p-doped silicon $p = 10^{19}cm^{-3}$ exposed to air and to nitrogen is reported in Figure 107. Optically induced step has the same negative sign but different amplitude. Recovery time constant for silicon exposed to air and exposed to nitrogen are equal to 1.18 ns and 1.81 ns, respectively. In both cases, the recombination may be attributed to SRH recombination. A contribution of Auger recombination cannot be excluded. The surface affects the amplitude of the step and recombination speed.

4.5.2 Trends of the amplitude of the step and of the recovery time

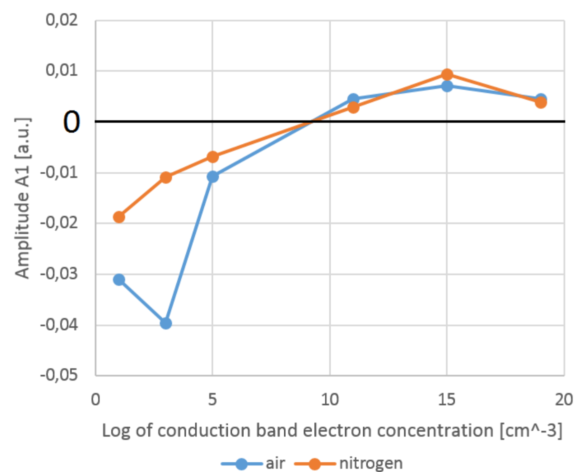

FIGURE 108 – AMPLITUDE OF THE SLOWEST COMPONENT OF THE FITTING AS A FUNCTION OF DOPING PARAMETER

Amplitude of the slowest component of the fitting are compared in Figure 108 as a function of the doping parameter. The evolution of the step amplitude appears nearly monotonic with electron concentration for silicon exposed to air. The only exceptions are the highly doped n-silicon and the p-doped silicon ($p = 10^{17} cm^{-3}$). In the highly doped n-silicon step however the contribution of the faster component is non negligible, so that the monotonic trends could be restored by including it. On the contrary the case of the p-doped silicon lies out of the experimental uncertainty and is to be understood. The trend appears as the superposition of two main components: 1) a negative contribution independent on the doping level, and 2) a monotonic growth with the doping parameter.

1) A couple of phenomena are candidates to explain the negative component. The first mechanism was proposed by the group of A. H. Zewail [28]; it relies on the loss of energy experienced by the secondary electrons along their travel through the material towards vacuum. The electron-hole pairs injected by the photon pulse might act as scattering centers, increasing the energy loss and reducing the number of electrons able to cross the vacuum barrier. A second mechanism that might contribute in a doping independent way, is the charging of the illuminated area due to the photoemitted electrons, which leaves a local positive charge and raise the vacuum barrier.
2) The monotonic growth of the step jump may imply a change of sign of the effect, depending on the value of the negative component at point 1). For a null negative component, this change arrives between the intrinsic and the first positive doping level for both type of surface preparations (exposed to air and to nitrogen), as shown in Figure 108. For larger negative components, the change would move to smaller values of the doping parameter (towards larger p doping).
   According to previous works [9,28,83], this enhancement of the SE emission with the doping parameter would be compatible with an increase of the average electron energy with respect to the vacuum level. As the population of electrons in the conduction band at equilibrium increases with the doping parameter, the optically excited electrons are obliged to fill states with higher energy, increasing the rate of SE emission. However, in the present case, the high photon fluence generates a nearly degenerate carrier concentration, nearly filling the conduction band, irrespective of the doping. Thus, this effect could hardly justify by itself the smooth change of differential SE contrast within such a large range of doping levels. Based on these findings and on the well-recognized surface sensitivity of the SE probe, we propose that a band flattening mechanism might play a fundamental role in the doping dependence of the step amplitude. Figure 96 shows the band curvature at a p-doped Si surface, due to pinning of the Fermi level by the surface states; the plasma created by the laser pulse at high injection levels makes the surface conductive and flattens the bands, allowing less electrons to escape towards vacuum from a p-doped silicon surface, and more electrons from a n-doped Si surface. Thus, this effect might account also for the change of sign of the step jump. Furthermore, the change of the barrier could also be due to photoinduced changes in the population of the trap states at the surface, pinning the Fermi level. If this effect would be confirmed, this would open the possibility to investigate the dynamics of trap surface states with a high sensitivity and mapping capabilities.

4.6 Conclusions

Ultrafast Scanning Electron Microscopy was used to investigate the Si(001) surface as a function of doping level, to get insight on the formation of differential SE contrast and on the surface dynamics of charges, electron-hole pairs and trap states. This information has a potential impact on the characterization and development of low

dimensional and ultra-thin semiconductor materials and devices. The investigation was carried on in the high injection regime, at about 10^{19} absorbed photons/cm^3, approaching the injection regime exploited in light emitting semiconductor devices.

The USEM apparatus was operated at a wavelength of 343 nm for the optical pump pulse, and 10 kV acceleration for the electron probe pulse, for an overall delay time resolution of 60 ps. The fluence of the photon pump pulse to attain the high injection regime was 30 μJ/cm^2, absorbed within about 10 nm of depth from the surface.

Time-resolved imaging allowed to scan the differential SE contrast as a function of the delay time. The investigation covered a set of six Si(001) surfaces, ranging from highly *p*-doped (10^{19} acceptors/cm^3) to highly n-doped (10^{19} donors/cm^3) samples. A strong, nearly monotonic dependence on the doping level of the SE emission was found, which suggest a leading role of the carrier population in the contrast generation mechanism. Each sample was prepared in two different ways: with an exposure to ambient air of about 10 minutes after the cleaning procedure or by protecting it in a dry nitrogen atmosphere up to the upload in the measurement chamber. The experimental results show a strong dependence on the preparation, supporting the surface sensitivity of the technique. The signal dynamics evolves over several timescales ranging from tens of picoseconds up to tens of nanoseconds. A preliminary interpretation of the physics behind the contrast formation involves, as main actors, the dynamics of charge carriers and of trap states at the surface, which determines a change of the vacuum barrier for the emitted electrons by a band flattening mechanism.

This work demonstrate several strengths of the USEM technique, including its surface sensitivity, doping sensitivity, granting USEM a significant role for the investigation of surface phenomena in bulky materials and devices.

5 USEM investigation of the color center charge dynamics at the surface of aluminum oxide

This chapter presents the results obtained on the surface of an insulator by USEM. Time-resolved SE contrast was used to study the dynamics of color center excitation in a thin film of aluminum oxide on silicon. First, the technological importance of the material and the experimental setup will be introduced, the experimental results will be presented, and a theoretical model will be proposed. The results obtained on aluminum oxide were accepted for publication by Ultramicroscopy [134]. The preprint version of the paper is reported in Appendix D: paper on aluminum oxide [134]

5.1 Aluminum oxide on silicon

Basic electronic circuits like MOS transistor are made of doped semiconductors, metal, and insulators. The most commonly used oxide in electronic industry is silicon oxide, thanks to the fact that it grows on silicon with the same lattice parameters, helping to passivate the surface. Electrical conduction through the insulating layer is one of the reasons of failure of electronic circuits. This phenomenon may be due to free electrons trapped in the

lattice defects [135]. Their dynamics could be excited optically, by finely tuning the photon wavelength at their resonance [39]. The experimental setup developed for Ultrafast Scanning Electron Microscopy uses an optical excitation with photon energy of 3.6 eV, compatible with the optical excitation energies already reported for the lattice defects of aluminum oxide [111] and magnesium oxide [136] [137]. Aluminum oxide was chosen as a test sample because more information about the ultrafast dynamics of its color centers are available with respect to magnesium oxide [42].

FIGURE 109 – OPTICAL PICTURE OF A MAGNESIUM OXIDE BULK SAMPLE OPTICALLY EXCITED WITH PHOTONS OF 3.6 EV

Aluminum oxide is an excellent electrical insulator with a bandgap of 8.7 eV in its pure crystal form [37]. It is used as a thermal and electrical insulator in industrial and aerospace applications. Nowadays, aluminum oxide is proposed as a substitute of silica in the gate oxides of metal oxide transistors, thanks to its insulating capabilities, mechanical stability and relatively low dielectric constant [135]. Aluminum oxide may absorb photons of energy lower than the gap when defects of its crystalline structures are present [138]. These defects may be introduced in the crystalline lattice by irradiating pure crystals with heavy ions [139], neutrons [140], electrons [41], gamma rays [141] or melting aluminum oxide powder in a graphite crucible [142].

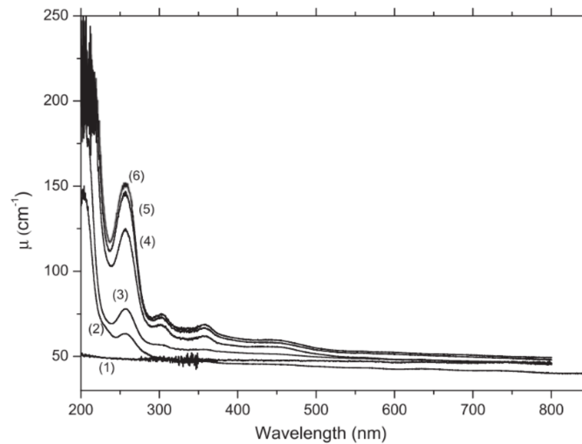

FIGURE 110 – OPTICAL ABSORPTION SPECTRUM OF ALUMINUM OXIDE IN ITS VIRGIN STATUS (1) AND AFTER EXPOSURE TO A NEUTRON FLUX OF $4.4 \cdot 10^{16}$ n/cm^2 (2), $1.3 \cdot 10^{17}$ n/cm^2 (3), $7.5 \cdot 10^{17}$ n/cm^2 (4) , $9.2 \cdot 10^{17}$ n/cm^2 (5), AND $1.4 \cdot 10^{18}$ n/cm^2 (6). REPRINTED FROM [140].

The absorption coefficient is related to the density of defects in the material, as is shown in Figure 110 that shows no optical absorption in the visible-UV region from a virgin aluminum oxide sample and an increasing absorption related to the exposure to neutron flux [140]. Lattice defects introduced by different damaging techniques shows common absorption peaks [41].

5.1.1 Lattice defects in aluminum oxide

Lattice defects in aluminum oxide may be related to vacancies either of an oxygen atoms, indicated by F, or of an aluminum atoms, indicated by V. are also known as color center thanks to the fact that they absorb visible light, making the crystal appearing coloured, and are indicated with the letter F, from Farben that means color in German. Color centers allows the interaction of alumina with UV light making it interesting for optoelectronics applications, both in radiation detection [143] and in data storage [111][38]. Oxygen vacancies are classified according to the number of missing atoms and to their electrical charge. Notation F is used for a vacancy determined by a single missing atom and F_2 for two vacancies placed next to each other.

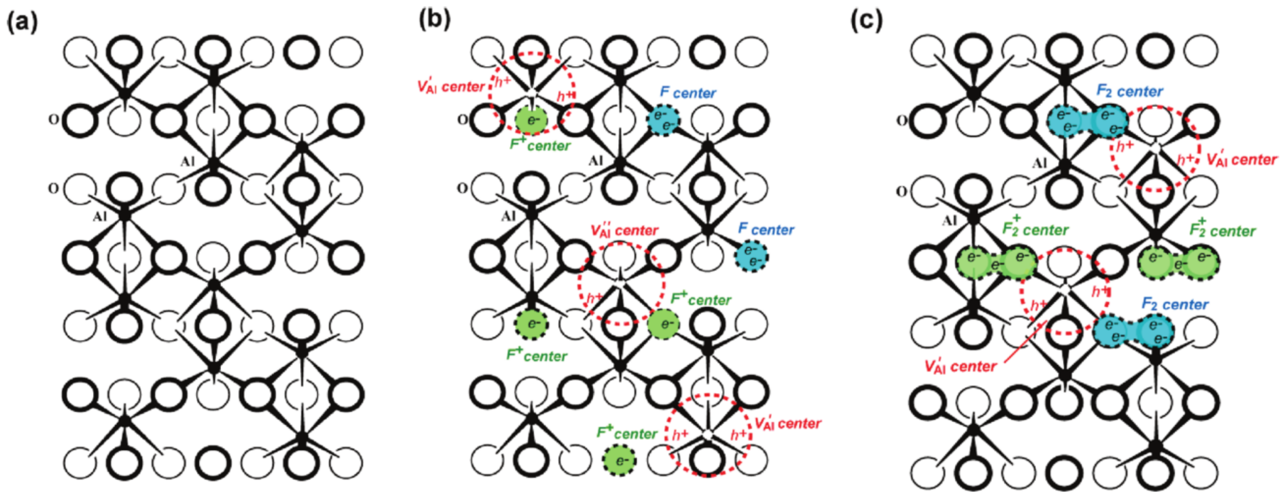

FIGURE 111 - POSSIBLE LATTICE DEFECTS IN A CRYSTAL OF ALUMINUM OXIDE. DRAWING A SHOWS THE CRYSTALLINE STRUCTURE WITHOUT DEFECTS, DRAWING B SHOWS THE VACANCIES WITH A SINGLE ATOM MISSING AND DRAWING C THE DOUBLE VACANCIES. LETTERS F AND V INDICATE VACANCIES OF OXYGEN AND ALUMINUM ATOMS, RESPECTIVELY. REPRINTED FROM [142].

Electrons trapped in the vacancies are localized and assume atomic-like wave functions depending on the hosting trap. The transition from different energy levels gives rise to characteristic absorption and emission peaks. The transition from ground state to excited level can be excited optically[138]. The radiative decay of excited color centers generates luminescence. Optical measurements allowed associating each peak in the optical absorption spectrum to the corresponding peak in the emission spectrum [39]. Groups, including an emission peak and the corresponding absorption one, were associated to the different oxygen vacancies [37]. The full sketch of the allowed transition in F color centers in aluminum oxide is reported in Figure 112 [41].

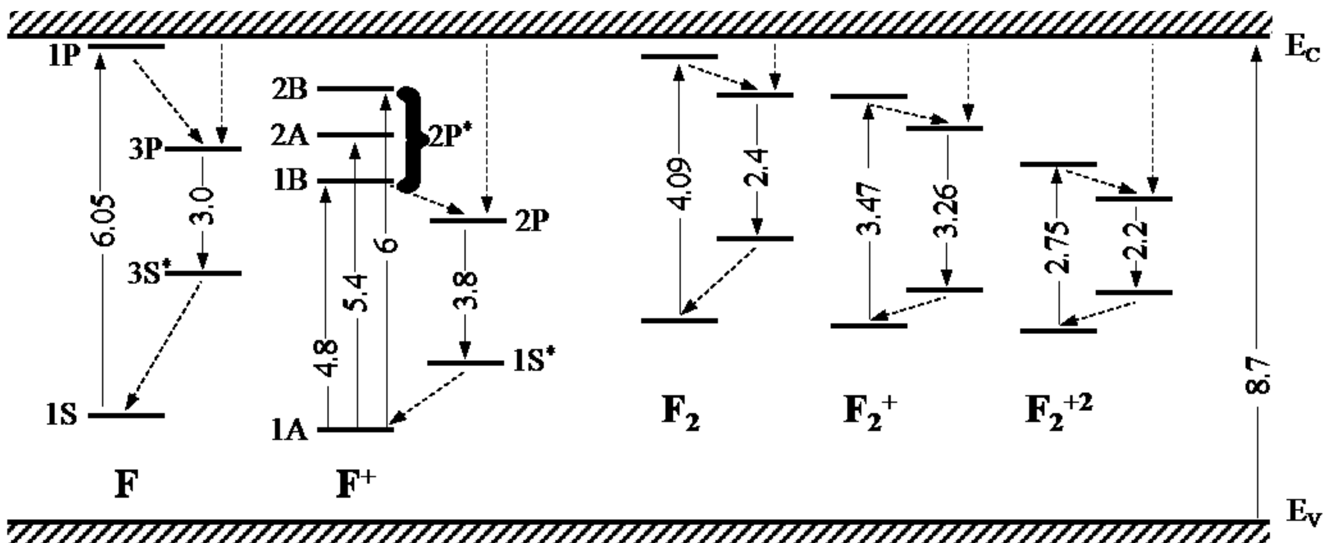

FIGURE 112 - BAND DIAGRAM OF ALUMINA SUMMARIZING THE MAIN ELECTRONIC PROCESSES FOR SINGLE (F TYPE) AND DOUBLE (F_2 TYPE) OXYGEN VACANCY [39,139]. THE NUMBERS WRITTEN VERTICALLY REFERS TO THE ENERGY VALUES EXPRESSED IN EV. REPRINTED FROM [134]

Therefore, both the absorption and the emission spectrum of aluminum oxide provide information about the density and the characteristic of the defects [41]. Aluminum oxide luminescence can also be stimulated by electron impact excitation, and emission peaks related to lattice vacancies were detected in cathodoluminescence experiments [43].

5.1.2 F-color centers dynamics

Time-resolved photoluminescence experiments allowed the determination of the lifetime of the excited states of the most common F color centers of aluminum oxide. The data, measured at room temperature, are reported in Table 7.

	Decay		Time constant according to:			
Name	Energy	Wavelength	[144]	[142]	[145]	[111]
F	3.0 eV	410 nm	25 ms	34ms	34 ms	35 ms
F^+	3.8 eV	326 nm	1.7 ns	<10 ns	2 ns	< 4.5 ns
F_2	2.4 eV	515 nm	1.6 ns	68.2 ms (@ 503 nm)	Nd	Nd
F_2^+	3.26 eV	380 nm	Nd	4.5 ns, 19 ns, 71 ns	Nd	80 ns (@ 750 nm)
F_2^{2+}	2.2 eV	560 nm	1.8 ns	Nd	Nd	9±3 ns (@ 520 nm)

TABLE 7 – REVIEW OF THE ENERGY, WAVELENGTH AND TIME CONSTANT OF THE DECAY OF EXCITED STATES OF OXYGEN VACANCIES OF ALUMINUM OXIDE ACCORDING TO THE REPORT AVAILABLE

The F color center, at room temperature, has a time constant commonly quantified in the scale of a few tens of milliseconds, due to a singlet to triplet transition. A faster decay for the F color center was also reported at 80 K with a time constant of 1.6 ns and a peak emission at 3.26 eV [40]. This component is negligible at room temperature with respect to the slow one. Both the excited states of the F^+ and F_2^{2+} colour center has a time constant of less than 10 ns, although theF_2^{2+} was not observed in some experiments. Two possible decay dynamics have been found for the F_2^+, both with time constant in the nanosecond range.

5.1.3 Objectives of the present work

The sensitivity of USEM to excited carriers in semiconductors was already proven [9,27,28]. However, no measurements were reported on insulators to my best knowledge. Nonetheless, aluminum oxide present an evident photon induced steady-state SE contrast, as reported in paragraph 3.5.1 Spatial alignment on a phosphor reference. The pump photons, with energy of 3.6 eV, cannot generate electron-hole pairs by direct or even two-photon absorption because the process requires an energy larger than the bandgap of 8.7 eV. The optical pump can, however, excite color centers related to oxygen vacancies in aluminum oxide. In this work, Ultrafast Scanning Electron Microscopy, using SE emission as a probe of the optical excitation, is proven sensitive to excited color centers, and used to measure the recovery time constant of color centers at the surface of aluminum oxide, within a depth of few nanometers.

5.2 Sample and experimental setup

The USEM experimental setup used to search for an ultrafast dynamic on aluminum oxide is similar to the one used on Si(001), previously described, with the significant variant that the SE contrast signal from the channeltron detector was frequency filtered by lock-in modulation. The filtering allowed reducing the intense detector background due to the CW component of the optically induced SE emission.

5.2.1 Pump wavelength

The experimental setup of the Ultrafast Scanning Electron Microscope delivers on the sample a laser beam with wavelength equal to 343 nm. Excitation-emission wavelength resolved contour map of aluminum oxide with oxygen vacancy is reported in Figure 113.

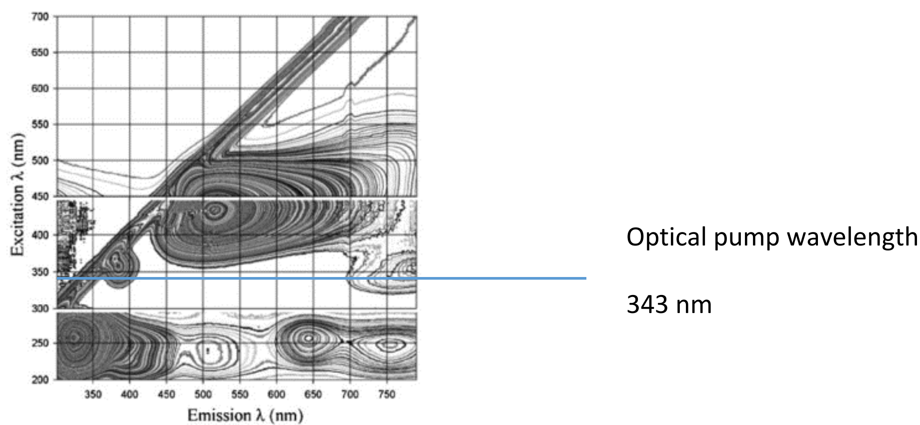

FIGURE 113 - EXCITATION-EMISSION SPECTROSCOPY ON ALUMINUM OXIDE WITH OXYGEN VACANCY. REPRINTED FROM [111]. THE BLUE LINE INDICATES THE EXCITATION WAVELENGTH USED IN THE ULTRAFAST SCANNING ELECTRON MICROSCOPY PRESENTED IN THIS THESIS

Figure 113 shows that aluminum oxide with oxygen vacancy is sensitive to the optical laser used in our Ultrafast Scanning Electron Microscopy experiment. Expected emission is at 380 nm and 780 nm, therefore, according to Figure 113 [111], the excited color centers are mainly of F_2^+ type.

5.2.2 Sample

The sample is made by a 100 nm thick layer of aluminum oxide deposited by sputtering on silicon. The chemical composition was confirmed by Auger measurements on the surface. Scanning electron microscopy images were acquired in cross section to evaluate the thickness of the layer of alumina.

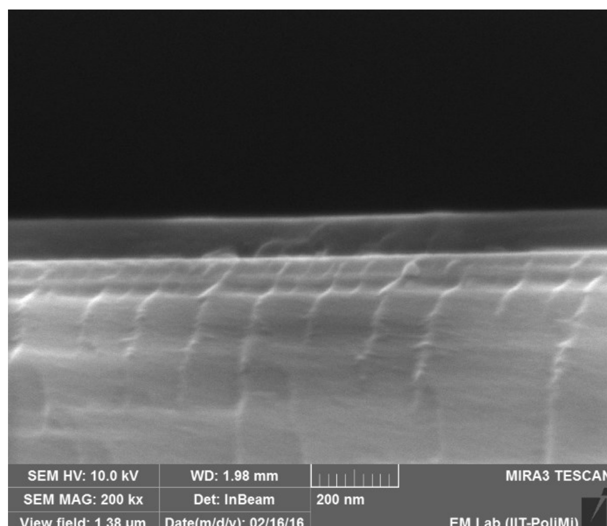

FIGURE 114 - CROSS-SECTION SCANNING ELECTRON MICROSCOPE IMAGE OF THE SAMPLE

5.2.3 Charging effects

In bulk insulators, the electrons deposited by the PE beam of a scanning electron microscope cannot discharge easily to the ground. Charges accumulation bring to sample charging until the breakdown limit is overcome and a discharge through the material takes place. The unpredictable electric fields that are generated deflects the PE beam preventing it to follow the raster scan, and the SEM image appears confused. These effects are known as charging effects [146]. Usually, in electronic systems, oxides are inserted among layers of semiconductors in heterostructures. The PE beam of an SEM is able to cross insulator layers up to few hundreds of nanometers. The excitation reduce the electrical resistance of the material towards the ground: sample neutrality is conserved, and charging effects are avoided [147].

5.2.4 Chopper and lock-in

A comparison of USEM images acquired on highly p-doped silicon and on aluminum oxide is reported in Figure 115. The images were acquired with the same viewfield equal to 393 µm, laser repetition rate equal to 10 MHz, and the same average PE current on the sample equal to 130 pA. Therefore, a time resolution of few tens of picosecond is expected. The fluence of the laser beam on the sample was set to 30 µJ/cm^2 for silicon, and to 520 µJ/cm^2 for aluminum oxide since no permanent effect was observed in exposure test.

USEM images at the surface of (001) p++ doped silicon

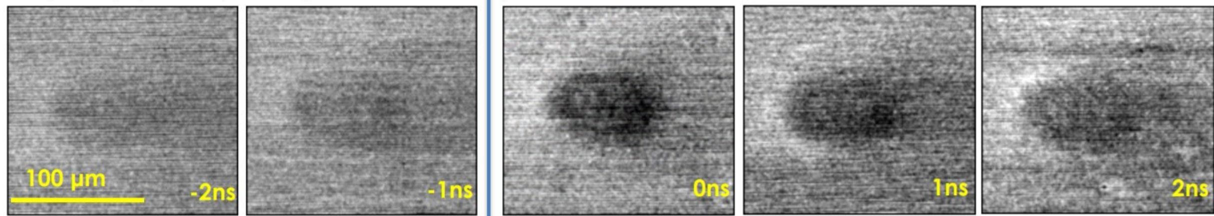

USEM images at the surface of 100 nm of aluminum oxide on silicon

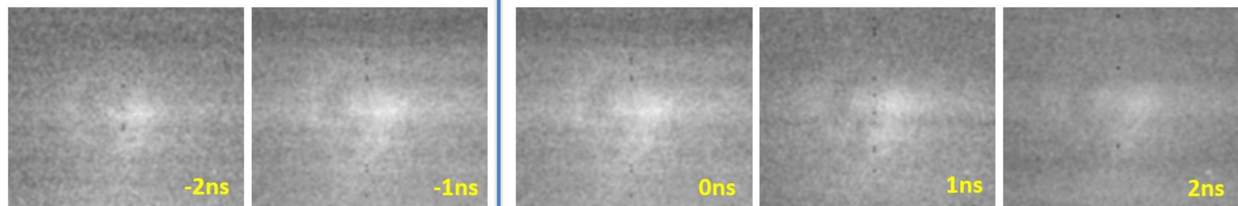

FIGURE 115 – COMPARISON OF USEM IMAGES ACQUIRED OH HIGHLY DOPED P-SILICON AND ON ALUMINUM OXIDE

The comparison of time-resolved images, reported in Figure 115 shows that the optical excitation determines a drop of the SE emission on silicon while determines almost negligible effect on aluminum oxide. The effect, discussed in paragraph 5.5.3 Stationary background, is attributed to the pile-up of the excitation due to slowly decaying color center. The intensity of the continuous background is strongly affected by instabilities on the power of the laser and, it was not possible to extract a time-resolved spectrum with a good signal to noise ratio when evaluating the differential contrast with the same algorithm used for silicon. Therefore, a heterodyne detection scheme for SE emission current, based on an optical chopper and a lock-in demodulator, was implemented. A comparison of the experimental setup of USEM and USEM with heterodyne detection is reported in Figure 116.

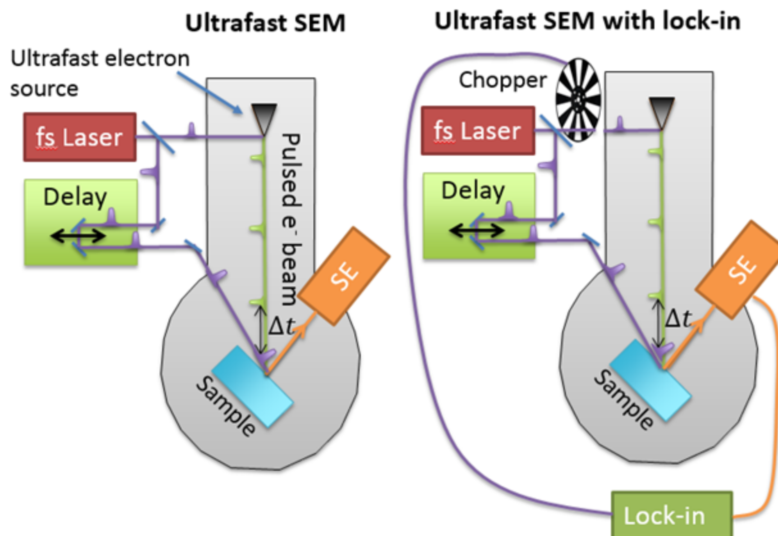

FIGURE 116 – USEM ON THE LEFT AND THE EXPERIMENTAL SETUP USED FOR MEASUREMENTS ON ALUMINA ON THE RIGHT

The continuous background is due to color centers with a lifetime longer than the time interval between two consecutive pulses of the laser, inverse of the repetition rate and equal to 100 ns. Lifetime of colors centers in aluminum oxide are reported in Table 7, and F color centers appears to be the best candidate to determine a slow pile-up, due to their lifetime of tens of milliseconds. F color centers are excited by the electron beam, since their excitation energy equal to 3 eV, is too much for the pump laser. The experimental setup of USEM allowed the possibility to install a chopper both on the optical path of the laser beam to the ultrafast electron source and to the sample. The optical chopper was installed on the optical path to the ultrafast electron source to filter the emission of electrons due to F color centers by turning it into a continuous background. In fact, they emit both when the PE beam is on, because they are excited, and when PE beam is off, because their decay time of tens of milliseconds is much longer than the duty cycle of the chopper. The operating frequency was set at around 1 kHz to avoid the mechanical resonances of the system in the frequency region between 0.7 and 0.9 kHz. The signal from the chopper was used as a reference for a lock-in used to demodulate SE signal. It was not possible to reconstruct a scanning electron microscopy images with the demodulated signal, since the maximum dwell time allowed by the microscope electronics is 25 μs while the integration time of the lock-in has to be set at least at 1 ms (a cycle of the chopper). Therefore, we chose to acquire a point signal by averaging the emission from an area of 38 μm x 41 μm inside the optically excited spot at the sample surface including the footprint of the laser excitation. The averaging was obtained by raster scanning a finite number of times the electron beam inside the area of interest. A SEM image of aluminum oxide excited by pump laser with averaging area highlighted is shown in Figure 117.

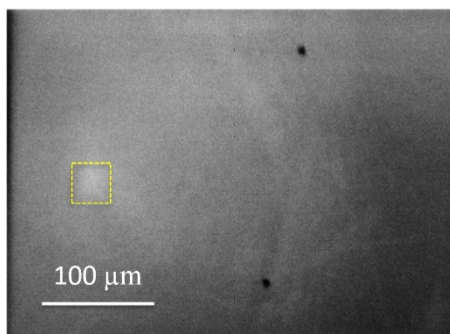

FIGURE 117 - SEM IMAGE OF ALUMINUM OXIDE EXCITED BY PUMP LASER. YELLOW RECTANGLE HIGHLIGHTS THE AVERAGING AREA

For each delay the SE signal was integrated for around 1 minute, normalized to the PE current and recorded.

5.3 Experimental data

Nineteen scans were acquired in different regions of the sample. The data acquired were:

- Normalized to the PE current;
- Normalized by the average value of the scan;

After normalization data points from different scan corresponding to the same delay were averaged. The plot of average SE current versus delay is reported in Figure 118.

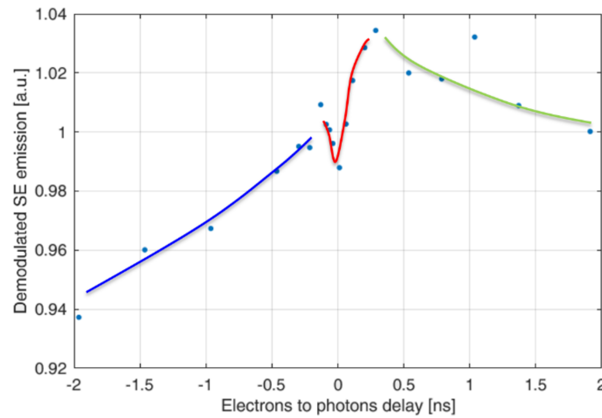

FIGURE 118 – TIME-RESOLVED DEMODULATED SE INTENSITY VERSUS ELECTRONS TO PHOTONS DELAY ON THE SURFACE OF ALUMINUM OXIDE. GREEN, RED AND BLUE CURVE HIGHLIGHT THE MAIN DYNAMICS

The physical phenomena that are suggested to determine the exponential evolution of the system are:

1. The enhancement of SE emission at zero delay and the recovery for positive delays (green curve in Figure 118);
2. The enhancement of SE emission at zero delay and the recovery for negative delays (blue curve in Figure 118);
3. The depletion of SE emission at zero delay and recovery for negative delays (red curve in Figure 118).

5.4 Data analysis

The experimental values obtained are fitted with a specific model.

5.4.1 Analytical model

The physical phenomena are fitted (see Equation 5.1) with the following exponential functions:

1. $A_1 e^{-t/\tau_1}$ for the enhancement of SE emission at zero delay and the recovery for positive delays with amplitude A_1 and time constant τ_1;
2. $A_2 e^{t/\tau_2}$ for the enhancement of SE emission at zero delay and the recovery for negative delays with amplitude A_2 and time constant τ_2;
3. $A_3 e^{-t/\tau_3}$ for the depletion of SE emission at zero delay and recovery for negative delays with amplitude A_3 and time constant τ_3.

Exponentials are multiplied by an appropriate Heaviside function (defined as $h(t) = 1$ for $t \geq 0$; $h(t) = 0$ for $t < 0$) and summed together. The step function comes from the consideration than the response of the system to the excitation time is faster than the time resolution of the system. The rising slope is therefore well approximated by a Heaviside step function centered at time zero. Then the recovery dynamic follows an exponential decay with a single time constant. The function is convolved with a Gaussian function with a standard deviation equal to σ = 24 ps attributed to the system resolution. Both temporal resolution and time zero were obtained from measurement on silicon reported in paragraph 3.7 Time resolution considering that the average PE current during the measurements done on alumina has been equal to 100 pA. Finally a constant background k, due to the usual SE emission of alumina without the illumination, is added to the expression reported in Equation 5.1.

$$f(t) = k + \left(A_1 h(t) e^{-t/\tau_1} + A_2 h(-t) e^{t/\tau_2} - A_3 h(t) e^{-t/\tau_3}\right) \otimes \left(\frac{1}{\sqrt{2\pi}\sigma} e^{-t^2/2\sigma^2}\right) \qquad (5.1)$$

The convolution of an exponential with a Gaussian has an analytical solution. The mathematical calculations are reported in Appendix E: Convolution of an exponential and a Gaussian.

5.4.2 Fitting

The fitting was performed in Matlab 2017 with the method 'NonlinearLeastSquares.' It regulates the free parameters of the trial function to minimize the distance, evaluated as least squares, from the data points. The free parameters are listed in Table 8. The algorithm requires a starting point for the value of the free parameters and allows to set a maximum and minimum value for the adjustment.

Description		**Symbol**	**Starting point**	**Minimum**	**Maximum**
Constant background	Amplitude	k	0.9	0.7	1.2
Enhancement that decays at positive delays (electrons after photons)	Amplitude	A_1	0.024	0	0.5
	Time constant	τ_1	1.5 ns	0 ns	30 ns
Enhancement that decays at negative delays (electrons before photons)	Amplitude	A_2	0.016	0	0.5
	Time constant	τ_2	0.8 ns	0 ns	60 ns
Depletion that decays at positive delays (electrons after photons)	Amplitude	A_3	-0.03	-1	0
	Time constant	τ_3	0.05 ns	0 ns	0.1 ns

TABLE 8 – LIST OF THE FREE PARAMETERS USED IN THE FITTING

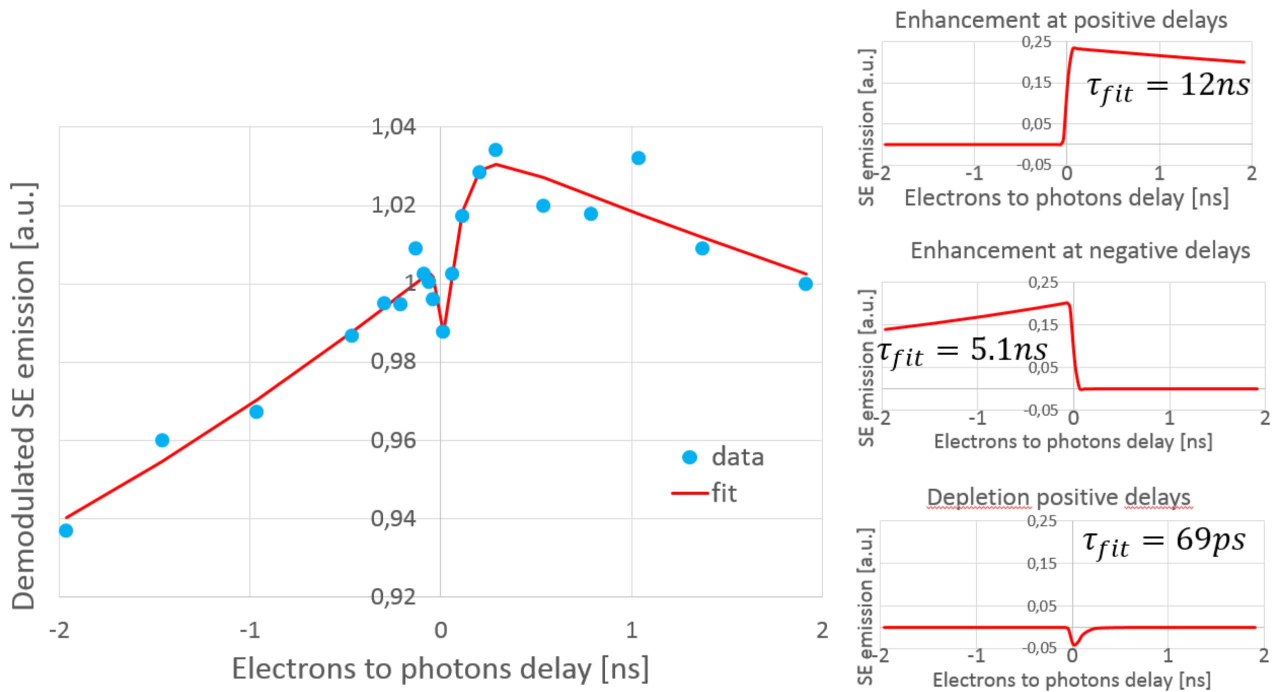

FIGURE 119 – ULTRAFAST DYNAMIC OF SE EMISSION FITTED WITH THE MODEL (ON THE LEFT) INCLUDING:

- **A CONSTANT BACKGROUND;**
- **AN ENHANCEMENT OF EMISSION AT TIME ZERO WITH EXPONENTIAL DECAY FOR POSITIVE DELAYS;**
- **AN ENHANCEMENT OF EMISSION AT TIME ZERO WITH EXPONENTIAL DECAY FOR NEGATIVE DELAYS**
- **A DEPLETION OF EMISSION AT TIME ZERO WITH EXPONENTIAL DECAY FOR POSITIVE DELAYS.**

AND CONTRIBUTION OF THE DIFFERENT PHENOMENA INVOLVED (ON THE RIGHT).

The model describes the dynamics showed by the data. The enhancement of the electron emission when the delay time approaches zero both from the negative and the positive side results in the positive values of A_1 and of A_2, while the depletion at zero in the negative value of A_3.

5.4.4 Fitting error

The optimum values estimated by the fitting model for the free parameters and the confidence bounds at 95% are reported in Table 9.

Description		Symbol	Optimum	Confidence interval at 95%	
				Minimum	Maximum
Constant background	Amplitude	k	0.8011	0.06621	1.536
Enhancement that decays at positive delays (electrons after photons)	Amplitude	A_1	0.1182	-0.2481	0.4846
	Time constant	τ_1	11.94 ns	-29.22 ns	53.09 ns
Enhancement that decays at negative delays (electrons before photons)	Amplitude	A_2	0.1022	-0.2629	0.4673
	Time	τ_2	5.115 ns	-16.9 ns	27.13 ns

	constant				
Depletion that decays at positive delays (electrons after photons)	Amplitude	A_3	-0.04209	-0.06279	-0.02139
	Time constant	τ_3	69.37 ps	15.39 ps	123.4 ps

TABLE 9 - RESULTS ESTIMATED BY THE FITTING MODEL FOR THE FREE PARAMETERS AND THE CONFIDENCE BOUNDS AT 95%

The confidence interval evaluated by the fit function is quite wide for all the parameters, probably due to the noisy data. Nonetheless, A_3 results negative with 95 % confidence, so that the fit confirms that there is a depletion at time zero, decaying at positive delays in few tens of picoseconds. The parameters describing both the amplitude and the decay of the enhancements are noisier, due to the limited delay time range available, shorter than the estimated time constant. In particular the confidence interval at 95% for both τ_1 and τ_2 spans from positive values to negative values. Since both the time constant of the decay of the enhancement were expected to be positive, further checks were done to improve the estimation of the confidence interval. The root mean square error was evaluated in dependence on the value of τ_1 in the interval from tens of picoseconds to tens of nanoseconds. The goal of fixing the value of τ_1 was obtained not setting its value as fixed but limiting the range allowed for the variable. Values lower than the optimum were obtained by limiting the upper limit while values higher than the optimum were obtained by increasing the lower limit. For each fitting the value of τ_1 obtained, and the root mean square errors were saved. The same process was repeated for τ_2 and τ_3. The dependence of the residual mean square error on the value of τ_1 and τ_2 is represented in Figure 120.

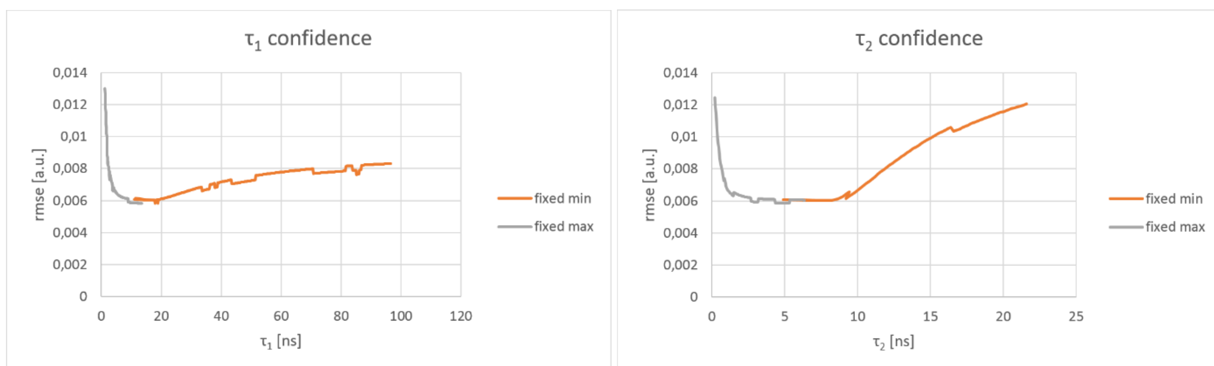

FIGURE 120 - ROOT MEAN SQUARE ERROR (RMSE) OF THE FIT VERSUS THE VALUE OF T_1 ON THE LEFT AND T_2 ON THE RIGHT

For both τ_1 , τ_2 , and τ_3 the residual mean squared error (rmse) shows a minimum corresponding to the optimal value of 0.006070. It is possible to estimate a confidence interval for both the parameter by limiting the increase of the root mean square error of the 5 %. The confidence interval results:

- τ_1 = 11.9 ns (confidence interval from 9.0 ns to 20.3 ns);
- τ_2 = 5.1 ns (confidence interval from 1.9 ns to 9.2 ns);
- τ_3 = 69 ps (confidence interval from 45 ps to 106 ps);

It is important to underline that, independently on the limit value chosen, the confidence interval for τ_1 and τ_2 cannot include negative values since the rmse diverges when approaching zero.

5.5 Theoretical model

The data show a constant background, an enhancement in SE emission that becomes stronger when approaching zero delay both from positive and from negative delays, and a dip of emission few tens of picoseconds after zero delay.

5.5.1 Enhancement at positive delays [134]

The dynamics of SE enhancement for positive time delays may be fitted with an average exponential decay with τ_1 = 12 ns. The enhancement is attributed to the increased efficiency of SE emission determined by color centers excitation. The photons of the optical pulses have energy of 3.6 eV corresponding to 343 nm and, among the known defects in alumina, they can excite only the double oxygen vacancy with one missing electron F_2^+ [39]. Two luminescence peaks are associated to it: one at 380 nm (3.26 eV) with multi-exponential decay and τ in a wide range from 4.5 ns to 71 ns [142], the other at 750 nm (1.65 eV) with a τ of 80 ns [111]. Our observed dynamics is attributed to the first relaxation channel of the excited color centers, which reduces their population and therefore the SE emission.

5.5.2 Enhancement at negative delays [134]

The dynamics of SE enhancement for negative time delays may be fitted with an exponential growth with τ_2 = 5 ns reaching the maximum at zero delay. The effect is attributable to an inversion of the role of the pump and the probe pulses with respect to what happens at positive delays: the sample is excited by the electron beam and probed by the laser. Cathodoluminescence measurements reported on alumina show that the electron beam is able to excite both F and F^+ color centers [43]; in both color centers the excited electrons are near the conduction band [39], and their reported electron affinity is lower than our pump photon energy [148]. The optical pulse may determine photoemission of excited electron of F^+ color centers acting as a probe of the excited population; in particular F^+ decay at 330 nm (3.76 eV) has a lifetime estimated to be less than or close to 7 ns [142] [149] [145], in accordance with the decay of our excited electrons.

5.5.3 Stationary background [134]

The F color centers can be either in the triplet excited state, with lifetime τ = 34 ms [142], or in the singlet state with τ estimated in less than 1.6 ns at room temperature [40]. The slow triplet decay, with a lifetime much longer than the repetition time of the laser (100 ns), can give rise to a stationary background of color centers, which is responsible for the bright spot of the long-lasting increased SE emission observed under optical excitation and seen in figure 1, middle panel. Due to the long response time of the detector, an electronic signal of "pure" photoemission would be revealed by the detector independently from the position of the electron beam on the sample, leading to an increase of the brightness of the SEM image throughout the whole field of view. Since the bright zone is limited to the laser spot area as shown in Figure 117, this shows that the enhanced electronic emission registered by the SEM image is mainly related to the electron beam that excite the color centers [43] and then the optical pulse determine the photoemission of these excited electrons.

5.5.4 Depletion at positive delays [134]

The dip in the SE around zero delay is the fastest dynamics observed, and its evolution can be fitted with a decay time of τ_3 = 70 ps, well above the experimental time resolution of the present setup. Based on a similar behavior observed on single crystal Si, we tentatively associate this feature to the dynamics of the sample surface states within a layer thinner than the typical probing depth of SE detection, which is less than 10 nm. This dynamics could arise both from the surface polarization and from the trapping of charge carriers at very shallow surface defects. As an example, charging of alumina surface due to multiphoton photoemission was already reported in literature and the decay time of the excess surface charges was measured to be 1 ps [150]. In the present case, the transient positive surface potential of the illuminated area could lead to the reduction of the SE emission.

5.6 Conclusions

An optically induced contrast was observed on a non-time-resolved SEM image of a sample made by a thin layer of aluminum oxide on silicon. The effect was attributed to a pile-up of the excitation of slowly decaying color centers pumped by the electron pulse and probed by the optical pulse. Time-resolved measurement were done with the goal of revealing the dynamics of the color center on the nanoseconds timescale. The ultrafast component of the optically-induced contrast was revealed once filtering the continuous background. A frequency shifted acquisition chain was implemented, modulating the PE beam and demodulating the SE emission by a lock-in. Ultrafast dynamics allows recognizing two excitation regimes. At positive delays, the optical pulse acts as a pump exciting electrons trapped in color center. The delayed electron pulse act as a probe since the excited population enhances the emission of SEs. The opposite happens at negative delays where the electron pulse excites electrons that are emitted by photoemission following the delayed electron pulse. Both dynamics show a time scale of the order of nanosecond. While confirming the results obtained on aluminum oxide by optical time and energy resolved techniques, the results obtained opens the road for real space-time-resolved imaging of photoexcited carrier dynamics in semiconductor and insulator heterostructures. USEM will allow to investigate surface defects and color centers of devices and structures at the nanoscale with the nm lateral and less 10 nm depth resolution typical of a SEM.

Conclusions

Ultrafast Scanning Electron Microscopy (USEM) is a novel technique that combines the spatial resolution of scanning electron microscopy with the temporal resolution typical of an ultrafast optical pump probe configuration. Such an approach allows investigating the optically excited surface dynamics, which impacts on applications in the electronic and photonic industry on the fields of energy harvesting, lighting, and sensing. On a more fundamental point of view, the technique has the potential to investigate the dynamics of charges, absorbed atoms, fields and crystal lattice at surfaces.

This thesis describes the development, commissioning and first application of a novel ultra-high-vacuum (UHV) USEM apparatus optimized for surface sensitivity. In our pump-probe setup, an UV femtosecond laser excitation pulse and a delayed picosecond electron probe pulse are spatially overlapped on the sample, triggering secondary electrons (SE) emission to the detector.

The development of the apparatus includes the realization of a novel ultrafast optically excited electron source and of the ultrafast laser setup, needed to drive the source and to optically pump the samples. The UHV conditions in the experimental chamber allow attaining unprecedented stability of the surface properties with respect to other competing apparatuses.

A thorough commissioning of the apparatus allowed to obtain the zero of the pump-probe delay and to characterize the temporal resolution down to about 5 picoseconds, which compares with the status of the art of similar applications. The delay time can span over a range of 4 nanoseconds between the optical pump pulse and the electron probe pulse. The spatial resolution of the pulsed electron beam is 80 nanometers. The experimental operating conditions were optimized for the investigation of semiconductors and insulating samples, with the use of a short wavelength photon excitation (343 nm) minimizing the absorption length.

In the case of semiconductor surfaces, time-resolved imaging allowed to scan the differential SE contrast as a function of the delay time. The investigation covered a set of six Si(001) surfaces, ranging from highly *p*-doped (10^{19} acceptors/cm^3) to highly n-doped (10^{19} donors/cm^3) samples in a regime of high photon injection (10^{19} absorbed photons/cm^3). This condition approaches the injection regime exploited in light emitting devices. A strong, nearly monotonic dependence on the doping level of the SE emission was found, which suggest a leading role of the carrier population in the contrast generation mechanism. The experimental results also show a strong dependence on the surface preparation, supporting the surface sensitivity of the technique. The dynamics evolves over several timescales ranging from tens of picoseconds up to tens of nanoseconds. A preliminary interpretation of the physics behind the contrast formation involves as main actors the dynamics of charge carriers and of trap states at the surface, which determines a change of the vacuum barrier for the emitted electrons by a band flattening mechanism.

The case of insulator surfaces was investigated by point measurements, using signal frequency modulation to filter out the continuous-wave component due to sample charging. A fast dynamics was measured on a 100 nm film of aluminum oxide on a silicon substrate, with components ranging from tens of picoseconds to few nanoseconds, that fits within the timescales typical of the ultraviolet color center evolution. The surface sensitivity of SE detection confirms the presence of active color centers at large gap insulator surfaces and broadens the field of application of USEM in todays nano-devices.

This work demonstrate several strengths of the USEM technique, including its surface sensitivity, doping sensitivity, and the possibility to characterize surfaces of very different nature like insulators. Although Ultrafast

Transmission Electron Microscopy (UTEM) has the premises to maintain a significant advantage in terms of temporal and spatial resolution, these achievements grant USEM a significant role for the investigation of surface phenomena in bulky materials and devices.

The technical perspective developments that are reasonably foreseen for our apparatus and for the technique in general, include the improvement of the temporal resolution, of the detection sensitivity, and of the spectral selectivity of the measurements. A temporal resolution below picosecond has been already demonstrated on other apparatuses at larger kinetic energies. The next challenge is reaching and maintaining sub-picosecond resolution at lower kinetic energy, between few keV and ten keV, where the SE signal from the surface is less contaminated by the contribution of backscattered electrons. At present, the sensitivity of our secondary electron detection is a couple of orders of magnitudes lower than the status of the art. Space charge effects within the electron pulse are one of the main limiting factors of the time resolution. The single electron emission regime at the electron source is the limit where to quench the space-charge effect. An improvement of about 5 orders of magnitude in detection sensitivity would be required to attain the single electron regime. Although this achievement seems far from being readily attained, large improvements are to be expected along this direction. Any improvement in the detection sensitivity would also grant both a faster acquisition, which would be largely beneficial for the stability and versatility of the technique, and an improved spatial resolution. The spectral selectivity relies on the monocromaticity and tunability of the pump pulse, which is nowadays readily available through the use of optical parametric amplifiers and oscillators.

On the scientific ground, the next steps for the application of USEM aim at widening the understanding of the differential secondary electron contrast in semiconductor and oxides. A few directions of development include the comparison of the results with other well-assessed techniques, like those used in the characterization of steady state and time-resolved transport properties in the bulk and at surfaces of semiconductors. The experimental basis should include different kinds of surfaces (high symmetry, miscut, nanostructured), of band alignment, and of semiconductor nature (band like or excitonic).

Appendix A: UED investigation of Verwey transition dynamics in magnetite

Magnetite is one of the oxides of iron with chemical composition Fe_3O_4. Crystals of magnetite could be found in nature as shown in Figure 121.

FIGURE 121 – CRYSTAL OF MAGNETITE (FROM ITALIAN ALPS)

Magnetite is the first known material with magnetic properties, discovered by the ancient Greeks. A piece of magnetite allowed to build the first compass, strongly improving the sea transport. More recently magnetite attracted the interest of scientist due to an abrupt decrease in electrical conductivity reported by Verwey when cooling below 120 K [151]. The discoverer proposed a model for the conductivity drop, but a full and widely accepted explanation of the phenomenon is still not available, even today. X-ray powder diffraction measurements proved that a structural phase transition is associated to the conductivity drop [152]. The crystalline structure was fully characterized by transmission electron diffraction measurements [153] while the mechanism have been studied by time-resolved techniques[154,155]. A pump-probe X-ray diffraction experiment also proved that:

- Verwey transition may be optically excited by heating the sample with a 800 nm laser pulse [155];
- Dynamic of the transition is of the order of few picoseconds [155].

Therefore, magnetite shows an ultrafast phase transition affecting the crystalline structure that may be excited optically. Absorption depth of the 800 nm pump wavelength is of the order of 10 nm [156], far lower than the penetration depth of X-rays. The goal of the experiment here reported was to study the dynamic of Verwey phase transition in magnetite by time-resolved electron diffraction. The main advantage of electron diffraction with respect to X-ray is the stronger surface sensitivity. The work is part of a research project of the Laboratory of Ultrafast Microscopy and Electron Spectroscopy (LUMES), directed by Prof. Carbone, at the Ecolè Polytechnique Federal de Lausanne (EPFL).

A.1 Ultrafast Electron Diffraction

Ultrafast Electron Diffraction is a time-resolved technique based on pump-probe [23]. The goal of the technique is to study lattice dynamics [71], including electron-phonon coupling[157], and phase transitions [5]. An optical pulse triggers the dynamics on the sample while a delayed electron pulse creates a diffraction pattern on a screen. The goal is to optimize temporal and reciprocal space resolution, at the expense of lateral spatial resolution. The technique was already introduced in paragraph 2.6 Diffraction contrast. The sketch of the experimental setup is reported in Figure 122 [88]. The light source is a KMLabs Wyvern Ti:sapphire amplified laser, mode-locked at a repetition rate of 20kHz. Central wavelength is 800 nm with a bandwidth of 40 nm. Pulse are 50 fs long with an energy of 700 μJ each. The output of the laser is beam splitted to generate the pump and probe beams. Pump passes through a delay stage, an optical setup with the goal to tilt the phase front with respect to propagation direction and reaches the sample perpendicularly to the surface [88]. The probe passes through a third harmonic generator and is converted into an electron beam by a transmission photocathode[22]. The beamline was designed to collect electrons emitted from the photocathode and to deliver them on the sample [22]. Electron beam hits the sample at grazing incidence, and the diffraction pattern is recorded by an intensified CCD [88].

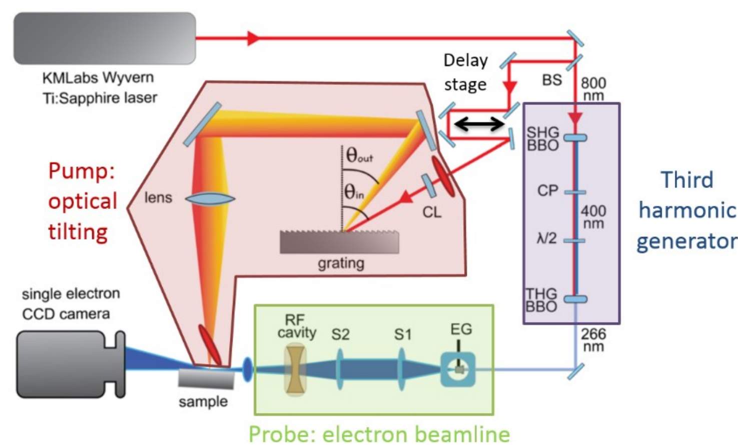

FIGURE 122 – EXPERIMENTAL UED SETUP WITH INTEGRATED OPTICAL PULSE TILTING SYSTEM, ADAPTED FROM [88]

The optical setup was designed to operate at grazing incidence [88]. The main issue is the group velocity mismatch between the electron beam and the laser beam as shown in Figure 123 panel A. Electrons are accelerated to 30 keV; their velocity is almost one third with respect to light speed in vacuum. Figure 123 panel B shows the excitation geometry at grazing incidence. Light beam hits the sample perpendicularly to the surface. Therefore, each point of the optically excited area is pumped with a negligible time spread. On the contrary, electrons arrives almost parallel to surface. Since the size of optically excited area along the direction of propagation of the electrons may be few millimeters the spread in the arrival time of the electrons may reach tens of picoseconds and cannot be neglected. The proposed solution, shown in Figure 123 panel C, consists in tilting the phase plane of the laser beam with respect to the propagation direction [88]. An optimal tilting angle was calculated to maximize the temporal superposition of the optical and electron beam on the surface of the sample, optimizing the temporal resolution [88].

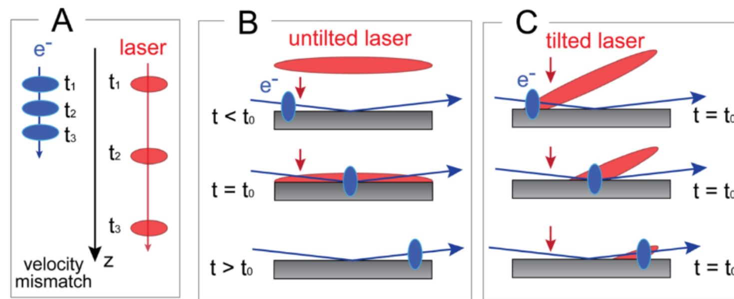

FIGURE 123 – GROUP VELOCITY MISMATCH AND TILTING PRINCIPLE, REPRINTED FROM [88]

The electronic beamline includes two magnetic lenses and a radiofrequency (RF) cavity [22]. The RF cavity allows to compensate the broadening of the electron pulse due to Coulomb repulsion[6]. The transverse size and the temporal spread of the electron pulses while propagating through the column are reported in Figure 124. Temporal spread increases while electrons are traveling from the photocathode to the cavity, then it decreases as a consequence of the effect of the cavity reaching a minimum at the sample [22]. The transverse size increases after electron emission then stabilizes thanks to a collimating solenoid [22]. The focusing solenoid grants the minimum electron spot size on the sample, also compensating the defocusing effect of the RF cavity [22]. Sample is installed on a cryogenic sample holder working with a flow of liquid helium [22].

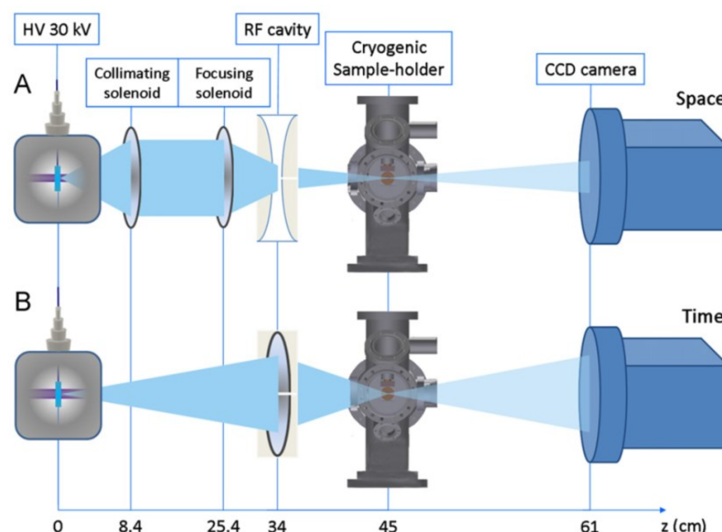

FIGURE 124 - TRANSVERSE SIZE AND THE TEMPORAL SPREAD OF THE ELECTRON PULSES WHILE PROPAGATING THROUGH THE BEAMLINE. REPRINTED FROM [22]

The full setup was tested by observing the dynamics of optically excited graphite [88]. The process studied is the energy transfer from electrons, excited by 800 nm optical pump, to strongly correlated optical phonons: one of the fastest known in condensed matter [78]. Sample was a highly oriented pyrolytic graphite while fluence was set to $6.5\ mJ/cm^2$: low enough to prevent surface dynamics induced by multiphoton photoemission [88]. Probe fluence was set to 10^5 electrons per pulse, high enough to have a good signal to noise ratio [22]. Measured rise time for the process is equal to 500 fs, assumed as an overestimation of the time resolution of the machine [88]. The results confirms the choice of RF cavity, that compensates coulumbian broadening allowing to operate with

10^5 electrons per pulse with the same temporal resolution of a single electron per pulse [22], and the correct implementation of the optical tilting system, that compensates group velocity mismatch in grazing incidence configuration [88].

A.2 Magnetite and Verwey transition

The main effect of the optical excitation at a wavelength of 800 nm on magnetite is thermal heating. If the sample is at room temperature heating determines a lattice expansion. If the temperature of the sample is below Verwey threshold, different effects may happen. At low fluences, the sample does not reach Verwey transition temperature, and lattice expansion happens. If the fluence is strong enough, Verwey transition may happen. Two different sets of measurements were done. In the first, the sample was at room temperature. Measurements of lattice expansion due to optically induced thermal heating allowed to study the dynamic of the heating and to test the full functionality of the system. In the second set of measurements, the initial temperature of the sample was set to 40 K, below the Verwey transition threshold. The effect observed depends on the dynamic of displacement of atoms during the phase transition. A comparison of the cubic cell, typical of the high-temperature phase, and the monoclinic cell, typical of the low temperature one, is shown in Figure 125.

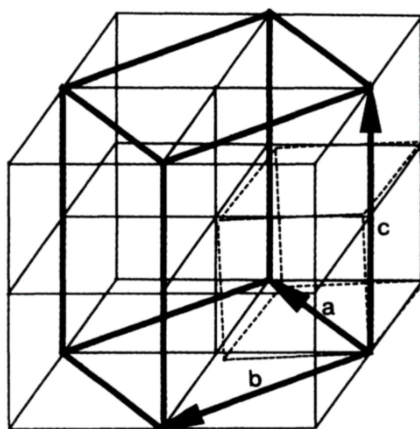

FIGURE 125 – COMPARISON OF MONOCLINIC CELL, DOUBLE LINE, WITH CUBIC CELL, DASHED LINE. REPRINT FROM [153]

The length of the edges of the monoclinic cells are reported in literature [153], while the corresponding ones of the cubic cell may be calculated from the measurement of the edge of the cube [153]. Values are reported in the Table 10.

Monoclinic (low T)			Cubic (high T)		Relative variation
Lattice parameter	Miller notation	Value	Miller notation	Value	
A	$[100]$	11.868 Å	$[110]$	11.874 Å	0.0005
B	$[010]$	11.851 Å	$[1\bar{1}0]$	11.874 Å	0.0019
C	$[001]$	16.752 Å	$[001]$	8.3963 Å	-0.4988

TABLE 10 – SIZE OF THE MONOCLINIC AND THE CUBIC CELL

The most relevant variation affects the lattice parameter c that is almost reduced to half by the transition. Nonetheless, the sample tested is a single crystal with cubic cell only in the high-temperature phase. The low-temperature phase is prepared by cooling a crystalline magnetite sample. The transition to the monoclinic structure generates a symmetry breaking and each of the three axis of the cube ($[100]$, $[010]$ and $[001]$) may be doubled becoming the c axis of the monoclinic cell [158]. The phenomenon is called twinning. Therefore, the sample in the low-temperature configuration is made by an ensemble of grains with different orientations [158]. Any crystalline axis of the high-temperature cubic phase would be projected along different crystalline directions in different grains. Electron diffraction at grazing incidence allows to observe only a limited number of Bragg spots, each one corresponding to a family of lattice planes. Bragg diffraction spot corresponding to lattice planes $(4\bar{4}0)$ of the cubic phase was observed. Due to the twinning, the low temperature phase is made of grains with different crystalline orientation. Lattice planes $(4\bar{4}0)$ of the cubic will correspond to:

- a combination of lattice planes (400) and lattice planes $(040)$of the monoclinic in one third of the grains;
- lattice planes (448) of the monoclinic in two thirds of the grains;

Lattice planes (400) and (040) of the monoclinic are perpendicular to the c-axis and therefore the interplane distance shows negligible changes because of the Verwey transition. The interatomic distance of the lattice planes (448) of the monoclinic has a component along the c-axis. In the latter case, Verwey transition determines a relevant change of the interatomic distance. When the sample is cooled Verwey transition from cubic to monoclinic determines a splitting of the Bragg spot in three parts, each describing differently oriented grains. Diffraction pattern in dependence on the temperature is reported in Figure 126. Due to limited resolution, it was not possible to resolved the splitting and a single average displacement in scattering angle was observed. During time-resolved measurement, the Verwey transition was induced by heating the sample. The measurement of the effect of the Verwey transition from low-temperature monoclinic phase to high-temperature cubic phase is an ensemble average over the different grains. The contribution of the grains were lattice planes (448) in the monoclinic becomes $(4\bar{4}0)$ of the cubic is the most relevant, due to the contraction of the interatomic plane distant component parallel to the c-axis of the monoclinic. The expected effect of the thermally induced Verwey transition in magnetite is, therefore, a contraction of the lattice.

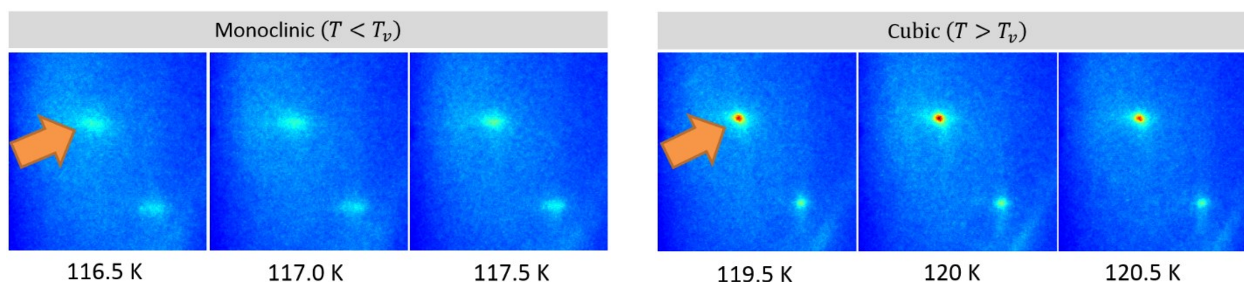

FIGURE 126 – DIFFRACTION PATTERN OF MAGNETITE IN DEPENDENCE ON TEMPERATURE, ARROW POINTS AT BRAGG DIFFRACTION SPOT CORRESPONDING TO LATTICE PLANES $(\mathbf{4\bar{4}0})$

From the diffraction pattern intensity and lattice strain were calculated. Intensity is the integral of the full volume of the peak in the plot of electrons count versus angular deviation. Intensity was normalized to 1 dividing

by the average values at far negative delays. Lattice strain was calculated from the position on the peak on the CCD, which is converted into angular deviation of the electron beam. Then angular deviation θ is related to interatomic plane distance d by Bragg diffraction formula when λ is the wavelength of the radiation used and n the order of diffraction.

$$dsen\theta = n\lambda$$

By looking at the same diffraction order with the same wavelength, depending on the electron energy, it is possible to determine a change in interatomic plane distance from a change in angular deviation.

$$d_1 sen\theta_1 = d_2 sen\theta_2$$

Approximating for small angles:

$$d_1\theta_1 = d_2\theta_2$$

Lattice strain ε may be calculated:

$$\varepsilon = \frac{d_2 - d_1}{d_1} = \frac{d_2}{d_1} - 1 = \frac{\theta_1}{\theta_2} - 1$$

A.3 Results at room temperature

Optically induced dynamic of Bragg spot corresponding to lattice planes $(4\bar{4}0)$ at room temperature is reported in Figure 127. Fluence of the optical pump is 3.65 mJ/cm^2.

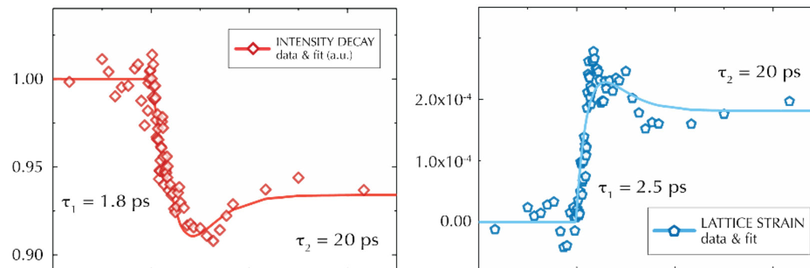

FIGURE 127 – INTENSITY AND LATTICE STRAIN VERSUS ELECTRONS TO PHOTONS DELAY AT ROOM TEMPERATURE. REPRINTED FROM [159,160]

Data reported in Figure 127 are fully compatible with a thermal expansion. A positive lattice strain confirms the expansion while the drop in intensity confirms the increase in the temperature of the crystals, according to the model proposed by Debye and Waller [161]. The model describes the effect of thermal noise on lattice structure, that reduces the number of atoms satisfying the Bragg diffraction condition affecting the intensity of the peak. The time constants might be attributed both to the rapid optically induced heating and to the following thermalization. A fluence dependence of the intensity and of the lattice strain is reported in Figure 128.

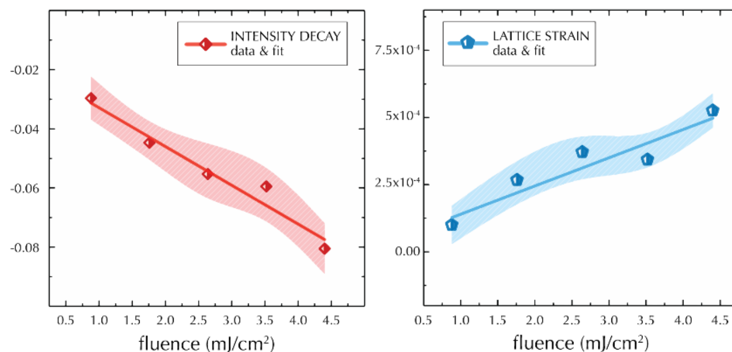

FIGURE 128 – INTENSITY AND LATTICE STRAIN VERSUS OPTICAL PUMP FLUENCE AT ROOM TEMPERATURE. REPRINTED FROM [159,160]

Data reported in Figure 128 shows a linear dependence of both intensity and lattice strain on the fluence. The result confirms that the effect observed may be attributed to a thermal expansion.

A.4 Results at temperature below Verwey threshold

Optically induced dynamic of Bragg spot corresponding to lattice planes $(4\bar{4}0)$ is reported in Figure 127. Initial temperature of the sample was set to 40 K while fluence of the optical pump is 2.28 mJ/cm^2.

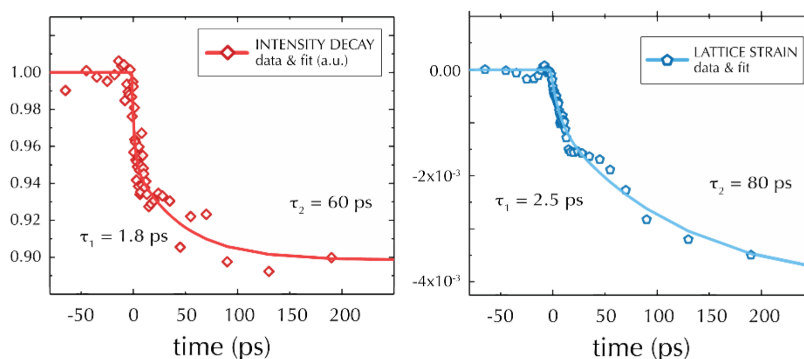

FIGURE 129 - INTENSITY, LATTICE STRAIN, AND AMPLITUDE VERSUS ELECTRONS TO PHOTONS DELAY. SAMPLE TEMPERATURE WAS BELOW VERWEY TRANSITION THRESHOLD BEFORE OPTICAL EXCITATION. REPRINTED FROM [159,160]

Data reported in Figure 129 are compatible with the optically induced Verwey transition in magnetite. The negative lattice strain confirms the contraction expected as reported in paragraph A.2 Magnetite and Verwey transition. The drop in intensity confirms the increase in the temperature of the crystals, according to the model proposed by Debye and Waller [161]. The time constants helps in understanding the dynamics of the Verwey transition in magnetite. The fastest might be attributed to a reduction of the population of frozen polarons called trimerons and the lowest to the following transition of the lattice to the high T phase, according to the model proposed by De Jong and coworkers for the dynamic of the transition [155]. A fluence dependence of the lattice strain is reported in Figure 128.

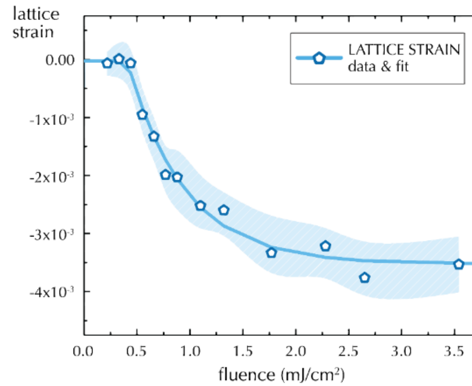

FIGURE 130 - LATTICE STRAIN VERSUS OPTICAL PUMP FLUENCE AT ROOM TEMPERATURE. SAMPLE TEMPERATURE WAS BELOW VERWEY TRANSITION THRESHOLD BEFORE OPTICAL EXCITATION. REPRINTED FROM [159,160]

Data reported in Figure 128 shows a threshold dependence of lattice strain on the fluence. The result is compatible with optically induced Verwey transition in magnetite. As already discussed in paragraph A.2 Magnetite and Verwey transition low fluence determines negligible effects while a fluence higher than a threshold value determines a contraction of the lattice, signature of the Verwey transition.

A.5 Conclusions

The time-resolved electron diffraction setup installed at EPFL by LUMES group has a temporal resolution of 500 fs in grazing incidence when operating with 10^5 electrons per pulse. The resolution obtained thanks to a specifically designed optical setup, and by an RF cavity was tested by measuring the dynamic of the optically induced phonons in graphite. The setup was used to study the dynamic of the Verwey transition in magnetite. The transition was optically induced by heating the magnetite sample with 800 nm pump. A lattice expansion was observed when the sample was at room temperature, above the threshold temperature for Verwey transition around 120 K. A lattice contraction, signature of the transition was observed when the sample temperature was below the threshold for Verwey transition. Independently on the initial temperature, an intensity drop of the Bragg spot confirmed the optical induced heating of the sample. Furthermore, the threshold fluence to photoinduce the Verwey transition was determined. The perspective is to fully understand the observed dynamics of lattice expansion and Vervey transition.

Appendix B: Data on silicon

The average of the SE emission intensity from the scan acquired on silicon samples exposed to nitrogen are reported. For each plot, the average was evaluated by averaging the results obtained point by point.

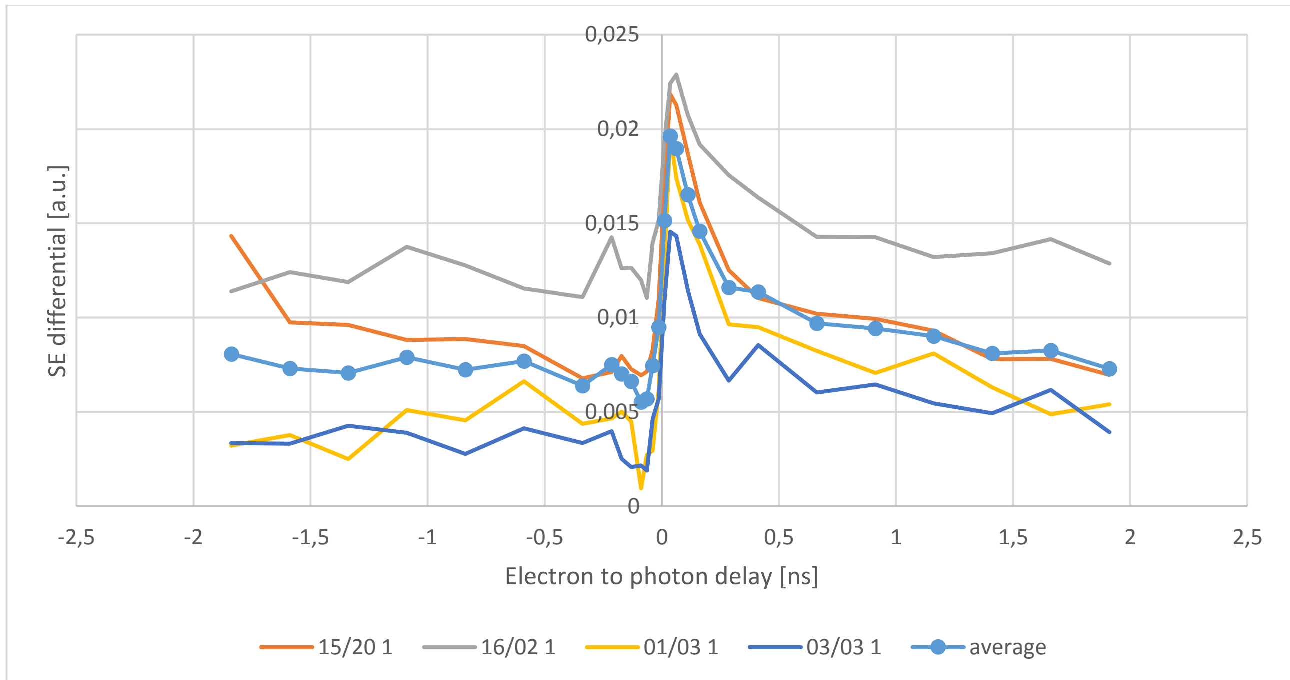

FIGURE 131 - SE EMISSION INTENSITY FROM THE OPTICALLY EXCITED AREA OF SILICON HIGHLY N-DOPED $(10^{19}\mathrm{cm}^{-3})$ VERSUS DELAY

All the scans acquired on silicon highly n-doped ($10^{19}\mathrm{cm}^{-3}$), reported in Figure 131, appears superimposed except for a vertical shift. An increased in SE emission is observed after optical excitation. Recovery is compatible with an exponential decay and a time constant of few hundreds of picoseconds.

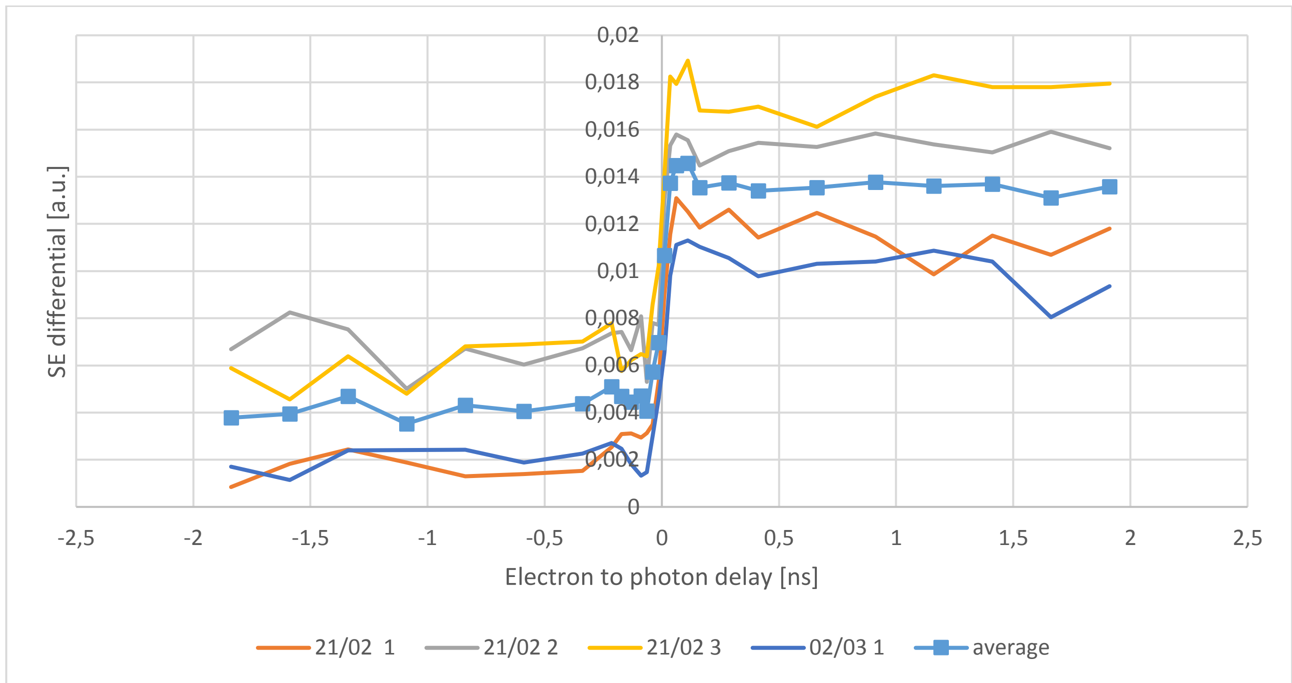

FIGURE 132 - SE EMISSION INTENSITY FROM THE OPTICALLY EXCITED AREA OF SILICON N-DOPED $(10^{15}\mathrm{cm}^{-3})$ VERSUS DELAY

All the scans acquired on silicon n-doped ($10^{15}\mathrm{cm}^{-3}$), reported in Figure 132, appears superimposed except for a vertical shift. An increase in SE emission is observed after optical excitation. A tenth of the effect is recovered by a fast process but once finished SE emission becomes constant with delay. The SE emission does not recover in 2 ns.

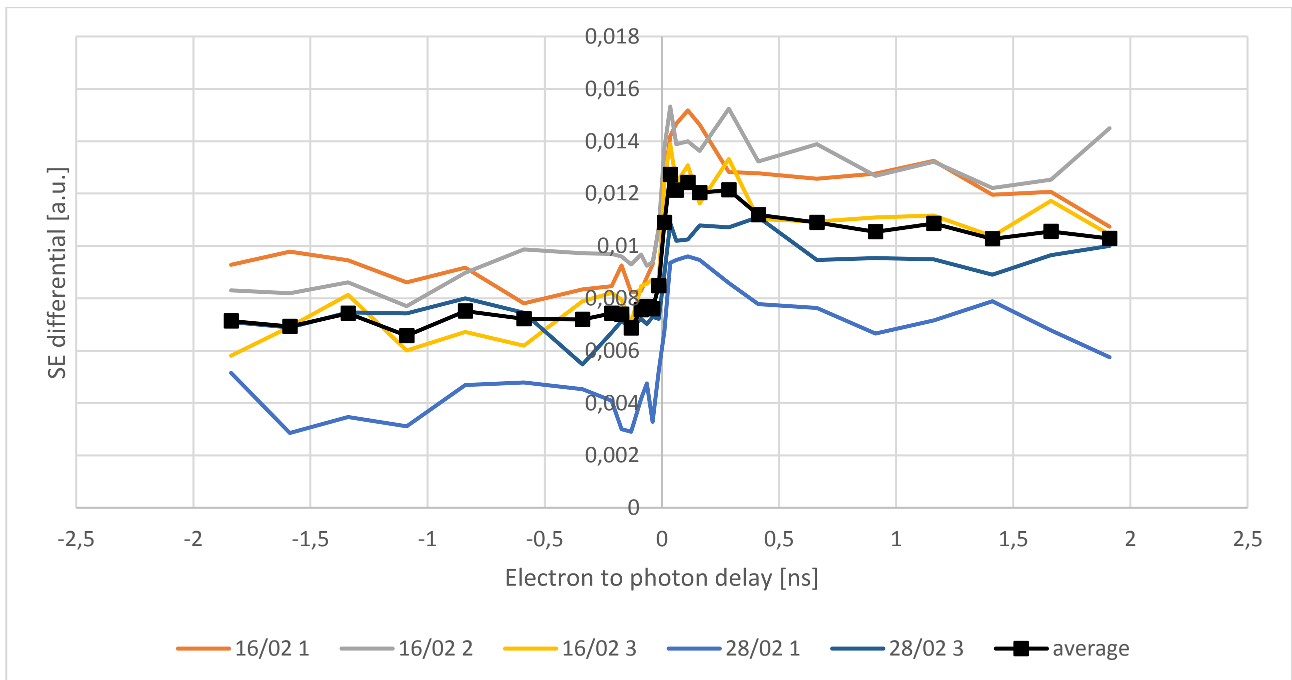

FIGURE 133 - SE EMISSION INTENSITY FROM THE OPTICALLY EXCITED AREA OF SILICON INTRINSIC $(10^{12}\mathrm{cm}^{-3})$ VERSUS DELAY

All the scans acquired on silicon intrinsic, reported in Figure 133, appears superimposed except for a vertical shift. An increase in SE emission is observed after optical excitation. Almost half of the effect is recovered with

an exponential decay with time constant of less than one nanoseconds, then the signal appears constant and does not recover in 2 ns.

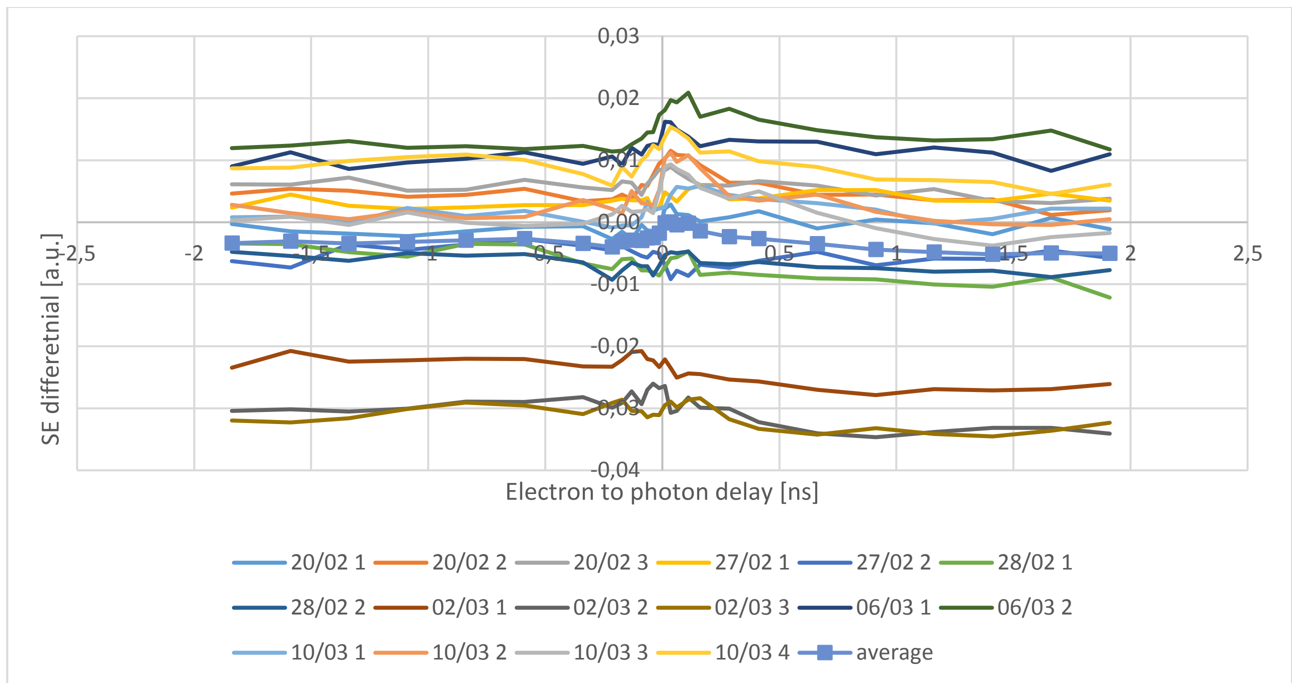

FIGURE 134 - SE EMISSION INTENSITY FROM THE OPTICALLY EXCITED AREA OF SILICON P-DOPED $(10^{15}\mathrm{cm}^{-3})$ VERSUS DELAY

The scans acquired on silicon p-doped ($10^{15}\mathrm{cm}^{-3}$), reported in Figure 134, show some variability. The vertical shift was subtracted by removing to each scan the average of the SE emission evaluated at negative delays. Then the standard deviation of the distribution of points at the same delay was evaluated.

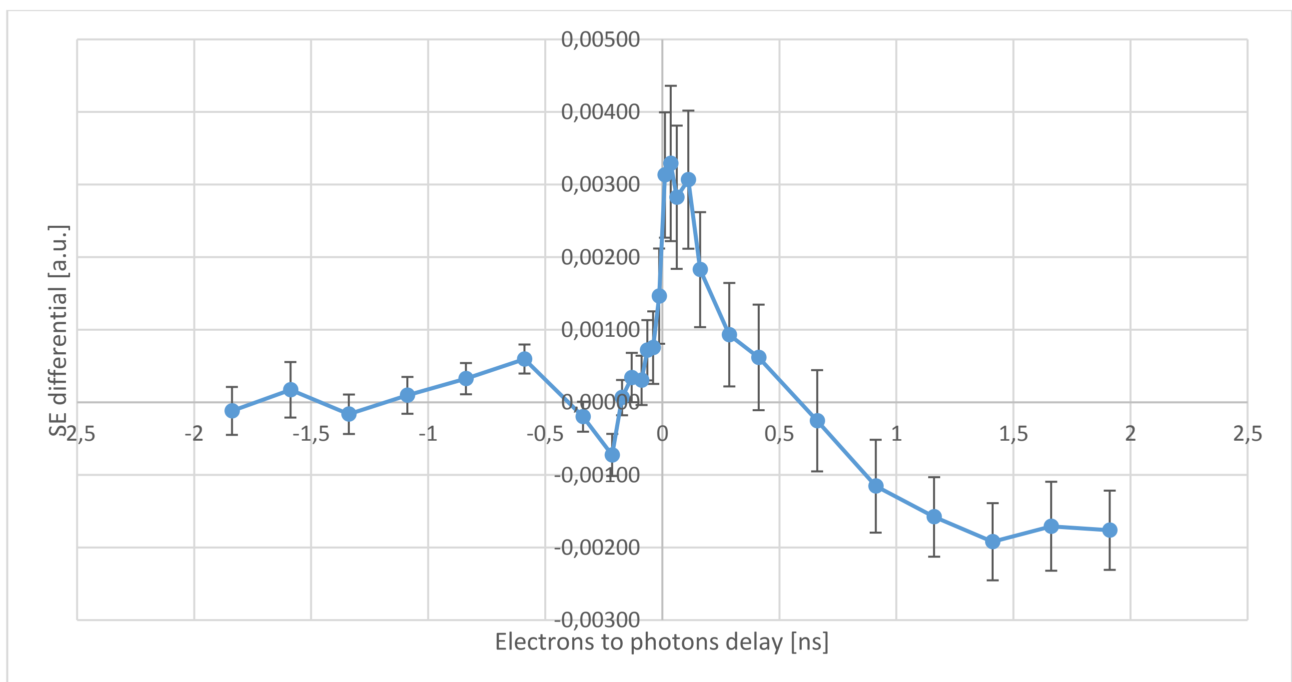

FIGURE 135 – AVERAGE SE EMISSION INTENSITY FROM THE OPTICALLY EXCITED AREA OF SILICON P-DOPED $(10^{15}\mathrm{cm}^{-3})$ VERSUS DELAY

In Figure 135 average of the signal acquired at the same delay is represented. Error bars represents, for each delay, the standard deviation of all the scans divided by the square root of number of measurements. Scans were also averaged in group of 4, chosen randomly among the 16 available, confirming the dynamic shown by the average. Optical excitation determines an increase in the SE emission followed by a recovery. The level of the SE emission at a delay equal to +2 ns appears below the one at negative delays.

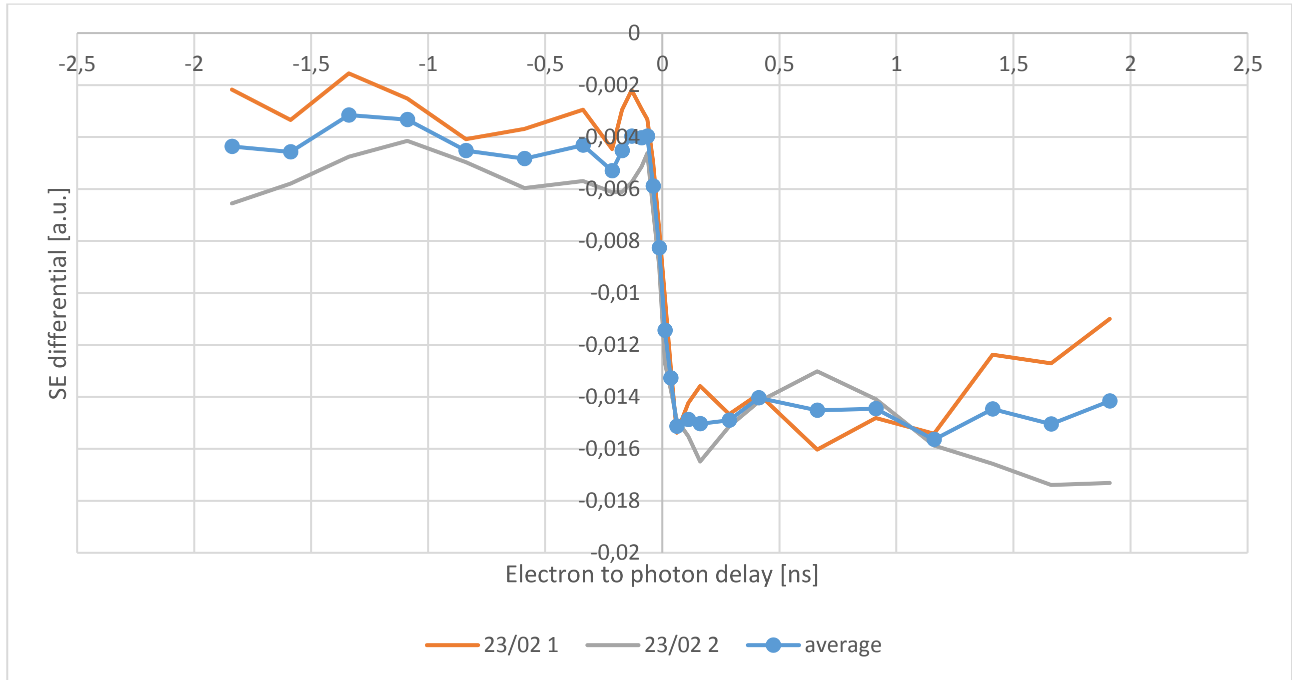

FIGURE 136 - SE EMISSION INTENSITY FROM THE OPTICALLY EXCITED AREA OF SILICON P-DOPED ($10^{17}\mathrm{cm}^{-3}$) VERSUS DELAY

All the scans acquired on silicon p-doped ($10^{17}\mathrm{cm}^{-3}$), reported in Figure 136, appears superimposed except for a vertical shift. A depletion in SE emission is observed after optical excitation. After the excitation, the signal appears constant, and no recovery is observed up to 2 ns. The dynamic is similar, but opposite of what was observed in silicon n doped ($10^{15}\mathrm{cm}^{-3}$).

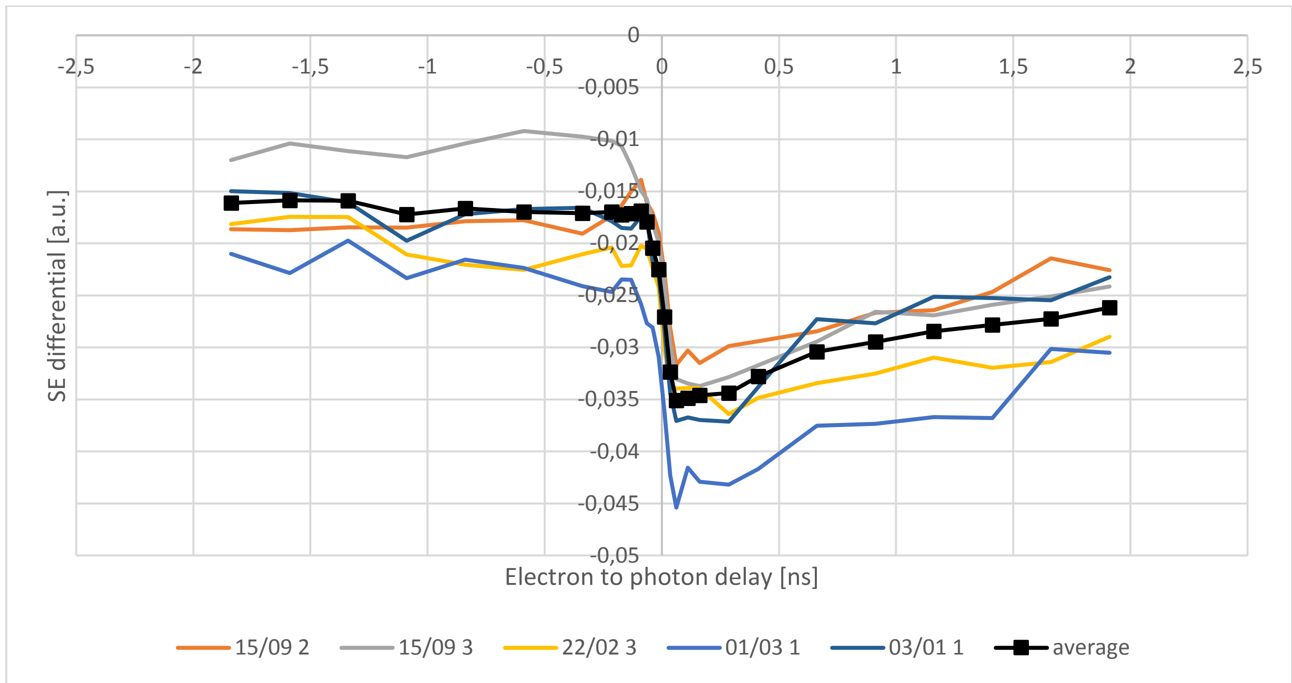

FIGURE 137 - SE EMISSION INTENSITY FROM THE OPTICALLY EXCITED AREA OF SILICON P-DOPED $(10^{19}\mathrm{cm}^{-3})$ VERSUS DELAY

All the scans acquired on silicon highly p-doped ($10^{19}\mathrm{cm}^{-3}$), reported in Figure 137, appears superimposed except for a vertical shift. A depletion in SE emission is observed after optical excitation. The effect is partially recovered with an exponential decay with time constant of the range of nanoseconds.

The average of the SE emission intensity from the scan acquired on silicon samples exposed to air for few minutes after cleaning in HF are reported. For each plot, the average was evaluated by averaging the results obtained point by point.

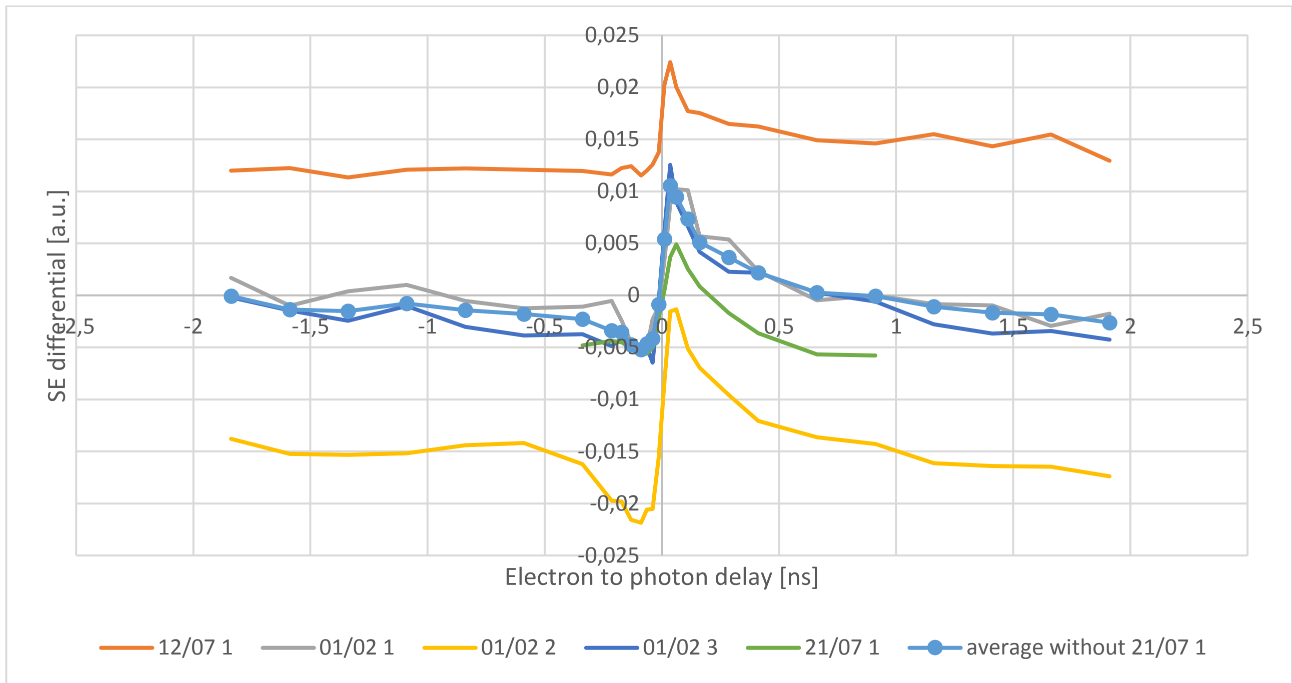

FIGURE 138 - SE EMISSION INTENSITY FROM THE OPTICALLY EXCITED AREA OF SILICON N-DOPED $(10^{19}\mathrm{cm}^{-3})$ EXPOSED TO AIR VERSUS DELAY

All the scans acquired on silicon highly n-doped ($10^{19}\mathrm{cm}^{-3}$) exposed to air, reported in Figure 138, appears superimposed except for a vertical shift. An increased in SE emission is observed after optical excitation. Recovery is compatible with an exponential decay and a time constant of few hundreds of picoseconds.

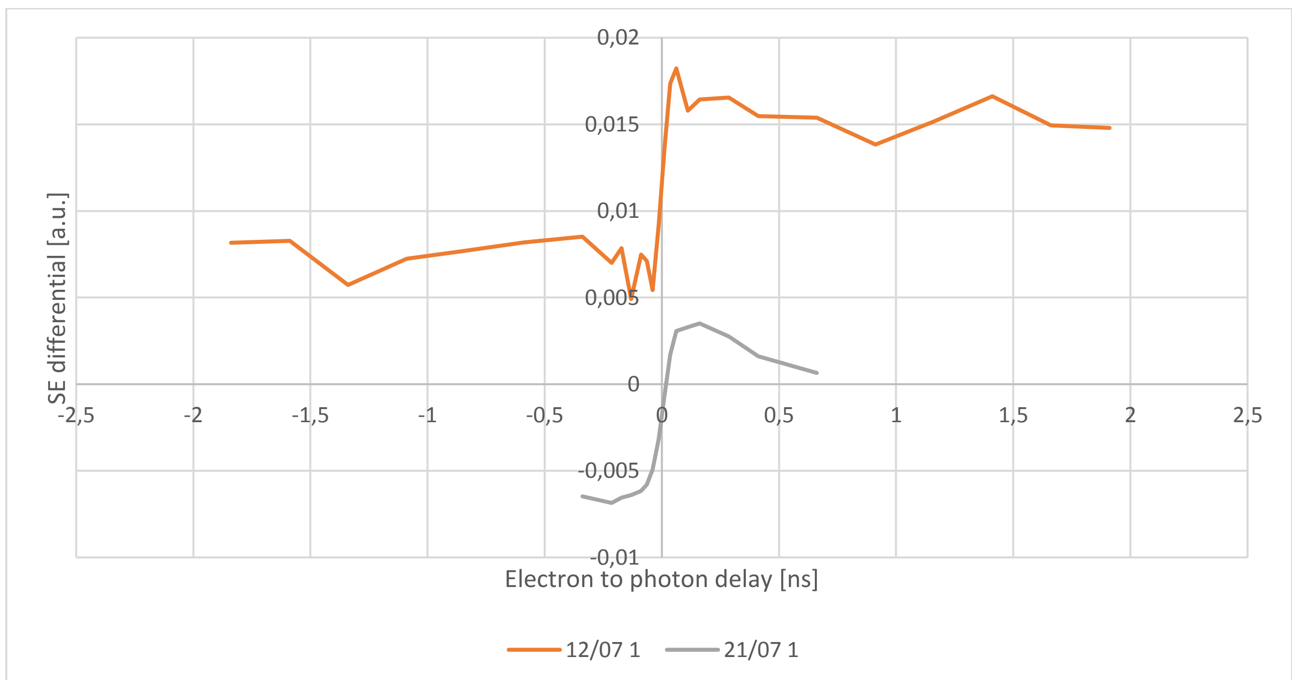

FIGURE 139 - SE EMISSION INTENSITY FROM THE OPTICALLY EXCITED AREA OF SILICON N-DOPED $(10^{15}\mathrm{cm}^{-3})$ EXPOSED TO AIR VERSUS DELAY

All the scans acquired on silicon n-doped ($10^{15}\mathrm{cm}^{-3}$), reported in Figure 139, appears superimposed except for a vertical shift. An increase in SE emission is observed after optical excitation. The effect is not recovered in 2 ns.

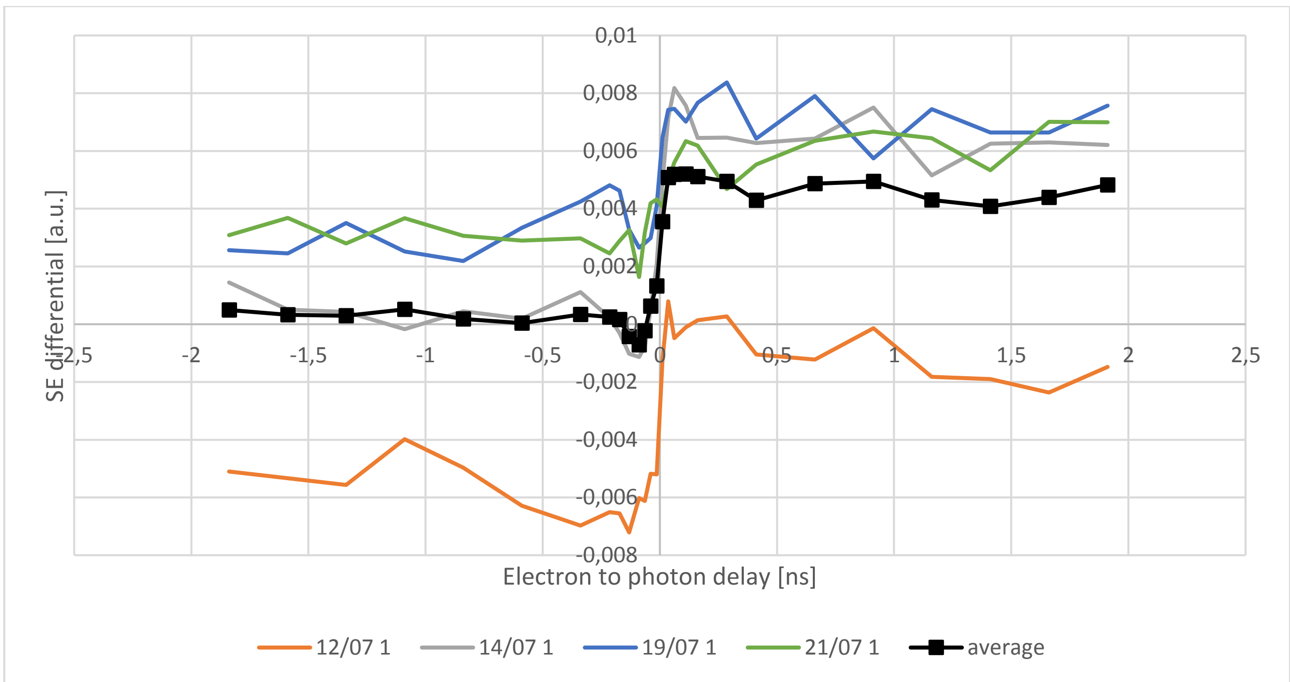

FIGURE 140 - SE EMISSION INTENSITY FROM THE OPTICALLY EXCITED AREA OF SILICON INTRINSIC ($10^{12}\mathrm{cm}^{-3}$) EXPOSED TO AIR VERSUS DELAY

All the scans acquired on silicon intrinsic, reported in Figure 140, appears superimposed except for a vertical shift. An increase in SE emission is observed after optical excitation. Almost no recovery is observed, and signal appears almost constant at positive delays.

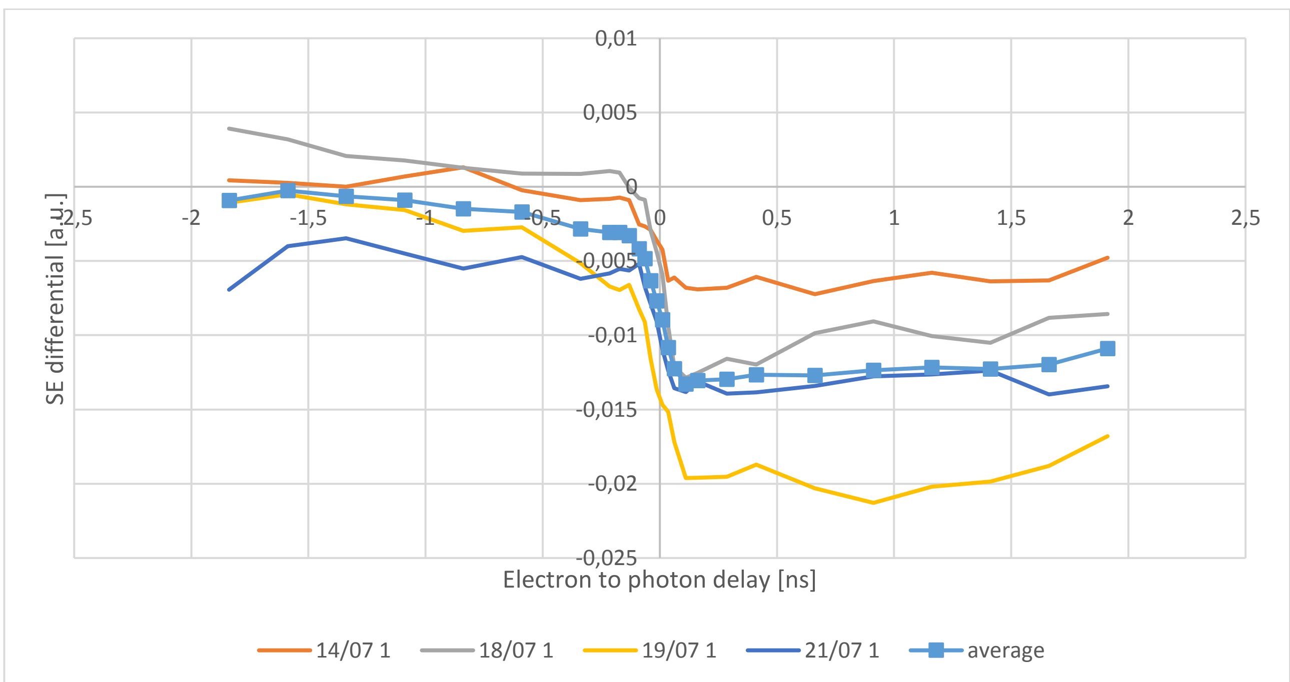

FIGURE 141 - SE EMISSION INTENSITY FROM THE OPTICALLY EXCITED AREA OF SILICON P-DOPED ($10^{15}\mathrm{cm}^{-3}$) EXPOSED TO AIR VERSUS DELAY

All the scans acquired on silicon p-doped ($10^{15}\mathrm{cm}^{-3}$), reported in Figure 141, appears superimposed except for a vertical shift. A depletion in SE emission is observed after optical excitation. Almost no recovery is observed, and signal appears almost constant at positive delays.

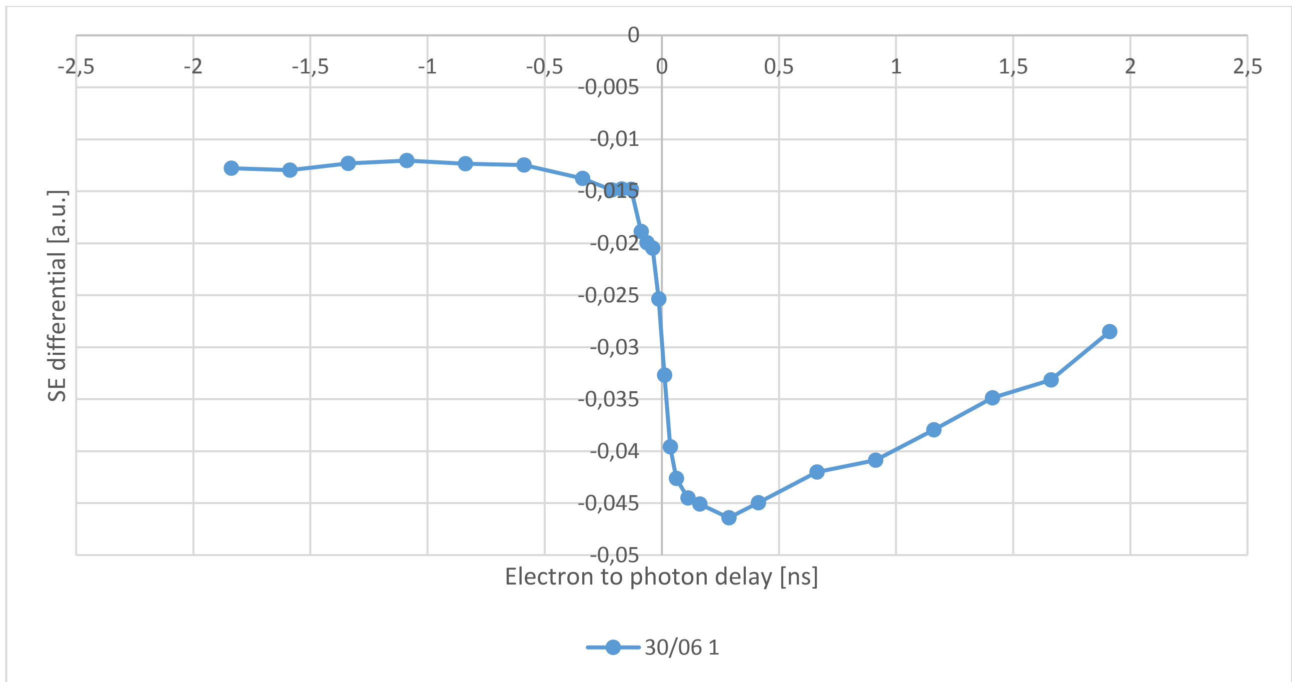

FIGURE 142 - SE EMISSION INTENSITY FROM THE OPTICALLY EXCITED AREA OF SILICON P-DOPED ($10^{17}\mathrm{cm}^{-3}$) EXPOSED TO AIR VERSUS DELAY

For silicon p-doped ($10^{17}\mathrm{cm}^{-3}$) a single scan, reported in Figure 142, is available. A depletion in SE emission is observed after optical excitation. The effect is partially recovered with an exponential decay with time constant of the range of nanoseconds.

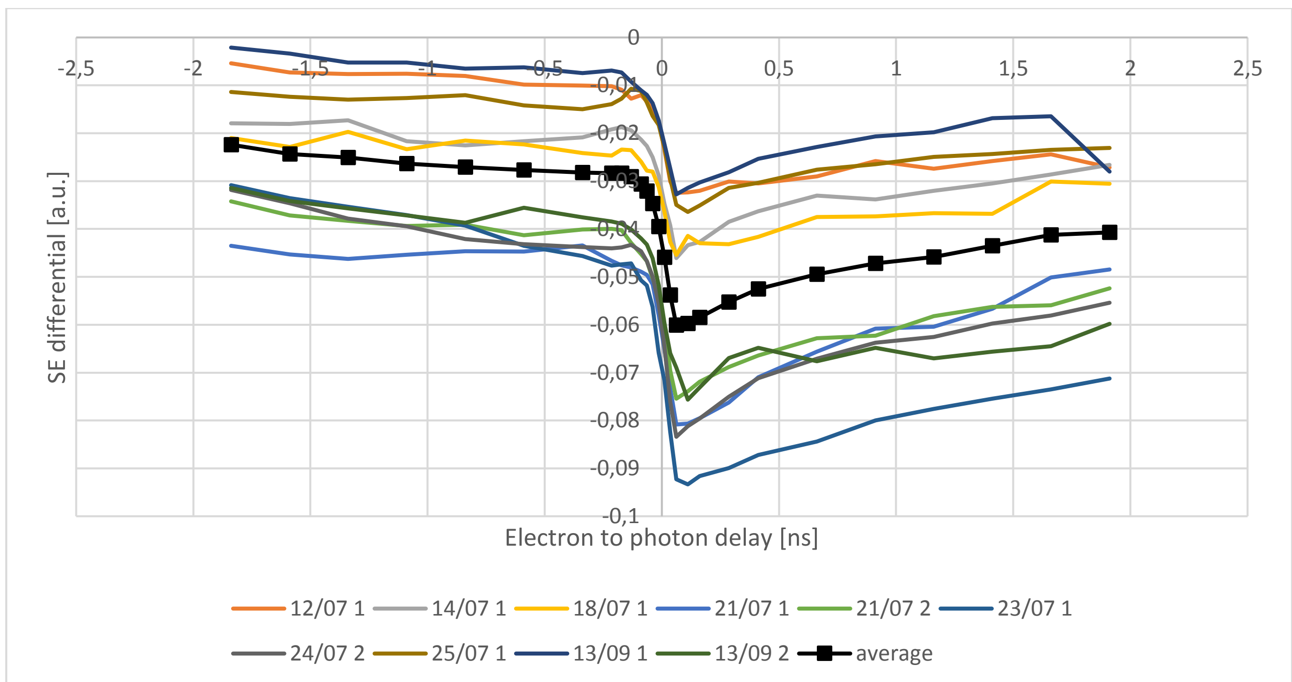

FIGURE 143 - SE EMISSION INTENSITY FROM THE OPTICALLY EXCITED AREA OF SILICON P-DOPED $(10^{19}\mathrm{cm}^{-3})$ EXPOSED TO AIR VERSUS DELAY

All the scans acquired on silicon highly p-doped ($10^{19}\mathrm{cm}^{-3}$), reported in Figure 143, appears superimposed except for a vertical shift. A depletion in SE emission is observed after optical excitation. The effect is partially recovered with an exponential decay with time constant of the range of nanoseconds.

Appendix C: fitting results

Results of the fitting are reported in Table 11 and Table 12. The doping parameter chosen is the logarithm of the electron concentration in conduction band called ‘Concentration’. For each parameter are reported:

- its best value;
- its standard error;
- the lower limit of the confidence interval at 95% (95% LCL);
- the upper limit of the confidence interval at 95% (95% UCL);
- the half-width of the confidence interval at 95% (CL Half-Width);
- the lower bound of the parameter set as input (Lower Bound);
- the upper bound of the parameter set as input (Upper Bound).

Concentration	Parameter	Value	Standard Error	95% LCL	95% UCL	CI Half-Width	Lower Bound	Upper Bound
19	y0	-0.00185	0.00198	-0.006	0.00229	0.00414	--	--
19	m0	-7.63E-04	0.00108	-0.00302	0.00149	0.00225	-0.001	0.001
19	A3	-0.00277	0.00191	-0.00677	0.00124	0.00401	--	0
19	t3	-0.3	0.4815	-1.30778	0.70778	1.00778	-0.6	-0.01
19	A2	0.00864	0.00733	-0.00671	0.02399	0.01535	--	--
19	t2	0.1855	0.15215	-0.13296	0.50396	0.31846	0.01	0.3
19	A1	0.00463	0.006	-0.00793	0.0172	0.01256	--	--
19	t1	1.14656	3.60227	-6.39308	8.6862	7.53964	0.3	30
15	y0	0.0079	0.00216	0.00337	0.01242	0.00453	--	--
15	m0	2.45E-04	0.00151	-0.00293	0.00342	0.00317	-0.01	0.01
15	A3	-0.00148	0.00202	-0.0057	0.00274	0.00422	--	--
15	t3	-0.22779	0.64841	-1.58493	1.12934	1.35714	-0.3	-0.06
15	A2	0.00251	0.00244	-0.00261	0.00762	0.00512	--	--
15	t2	0.2634	0.50601	-0.79569	1.32249	1.05909	0.06	0.3
15	A1	0.00716	0.00339	5.52E-05	0.01427	0.00711	0	--
15	t1	30	308.1283	-614.92	674.92	644.92	0.3	30
11	y0	2.00E-04	0.00113	-0.00217	0.00257	0.00237	--	--
11	m0	-1.03E-04	7.27E-04	-0.00162	0.00142	0.00152	-0.01	0.01
11	A3	-8.51E-05	9.85E-04	-0.00215	0.00198	0.00206	--	--
11	t3	-0.3	6.75804	-14.4447	13.84474	14.14474	-0.3	-0.06
11	A2	4.00E-04	7.62E-04	-0.0012	0.00199	0.00159	0	--
11	t2	0.23197	0.95428	-1.76535	2.22929	1.99732	0.06	0.3
11	A1	0.00462	0.00133	0.00184	0.0074	0.00278	--	--
11	t1	30	200.922	-390.534	450.5345	420.5345	0.3	30
5	y0	-0.00272	4.25E-04	-0.00361	-0.00184	8.89E-04	--	--
5	m0	-0.00134	3.64E-04	-0.0021	-5.76E-04	7.63E-04	-0.01	0.01
5	A3	-0.00671	0.00101	-0.00883	-0.0046	0.00212	--	--
5	t3	-0.0669	0.01893	-0.10653	-0.02726	0.03963	-0.3	-0.06
5	A2	0.00536	9.42E-04	0.00339	0.00733	0.00197	--	--
5	t2	0.06	0.02226	0.01341	0.10659	0.04659	0.06	0.3
5	A1	-0.01065	5.89E-04	-0.01188	-0.00941	0.00123	--	--
5	t1	3.66317	1.12718	1.30395	6.02239	2.35922	0.3	30
3	y0	-0.01183	0.00102	-0.01397	-0.0097	0.00214	--	--
3	m0	6.15E-04	8.04E-04	-0.00107	0.0023	0.00168	-0.01	0.01
3	A3	-0.01373	0.00132	-0.01649	-0.01096	0.00276	--	--
3	t3	-0.11973	0.02597	-0.17409	-0.06537	0.05436	-0.3	-0.06
3	A2	0.01562	0.0015	0.01248	0.01875	0.00313	--	--
3	t2	0.09581	0.02121	0.05142	0.1402	0.04439	0.06	0.3
3	A1	-0.03949	0.00131	-0.04223	-0.03675	0.00274	--	--
3	t1	2.74571	0.47393	1.75377	3.73766	0.99194	0.3	30
1	y0	-0.02995	3.84E-04	-0.03076	-0.02915	8.06E-04	--	--
1	m0	-0.00334	2.94E-04	-0.00396	-0.00272	6.18E-04	-0.01	0.01
1	A3	-0.01592	0.01907	-0.05599	0.02416	0.04007	--	--
1	t3	-0.03846	0.00646	-0.05203	-0.02489	0.01357	-0.3	-0.01
1	A2	0.02993	0.10889	-0.19884	0.25871	0.22877	--	--
1	t2	0.01588	0.00575	0.0038	0.02795	0.01208	0.01	0.3
1	A1	-0.03097	0.00119	-0.03347	-0.02847	0.0025	--	--
1	t1	1.18956	0.08081	1.01978	1.35934	0.16978	0.3	30

TABLE 11 – RESULTS OF THE FITTING FOR SILICON EXPOSED TO AIR

Concentration	Parameter	Value	Standard Error	95% LCL	95% UCL	CI Half-Width	Lower Bound	Upper Bound
19	y0	0.00679	0.00375	-0.00106	0.01463	0.00784	--	--
19	m0	-5.70E-04	0.00205	-0.00487	0.00373	0.0043	-0.001	0.001
19	A3	-9.53374E-05	0.00353	-0.00749	0.0073	0.0074	--	0
19	t3	-0.3	22.3961	-47.17557	46.57557	46.87557	-0.6	-0.1
19	A2	0.0101	0.00296	0.0039	0.0163	0.0062	--	--
19	t2	0.18289	0.07499	0.02593	0.33985	0.15696	0.01	0.3
19	A1	0.00397	0.00222	-0.000681885	0.00863	0.00466	--	--
19	t1	2.66774	13.38486	-25.3471	30.68257	28.01483	0.3	30
15	y0	0.00449	0.000402656	0.00365	0.00534	0.000842769	--	--
15	m0	3.34E-04	0.0003522	-0.000403026	0.00107	0.000737164	-0.01	0.01
15	A3	0.00198	0.0011	-0.000318419	0.00427	0.0023	--	--
15	t3	-0.06	0.0595	-0.18453	0.06453	0.12453	-0.3	-0.06
15	A2	-0.000809334	0.000925897	-0.00275	0.00113	0.00194	--	--
15	t2	0.06	0.14128	-0.23571	0.35571	0.29571	0.06	0.6
15	A1	0.00943	0.000578624	8.22E-03	0.01064	0.00121	0	--
15	t1	14.12563	12.04139	-11.07729	39.32855	25.20292	0.3	30
11	y0	7.27E-03	0.000230762	0.00678	0.00775	0.000482991	--	--
11	m0	1.21E-04	2.02E-04	-0.000302196	0.000543945	0.000423071	-0.01	0.01
11	A3	8.61E-04	5.95E-04	-0.000385235	0.00211	0.00125	--	--
11	t3	-0.06	0.07653	-0.22017	0.10017	0.16017	-0.3	-0.06
11	A2	2.39E-03	3.29E-03	-0.00449	0.00927	0.00688	0	--
11	t2	0.6	0.85956	-1.19908	2.39908	1.79908	0.06	0.6
11	A1	0.00293	0.00341	-0.00421	0.01006	0.00713	--	--
11	t1	28.79289	445.3558	-903.34751	960.93329	932.1404	0.3	30
5	y0	-0.00331	2.69E-04	-0.00388	-0.00275	5.64E-04	--	--
5	m0	-7.35789E-05	2.30E-04	-0.000554956	4.08E-04	4.81E-04	-0.01	0.01
5	A3	0.00108	0.000564056	-0.000104432	0.00226	0.00118	--	--
5	t3	-0.07043	0.07382	-0.22495	0.08408	0.15451	-0.6	-0.06
5	A2	0.01029	4.49E-02	-0.08363	0.1042	0.09392	--	--
5	t2	0.834	1.47963	-2.2629	3.93089	3.0969	0.06	1
5	A1	-0.00679	4.50E-02	-0.10091	0.08733	0.09412	--	--
5	t1	2.07443	7.88933	-14.43813	18.58699	16.51256	1	30
3	y0	-0.00417	0.000584483	-0.00539	-0.00295	0.00122	--	--
3	m0	-7.34E-05	5.11E-04	-0.00114	0.000996719	0.00107	-0.01	0.01
3	A3	-0.00356	0.00159	-0.00689	-0.000231495	0.00333	--	--
3	t3	-0.06	0.04795	-0.16037	0.04037	0.10037	-0.3	-0.06
3	A2	0.00192	0.00134	-0.000882931	0.00473	0.00281	--	--
3	t2	0.06	0.08574	-0.11945	0.23945	0.17945	0.06	0.3
3	A1	-0.01085	0.000840147	-0.01261	-0.0091	0.00176	--	--
3	t1	30	63.14115	-102.15595	162.15595	132.15595	0.3	30
1	y0	-0.01819	3.96E-04	-0.01902	-0.01736	8.29E-04	--	--
1	m0	-0.000656893	3.63E-04	-0.00142	0.000102853	7.60E-04	-0.001	0.001
1	A3	-0.00876	0.00221	-0.01338	-0.00414	0.00462	--	--
1	t3	-0.04062	0.0136	-0.06908	-0.01216	0.02846	-0.3	-0.01
1	A2	0.01224	0.00275	0.00649	0.01798	0.00575	--	--
1	t2	0.0179	0.00589	0.00558	0.03022	0.01232	0.01	1
1	A1	-0.01869	0.000532128	-0.01981	-0.01758	0.00111	--	--
1	t1	1.812	0.2407	1.30821	2.31578	0.50379	1	30

TABLE 12 – RESULTS OF THE FITTING FOR SILICON EXPOSED TO NITROGEN

Appendix D: paper on aluminum oxide [134]

Charge dynamics in aluminum oxide thin film studied by Ultrafast Scanning Electron Microscopy

Maurizio Zani [1, *], Vittorio Sala [1, 2, *], Gabriele Irde [1, 2], Silvia Maria Pietralunga [2, 3], Cristian Manzoni [3], Giulio Cerullo [1,3], Guglielmo Lanzani [1, 2], Alberto Tagliaferri [1, 2]

1) Dipartimento di Fisica, Politecnico di Milano, Piazza Leonardo da Vinci 32, Milano, Italy

2) CNST@PoliMi, Istituto Italiano di Tecnologia (IIT), Via Giovanni Pascoli 70/3, Milano, Italy

3) Istituto di Fotonica e Nanotecnologie (IFN), CNR, Piazza Leonardo da Vinci 32, Milano, Italy

* Authors contributed equally to this work

Corresponding author: maurizio.zani@polimi.it

Abstract

The excitation dynamics of defects in insulators plays a central role in a variety of fields from Electronics and Photonics to Quantum computing. We report here a time-resolved measurement of electron dynamics in 100 nm film of aluminum oxide on silicon by Ultrafast Scanning Electron Microscopy (USEM). In our pump-probe setup, an UV femtosecond laser excitation pulse and a delayed picosecond electron probe pulse are spatially overlapped on the sample, triggering SEs (SE) emission to the detector. The zero of the pump-probe delay and the time resolution were determined by measuring the dynamics of laser-induced SE contrast on silicon. We observed fast dynamics with components ranging from tens of picoseconds to few nanoseconds, that fits within the timescales typical of the UV color center evolution. The surface sensitivity of SE detection gives to the USEM the potential of applying pump-probe investigations to charge dynamics at surfaces and interfaces of current nano-devices. The present work demonstrates this approach on large gap insulator surfaces.

Keywords

USEM; Ultrafast Scanning Electron Microscopy; Aluminum oxide; SEs dynamics; Color centers charge dynamics; Lock-in detection

1. Introduction

Crystalline aluminum oxide is an excellent electrical insulator with a bandgap of 8.7 eV [1]. Thanks also to its mechanical stability and relatively low dielectric constant it was proposed as a substitute for silica in the gate oxides of metal oxide transistors [2]. It has been shown that it is possible to create oxygen vacancies in its crystalline lattice by irradiating pure crystals with heavy ions [3], neutrons [4], electrons [5], gamma rays [6] as well as by vacuum heating polycrystalline alumina powder [7]; the vacancies act as color centers, giving rise to characteristic absorption bands at energies below the bandgap [8]. The interaction of color centers with UV light makes alumina interesting also for optoelectronics applications, both in radiation detection [9] and in data storage [10, 11]. Excitation, lifetime and decay pathways of excited states of the most common oxygen vacancies in alumina have been studied by photoluminescence [12] and cathodoluminescence [13]. The development of femtosecond electron sources [14, 15] makes it now possible to study ultrafast electron dynamics by a novel technique called Ultrafast Electron Microscopy [16, 17, 18], which combines the spatial resolution of an Electron Microscope (EM) and the temporal resolution typical of an ultrafast optical pump-probe configuration: the sample is excited by two ultrashort pulses, one optical and one electronic, and the effect on typical electron microscope probes, such as SE, is measured as a function of the delay between the two pulses. The nanometer escape depth of the SE probe [19, 20] gives the potential to address dynamics at surfaces and interfaces of today's nano-scale devices, where many applications rely on the interplay between semiconductors and insulators. Measurements performed with USEM have shown that SE are sensitive to the excitation of electrons in semiconductors triggered by optical pulses [21, 22, 23], but the technique has never been applied to insulators. In this paper we report the first USEM measurement on a thin film of alumina on silicon. The introduction of an electron beam modulation and lock-in detection technique has allowed us to extrapolate the weak ultrafast electronic signal superimposed on a large electronic background. Our results show that SE dynamics can be excited both by the optical and by the electronic pulse.

2. Experimental setup and measurement technique

Our experimental setup (see Figure 1) consists of a customized commercial Scanning Electron Microscope (SEM) Perkin Elmer model PHI-660, working in Ultra High Vacuum (UHV), at 10^{-7} Pa during the present work, with the pulsed PE source driven by an ultrafast laser. The femtosecond electron source has been realized by replacing the original lanthanum hexaboride assembly with a Schottky field emission setup, where a lateral MgF_2 view-port grants the laser beam access to the tip.

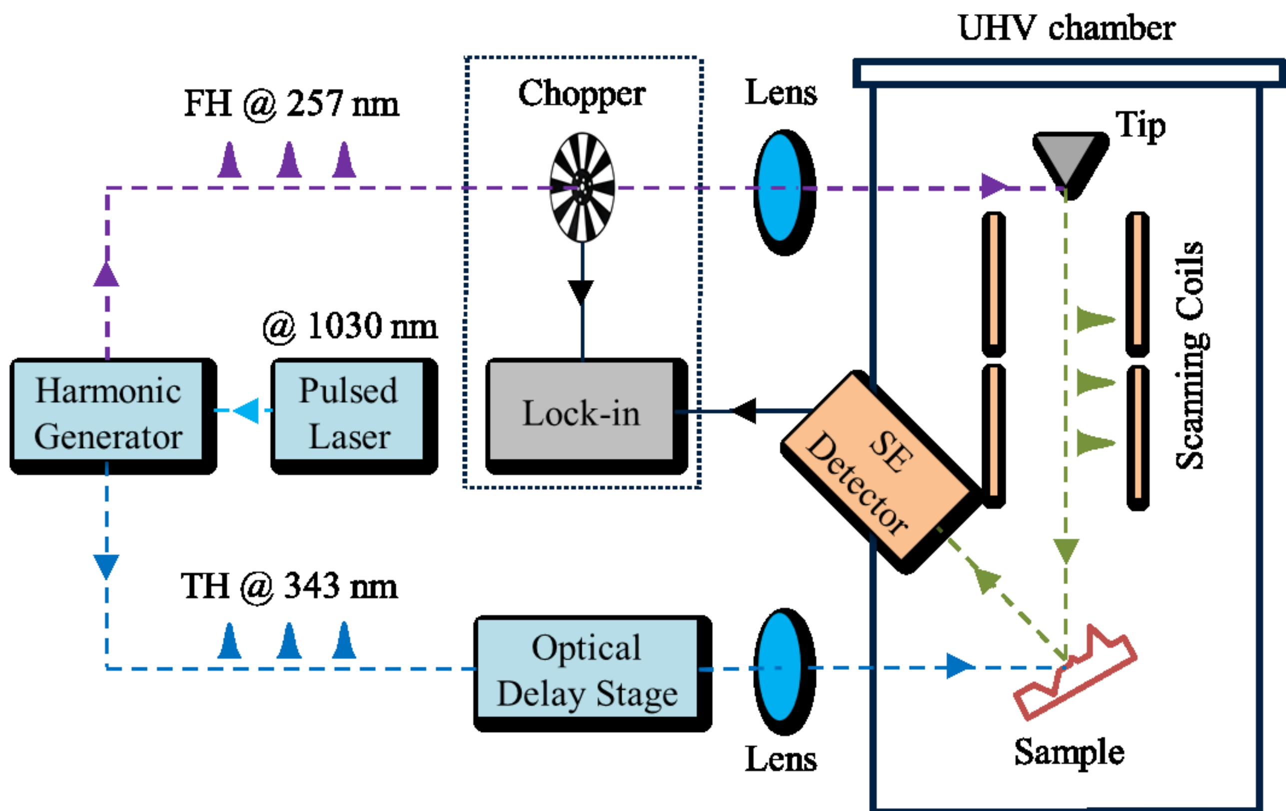

Figure 1 - Experimental setup of the apparatus. A pulsed laser beam pass through an Harmonic Generator: the Fourth Harmonic (FH) beam impinges on the tip where it photoemits electron pulses, whereas the Third Harmonic (TH) propagates through an Optical Delay Stage, which allows tuning its delay with respect to the electron pulses before reaching the sample. SE emission is collected by a channeltron based detector. A chopper and a lock-in (dotted rectangle) can be added to the apparatus in order to modulate the electron beam and suppress the continuous component of the SE signal due to the optical pulse.

We use an ultrafast fiber laser Amplitude Systèmes model Satsuma, emitting pulses at 1030 nm, corresponding to 1.2 eV photon energy, with a pulse duration of 270 fs, a repetition rate of 10 MHz and an average power of 10 W. The optical pulses are separated by a beam splitter into two synchronized arms: the first one is frequency quadrupled by a Fourth Harmonic (FH) generation

stage delivering pulses with 4.8 eV energy, that impinge on the tip and photoemit ultrafast electron pulses [15, 24]. The second arm is frequency tripled in a Third Harmonic (TH) generation stage to obtain photons with an energy of 3.6 eV, which will optically excite the sample. A fully pulsed electron beam is obtained only for tip temperature just below the thermal emission threshold; excessive tip cooling is avoided to prevent surface contamination. The electron beam generated by the source is accelerated to 10 keV, focused and raster scanned on the sample. SE emission, detected by a channeltron based detector, is recorded into SEM images. The pulsed primary current may be regulated by acting on the optical power impinging on the tip; the maximum emitted current is about 700 nA, but a large portion of the electrons is lost in the gun area and in the column, so that the maximum value achievable at the sample is 180 pA (measured by biasing the sample at +100 V), corresponding to 110 electrons per pulse. Once the current is set, the sample is grounded and the primary beam is raster scanned on the surface, while measuring SE emission.

The TH pulses are delayed with respect to the electron pulses by changing the length of the optical path through a 60 cm adjustable delay stage. The length of the optical path was set, keeping into consideration the travel time of the primary electrons into the electronic column of the microscope, in order to guarantee regulation of the delay on the sample between +2 and -2 ns. The stage is controlled by a servo motor working in closed loop with an encoder with 1 μm resolution, corresponding to a delay resolution of 6 fs. Both the optical setup and the microscope are installed on two anti-vibration tables mechanically joined to reduce oscillations that could affect pointing stability of the laser on the tip and on the sample.

Samples used are a slab of B-doped Si (100) and a thin film of aluminum oxide (100 nm) on silicon; both were cleaned by sonication in acetone and ethanol. Furthermore, bare silicon samples were immersed in 5% HF for 45 s and then in deionized water to remove native silicon oxide and passivate the surface. They were installed on the same sample holder with carbon tape and inserted in the UHV chamber through a load-lock.

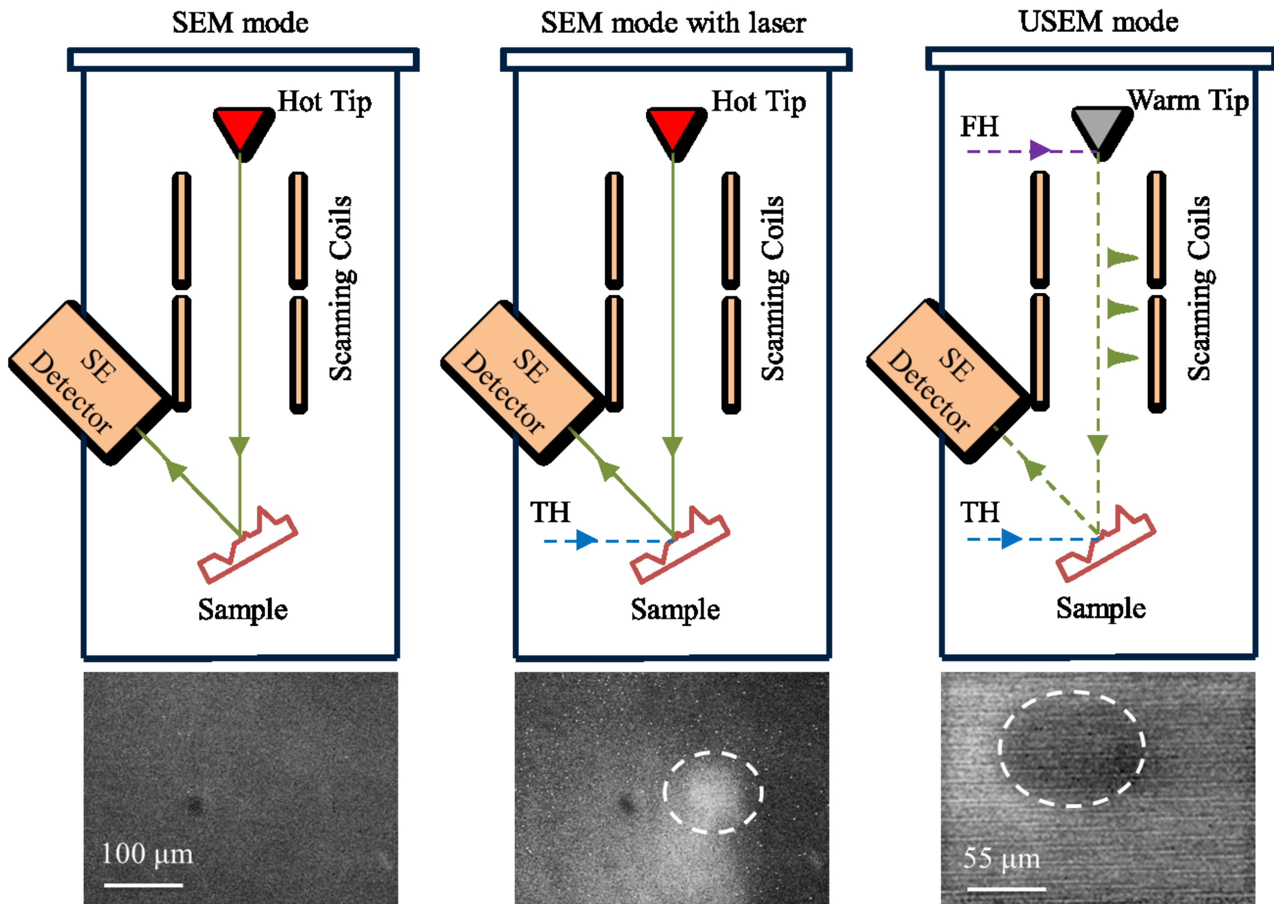

Figure 2 - Different measurement modes of the microscope:

- (left) classical SEM allows to image morphology of alumina, that appears uniform on the micrometer scale;
- (middle) effect of the laser pump on the SEM image of alumina, showing a bright zone mainly in the laser spot area (dashed line);
- (right) example of USEM image obtained on silicon pumping with pulsed UV laser and probing with 1 ns delayed pulsed electron beam. The footprint contrast, negative in this case, depends on the pump-probe delay, as it is shown hereafter.

In conventional SEM imaging, the tip is heated above the thermal emission threshold and a continuous electron beam is emitted and raster scanned over the surface of the sample. SE contrast gives information about the morphology of the surface, as reported in Figure 2 (left).

Using a continuous electron beam it's possible also to check the effect of the laser-induced contrast on the sample in real time. On alumina, the laser pump (with a fluence per pulse equal to 520 $\mu J/cm^2$) enhances SE emission in the area of the laser fingerprint as shown in Figure 2 (middle). On

silicon the optical excitation fluence had to be reduced below 30 $\mu J/cm^2$ to avoid permanent damages; nonetheless, no CW component of laser excitation was observed.

USEM images are instead obtained by optically exciting the sample and raster scanning the pulsed PE beam on an area that includes the laser spot. The SE contrast depends both on the sample morphology and on the delay between the pulses as shown in Figure 2 (right).

The lateral resolution on the uniform alumina surface is limited by the size of the optical beam spot, while the depth resolution is determined by the escape depth of SE, that is of the order of few nanometers [19, 20]. In the present work we focus on the physical mechanisms underlying the USEM contrast generation in large gap insulators, giving insight into the electron dynamics at the first atomic layers from the surface of the material; the USEM technique has thus the potential to complement the information from full optical pump-probe that has intrinsically a larger depth sensitivity and a bulkier nature.

3. Results and discussion

The SE dynamics measured on a slab of B-doped Si (100) allows to define the zero of the delay and to evaluate the effect of PE current on the time resolution of the system [25]. The dynamics obtained on silicon using different values of the electronic current is shown in Figure 3; our data show that SE emission at positive delays (electronic pulse after the optical one) decreases with respect to negative delays (optical pulse before the electronic one) as will be reported elsewhere [1], and the intensity of the SE emission jump near zero delay follows the intensity of the electronic current impinging on the sample. The optical pump-induced decrease of the SE current has been fitted with an error function to determine the effective zero in the relative delay, i.e. the position of the delay stage corresponding to optical and electronic pulses being temporally overlapped on the sample, as well as the temporal resolution of the setup determined by the duration of the electron pulse.

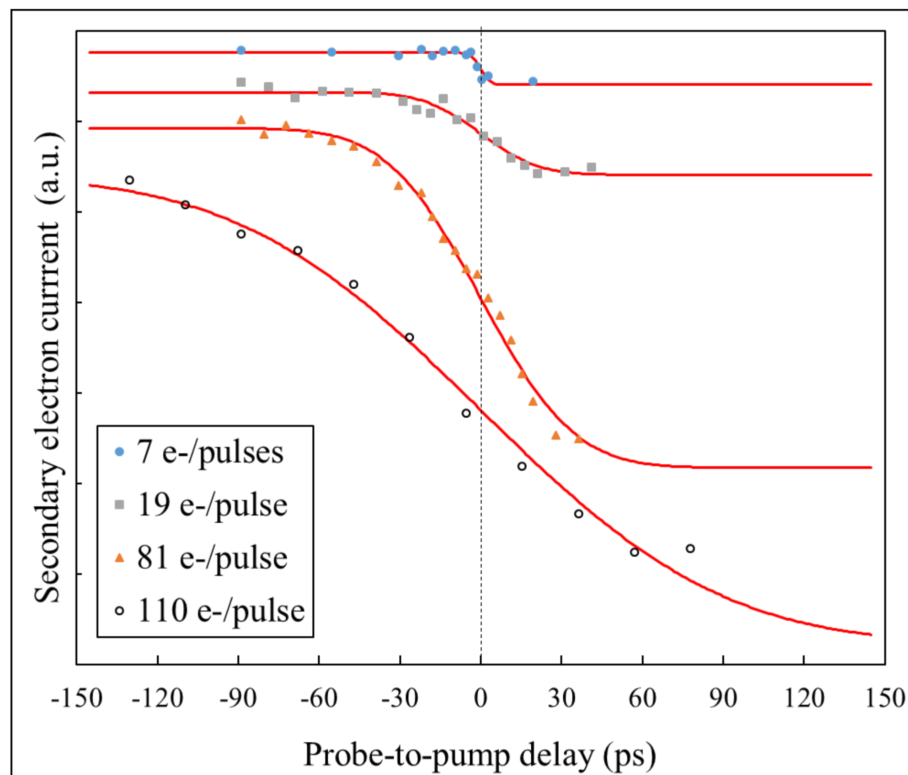

Figure 3 - Time-resolved measurement of SE current (dots) emitted from silicon near zero delay for different number of electrons per pulse. For each excitation current the error function fit (thin line) is reported.

[1] in preparation

The rise time (see Table 1) appears to be strongly dependent on the number of electrons per pulse reaching the sample; this is attributed to a broadening of the electron probe pulse along the longitudinal direction of the microscope column due to coulombian repulsion forces acting among electrons during propagation from the tip to the sample [25], which limits the time resolution of the system.

energy per pulse (nJ)	**current (pA)**	**electrons per pulse**	**rise time (ps)**	**std dev. (ps)**
6.7	180	110	120	71
3.9	130	81	46	27
0.56	30	19	28	17
0.14	11	7	5	3

Table 1 - Summary of the correspondence between (from left to right) the energy per pulse measured before the lateral view-port (the declared transmission of the view-port @ 257 nm is about 92%, and the estimated diameter of the laser beam focused on the tip is 10 μm), the primary current reaching the sample, the number of electrons per pulse, the measured rise-time from 20% to 80% of the overall signal, and the relative standard deviation of the corresponding gaussian temporal profile describing the electron pulse.

In order to disentangle the continuous component of the SE signal due to optical excitation of alumina (see Figure 2 - middle) from its ultrafast component as probed by the delayed interaction of the optical pulse with the electron pulse, a modulation technique is used. The optical beam driving the electron source is modulated using a mechanical chopper at 1.2 kHz; the PE beam, pulsed and modulated, is raster scanned only inside the area of the optically excited surface, and the SE signal is demodulated with a lock-in amplifier. For each delay, the demodulated signal is integrated for 1 minute, normalized to the PE current and recorded; the measured dynamics is reported in Figure 4.

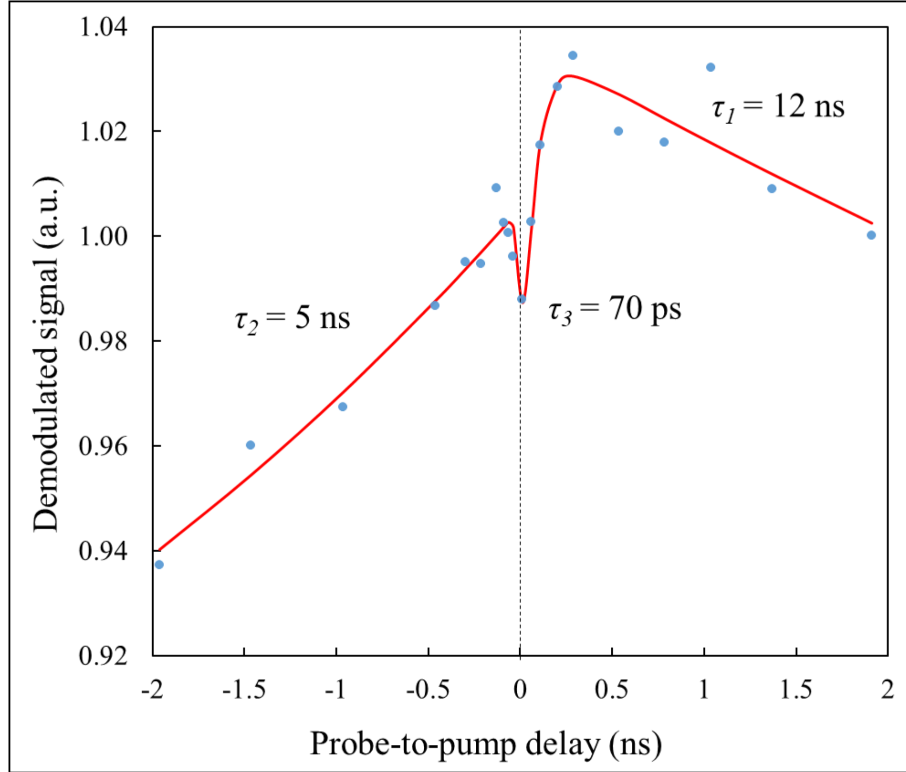

Figure 4 - Time-resolved measurement of demodulated signal (dots) acquired on aluminum oxide on silicon and relative fitting (thin line); the time constants of the different exponential functions involved in the fitting are reported. The fitting model is explained in the text.

The data show an enhancement in SE emission that becomes stronger when approaching from both the negative and the positive side the zero delay, where a dip in the emission appears. The experimental values are fitted (see Equation 1) with a constant background k (due to the usual SE emission of alumina in the absence of optical pumping) and three exponential functions multiplied by an appropriate Heaviside function (defined as $h(t) = 1$ for $t \geq 0$; $h(t) = 0$ for $t < 0$) and convolved with a gaussian function with a standard deviation equal to $\sigma = 24$ ps attributed to the system resolution (the present data were acquired using an electron beam current of 100 pA due to sensitivity reasons)

$$f(t) = k + \left(A_1 h(t) e^{-t/\tau_1} + A_2 h(-t) e^{t/\tau_2} - A_3 h(t) e^{-t/\tau_3}\right) \otimes \left(\frac{1}{\sqrt{2\pi}\sigma} e^{-t^2/2\sigma^2}\right) \qquad (1)$$

hereafter explained also using the band diagram reported in Figure 5.

- The dynamics of SE enhancement for positive time delays is fitted with an average exponential decay with $\tau_1 = 12$ ns. The enhancement is attributed to the increased efficiency

of SE emission determined by the increased availability of electrons due to the color centers excitation. Optical pulse photons have energy of 3.6 eV corresponding to 343 nm and, among the known defects in alumina, may excite only the double oxygen vacancy with one missing electron F_2^+ [10, 12]. Two luminescence peaks are associated to that: one at 380 nm (3.26 eV) with multi-exponential decay and τ in a wide range from 4.5 ns to 71 ns [7], the other at 750 nm (1.65 eV) with a τ of 80 ns [10]. Our observed dynamics is attributed to the first relaxation channel of the excited color centers, which reduces their population and therefore the SE emission.

- The dynamics of SE enhancement for negative time delays is fitted with an exponential growth with τ_2 = 5 ns reaching the maximum in zero, due to an inversion of the role of the pump and the probe pulses with respect to the positive delays: the sample is excited by the electron beam and probed by the laser. Cathodoluminescence measurements reported on alumina show that the electron beam is able to excite both F and F^+ color centers [13]; in both color centers the excited electrons are near the conduction band [12], and their reported electron affinity is lower than our pump photon energy [26]. The optical pulse may determine photoemission of excited electron of F^+ color centers acting as a probe of the excited population; in particular F^+ decay at 330 nm (3.76 eV) has a lifetime estimated to be less than or close to 7 ns [7, 27, 28], in accordance with the decay of our emitted electrons.

- The F color centers can be either in the triplet excited state, with lifetime τ = 34 ms [7], or in the singlet state with τ estimated in less than 1.6 ns at room temperature [29]. The slow triplet decay, with a lifetime much longer than the repetition time of the laser (100 ns), can give rise to a stationary background of excited color centers, which is responsible for the bright spot of the long-lasting increased SE emission observed under optical excitation and seen in Figure 2, middle panel. Due to the long response time of the detector, an electronic signal of "pure" photoemission would be revealed by the detector independently from the position of the electron beam on the sample, leading to an increase of the brightness of the SEM image throughout the whole field of view. Since the bright zone is limited to the laser spot area, this shows that the enhanced electronic emission registered by the SEM image is mainly related to the combined effect of the electron beam that excites the color centers [13] and the optical pulse that determines the photoemission of these excited electrons.

- The dip in the SE around zero delay is the fastest dynamics observed and its evolution can be fitted with a decay time of τ_3 = 70 ps, well above the experimental time resolution of the present setup. Based on a similar behavior observed on single-crystal Si [2], we tentatively associate this feature to the dynamics of the sample surface states within a layer thinner than the typical probing depth of SE detection, which is less than 10 nm. This dynamics could arise both from the surface polarization and from the trapping of charge carriers at very shallow surface defects. As an example, charging of alumina surface due to multiphoton photoemission was already reported in literature and the decay time of the excess surface charges was measured to be 1 ps [30]. In the present case, the transient positive surface potential of the illuminated area could lead to the reduction of the SE emission.

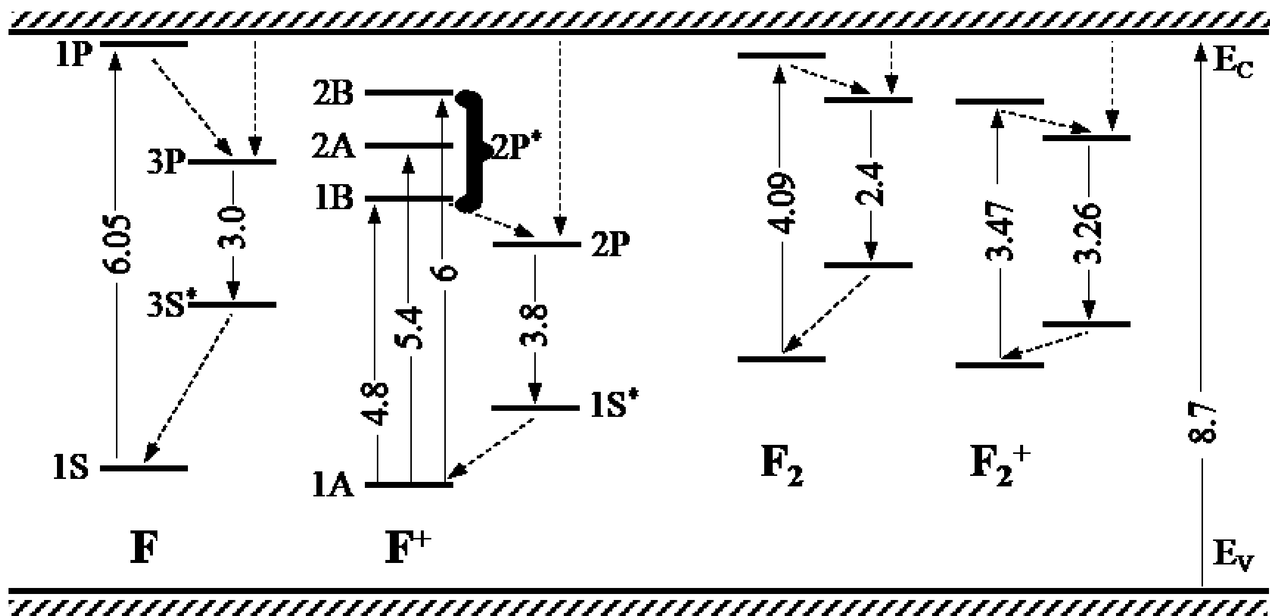

Figure 5 - Band diagram of alumina summarizing the main electronic processes for single (F type) and double (F_2 type) oxygen vacancy [3, 12]. The numbers written vertically refers to the energy values expressed in eV.

[2] in preparation

4. Conclusions

This paper reports on an USEM working in UHV and combining a pulsed electron beam excitation with an optical pulse. The effect on the SEM image of a laser excitation of a thin layer of alumina on silicon was observed. By exploiting a lock-in demodulation technique, it was possible to extrapolate the weak ultrafast electronic signal superimposed on a remarkably slow electronic background in the laser spot area, due to the optical pulse that excites electrons to energy levels with a lifetime much longer than the repetition time of the experiment. The time resolved measurement on alumina allows recognizing two excitation regimes, in which the optical pulse and the electron pulse proved to be able to act either as a pump or a probe, giving rise to dynamics of the order of nanoseconds, compatible with the electron dynamics in color centers; moreover, we find a faster dynamics on the tens of picoseconds, that is tentatively associated to dynamics at the first atomic layers from the surface, which can be effectively accessed thanks to the nanometers depth resolution of the USEM technique. While confirming the results obtained on other insulators, our study opens the road for real space time-resolved imaging of photoexcited carrier dynamics in semiconductor and insulator heterostructures; the technique will perspectively allow to investigate surface defects and color centers of devices and structures at the nanoscale with the nm lateral and less 10 nm depth resolution typical of a SEM.

Acknowledgments

The authors are thankful to Stefano Perugini, 2M Strumenti, for providing the alumina sample.

References

[1] S. Ciraci, and I. P. Batra, "Electronic structure of α-alumina and its defect states", Physical Review B **28**, 2, 982-992 (1983), https://doi.org/10.1103/PhysRevB.28.982

[2] J. Kolodzey, E. A. Chowdhury, T. N. Adam, G. Qui, I. Rau, J. O. Olowolafe, J. S. Suehle, and Y. Chen, "Electrical Conduction and Dielectric Breakdown in Aluminum Oxide Insulators on Silicon", IEEE Transactions on Electron Devices **47**, 1, 121-128 (2000), https://doi.org/10.1109/16.817577

[3] Y. Song, C. H. Zhang, Z. G. Wang, Y. M. Sun, Y. L. Duan, and Z. M. Zhao, "Photoluminescence of inert-gas ion implanted sapphire after 230-MeV Pb ion irradiation", Nuclear Instruments and Methods in Physics Research B **245**, 1, 210-213 (2006), https://doi.org/10.1016/j.nimb.2005.11.134

[4] M. Izerrouken, and T. Benyahia, "Absorption and photoluminescence study of Al2O3 single crystal irradiated with fast neutrons" Nuclear Instruments and Methods in Physics Research B **268**, 19, 2987-2990 (2010), https://doi.org/10.1016/j.nimb.2010.05.024

[5] B. D. Evans, "A review of the optical properties of anion lattice vacancies, and electrical conduction in Al_2O_3: their relation to radiation-induced electrical degradation", Journal of Nuclear Materials **219**, 202-223 (1995), https://doi.org/10.1016/0022-3115(94)00529-X

[6] V. S. Kortov, V. A. Pustovarov, S. V. Zvonarev, and T. V. Shtang, "Luminescence and radiation-induced color centers in anion-defective alumina crystals after high-dose irradiation", Radiation Measurements **90**, 90-93 (2016), https://doi.org/10.1016/j.radmeas.2016.01.010

[7] M. Itou, A. Fujiwara, and T. Uchino, "Reversible photoinduced interconversion of color centers in α-Al_2O_3 prepared under vacuum", Journal of Physical Chemistry C **113**, 49, 20949-20957 (2009), https://doi.org/10.1021/jp908417m

[8] P. W. Levy, "Color Centers and Radiation-Induced Defects in Al_2O_3", Physical Review **123**, 4, 1226-1233 (1961), https://doi.org/10.1021/jp908417m

[9] V. S. Kortov, S. V. Zvonarev, A. N. Kiryakov, and D. V. Ananchenko, “Dosimetric phosphor based on oxygen-deficient alumina ceramics”, Radiation Measurements **90**, 196-200 (2016), https://doi.org/10.1016/j.radmeas.2016.02.015

[10] M. S. Akselrod, A. E. Akselrod, S. S. Orlov, S. Sanyal, and T. H. Underwood, “Fluorescent aluminum oxide crystals for volumetric optical data storage and imaging applications”, Journal of Fluorescence **13**, 6, 503-511 (2003), https://doi.org/10.1023/B:JOFL.0000008061.71099.55

[11] Y. Seung-Won, S. Sang-Chul, K. Tan-Young, H. J. Hyeon, L. Yun-Hi, S. W. Jae, and J. Byeong-Kwon, “Transparent resistive switching memory using aluminum oxide on a flexible substrate”, Nanotechnology **27**, 7, 1 (2016), https://doi.org/10.1088/0957-4484/27/7/07LT01

[12] B. D. Evans, G. J. Pogatshnik, and Y. Chen, “Optical properties of lattice defects in α-Al_2O_3”, Nuclear Instruments and Methods in Physics Research B **91**, 1-4, 258-262 (1994), https://doi.org/10.1016/0168-583X(94)96227-8

[13] E. C. Kouroukla, I. K. Bailiff, I. Terry, and L. Bowen, “Luminescence characterisation of alumina substrates using cathodoluminescence microscopy and spectroscopy”, Radiation Measurements **71**, 117-121 (2014), https://doi.org/10.1016/j.radmeas.2014.03.018

[14] K. Bücker, and M. Picher, O. Crégut, T. LaGrange, B. W. Reed, S. T. Park, D. J. Masiel, and F. Banhart, “Electron beam dynamics in an ultrafast transmission electron microscope with Wehnelt electrode”, Ultramicroscopy **171**, 8-18 (2016), https://doi.org/10.1016/j.ultramic.2016.08.014

[15] C. Ropers, D. R. Solli, C. P. Schulz, C. Lienau, and T. Elsaesser, “Localized Multiphoton Emission of Femtosecond Electron Pulses from Metal Nanotips”, Physical Review Letters **98**, 043907 (2007), https://doi.org/10.1103/PhysRevLett.98.043907

[16] A. H. Zewail, “Four-Dimensional Electron Microscopy”, Science **328**, 5975, 187-193 (2010), https://doi.org/10.1126/science.1166135

[17] F. Carbone, “Modern electron microscopy resolved in space, energy and time”, The European Physical Journal - Applied Physics **54**, 3, 33503 (2011), https://doi.org/10.1051/epjap/2010100354

[18] G. M. Vanacore, A. W. P. Fitzpatrick, and A. H. Zewail, "Four-dimensional electron microscopy: Ultrafast imaging, diffraction and spectroscopy in materials science and biology", Nano Today **11**, 2, 228-249 (2016), https://doi.org/10.1016/j.nantod.2016.04.009

[19] H. Seiler, "SE Emission in the Scanning Electron Microscope", Journal of Applied Physics **54**, 11, R1 (1983), https://doi.org/10.1063/1.332840

[20] C. J. Powell, and A. Jablonsky, NIST Electron Effective-Attenuation-Length Database, Version 1.3, SRD 82, National Institute of Standards and Technology, Gaithersburg, MD (2011) https://www.nist.gov/srd/nist-standard-reference-database-82

[21] O. F. Mohammed, Y. Ding-Shyue, P. K. Samir, and A. H. Zewail, "4D Scanning Ultrafast Electron Microscopy: Visualization of Materials Surface Dynamics", Journal of the American Chemical Society **133**, 20, 7708-7711 (2011), https://doi.org/10.1021/ja2031322

[22] J. Cho, T. Y. Hwang, and A. H. Zewail, "Visualization of carrier dynamics in p(n)-type GaAs by scanning ultrafast electron microscopy", Proceeding of the National Academy of Sciences of the United States of America **111**, 6, 2094-2099 (2014), https://doi.org/10.1073/pnas.1400138111

[23] J. Sun, A. Adhikari, B. S. Shaheen, H. Yang, and O. F. Mohammed, "Mapping Carrier Dynamics on Material Surfaces in Space and Time using Scanning Ultrafast Electron Microscopy", Journal of Physical Chemistry Letters **7**, 6, 985-994 (2016), https://doi.org/10.1021/acs.jpclett.5b02908

[24] Y. Ding-Shyue, O. F. Mohammed, and A. H. Zewail "Scanning Ultrafast Electron Microscopy" Proceedings of the National Academy of Sciences **107**, 34, 14993-149998 (2010) https://doi.org/10.1073/pnas.1009321107

[25] J. Sun, V. A. Melnikov, J. I. Khan, and O. F. Mohammed, "Real-Space Imaging of Carrier Dynamics of Materials Surfaces by Second-Generation Four-Dimensional Scanning Ultrafast Electron Microscopy", Journal of Physical Chemistry Letters **6**, 19, 3884-3890 (2015), https://doi.org/10.1021/acs.jpclett.5b01867

[26] J. Robertson, “Band offsets of wide-band-gap oxides and implications for future electronic devices”, Journal of Vacuum Science & Technology B **18**, 3, 1785-1791 (2000), https://doi.org/10.1116/1.591472

[27] B. D. Evans, and M. Stapelbroek, “Optical properties of the F^+ center in crystalline Al_2O_3”, Physical Review B **18**, 12, 7089-7098 (1978), https://doi.org/10.1103/PhysRevB.18.7089

[28] A. I. Surdo, V. A. Pustavarov, V. S. Kortov, A. S. Kishka, and E. I. Zinin, “Luminescence in anion-defective α-Al_2O_3 crystals over the nano-, micro- and millisecond intervals”, Nuclear Instruments and Methods in Physics Research A **543**, 1, 234-238 (2005), https://doi.org/10.1016/j.nima.2005.01.189

[29] A. I. Surdo, V. S. Kortov, V. A. Pustovarov, V. Yu. Yakovlev, “UV luminescence of F-centers in aluminum oxide”, Physica Status Solidi C **2**, 1, 527-530 (2005), https://doi.org/10.1002/pssc.200460225

[30] R. Stoian, A. Rosenfeld, D. Ashkenasi, I. V. Hertel, N. M. Bulgakova, and E. E. B. Campbell, “Surface charging and impulsive ion ejection during ultrashort pulsed laser ablation”, Physical Review Letters **88**, 9, 097603 (2002), https://doi.org/10.1103/PhysRevLett.88.097603

Appendix E: Convolution of an exponential and a Gaussian

The convolution of an exponential with a Gaussian has an analytical solution that will be presented both for positive and for negative delays. For positive delays, the integral to be solved is expressed in equation 5.2 where τ_1 is the time constant, A_1' is an amplitude coefficient and σ is the variance of the Gaussian function:

$$A_1'\left(H(t)e^{\frac{x}{\tau_1}}\right) \otimes e^{-\frac{x^2}{2\sigma^2}} = A_1' \int_0^{+\infty} e^{-\frac{x}{\tau_1}} e^{-\frac{(x-u)^2}{2\sigma^2}} dx \tag{5.2}$$

Equation 5.3 is the solution of the indefinite integral:

$$A_1' \int e^{-\frac{x}{\tau_1}} e^{-\frac{(x-u)^2}{2\sigma^2}} dx = A_1 e^{-\frac{u}{\tau_1}} erf\left(\frac{\sigma}{\sqrt{2}\tau_1} + \frac{x-u}{\sqrt{2}\sigma}\right) \tag{5.3}$$

Where a new amplitude coefficient was defined to simplify the expression as shown in Equation 5.4:

$$A_1 = A_1'\left(\sqrt{\frac{\pi}{2}}\sigma e^{\frac{\sigma^2}{2\tau_1^2}}\right) \tag{5.4}$$

The steps to solve the definite integral are shown in equation 5.5 where u is the probe to pump delay:

$$A_1'\left(H(t)e^{-\frac{t}{\tau_1}}\right) \otimes e^{-\frac{t^2}{2\sigma^2}} = A_1 \left[e^{-\frac{u}{\tau_1}} erf\left(\frac{\sigma}{\sqrt{2}\tau_1} + \frac{x-u}{\sqrt{2}\sigma}\right)\right]_0^{+\infty} =$$

$$= A_1 \lim_{x\to+\infty}\left(e^{-\frac{u}{\tau_1}} erf\left(\frac{\sigma}{\sqrt{2}\tau_1} + \frac{x-u}{\sqrt{2}\sigma}\right)\right) - A_1\left(e^{-\frac{u}{\tau_1}} erf\left(\frac{\sigma}{\sqrt{2}\tau_1} + \frac{x-u}{\sqrt{2}\sigma}\right)\right|_{x=0} =$$

$$= A_1 \lim_{x\to+\infty}\left(erf(x)\right) - A_1 e^{-\frac{u}{\tau_1}} erf\left(\frac{\sigma}{\sqrt{2}\tau_1} - \frac{u}{\sqrt{2}\sigma}\right) = A_1\, e^{-\frac{u}{\tau_1}}\left(1 - erf\left(\frac{\sigma}{\sqrt{2}\tau_1} - \frac{u}{\sqrt{2}\sigma}\right)\right) \tag{5.5}$$

The mathematical expression found for the enhancement at positive delays in equation 5.5 may also describe the depletion. The time constant τ_1 is substituted by τ_3 and the amplitude coefficient A_1 by A_3. The amplitude coefficient of the depletion is expected to be negative. The depletion term is reported in equation 5.6

$$A_3'\left(H(t)e^{-\frac{t}{\tau_3}}\right) \otimes e^{-\frac{t^2}{2\sigma^2}} = A_3\, e^{-\frac{u}{\tau_3}}\left(1 - erf\left(\frac{\sigma}{\sqrt{2}\tau_3} - \frac{u}{\sqrt{2}\sigma}\right)\right) \tag{5.6}$$

where a new coefficient has been defined as shown in equation 5.7

$$A_3 = A_3'\left(\sqrt{\frac{\pi}{2}}\sigma e^{\frac{\sigma^2}{2\tau_3^2}}\right) \tag{5.7}$$

For negative delays, the integral to be solved is expressed in equation 5.8 where τ_2 is the time constant, A_2' is an amplitude coefficient and σ is the variance of the Gaussian function:

$$A_2'\left(H(-t)e^{\frac{x}{\tau_2}}\right) \otimes e^{-\frac{x^2}{2\sigma^2}} = A_2' \int_{-\infty}^{0} e^{\frac{x}{\tau_2}} e^{-\frac{(x-u)^2}{2\sigma^2}} dx \tag{5.8}$$

Equation 5.9 is the solution of the indefinite integral:

$$A_2' \int e^{\frac{x}{\tau_2}} e^{-\frac{(x-u)^2}{2\sigma^2}} dx = -A_2 e^{\frac{u}{\tau_2}} erf\left(\frac{\sigma}{\sqrt{2}\tau_2} + \frac{u-x}{\sqrt{2}\sigma}\right) \qquad (5.9)$$

where a new amplitude coefficient was defined to simplify the expression as shown in Equation 5.10:

$$A_2 = A_2' \left(\sqrt{\frac{\pi}{2}} \sigma \mathrm{e}^{\frac{\sigma^2}{2\tau_2^2}}\right) \qquad (5.10)$$

The steps to solve the definite integral are shown in equation 5.11 where u is the probe to pump delay

$$A_2' \left(H(-t) e^{\frac{t}{\tau_2}}\right) \otimes e^{-\frac{t^2}{2\sigma^2}} = A_2 \left[-e^{\frac{u}{\tau_2}} erf\left(\frac{\sigma}{\sqrt{2}\tau_2} + \frac{u-x}{\sqrt{2}\sigma}\right)\right]_{-\infty}^{0} =$$

$$= A_2 \left(-e^{\frac{u}{\tau_2}} erf\left(\frac{\sigma}{\sqrt{2}\tau_2} + \frac{u-x}{\sqrt{2}\sigma}\right)\right)\Big|_{x=0} - A_2 \lim_{x \to -\infty} \left(-e^{\frac{u}{\tau_2}} erf\left(\frac{\sigma}{\sqrt{2}\tau_2} + \frac{u-x}{\sqrt{2}\sigma}\right)\right) =$$

$$= -A_2 e^{\frac{u}{\tau_2}} erf\left(\frac{\sigma}{\sqrt{2}\tau_2} + \frac{u}{\sqrt{2}\sigma}\right) - A_2 \lim_{x \to -\infty} \left(-erf(-x)\right) = A_2\, e^{\frac{u}{\tau_2}} \left(1 - erf\left(\frac{\sigma}{\sqrt{2}\tau_2} + \frac{u}{\sqrt{2}\sigma}\right)\right) \qquad (5.11)$$

Summing up all the terms the full analytical expression for the fitting is reported in equation 5.12

$$f(t) = k + A_1\, e^{-\frac{u}{\tau_1}} \left(1 - erf\left(\frac{\sigma}{\sqrt{2}\tau_2} - \frac{u}{\sqrt{2}\sigma}\right)\right) + A_2\, e^{\frac{u}{\tau_2}} \left(1 - erf\left(\frac{\sigma}{\sqrt{2}\tau_2} + \frac{u}{\sqrt{2}\sigma}\right)\right) + A_3\, e^{-\frac{u}{\tau_3}} \left(1 - erf\left(\frac{\sigma}{\sqrt{2}\tau_3} - \frac{u}{\sqrt{2}\sigma}\right)\right) \qquad (5.12)$$

Appendix F: other works [162]

The Role of Higher Lying Electronic States in Charge Photogeneration in Organic Solar Cells

Giulia Grancini[1],* Maddalena Binda[1], Stefanie Neutzner[1,2], Luigino Criante[1], Vittorio Sala[2], Alberto Tagliaferri[2], and Guglielmo Lanzani*[1,2]

1) Center for Nano Science and Technology@Polimi Istituto Italiano di Tecnologia, via Giovanni Pascoli 70/3, 20133 Milan, Italy

2) Dipartimento di Fisica, Politecnico di Milano, Piazza L. da Vinci, 32, 20133 Milan, Italy

Abstract

The role of excess photon energy on charge generation efficiency in bulk heterojunction solar cells is still an open issue for the organic photovoltaic community. Here, the spectral dependence of the internal quantum efficiency (IQE) for a poly[2,6-(4,4-bis-(2-ethylhexyl)-4H-cyclopenta[2,1b;3,4-b]dithiophene)-alt-4,7-(2,1,3-benzothiadiazole)]:6,6-phenyl-C61-butyric acid methyl ester (PCPDTBT:PC60BM)-based solar cell is derived combining accurate optoelectronic characterization and comprehensive optical modeling. This joint approach is shown to be essential to get reliable values of the IQE. Photons with energy higher than the bandgap of the donor material can effectively contribute to enhance the IQE of the solar cell. This holds true independently of the device architecture, reflecting an intrinsic property of the active material. Moreover, the nanomorphology of the bulk heterojunction plays a crucial role in determining the IQE spectral dependence: the coarser and more crystalline, the lesser the gain in IQE upon high energy excitation.

Introduction

In organic photovoltaic blends, charge generation is a multi-step process: the absorbed photon generates a singlet excited state that can further dissociate, upon diffusion to the donor acceptor interface, into a pair of opposite charge carriers. [1–4] A fraction of these carriers is eventually collected at the electrodes generating a current. If the nascent neutral excited state lies high in energy, it can first thermalize, by internal conversion (IC) and internal vibrational distribution (IVR), to the lowest singlet state and then dissociate (the cold dissociation process) or it can dissociate before thermalization (hot exciton dissociation). In the first case, excess energy is lost and the system does not have memory of the photon energy, except for a possible local increase of temperature. [5] The second case is expected in disordered semiconductors, where the distance between the resulting charge carriers is a sub-linear function of the excess photon energy. [6] A requisite for hot dissociation to occur is that the dissociation rate should be faster than both, IC and IVR. When this happens, the split pair of charges may retain some or all the excess energy with respect to the lowest excited state, in the form of kinetic energy or potential energy. [2,7–9] Ultimately, this energy may assist full charge separation. [7–9] Hot

dissociation has indeed been observed in the ultrafast timescale for a blend of low-bandgap poly[2,6-(4,4-bis(2-ethylhexyl)-4 H- cyclopenta[2,1-b;3,4-b]dithiophene)-alt-4,7-(2,1,3-benzothiadiazole)] (PCPDTBT) donor and fullerene acceptor. [10] If the charge pair formed by hot dissociation has a higher chance to escape recombination, perhaps proportional to the amount of excess energy involved, hot dissociation would lead to a higher quantum efficiency of charge generation for higher photon energy. The latter is however a highly debated question. [11–17]

The main spectral figure of a solar cell is the external quantum efficiency (EQE). EQE is defined as the ratio of the charge carriers collected by the device to the number of incident photons of a given energy. The EQE does not provide specific information on the losses in the device or the role of different layers. The internal quantum efficiency (IQE), i.e., the fraction of extracted electrons per absorbed photon, on the contrary, gives an insight into the charge generation process. As is, it would still be a property of the device, corrected for reflection, diffusion and eventually transmission of incident light. It is however common use to define IQE for the active layer only, i.e., IQE is the ratio between the number of extracted electrons and the number of the absorbed photons in the active layer. This strict definition implies that measuring the IQE is difficult, since the isolated absorption of the active material within a full device structure is not a directly experimentally accessible quantity. [17] Although the absolute value of the IQE depends on the specific device structure, encompassing the effects of internal fields, transport, recombination and collection of charge carriers, its spectral shape yields important information about the active material. Notably device-related effects, as mentioned above, should have a weak dependence on the initial photon energy. Therefore, characteristic features observed in the spectral shape can be confidently attributed to the properties of the active layer.

For energy conversion, the crucial point is the final outcome of hot dissociation over quantum efficiency. Hot dissociation could occur but still be irrelevant if the nascent charge pair does not bear any memory of the initial excess energy (e.g., a fixed intercharge distance) or loses its energy before any further step towards separation. [9] For this reason, measuring the IQE seems the crucial step to assess the role of hot dissociation in photovoltaic bulk heterojunction (BHJ).

Here, we report on a detailed investigation of the IQE in photovoltaic cells based on PCPDTBT/6,6-phenyl-C 61 -butyric acid methyl ester (PC60BM) (1:3) as an active layer blend. We find that the IQE has a week dependence within the lowest singlet vibronic manifold, down to about 550 nm, and start to rise at shorter wavelengths, when higher electronic levels (S2 and S4, [10] are progressively excited).

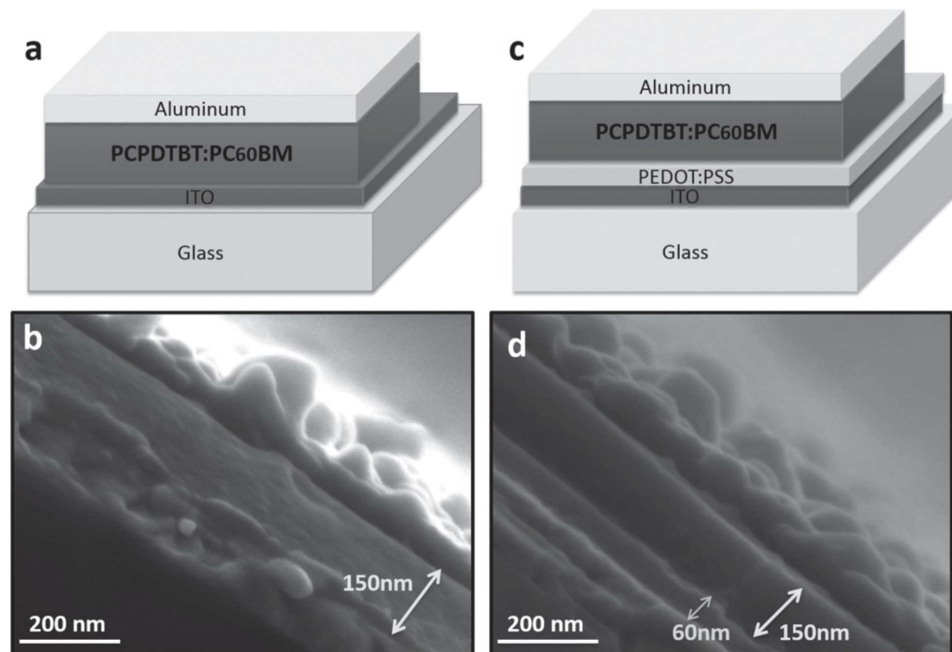

Figure 1. a,c) Sketch of the device architecture; b,d) high-resolution SEM images of the device cross section, the arrows indicate the active layer (150 nm) and the PEDOT:PSS layer (60 nm).

Results

Figure 1a,c shows the sketches of the vertical device structures that we investigated. In addition, as presented later, we also explore a planar structure with interdigitated electrodes. We compare two vertical architectures differing for the presence of the PEDOT:PSS layer, which is commonly used in devices to improve the cell performance. Our goal is to investigate how the interfacial charge generation process is affected by the active layer morphology. To optimize the charge generation efficiency, we use a blend with small domains size that has the highest interface extent at the expense of transport performance. To obtain this, we avoid the use of additives, reported in the literature as a tool to enhance phase segregation, [18] and we do not apply any thermal annealing to the deposited fi lm. In order to correctly evaluate the optical absorption of the active layer within the stack, that is essential to derive the information on the IQE, we measure the thickness of all the individual layers by means of 5 kV cross-sectional scanning electron microscopy (SEM) image (≈5 nm lateral resolution) directly on the device. As shown in Figure 1 b ,d, the active layer, 150 nm thick, is in both cases uniform and smooth with a surface roughness comparable to our resolution. Standard setups for EQE measurements are usually based on a white lamp coupled into a monochromator to generate monochromatic light stimulation of the device. As a result, the light spectrum impinging on the device is given by the convolution of the lamp emission spectrum with the monochromator transmission. Moreover, these setups generally make use of lenses that are affected by severe chromatic aberration. As a consequence, the excitation intensity is far from constant over the spectral range. This yields a spurious dependence of the photogenerated charge density on the excitation wavelength, contributing to often misevaluate the spectral shape of the IQE. On the other hand, the photocurrent transient behavior is typically not monitored by such systems, while the correct evaluation of the extracted carriers must be done at steady-state conditions. In order to circumvent these limitations, that are overlooked in most published work, [11,16] in our measurements the devices were

stimulated with pulsed LED monochromatic light over a 405–840 nm range. The corresponding device photocurrent in short-circuit condition (JSC, A mm −2) was read by a transimpedance amplifier and recorded with an oscilloscope. The impinging light intensity (I, W mm −2) at each wavelength was calibrated by means of a silicon photodiode (Siemens BPX-65) having the same photoactive area (dimension and shape) as the device under test (1 mm 2). This represents a key point, often neglected, to ensure high precision of the calibration regardless the spatial uniformity features of the incident light beam. A simulated light absorption profile in the active material was used to set the LEDs intensity in order to ensure comparable photogenerated charge density at each wavelength across the measurement range. The transient behavior of the photocurrent signal is monitored and the steady-state value is taken for calculation of the EQE. The EQE of the devices was then given by: EQE (%) = 100 · (1240 · JSC) / (λ [nm] · I), with obvious meanings of the various parameters, as described previously. All the electrical measurements were carried out in high vacuum (≈10− 6 mbar) to remove any possible artifact due to oxygen and moisture contamination.

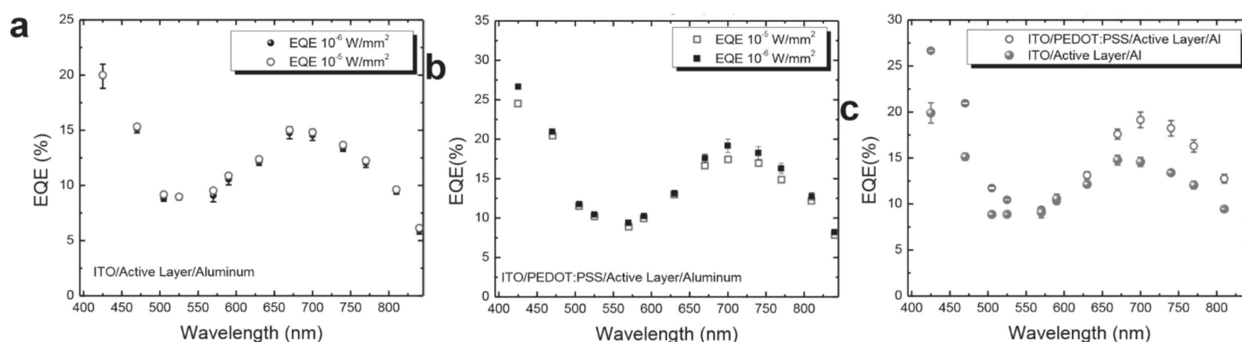

Figure 2. External quantum efficiency (EQE) measurements on a) ITO/ PCPDTBT:PC60BM/Al and b) ITO/PEDOT:PSS/PCPDTBT:PC60BM/Al vertical device. In order to rule out any possible charge-density-dependent effect, we kept equal the number of absorbed photons per each wavelength and we repeated the measurement at two different ranges of light intensity; c) comparison of the EQE for the different architectures with and without PEDOT:PSS layer. Error bars: statistic on a series of 10 devices.

Figure 2 shows the extracted EQE for the devices under investigation. In fair agreement with data reported in literature, [11] values around 20% at the absorption peak have been obtained, slightly higher for the case with PEDOT:PSS layer.

So extract the IQE, the EQE must be divided by the fraction of light absorbed by the active layer only (Abs AL) as: IQE(λ) = EQE(λ)/Abs AL .

Different methods can be used to obtain Abs AL , including simulation only or a combination of modeling and experiments leading a more accurate value, from which different IQE(λ) spectra can be derived. [17] In particular , three different cases can be evaluated, as shown in Figure 3: i) one can rely on the simulated absorption of the active layer within the stack (Figure 3 a). The transfer matrix method (TTM) is a computing technique usually applied to simulate complex multilayer structures (with layer thicknesses comparable to the visible wavelength). [17] In such simulation, a multilayer is a stack of homogeneous thin films with different indices of refraction that can be modeled assuming the invariance of dielectric properties with respect to

continuous translation in two orthogonal directions and not in the third one. The basic formalism provides the amplitude of the electromagnetic field of monochromatic waves reflected by and transmitted through the mentioned multilayered structure. The solution is achieved through propagation of the fields in the homogeneous layers constituting the structure, and applying the proper boundary conditions at their interface. Each layer is described in terms of its (coherent) wave propagation coefficient and interface matrix, considering the complex refractive index of the materials, the layer thicknesses as well as the incidence angle and polarization of the incident light. With the exception of approximations in the chosen model, i.e., simplified dimensionality and initial conditions, this analytical method is exact. Therefore, it takes into account all the electromagnetic field effect within the thin layer structure as the destructively or constructively interference effects, if occurred, of the electromagnetic wave. Reflection and transmission of the thick glass substrate is treated incoherently (transmission and reflection of a slab approximated as an infinite medium) and included in the algorithm.

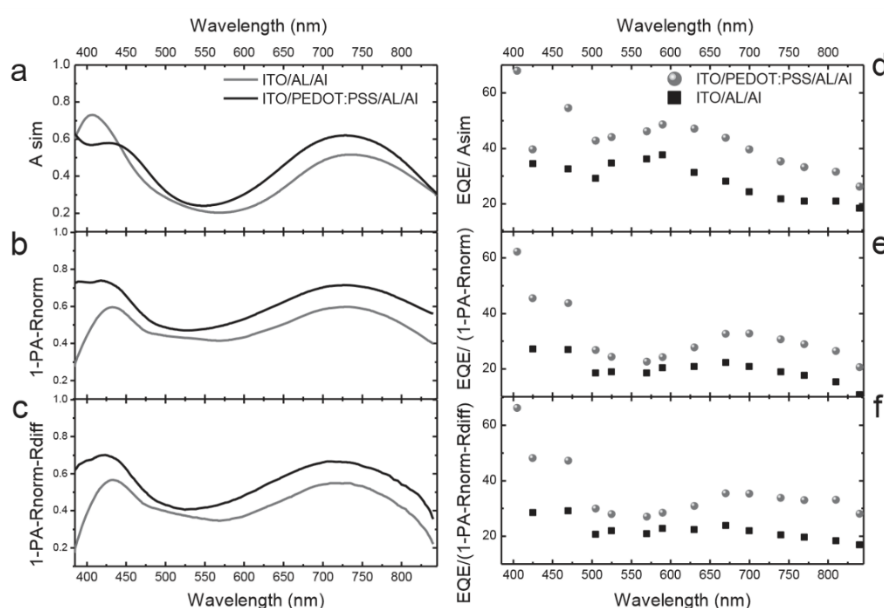

Figure 3. Active layer absorption for the two device architectures with and w/o PEDOT:PSS layer using a) simulated absorption; b) 1-simulated parasitic absorption (PA)—measured reflectance at normal direction (Rnorm) ; c) 1 − PA − Rnorm- scattered component (R diff); d–f) IQE derived by dividing the measured EQE by the absorption as in (a–c).

The simulated absorption of the active layer (Abs AL-Sim) is presented for the two architectures in Figure 3 a (Abs AL-sim, parametric on the active layer thicknesses are shown in Figure S1, Supporting Information). Note that the PEDOT:PSS layer introduces a non-negligible contribution to the interference effects, thus explaining the difference in magnitude of the active layer absorption. The derived IQE is shown in Figure 3 d; ii) in the previous approach, the exact knowledge of the complex dielectric tensor of the stack is crucial. In order to overcome the experimental uncertainty of these parameters, which are notoriously difficult to measure, we follow the method proposed by Burkhard et al. [17] that minimizes this error by using the TTM model to calculate the parasitic absorption (PA). PA is defined as the absorption by all the layers that do not contribute to the photocurrent.

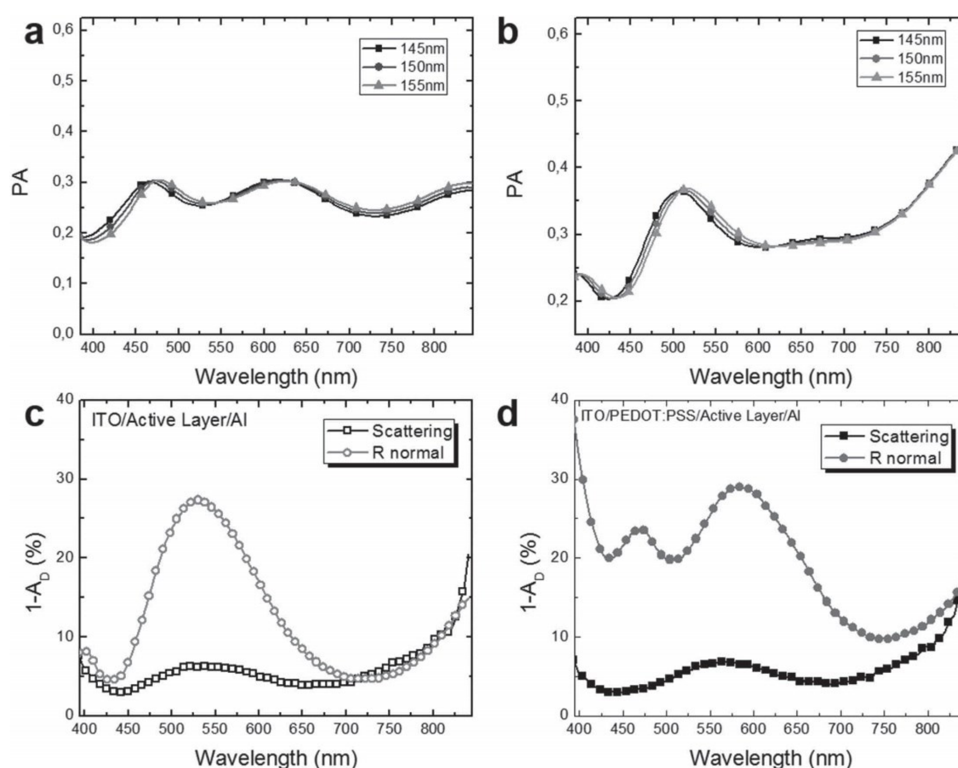

Figure 4. a,b) Calculated parasitic absorption (PA) for three different thicknesses of the active layer as in the legend for the device w/o and with PEDOT:PSS layer, respectively. PA = Absorption of light in all the stack of the device, except the active layer. c,d) Normal and diffuse reflectance spectra for the device w/o and with the PEDOT:PSS layer, respectively.

A thickness dependence of PA is calculated and shown in Figure 4 a,b. By subtracting this from the experimentally measured total device reflectance (R), shown in Figure 4 c,d, one obtains Abs AL = 1 − PA − R . Note that because R is highly accurate, errors in the resulting Abs AL are only as small as the small errors in the PA, loosening the requirements for the accuracy of the optical constants of the blend. [17] In this way, we obtain the IQE shape reported in Figure 3 e ; iii) in the literature R is usually measured only at near-normal condition (Rnorm) while the diffuse scattering and the spatially dependent optical constants of the blend layer are not taken into account. [11,16] To further improve the analysis, we use a home-made system that allows us to simultaneously get the near-normal incidence reflectance spectra and the effective losses of the sample (as in Figure 4 c ,d). This allows accounting for second-order phenomena such as optical scattering from rough fi lm surfaces and interfaces, that are usually neglected, [11,16] and the amount of incident light power "guided" in the substrate toward its edges that never reach the absorbent layer. The latter component is closely related to the substrate thickness. This last method leads to IQE as reported in Figure 3 f.

The IQE plots reported in Figure 3 all display a rising trend with reducing wavelength (from around 15% in the red region to approximately 30% in the blue region). Such discrete wavelengths spectra are highly accurate, yet the rising component is identified only by two experimental points. We thus turn to a continuous light source, using the LED-based measurement as a test to validate the calibration upon excitation density dependence,

which is harder when using the lamp. In Figure 5, our best IQE obtained by using the LED set-up is compared with that measured by using a monocromated lamp (solid line).

The two sets of data are consistent within the confidence range.

To sum up, the measured IQE suggests that higher lying electronic states are keener to generate charge carriers and to contribute to the photocurrent, in agreement with other results and notably with a recent investigation based on electric field saturation. [19,20]

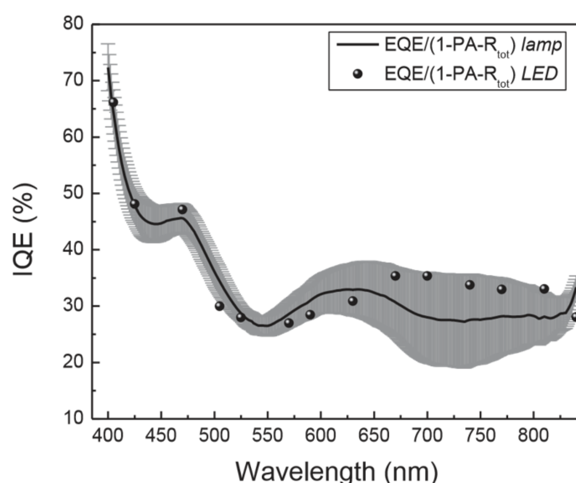

Figure 5. I QE derived by dividing by (1 − PA − Rnorm − Rdiff) the measured EQE obtained by using the LED set-up (with equalized number of absorbed photons at each wavelength) and obtained by using a standard set-up based on monocromated lamp (solid line). The gray area defines the interval of confidence evaluated considering the error bar for each measurement. In particular, the relative variation (grey line) is defined by: ΔIQE = dIQE/dEQE × ΔEQE + dIQE/dPA × ΔPA + dIQE/d R × ΔR , thus

Δ = ([1/(1 − PA − R)) × ΔEQE] 2 + [EQE/(1 − PA − R) 2 × ΔPA] 2 + [EQE/(1 − PA − R) 2 × Δ R] 2) 0.5 .

Discussion

The observation of hot dissociation in the ultrafast time scale, as reported earlier, is a reasonable explanation for the increasing IQE at higher excitation energy. Hot dissociation would somehow exploit excess energy for enhanced charge separation. However, we should first consider other possible interpretations for the high-energy increase of the IQE. Perhaps the most relevant is the role of PC60BM. Upon raising photon energy, absorption within PC60BM molecules augments. This might be followed by hole transfer to the polymer and contribute to the photocurrent. In order for this to explain the observed trend, one should assume that there is a higher efficiency for hole transfer from PC60BM to the polymer than for the electron transfer from the polymer to PC60BM. The later has never been reported and seems unlikely because hole transfer occurs in the 100 ps time scale in P3HT:PC60BM blend, [21] while electron transfer is much faster. In addition, on the ultrafast time scale, changing the PC60BM concentration does not affect the dynamics, [10] suggesting that PC60BM is not involved in the hot process. Based on this observation not only the absorption in PC60BM should be ruled out as an explanation for a higher IQE, but it should be considered that this may have an opposite effect: a less

effective charge separation following absorption into PC60BM would lead to a decrease of the IQE, masking the hot dissociation effect.

The model of charge generation in disordered semiconductors, where localized states are distributed into an incoherent energy band, could offer a simple explanation for the energy dependent IQE. [6] Larger excess energy leads to a larger separation distance within the initial charge pair, which has a higher escape probability, according to the Onsager or Braun–Onsager model. [7,8] For a donor/acceptor blend, such a model is how ever questionable, as the initial charge separation distance is assumed to be that of the D/A separation. This implicitly assumes a cold dissociation model, as in the Popovic–Noolandi–Hong theory. [22,23] Recently, however, a growing body of evidence suggests that the nascent pair is delocalized beyond the nearest neighbor distance [24–26] and points to the role of excess energy even at the donor/acceptor interface. Particularly relevant for our discussion is the very recent report [20] on the decrease in the extraction field saturation (defined as the electric field for 100% charge carrier quantum yield) upon increasing the excitation energy. This is an indication that pairs formed after higher energy excitations are less bounded. Several phenomena may explain the reduced binding energy following a “hot” process. Higher lying states in the donor polymer are more delocalized. [20] This implies a lower binding energy and a higher yield of dissociation into less-bounded pairs. Higher lying states have access to higher density of states that boosts the dissociation rate and couples to more delocalized charge pairs. IC from a higher lying state dissipates more energy and may lead to a higher local temperature that in turn can favor charge carrier escape. At this regard, however, it should be noted that excitation within the first vibronic band does not seem to lead to an energy-dependent IQE, suggesting that it is not just a matter of excess energy and eventually local temperature, but rather a more subtle effect, linked to the nature of the electronic states. This is indeed changing while going higher in energy, thereby increasing the ionic character and the wave function delocalization of the state.

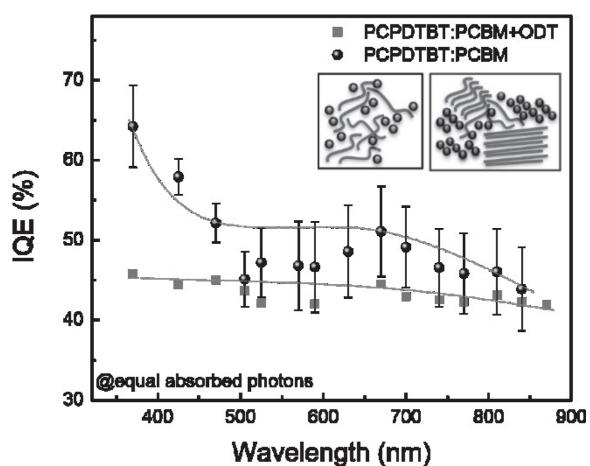

Figure 6. I QE derived by dividing the measured EQE obtained by using the LED on a planar device based on a PCPDTBT:PC60BM blend (error bar is related to the uncertainty on the thickness of the active materials of ±10 nm) or a PCPDTBT:PC60BM+ODT blend at equal absorbed photons condition for each wavelength. Dashed lines only represent an eye-guideline.

It seems that in many studies on the IQE the energy dependence is overlooked. [11,16,27] In the correspondence appeared in ref. [2 7] , the proposed plot for the IQE is squeezed by the scale, and a dependence on energy difficult to appreciate. A proper rescaling of the same data however shows exactly the same behavior that we report here. In other works, the IQE is reported in log scale over many orders of magnitude, obscuring the rise at high energy. Furthermore when large extraction fields are used to collect the photo-generated charges the eventual distribution in binding energy is washed out. Finally, it should be taken into account that morphology is affecting generation, transport, and recombination, thus becoming responsible for a certain spread in experimental results. Transport is very important in planar devices that are in principle a simple system to be investigated. Also in a planar device however, after careful calibration of all possible artifacts, we measure consistently a rise of the IQE (Figure 6). On the contrary when using an additive that changes the morphology towards larger domains with reduced extension of donor/acceptor interfaces, we obtain a virtually flat IQE (shown in Figure 6). This very well demonstrates the role of morphology.

Conclusion

The IQE in polymer BHJs with small domain morphology increases upon excitation of higher lying singlet electronic states. This might be associated with hot dissociation, occurring before energy relaxation and leading to a less-bounded charge pair. The outcome is well consistent with standard pictures for charge generation in disordered semiconductors and molecular solids, and finds large agreement with other recently published experiments and theory. This suggests that hot dissociation of higher lying states may play a role and possibly be considered when designing new organic photovoltaic cells.

Experimental Section

Device Fabrication: Vertical devices were fabricated on glass substrates with prepatterned ITO electrodes (Xin Yan Technology LTD., 15 Ω/). Before the PEDOT:PSS deposition and after accurate cleaning in bidistilled water, acetone, and isopropanol, substrates underwent O_2 plasma treatment. PEDOT:PSS (Clevios 4083) was deposited by spin coating at 2000 rpm from 0.2 µm PVDF filtered solution. Thermal annealing at 110 °C for 15 min in nitrogen atmosphere was performed. The 1:3.7 by weight PCPDTBT:PC60BM solution, with a concentration of 10 mg mL^{-1} , was spun cast at 1000 rpm. The aluminum cathode was thermally evaporated through a suitable shadow mask giving a pixel active area of 1 mm^2.

Planar devices were realized by spin casting the blend with the same recipe as for vertical devices onto fused silica substrates provided with prepatterned interdigitated gold electrodes with a channel length of 6 µm. In the case of devices provided with an additive to increase phase segregation, 1-octadecanethiol was added to the blend solution (4% by volume).

Scanning Electron Microscopy Measurements: A Tescan MIRA3 SEM was used for scanning electron microscopy imaging. The pictures was acquired by the in-column secondary electron detector with the following parameter: acceleration voltage 5 kV, beam current of about 10 pA, working distance 0.5 mm, and acquisition times ranging from 30 s to a couple of minutes.

Diffuse Reflectance Measurements: To measure the reflectance, both normal and effective diffusive components simultaneously, a homemade system was developed. It was based on fiber optic reflection probe coupled into an integrating sphere. It had one illuminating fiber in the center surrounded by six fibers able to collect the device normal reflectance. The seven individual fibers were multimodal (0.22 NA) and transmission in the 350–2000 nm spectral ranges. The special probe, which had been placed within the integrating sphere very close and at normal position with respect to the device surface, allowed maintaining an incident plane wave condition until a few mm from the tip (working distance). The shining light uniformly illuminated the sample area. On the same time, the integrating sphere, coupled with a standard spectrofluorimeter (NanoLog Horiba Jobin Yvon) was used to collect the diffuse component.

Acknowledgements

G .G. and M.B. contributed equally to this work. The authors thank Dr. Stefano Perissinotto for the help with the absorption/reflectance measurements and Dr. Maurizio Zani for the help with the SEM measurements. The authors also acknowledge Carlo Brambilla and Mauro Scarparo for the help in the fabrication of the home-made setup for reflection measurements. The research leading to these results has received funding from the European Union's Horizon 2020 research and innovation programme under the Marie-Sklodowska-Curie grant agreement No 643238.

References

[1] H. Hoppe, N. S. Sariciftci, J. Mater. Res. **2004**, 19, 1924.
[2] G. Lanzani, The Photophysics Behind Photovoltaics and Photonics , Wiley-VCH , Weinheim, Germany **2012**.
[3] T. M. Clarke, J. R. Durrant, Chem. Rev. **2010**, 110, 6736.
[4] G. Grancini, D. Polli, D. Fazzi, J. Cabanillas-Gonzalez, G. Cerullo, G. Lanzani, J. Phys. Chem. Lett. **2011**, 2, 1099.
[5] V. I. Arkhipov, E. V. Emelianova, H. Bässler, Phys. Rev. Lett. **1999**, 82, 1321.
[6] D. M. Pai, R. C. Enk, Phys. Rev. B **1975**, 11, 5163.
[7] L. Onsager, J. Chem. Phys. **1934**, 2, 599.
[8] C. L. Braun, J. Chem. Phys. **1984**, 80, 4157.
[9] D. Fazzi, G. Grancini, M. Maiuri, D. Brida, G. Cerullo, G. Lanzani, Phys. Chem. Chem. Phys. **2012**, 14, 6367.
[10] G. Grancini, M. Maiuri, D. Fazzi, A. Petrozza, H.-J. Egelhaaf, D. Brida, G. Cerullo, G. Lanzani, Nat. Mater. **2013**, 12, 29.
[11] A. Armin, M. Velusamy, P. Wolfer, Y. Zhang, P. L. Burn, P. Meredith, A. Pivrikas, ACS Photonics **2014**, 1, 173.
[12] G. Grancini, M. Binda, L. Criante, S. Perissinotto, M. Maiuri, D. Fazzi, A. Petrozza, H.-J. Egelhaaf, D. Brida, G. Cerullo, G. Lanzani, Nat. Mater. **2013**, 12, 594.
[13] S. D. Dimitrov, J. R. Durrant, Chem. Mater. **2014**, 26, 616.
[14] A. A. Bakulin, A. Rao, V. G. Pavelyev, P. H. M. van Loosdrecht, M. S. Pshenichnikov, D. Niedzialek, J. Cornil, D. Beljonne, R. H. Friend, Science **2012**, 335, 1340.

[15] K. Vandewal, S. Albrecht, E. T. Hoke, K. R. Graham, J. Widmer, J. D. Douglas, M. Schubert, W. R. Mateker, J. T. Bloking, G. F. Burkhard, A. Sellinger, J. M. J. Fréchet, A. Amassian, M. K. Riede, M. D. McGehee, D. Neher, A. Salleo, Nat. Mater. **2014**, 13, 63.

[16] A. Armin, I. Kassal, P. E. Shaw, M. Hambsch, M. Stolterfoht, D. M. Lyons, J. Li, Z. Shi, P. L. Burn, P. Meredith, J. Am. Chem. Soc. **2014**, 136, 11465.

[17] G. F. Burkhard, E. T. Hoke, M. D. McGehee, Adv. Mater. **2010**, 22, 3293.

[18] S. H. Park, A. Roy, S. Beaupré, S. Cho, N. Coates, J. S. Moon, D. Moses, M. Leclerc, K. Lee, A. J. Heeger, Nat. Photonics **2009**, 3, 297.

[19] L. A. A. Pettersson, L. S. Roman, O. Inganäs, J. Appl. Phys. **1999**, 86, 487.

[20] T. Hahn, J. Geiger, X. Blase, I. Duchemin, D. Niedzialek, S. Tscheuschner, D. Beljonne, H. Bässler, A. Köhler, Adv. Funct. Mater. **2015**, 25, 1287.

[21] A. R. Srimath Kandada, G. Grancini, A. Petrozza, S. Perissinotto, D. Fazzi, S. S. Kumar Raavi, G. Lanzani, Sci. Rep. 2013 , 3 , 1 . [22] Z. Noolandi, K. M. Hong, J. Chem. Phys. **1979**, 70, 3230.

[23] N. E. Geacintov, M. J. Pope, Chem. Phys. **1965**, 47, 1194.

[24] A. E. Jailaubekov, A. P. Willard, J. R. Tritsch, W.-L. Chan, N. Sai, R. Gearba, L. G. Kaake, K. J. Williams, K. Leung, P. J. Rossky, X.-Y. Zhu, Nat. Mater. **2013**, 12, 66.

[25] S. Gélinas, A. Rao, A. Kumar, S. L. Smith, A. W. Chin, J. Clark, T. S. van der Poll, G. C. Bazan, R. H. Friend, Science **2013**, 343, 512.

[26] F. Provencher, N. Bérubé, A. W. Parker, G. M. Greetham, M. Towrie, C. Hellmann, M. Côté, N. Stingelin, C. Silva, S. C. Hayes, Nat. Commun. **2014**, 5, 1.

[27] A. Armin, Y. Zhang, P. L. Burn, P. Meredith, A. Pivrikas, Nat. Mater. **2013**, 12, 593.

References

[1] M. Knoll, E. Ruska, Das Elektronenmikroskop., Zeitschrift Fur Phys. 318 (1932) 318–339. doi:10.1007/BF01342199.

[2] T. Sekiguchi, K. Sumino, Quantitative electron-beam tester for defects in semiconductors (CL/EBIC/SDLTS system), Rev. Sci. Instrum. 66 (1995) 4277–4282. doi:10.1063/1.1145382.

[3] M. Merano, S. Sonderegger, A. Crottini, S. Collin, P. Renucci, E. Pelucchi, A. Malko, M.H. Baier, E. Kapon, B. Deveaud, J.-D. Ganière, Probing carrier dynamics in nanostructures by picosecond cathodoluminescence, Nature. 438 (2005) 479–482. doi:10.1038/nature04298.

[4] K. Bücker, M. Picher, O. Crégut, T. LaGrange, B.W. Reed, S.T. Park, D.J. Masiel, F. Banhart, Electron beam dynamics in an ultrafast transmission electron microscope with Wehnelt electrode, Ultramicroscopy. 171 (2016) 8–18. doi:10.1016/j.ultramic.2016.08.014.

[5] P. Baum, D.-S. Yang, A.H. Zewail, 4D Visualization of Transitional Structures in Phase Transformations by Electron Diffraction, Science (80-.). 318 (2007) 788–792. doi:10.1126/science.1147724.

[6] P. Baum, A.H. Zewail, Breaking resolution limits in ultrafast electron diffraction and microscopy, Proc Natl Acad Sci U S A. 103 (2006) 16105–16110. doi:10.1073/pnas.0607451103.

[7] D.J. Flannigan, A.H. Zewail, 4D Electron Microscopy: Principles and Applications, Acc. Chem. Res. 45 (2012) 1828–1839. doi:10.1021/ar3001684.

[8] B.J. Siwick, J.R. Dwyer, R.E. Jordan, R.J.D. Miller, An atomic-level view of melting using femtosecond electron diffraction., Science (80-.). 302 (2003) 1382–5. doi:10.1126/science.1090052.

[9] O.F. Mohammed, D.S. Yang, S.K. Pal, A.H. Zewail, 4D scanning ultrafast electron microscopy: Visualization of materials surface dynamics, J. Am. Chem. Soc. 133 (2011) 7708–7711. doi:10.1021/ja2031322.

[10] J. Gregor Gatzmann, T. Eggebrecht, A. Feist, V. Zbarsky, M. Münzenberg, C. Ropers, S. Schäfer, J.G. Gatzmann, T. Eggebrecht, A. Feist, V. Zbarsky, M. Münzenberg, C. Ropers, S. Schäfer, In-Situ Lorentz Microscopy with Femtosecond Optical Illumination, Microsc. Microanal. 20 (2014) 1578–1579. doi:10.1017/S1431927614009623.

[11] M.S. Grinolds, V.A. Lobastov, J. Weissenrieder, A.H. Zewail, Four-dimensional ultrafast electron microscopy of phase transitions, Proc. Natl. Acad. Sci. 103 (2006) 18427–18431. doi:10.1073/pnas.0609233103.

[12] A.H. Zewail, Four-Dimensional Electron Microscopy, Science (80-.). 328 (2010) 187–193. doi:10.1126/science.1166135.

[13] L. Piazza, D.J.J. Masiel, T. LaGrange, B.W.W. Reed, B. Barwick, F. Carbone, Design and implementation of a fs-resolved transmission electron microscope based on thermionic gun technology, Chem. Phys. 423 (2013) 79–84. doi:10.1016/j.chemphys.2013.06.026.

[14] A. Feist, N. Bach, N. Rubiano, T. Danz, M. Möller, K.E. Priebe, T. Domröse, J.G. Gatzmann, S. Rost, J. Schauss, S. Strauch, R. Bormann, M. Sivis, S. Schäfer, C. Ropers, Ultrafast transmission electron microscopy using a laser-driven fi eld emitter : Femtosecond resolution with a high coherence electron beam, Ultramicroscopy. 176 (2017) 63–73. doi:10.1016/j.ultramic.2016.12.005.

[15] D.J. Flannigan, P.C. Samartzis, A. Yurtsever, A.H. Zewail, Nanomechanical motions of cantilevers: direct imaging in real space and time with 4D electron microscopy, Nano Lett. 9 (2009) 875–881. doi:10.1021/n1803770e.

[16] D.A. Plemmons, P.K. Suri, D.J. Flannigan, Probing structural and electronic dynamics with ultrafast electron microscopy, Chem. Mater. 27 (2015) 3178–3192. doi:10.1021/acs.chemmater.5b00433.

[17] T.T.A. Lummen, R.J. Lamb, G. Berruto, T. LaGrange, L. Dal Negro, F.J. García de Abajo, D. McGrouther, B.

Barwick, F. Carbone, Imaging and controlling plasmonic interference fields at buried interfaces, Nat. Commun. 7 (2016) 13156. doi:10.1038/ncomms13156.

[18] B. Barwick, D.J. Flannigan, A.H. Zewail, Photon-induced near-field electron microscopy, Nature. 462 (2009) 902–906. doi:10.1038/nature08662.

[19] B. Barwick, A.H. Zewail, Photonics and Plasmonics in 4D Ultrafast Electron Microscopy, ACS Photonics. 2 (2015) 1391–1402. doi:10.1021/acsphotonics.5b00427.

[20] L. Piazza, T.T.A. Lummen, E. Quiñonez, Y. Murooka, B.W. Reed, B. Barwick, F. Carbone, Simultaneous observation of the quantization and the interference pattern of a plasmonic near-field, Nat. Commun. 6 (2015) 6407. doi:10.1038/ncomms7407.

[21] A. Feist, K.E. Echternkamp, J. Schauss, S. V. Yalunin, S. Schäfer, C. Ropers, Quantum coherent optical phase modulation in an ultrafast transmission electron microscope, Nature. 521 (2015) 200–203. doi:10.1038/nature14463.

[22] G. Fulvia, B. Mansart, S. Pagano, B. Van Der Geer, M. De Loos, G.F. Mancini, B. Mansart, S. Pagano, B. van der Geer, M. de Loos, F. Carbone, G. Fulvia, B. Mansart, S. Pagano, B. Van Der Geer, M. De Loos, Design and implementation of a flexible beamline for fs electron diffraction experiments, Nucl. Inst. Methods Phys. Res. A. 691 (2012) 113–122. doi:10.1016/j.nima.2012.06.057.

[23] D.-S. Yang, N. Gedik, A.H. Zewail, Ding-Shyue Yang, A. Nuh Gedik, A.H. Zewail*, Ultrafast Electron Crystallography. 1. Nonequilibrium Dynamics of Nanometer-Scale Structures, J. Phys. Chem. C. 111 (2007) 4889–4919. doi:10.1021/jp067466+.

[24] G.M. Vanacore, J. Hu, W. Liang, S. Bietti, S. Sanguinetti, A.H. Zewail, Diffraction of quantum dots reveals nanoscale ultrafast energy localization, Nano Lett. 14 (2014) 6148–6154. doi:10.1021/nl502293a.

[25] C.-Y. Ruan, F. Vigliotti, V.A. Lobastov, S. Chen, A.H. Zewail, Ultrafast electron crystallography: transient structures of molecules, surfaces, and phase transitions., Proc. Natl. Acad. Sci. U. S. A. 101 (2004) 1123–8. doi:10.1073/pnas.0307302101.

[26] D.-S. Yang, O.F. Mohammed, A.H. Zewail, Scanning ultrafast electron microscopy., Proc. Natl. Acad. Sci. 107 (2010) 14993–8. doi:10.1073/pnas.1009321107.

[27] J. Sun, V.A. Melnikov, J.I. Khan, O.F. Mohammed, Real-Space Imaging of Carrier Dynamics of Materials Surfaces by Second-Generation Four-Dimensional Scanning Ultrafast Electron Microscopy, J. Phys. Chem. Lett. 6 (2015) 3884–3890. doi:10.1021/acs.jpclett.5b01867.

[28] J. Cho, T.Y. Hwang, A.H. Zewail, Visualization of carrier dynamics in p(n)-type GaAs by scanning ultrafast electron microscopy, Proc. Natl. Acad. Sci. 111 (2014) 2094–2099. doi:10.1073/pnas.1400138111.

[29] D.S. Yang, O.F. Mohammed, A.H. Zewail, Environmental scanning ultrafast electron microscopy: Structural dynamics of solvation at interfaces, Angew. Chemie - Int. Ed. 52 (2013) 2897–2901. doi:10.1002/anie.201205093.

[30] R. Bose, J. Sun, J.I. Khan, B.S. Shaheen, A. Adhikari, T.K. Ng, V.M. Burlakov, M.R. Parida, D. Priante, A. Goriely, B.S. Ooi, O.M. Bakr, O.F. Mohammed, Real-Space Visualization of Energy Loss and Carrier Diffusion in a Semiconductor Nanowire Array Using 4D Electron Microscopy, Adv. Mater. (2016) 5106–5111. doi:10.1002/adma.201600202.

[31] J.I. Khan, A. Adhikari, J. Sun, D. Priante, R. Bose, B.S. Shaheen, T.K. Ng, C. Zhao, O.M. Bakr, B.S. Ooi, O.F. Mohammed, Enhanced Optoelectronic Performance of a Passivated Nanowire-Based Device: Key Information from Real-Space Imaging Using 4D Electron Microscopy, Small. 12 (2016) 2313–2320. doi:10.1002/smll.201503651.

[32] B.S. Shaheen, J. Sun, D.-S. Yang, O.F. Mohammed, Spatiotemporal Observation of Electron-Impact Dynamics in Photovoltaic Materials Using 4D Electron Microscopy, J. Phys. Chem. Lett. 8 (2017) 2455–2462. doi:10.1021/acs.jpclett.7b01116.

[33] E. Najafi, T.D. Scarborough, J. Tang, A. Zewail, Four-dimensional imaging of carrier interface dynamics in p-n junctions, Science (80-.). 347 (2015) 164–167. doi:10.1126/science.aaa0217.

[34] E. Najafi, V. Ivanov, A. Zewail, M. Bernardi, Super-diffusion of excited carriers in semiconductors, Nat. Commun. 8 (2017) 15177. doi:10.1038/ncomms15177.

[35] W. Shockley, W.T. Read, Statistics of the Recombinations of Holes and Electrons, Phys. Rev. 87 (1952) 835–842. doi:10.1103/PhysRev.87.835.

[36] R.N. Hall, Electron-Hole Recombination in Germanium, Phys. Rev. 87 (1952) 387. doi:10.1103/PhysRev.175.823.

[37] S. Ciraci, I.P. Batra, Electronic structure of α-alumina and its defect states, Phys. Rev. B - Condens. Matter Mater. Phys. 28 (1983) 982–992. doi:10.1103/PhysRevB.28.982.

[38] S.-W. Yeom, S.-C. Shin, T.-Y. Kim, H.J. Ha, Y.-H. Lee, J.W. Shim, B.-K. Ju, Transparent resistive switching memory using aluminum oxide on a flexible substrate., Nanotechnology. 27 (2016) 07LT01. doi:10.1088/0957-4484/27/7/07LT01.

[39] B.D. Evans, G.J. Pogatshnik, Y. Chen, Optical properties of lattice defects in α-Al2O3, Nucl. Inst. Methods Phys. Res. B. 91 (1994) 258–262. doi:10.1016/0168-583X(94)96227-8.

[40] A.I. Surdo, V.S. Kortov, V.A. Pustovarov, V.Y. Yakovlev, UV luminescence of F-centers in aluminum oxide, Phys. Status Solidi C Conf. 2 (2005) 527–530. doi:10.1002/pssc.200460225.

[41] B.D. Evans, A review of the optical properties of anion lattice vacancies, and electrical conduction in α-Al2O3: Their relation to radiation-induced electrical degradation, J. Nucl. Mater. 219 (1995) 202–223. doi:10.1016/0022-3115(94)00529-X.

[42] G.P.P. Williams, G.H.H. Rosenblatt, M.J.J. Ferry, R.T.T. Williams, Y. Chen, Time resolved luminescence and absorption spectroscopy of defects in MgO and AL2O3, J. Lumin. 40–41 (1988) 339–340. doi:10.1016/0022-2313(88)90222-0.

[43] E.C. Kouroukla, I.K. Bailiff, I. Terry, L. Bowen, Luminescence characterisation of alumina substrates using cathodoluminescence microscopy and spectroscopy, Radiat. Meas. 71 (2014) 117–121. doi:10.1016/j.radmeas.2014.03.018.

[44] L. Reimer, Scanning Electron Microscopy: Physics of Image Formation and Microanalysis, 1998. doi:10.1007/978-3-540-38967-5.

[45] H.H. Pattee, The Scanning X-Ray Microscope, J. Opt. Soc. Am. 43 (1953) 61. doi:10.1364/JOSA.43.000061.

[46] J.J. Lander, Auger peaks in the energy spectra of secondary electrons from various materials, Phys. Rev. 91 (1953) 1382–1387. doi:10.1103/PhysRev.91.1382.

[47] P.M. Williams, A.D. Yoffe, Scanning electron microscope studies of cathodoluminescence in ZnSe single crystals, Philos. Mag. 18 (1968) 555–560. doi:10.1080/14786436808227460.

[48] H. Seiler, Secondary electron emission in the scanning electron microscope, J. Appl. Phys. 54 (1983) R1–R18. doi:10.1063/1.332840.

[49] A. Shih, J. Yater, C. Hor, R. Abrams, Secondary electron emission studies, Appl. Surf. Sci. 111 (1997) 251–258. doi:10.1016/S0169-4332(96)00729-5.

[50] L.C. Gontard, R. Schierholz, S. Yu, J. Cintas, R.E. Dunin-Borkowski, Photogrammetry of the three-dimensional shape and texture of a nanoscale particle using scanning electron microscopy and free software, Ultramicroscopy. 169 (2016) 80–88. doi:10.1016/j.ultramic.2016.07.006.

[51] G.M. Vanacore, M. Zani, G. Isella, J. Osmond, M. Bollani, A. Tagliaferri, Quantitative investigation of the influence of carbon surfactant on Ge surface diffusion and island nucleation on Si(100), Phys. Rev. B - Condens. Matter Mater. Phys. 82 (2010) 1–11. doi:10.1103/PhysRevB.82.125456.

[52] B. THIEL, In situMechanical Testing of Fully Hydrated Carrots (Daucus carota) in the Environmental SEM, Ann. Bot. 82 (1998) 727–733. doi:10.1006/anbo.1998.0732.

[53] O. Bostanjoglo, R. Liedtke, Tracing fast phase transitions by electron microscopy, Phys. Status Solidi. 60 (1980) 451–455. doi:10.1002/pssa.2210600215.

[54] O. Bostanjoglo, J. Kornitzky, R.P. Tornow, Nanosecond double-frame electron microscopy of fast phase transitions, J. Phys. E. 22 (1989) 1008–1011. doi:10.1088/0022-3735/22/12/010.

[55] T. LaGrange, M.R. Armstrong, K. Boyden, C.G. Brown, G.H. Campbell, J.D. Colvin, W.J. DeHope, A.M. Frank, D.J. Gibson, F. V. Hartemann, J.S. Kim, W.E. King, B.J. Pyke, B.W. Reed, M.D. Shirk, R.M. Shuttlesworth, B.C. Stuart, B.R. Torralva, N.D. Browning, Single-shot dynamic transmission electron microscopy, Appl. Phys. Lett. 89 (2006). doi:10.1063/1.2236263.

[56] P. May, J.M. Halbout, G. Chiu, Picosecond photoelectron scanning electron microscope for noncontact testing of integrated circuits, Appl. Phys. Lett. 51 (1987) 145–147. doi:10.1063/1.98596.

[57] H. Ohkita, S. Cook, Y. Astuti, W. Duffy, S. Tierney, W. Zhang, M. Heeney, I. McCulloch, J. Nelson, D.D.C. Bradley, J.R. Durrant, Charge carrier formation in polythiophene/fullerene blend films studied by transient absorption spectroscopy, J. Am. Chem. Soc. 130 (2008) 3030–3042. doi:10.1021/ja076568q.

[58] G. Grancini, D. Polli, D. Fazzi, J. Cabanillas-gonzalez, G. Cerullo, G. Lanzani, Transient Absorption Imaging of P3HT : PCBM Photovoltaic Blend, J. Phys. Chem. Lett. 2 (2011) 1099–1105. doi:10.1021/jz200389b.

[59] R.W. Schoenlein, W.Z. Lin, J.G. Fujimoto, G.L. Eesley, Femtosecond studies of nonequilibrium electronic processes in metals, Phys. Rev. Lett. 58 (1987) 1680–1683. doi:10.1103/PhysRevLett.58.1680.

[60] A.J. Sabbah, D.M. Riffe, Femtosecond pump-probe reflectivity study of silicon carrier dynamics, Phys. Rev. B. 66 (2002) 165217. doi:10.1103/PhysRevB.66.165217.

[61] D. Polli, P. Altoè, O. Weingart, K.M. Spillane, C. Manzoni, D. Brida, G. Tomasello, G. Orlandi, P. Kukura, R.A. Mathies, M. Garavelli, G. Cerullo, Conical intersection dynamics of the primary photoisomerization event in vision, Nature. 467 (2010) 440–443. doi:10.1038/nature09346.

[62] M.M. Gabriel, J.R. Kirschbrown, J.D. Christesen, C.W. Pinion, D.F. Zigler, E.M. Grumstrup, B.P. Mehl, E.E.M. Cating, J.F. Cahoon, J.M. Papanikolas, Direct Imaging of Free Carrier and Trap Carrier Motion in Silicon Nanowires by Spatially-Separated Femtosecond Pump−Probe Microscopy, Nano Lett. 13 (2013) 1336–1340. doi:10.1021/nl400265b.

[63] K. Fukumoto, K. Onda, Y. Yamada, T. Matsuki, T. Mukuta, S. Tanaka, S. Koshihara, Femtosecond time-resolved photoemission electron microscopy for spatiotemporal imaging of photogenerated carrier dynamics in semiconductors, Rev. Sci. Instrum. 85 (2014) 83705. doi:10.1063/1.4893484.

[64] W.C. Nixon, G.S. Plows, Stroboscopic scanning electron microscopy, J. Sci. Instruments (Journal Phys. E). 1 (1968) 595–600. doi:10.1088/0022-3735/1/6/302.

[65] R.O.J.M. Oerland, I.G.E.C.W. Eppelman, M. Athijs, W.H.G. Arming, P.I.K. Ruit, J.A.P.H. Oogenboom, Time-resolved cathodoluminescence microscopy with sub-nanosecond beam blanking for direct evaluation of the local density of states, Opt. Express. 24 (2016) 499–504. doi:10.1364/OE.24.024760.

[66] B.J. Siwick, J.R. Dwyer, R.E. Jordan, R.J.D. Miller, B.J. Siwick, J.R. Dwyer, R.E. Jordan, R.J.D. Miller, Ultrafast electron optics : Propagation dynamics of femtosecond electron packets, J. Appl. Phys. 92 (2002) 1643–1648. doi:10.1063/1.1487437.

[67] A. Zewail, V. Lobastov, Method and system for ultrafast photoelectron microscope, United States Pat. 7154091 (2006).

[68] N.F. Scberer, J.L. Knee, D.D. Smith, A.H. Zewail, Femtosecond Photofragment Spectroscopy: The Reaction ICN - CN + I, J. Phys. Chem. 89 (1985) 5141–5143. doi:10.1021/j100270a001.

[69] B. Barwick, H.S. Park, O.-H. Kwon, S.J. Baskin, A.H. Zewail, 4D Imaging of Transient Structures and

Morphologies in Ultrafast Electron Microscopy, Science (80-.). 322 (2008) 1227–1231. doi:10.1126/science.1164000.

[70] V.A. Lobastov, R. Srinivasan, A.H. Zewail, Four-dimensional ultrafast electron microscopy., Proc. Natl. Acad. Sci. U. S. A. 102 (2005) 7069–73. doi:10.1073/pnas.0502607102.

[71] C.Y. Ruan, F. Vigliotti, V.A. Lobastov, S.Y. Chen, A.H. Zewail, Ultrafast electron crystallography: Transient structures of molecules, surfaces, and phase transitions, Proc. Natl. Acad. Sci. U. S. A. 101 (2004) 1123–1128. doi:10.1073/pnas.0307302101.

[72] V. Ortalan, A.H. Zewail, 4D scanning transmission ultrafast electron microscopy: Single-particle imaging and spectroscopy, J. Am. Chem. Soc. 133 (2011) 10732–10735. doi:10.1021/ja203821y.

[73] G.M. Vanacore, A.W.P. Fitzpatrick, A.H. Zewail, Four-dimensional electron microscopy : Ultrafast imaging , diffraction and spectroscopy in materials science and biology, Nano Today. 11 (2016) 228–249. doi:10.1021/nl502293a.

[74] P. Baum, On the physics of ultrashort single-electron pulses for time-resolved microscopy and diffraction, Chem. Phys. 423 (2013) 55–61. doi:10.1016/j.chemphys.2013.06.012.

[75] K. Németh, K.C. Harkay, M. Van Veenendaal, L. Spentzouris, M. White, K. Attenkofer, G. Srajer, High-brightness photocathodes through ultrathin surface layers on metals, Phys. Rev. Lett. 104 (2010) 1–4. doi:10.1103/PhysRevLett.104.046801.

[76] A. V. Crewe, D.N. Eggenberger, J. Wall, L.M. Welter, Electron gun using a field emission source, Rev. Sci. Instrum. 39 (1968) 576–583. doi:10.1063/1.1683435.

[77] F.O. Kirchner, A. Gliserin, F. Krausz, P. Baum, Laser streaking of free electrons at 25 keV, Nat. Photonics. 8 (2013) 52–57. doi:10.1038/nphoton.2013.315.

[78] R.P. Chatelain, V.R. Morrison, C. Godbout, B.J. Siwick, R.P. Chatelain, V.R. Morrison, C. Godbout, B.J. Siwick, Ultrafast electron diffraction with radio-frequency compressed electron pulses, App. 101 (2012) 1–4. doi:10.1063/1.4747155.

[79] P. May, J.M. Halbout, C.T. Chuang, G.P. Li, Waveform Measurements in High-Speed Silicon Bipolar Circuits Using a Picosecond Photoelectron Scanning Electron Microscope, IEEE Trans. Electron Devices. 35 (1988) 1126–1129. doi:10.1109/16.3373.

[80] K.C.A. Smith, C.W. Oatley, The scanning electron microscope and its fields of application, Br. J. Appl. Phys. 6 (1955) 391. doi:10.1088/0508-3443/6/11/304.

[81] A. Gahlmann, S. Tae Park, A.H. Zewail, Ultrashort electron pulses for diffraction, crystallography and microscopy: theoretical and experimental resolutions, Phys. Chem. Chem. Phys. 10 (2008) 2894. doi:10.1039/b802136h.

[82] C. Zhao, T.K. Ng, A. Prabaswara, M. Conroy, S. Jahangir, T. Frost, J. O'Connell, J.D. Holmes, P.J. Parbrook, P. Bhattacharya, B.S. Ooi, W.K. Ge, B. Shen, A. Trampert, U. Jahn, H. Riechert, An enhanced surface passivation effect in InGaN/GaN disk-in-nanowire light emitting diodes for mitigating Shockley-Read-Hall recombination., Nanoscale. 7 (2015) 16658–65. doi:10.1039/c5nr03448e.

[83] J. Sun, A. Adhikari, B.S. Shaheen, H. Yang, O.F. Mohammed, Mapping Carrier Dynamics on Material Surfaces in Space and Time using Scanning Ultrafast Electron Microscopy, J. Phys. Chem. Lett. 7 (2016) 985–994. doi:10.1021/acs.jpclett.5b02908.

[84] B. Liao, H. Zhao, E. Najafi, X. Yan, H. Tian, J. Tice, A.J. Minnich, H. Wang, A.H. Zewail, Spatial-Temporal Imaging of Anisotropic Photocarrier Dynamics in Black Phosphorus, Nano Lett. 17 (2017) 3675–3680. doi:10.1021/acs.nanolett.7b00897.

[85] R. Brunetti, C. Jacoboni, F. Nava, L. Reggiani, G. Bosman, R.J.J. Zijlstra, Diffusion coefficient of electrons in silicon, J. Appl. Phys. 52 (1981) 6713–6722. doi:10.1063/1.328622.

[86] J.F. Young, H.M. Van Driel, Ambipolar diffusion of high-density electrons and holes in Ge, Si, and GaAs: Many-body effects, Phys. Rev. B. 26 (1982) 2147–2158. doi:10.1103/PhysRevB.26.2147.

[87] L.J. Brillson, Applications of depth-resolved cathodoluminescence spectroscopy, J. Phys. D. Appl. Phys. 45 (2012). doi:10.1088/0022-3727/45/18/183001.

[88] F. Pennacchio, G.M. Vanacore, G.F. Mancini, M. Oppermann, R. Jayaraman, P. Musumeci, P. Baum, F. Carbone, Design and implementation of an optimal laser pulse front tilting scheme for ultrafast electron diffraction in reflection geometry with high temporal resolution, Struct. Dyn. 4 (2017) 44032. doi:10.1063/1.4991483.

[89] L.H. Germer, Low-energy electron diffraction, Phys. Today. 17 (1964) 19–23. doi:10.1063/1.3051686.

[90] J.J.I. Wong, A.G. Swartz, R. Zheng, W. Han, R.K. Kawakami, Electric field control of the Verwey transition and induced magnetoelectric effect in magnetite, Phys. Rev. B - Condens. Matter Mater. Phys. 86 (2012) 1–4. doi:10.1103/PhysRevB.86.060409.

[91] J.H. Neave, B.A. Joyce, P.J. Dobson, S.R.H.U. K, P.J. Dobson, Dynamic RHEED Observations of the MBE Growth of GaAs, Appl. Phys. A Solids Surfaces. 34 (1984) 179–184. doi:10.1007/BF00616915.

[92] U. Korte, G. Meyer-Ehmsen, The structure of the Pt(110)1 × 2 surface and its 1×2 ⇌ 1×1 structural transition I. RHEED from the periodic part of the structure, Surf. Sci. 271 (1992) 616–640. doi:10.1016/0039-6028(92)90923-T.

[93] K. Saiki, T. Kono, K. Ueno, A. Koma, Highly sensitive reflection high-energy electron diffraction measurement by use of micro-channel imaging plate, Rev. Sci. Instrum. 71 (2000) 3478. doi:10.1063/1.1287625.

[94] F.J. Humphreys, Characterisation of fine-scale microstructures by electron backscatter diffraction (EBSD), Scr. Mater. 51 (2004) 771–776. doi:10.1016/j.scriptamat.2004.05.016.

[95] M. Calcagnotto, D. Ponge, E. Demir, D. Raabe, Orientation gradients and geometrically necessary dislocations in ultrafine grained dual-phase steels studied by 2D and 3D EBSD, Mater. Sci. Eng. A. 527 (2010) 2738–2746. doi:10.1016/j.msea.2010.01.004.

[96] Z. Keshavarz, M.R. Barnett, EBSD analysis of deformation modes in Mg-3Al-1Zn, Scr. Mater. 55 (2006) 915–918. doi:10.1016/j.scriptamat.2006.07.036.

[97] G.F. Mancini, T. Latychevskaia, F. Pennacchio, J. Reguera, F. Stellacci, F. Carbone, Order/Disorder Dynamics in a Dodecanethiol-Capped Gold Nanoparticles Supracrystal by Small-Angle Ultrafast Electron Diffraction, Nano Lett. 16 (2016) 2705–2713. doi:10.1021/acs.nanolett.6b00355.

[98] Marco T. Seidel, A. Songye Chen, A.H. Zewail*, M.T. Seidel, S. Chen, A.H. Zewail, Ultrafast Electron Crystallography. 2. Surface Adsorbates of Crystalline Fatty Acids and Phospholipids, J. Phys. Chem. C. 111 (2007) 4920–4938. doi:10.1021/JP0674672.

[99] S. Schäfer, W. Liang, A.H. Zewail, Structural dynamics and transient electric-field effects in ultrafast electron diffraction from surfaces, Chem. Phys. Lett. 493 (2010) 11–18. doi:10.1016/j.cplett.2010.04.049.

[100] D. Chen, J.C. Kuo, W.T. Wu, Effect of microscopic parameters on EBSD spatial resolution, Ultramicroscopy. 111 (2011) 1488–1494. doi:10.1016/j.ultramic.2011.06.007.

[101] J. Miao, P. Ercius, S.J.L. Billinge, Atomic electron tomography: 3D structures without crystals, Science (80-.). 353 (2016) aaf2157. doi:10.1126/science.aaf2157.

[102] M.C. Scott, C.-C. Chen, M. Mecklenburg, C. Zhu, R. Xu, P. Ercius, U. Dahmen, B.C. Regan, J. Miao, Electron tomography at 2.4-ångström resolution, Nature. 483 (2012) 444–447. doi:10.1038/nature10934.

[103] R. Xu, C.-C. Chen, L. Wu, M.C. Scott, W. Theis, C. Ophus, M. Bartels, Y. Yang, H. Ramezani-Dakhel, M.R. Sawaya, H. Heinz, L.D. Marks, P. Ercius, J. Miao, Three-dimensional coordinates of individual atoms in materials revealed by electron tomography, Nat. Mater. 14 (2015) 1099–1103. doi:10.1038/nmat4426.

[104] M. Adrian, J. Dubochet, J. Lepault, A.W. McDowall, Cryo-electron microscopy of viruses, Nature. 308 (1984)

32–36. doi:10.1038/308032a0.

[105] D. Shechtman, I. Blech, D. Gratias, J.W. Cahn, Metallic phase with long-range orientational order and no translational symmetry, Phys. Rev. Lett. 53 (1984) 1951–1953. doi:10.1103/PhysRevLett.53.1951.

[106] O.-H.H. Kwon, B. Barwick, H.S. Park, J.S. Baskin, A.H. Zewail, Nanoscale mechanical drumming visualized by 4D electron microscopy, Nano Lett. 8 (2008) 3557–3562. doi:10.1021/nl8029866.

[107] M.T. Postek, An approach to the reduction of hydrocarbon contamination in the scanning electron microscope, Scanning. 18 (2006) 269–274. doi:10.1002/sca.1996.4950180402.

[108] I.C. Chen, L.H. Chen, C. Orme, A. Quist, R. Lal, S. Jin, Fabrication of high-aspect-ratio carbon nanocone probes by electron beam induced deposition patterning, Nanotechnology. 17 (2006) 4322–4326. doi:10.1088/0957-4484/17/17/007.

[109] H.R. Phillip, E.A. Taft, Optical Constants of Silicon in the Region 1 to 10 eV, Phys. Rev. 120 (1960) 37–38. doi:10.1103/PhysRev.120.37.

[110] M.A. Green, M.J. Keevers, Optical Properties of Intrinsic Silicon at 300K, Prog. Photovolt. 3 (1995) 189–192. doi:10.1002/pip.4670030303.

[111] M.S. Akselrod, A.E. Akselrod, S.S. Orlov, S. Sanyal, T.H. Underwood, Fluorescent Aluminum Oxide Crystals for Volumetric Optical Data Storage and Imaging Applications, J. Fluoresc. 13 (2003) 503–511. doi:10.1117/12.533060.

[112] T.E. Everhart, R.F.M. Thornley, Wide-band detector for micro-microampere low-energy electron currents, J. Sci. Instrum. 37 (1960) 246–248. doi:10.1088/0950-7671/37/7/307.

[113] R.T. Bayard, D. Alpert, Extension of the Low Pressure Range of the Ionization Gauge, Rev. Sci. Instrum. 21 (1950) 571–572. doi:10.1063/1.1745653.

[114] N. Samoto, R. Shimizu, H. Hashimoto, N. Tamura, K. Gamo, S. Namba, A stable high-brightness electron gun with Zr/W-tip for nanometer lithography. I. emission properties in schottky-and thermal field-emission regions, Jpn. J. Appl. Phys. 24 (1985) 766–771. doi:10.1143/JJAP.24.766.

[115] E.L. Murphy, R.H. Good, Thermionic Emission, Field Emission, and the Transition Region, Phys. Rev. 102 (1956) 1464–1473. doi:10.1103/PhysRev.102.1464.

[116] L. Gallais, D.-B. Douti, M. Commandré, G. Batavičiūtė, E. Pupka, M. Ščiuka, L. Smalakys, V. Sirutkaitis, A. Melninkaitis, Wavelength dependence of femtosecond laser-induced damage threshold of optical materials, J. Appl. Phys. 117 (2015) 223103. doi:10.1063/1.4922353.

[117] Y. Tomizawa, T. Imamura, M. Soeda, Y. Ikeda, T. Shiro, Laser doping of boron-doped Si paste for high-efficiency silicon solar cells, Jpn. J. Appl. Phys. 54 (2015) 6–11. doi:10.7567/JJAP.54.08KD06.

[118] T. Ichibayashi, K. Tanimura, Ultrafast carrier relaxation in Si studied by time-resolved two-photon photoemission spectroscopy: Intravalley scattering and energy relaxation of hot electrons, Phys. Rev. Lett. 102 (2009) 1–4. doi:10.1103/PhysRevLett.102.087403.

[119] J. Dziewior, W. Schmid, Auger coefficients for highly doped and highly excited silicon, Appl. Phys. Lett. 31 (1977) 346–348. doi:10.1016/0038-1098(78)90646-4.

[120] C.S. Wang, B.M. Klein, First-principles electronic structure of Si, Ge, GaP, GaAs, ZnS, and ZnSe. I. Self-consistent energy bands, charge densities, and effective masses, Phys. Rev. B. 24 (1981) 3393–3416. doi:10.1103/PhysRevB.24.3393.

[121] J. Bokor, N.J. Halas, Time-resolved study of silicon surface recombination, Quantum Electron. IEEE J. 25 (1989) 2550–2555. doi:10.1109/3.40641.

[122] M.J. Kerr, a Cuevas, Very low bulk and surface recombination in oxidized silicon wafers, Semicond. Sci. Technol. 17 (2002) 35–38. doi:10.1088/0268-1242/17/1/306.

[123] N.J. Halas, J. Bokor, Surface Recombination on the Si(111)2 x 1 Surface, Phys. Rev. 62 (1989) 1679–1682. doi:10.1103/PhysRevLett.62.1679.

[124] A.J. Sabbah, D.M. Riffe, Measurement of silicon surface recombination velocity using ultrafast pump–probe reflectivity in the near infrared, J. Appl. Phys. 88 (2000) 6954–6956. doi:10.1063/1.1316047.

[125] P. Maartensson, A. Cricenti, G. V Hansson, Photoemission study of the surface states that pin the Fermi level at Si(100)2x1 surfaces, Phys. Rev. B. 33 (1986) 8855–8858. doi:10.1103/PhysRevB.33.8855.

[126] W. Shockley, The Theory of p-n Junctions in Semiconductors and p-n Junction Transistors, Bell Syst. Tech. J. 28 (1948) 435–489. doi:10.1002/j.1538-7305.1949.tb03645.x.

[127] D.K. Schroder, Surface voltage and surface photovoltage : history , theory and applications, Meas. Sci. Technol. 12 (2001) R16. doi:10.1088/0957-0233/12/3/202.

[128] J.P. Long, H.R. Sadeghi, J.C. Rife, M.N. Kabler, Surface Space-Charge Dynamics and Surface Recombination on Silicon (111)Surfaces Measured with Combined Laser and Synchrotron Radiation, Phys. Rev. Lett. 64 (1990) 1158–1161. doi:10.1103/PhysRevLett.64.1158.

[129] D. Cavalcoli, A. Cavallini, Surface photovoltage spectroscopy - method and applications, Phys. Status Solidi. 7 (2010) 1293–1300. doi:10.1002/pssc.200983124.

[130] W.R. Thurber, R.L. Mattis, Y.M. Liu, J.J. Filliben, Resistivity-Dopant Density Relationship for Phosphorus-Doped Silicon, J. Electrochem. Soc. 127 (1980) 1807. doi:10.1149/1.2130006.

[131] W.R. Thurber, R.L. Mattis, Y.M. Liu, J.J. Filliben, Resistivity-Dopant Density Relationship for Boron-Doped Silicon, J. Electrochem. Soc. 127 (1980) 2291. doi:10.1149/1.2129394.

[132] M. Morita, T. Ohmi, E. Hasegawa, M. Kawakami, M. Ohwada, Growth of native oxide on a silicon surface, J. Appl. Phys. 68 (1990) 1272–1281. doi:10.1063/1.347181.

[133] D. Lau, A.E. Hughes, T.H. Muster, T.J. Davis, A.M. Glenn, Electron-Beam-Induced Carbon Contamination on Silicon: Characterization Using Raman Spectroscopy and Atomic Force Microscopy, Microsc. Microanal. 16 (2010) 13–20. doi:10.1017/S1431927609991206.

[134] M. Zani, V. Sala, G. Irde, S.M. Pietralunga, C. Manzoni, G. Cerullo, G. Lanzani, A. Tagliaferri, Charge dynamics in aluminum oxide thin film studied by ultrafast scanning electron microscopy, Ultramicroscopy. 187C (2018) 93–97. doi:10.1016/j.ultramic.2018.01.010.

[135] J. Kolodzey, E.A. Chowdhury, T.N. Adam, G. Qui, I. Rau, J.O. Olowolafe, J.S. Suehle, Y. Chen, Electrical conduction and dielectric breakdown in aluminum oxide insulators on silicon, IEEE Trans. Electron Devices. 47 (2000) 121–128. doi:10.1109/16.817577.

[136] P. Rinke, A. Schleife, E. Kioupakis, A. Janotti, C. Roedl, F. Bechstedt, M. Scheffler, C.G. de Walle, First-Principles Optical Spectra for Centers in MgO, Phys. Rev. Lett. 108 (2012) 126404. doi:10.1103/PhysRevLett.108.126404.

[137] R. Halder, S. Bandyopadhyay, Synthesis and optical properties of anion deficient nano MgO, (2017). doi:10.1016/j.jallcom.2016.09.164.

[138] P.W. Levy, Color centers and radiation-induced defects in Al2O3, Phys. Rev. 123 (1961) 1226–1233. doi:10.1103/PhysRev.123.1226.

[139] Y. Song, C.H. Zhang, Z.G. Wang, Y.M. Sun, J.L. Duan, Z.M. Zhao, Photoluminescence of inert-gas ion implanted sapphire after 230-MeV Pb ion irradiation, Nucl. Instruments Methods Phys. Res. Sect. B Beam Interact. with Mater. Atoms. 245 (2006) 210–213. doi:10.1016/j.nimb.2005.11.134.

[140] M. Izerrouken, T. Benyahia, Absorption and photoluminescence study of Al2O3 single crystal irradiated with fast neutrons, Nucl. Instruments Methods Phys. Res. Sect. B Beam Interact. with Mater. Atoms. 268 (2010) 2987–2990. doi:10.1016/j.nimb.2010.05.024.

[141] V.S. Kortov, V.A. Pustovarov, S. V. Zvonarev, T. V. Shtang, Luminescence and radiation-induced color centers in

anion-defective alumina crystals after high-dose irradiation, Radiat. Meas. 90 (2016) 90–93. doi:10.1016/j.radmeas.2016.01.010.

[142] M. Itou, A. Fujiwara, T. Uchino, Reversible Photoinduced Interconversion of Color Centers in α-Al2O3 Prepared under Vacuum, J. Phys. Chem. C. 113 (2009) 20949–20957. doi:10.1016/j.radmeas.2009.11.018.

[143] V.S. Kortov, S. V. Zvonarev, A.N. Kiryakov, D. V. Ananchenko, Dosimetric phosphor based on oxygen-deficient alumina ceramics, Radiat. Meas. 90 (2016) 196–200. doi:10.1016/j.radmeas.2016.02.015.

[144] R. Toshima, H. Miyamaru, J. Asahara, T. Murasawa, A. Takahashi, Ion-induced Luminescence of Alumina with Time-resolved Spectroscopy, J. Nucl. Sci. Technol. 39 (2002) 15–18. doi:10.1080/18811248.2002.9715152.

[145] A.I.I. Surdo, V.A.A. Pustovarov, V.S.S. Kortov, A.S.S. Kishka, E.I.I. Zinin, Luminescence in anion-defective α-Al2O3 crystals over the nano-, micro- and millisecond intervals, Nucl. Instruments Methods Phys. Res. Sect. A Accel. Spectrometers, Detect. Assoc. Equip. 543 (2005) 234–238. doi:10.1016/j.nima.2005.01.189.

[146] T.J. Shaffner, R.J. Van Veld, “Charging” effects in the scanning electron microscope, J. Phys. E. 4 (1970) 633–637. doi:10.1088/0022-3735/4/9/002.

[147] X. Meyza, D. Goeuriot, C. Guerret-Piécourt, D. Tréheux, H.J. Fitting, Secondary electron emission and self-consistent charge transport and storage in bulk insulators: Application to alumina, J. Appl. Phys. 94 (2003) 5384–5392. doi:10.1063/1.1613807.

[148] J. Robertson, Band offsets of wide-band-gap oxides and implications for future electronic devices, J. Vac. Sci. Technol. B Microelectron. Nanom. Struct. 18 (2000) 1785–1791. doi:10.1116/1.591472.

[149] B.D. Evans, M. Stapelbroek, Optical properties of the F+ center in crystalline Al2O3, Phys. Rev. B. 18 (1978) 7089–7098. doi:10.1103/PhysRevB.18.7089.

[150] R. Stoian, A. Rosenfeld, D. Ashkenasi, I. V. Hertel, N.M. Bulgakova, E.E. Campbell, Surface charging and impulsive ion ejection during ultrashort pulsed laser ablation, Phys. Rev. Lett. 88 (2002) 976031–976034. doi:10.1103/PhysRevLett.88.097603.

[151] E.J.W. VERWEY, Electronic Conduction of Magnetite (Fe3O4) and its Transition Point at Low Temperatures, Nature. 144 (1939) 327–328. doi:10.1038/144327b0.

[152] N.C. Tombs, H.P. Rooksby, Structure transition and antiferromagnetism in magnetite, Acta Crystallogr. 4 (1951) 474–475. doi:10.1107/S0365110X51001549.

[153] J.C.H. Spence, J.M. Zuo, W. Petuskey, J.C.H. Spence, W. Petuskey, Charge ordering in magnetite at low temperatures, Phys. Rev. B. 42 (1990) 8451–8464. doi:10.1103/PhysRevB.42.8451.

[154] S. Borroni, E. Baldini, V.M. Katukuri, A. Mann, K. Parlinski, D. Legut, C. Arrell, F. Van Mourik, J. Teyssier, A. Kozlowski, P. Piekarz, O. V. Yazyev, A.M. Oleś, J. Lorenzana, F. Carbone, Coherent generation of symmetry-forbidden phonons by light-induced electron-phonon interactions in magnetite, Phys. Rev. B. 96 (2017). doi:10.1103/PhysRevB.96.104308.

[155] S. de Jong, R. Kukreja, C. Trabant, N. Pontius, C.F. Chang, T. Kachel, M. Beye, F. Sorgenfrei, C.H. Back, B. Bräuer, W.F. Schlotter, J.J. Turner, O. Krupin, M. Doehler, D. Zhu, M.A. Hossain, A.O. Scherz, W.S. Lee, Y.D. Chuang, D.H. Lu, R.G. Moore, M. Yi, M. Trigo, P. Kirchmann, L. Pathey, M.S. Golden, M. Buchholz, P. Metcalf, F. Parmigiani, W. Wurth, A. Föhlisch, C. Schüßler-Langeheine, H.A. Dürr, Speed limit of the insulator--metal transition in magnetite, Nat. Mater. 12 (2013). doi:10.1038/NMAT3718.

[156] a Schlegel, S.F. Alvarado, P. Wachter, Optical properties of magnetite (Fe 3 O 4), J. Phys. C Solid State Phys. 12 (1979) 1157. doi:10.1088/0022-3719/12/6/027.

[157] V. Giovanni M., J. Hu, W. Liang, S. Bietti, S. Sanguinetti, F. Carbone, A.H. Zewail, Ultrafast atomic-scale visualization of acoustic phonons generated by optically excited quantum dots, Struct. Dyn. 4 (2017) 1–10. doi:10.1063/1.4998009.

[158] R.S. Hargrove, W. Kündig, Mössbauer measurements of magnetite below the Verwey transition, Solid State

Commun. 8 (1970) 303–308. doi:10.1016/0038-1098(70)90455-2.

[159] F. Pennacchio, V. Sala, et al., Light-induced control of the Verwey Transition in Magnetite via Ultrafast Electron Diffraction, Prep. (n.d.).

[160] F. Pennacchio, Spatio-temporal observation of dynamical structures in order-disorder phenomena and phase transitions via Ultrafast Electron Diffraction, PhD Thesis, EPFL, 2018.

[161] E.R. Jones, J.T. McKinney, M.B. Webb, Surface Lattice Dynamics of Silver. I. Low-Energy Electron Debye-Waller Factor, Phys. Rev. 151 (1966) 476–483. doi:10.1103/PhysRev.151.476.

[162] G. Grancini, M. Binda, S. Neutzner, L. Criante, V. Sala, A. Tagliaferri, G. Lanzani, The Role of Higher Lying Electronic States in Charge Photogeneration in Organic Solar Cells, Adv. Funct. Mater. 25 (2015) 6893–6899. doi:10.1002/adfm.201501873.

List of figures

Figure 1 - Volume excited by the primary beam and the different depth probed by X-rays and by electrons on the left. On the right energy spectrum of emitted electrons after the interaction of a beam of electrons with energy E with a bulk sample. Adapted from [44] 9
Figure 2 – Gold microstructures on silicon: SE image on the left and BSE image on the right 11
Figure 3 – Energy spectrum of emitted electrons from a carbon sample, in the inset the comparison between the Auger peak and the X-ray peak of carbon. Reprinted with permission from [46] 12
Figure 4 – Sequence of SEM images showing opening of a crack in a carrot due to tensile loading. Reprinted with permission from [52] 12
Figure 5 – Relative transmission of rhodopsin molecule versus probe to pump delay for two different probe wavelengths and scheme of the reaction. Reprinted with permission from [61] 13
Figure 6 – Experimental setup for optical pump-probe 14
Figure 7 - Optical pump-probe on bulk silicon (001) with 28 fs resolution. Reprinted with permission from [60] 15
Figure 8 - Optical pump-probe on silicon nanowires with 500 fs time resolution. Reprinted with permission from [62] 16
Figure 9 – Optical pump-probe images acquired at constant time delay in silicon nanowires. The measurements refer to three different nanowires: for each one, a SEM image shows the morphology of the sample and the position of the pump. Reprinted with permission from [62] 17
Figure 10 – Experimental setup for a time-resolved transmission electron microscope. Reprinted with permission from [69] 18
Figure 11 – Laser powered ultrafast electron sources. Reprinted with permission from [74] 19
Figure 12 – Experimental setup of the Ultrafast Scanning Electron Microscope. Reprinted with permission from *[26]* 21
Figure 13 – USEM image acquired with pulsed PE beam. During the acquisition of the image, the laser to the ultrafast electron source was stopped. Reprinted with permission from [26] 22
Figure 14 – SEM images (upper A,C,E) and USEM (lower B,D,F) images of nanostructures. Carbon nanotubes on a copper grid (A,B), carbon nanotubes (C,D) and zinc oxide nanowires (E,F). Reprinted with permission from *[26]* 22
Figure 15 – Time-resolved USEM images acquired on silicon (undeclared surface orientation) at negative delay (t<0) and positive delay (t>0). Dashed orange ellipse highlights laser footprint. Reprinted with permission from *[9]* 23

Figure 16 – Normalized SE intensity from optically excited area of silicon versus probe to pump delay. Reprinted with permission from *[9]* 23
Figure 17 – Time-resolved dynamics of SE emission from gallium arsenide and silicon after optical excitation. Reprinted with permission from *[28]* 24
Figure 18 – Flat band energy diagram showing the contributions of the photon pulse and the electron pulse in dependence on the doping (a), at negative delays (b), and at positive delays (c). Reprinted with permission from *[28]*.......... 25
Figure 19 – Time-resolved SE images of InGaN nanowires as-grown and passivated with octadecyl thiol (ODT) on the left, intensity of the emission from the laser-excited area in dependence on the probe to pump delay on the right. Reprinted with permission from *[31]*.......... 26
Figure 20 – Time-resolved SE emission from optically excited area of cadmium selenide. Reprinted with permission from *[27]* 27
Figure 21 – Regime of pumping and probing of semiconductor sample by ultrafast scanning electron microscopy. Reprinted with permission from *[9]* 27
Figure 22 – Comparison of time-resolved images acquired on Cadmium Selenide with PE energy of 30 keV and 1 keV. Reprinted with permission from [83] 28
Figure 23 – Time-resolved USEM images acquired on surfaces (0001) and $(\mathbf{1010})$ in vacuum and exposed to water vapor. Reprinted with permission from *[29]*.......... 29
Figure 24 – Time-resolved intensity SE emission from optically excited area of on surfaces (0001) and $\mathbf{1010}$ surfaces of cadmium selenide exposed to water vapor. Reprinted with permission from *[29]* 29
Figure 25 – Time-resolved SEM images of silicon p and n doped and of a pn junction. Reprinted with permission from *[33]*.......... 30
Figure 26 – Excitation dynamics of electrons in p-type silicon (on the left) and of holes on n-type silicon (on the right). Reprinted with permission from [34] 31
Figure 27 – Panel a shows a sketch of the experimental setup of time-resolved cathodoluminescence, panel b an SEM image where gray levels represents intensity of SEs of a sample of gold nanoparticles on carbon, and panel c shows a time-resolved measurement of the cathodoluminescence signal from GaN. Reprinted with permission from *[3]*.......... 33
Figure 28 - From the left to the right: a model of the sample with the low dimensional structures, SEM image of the micro pyramids in a perspective view and cathodoluminescence energy spectrum. For each peak of the energy spectrum, the corresponding energy resolved cathodoluminescence image is reported, to be compared to the SE image in the corner. QD means Quantum Dot, QWR Quantum Wire, VQWR Vertical Quantum Wire, QW Quantum Well and VQW Vertical Quantum Well. Reprinted with permission from *[3]* 34
Figure 29 - On the right, energy and time-resolved cathodoluminescence spectrum obtained by pumping a lateral face with the electron beam. On the left, sketch of the propagation of the charges from the lateral face towards the quantum dot, the structure with the smaller bandgap. Reprinted with permission from *[3]*.......... 34
Figure 30 – Basic principles of Time-Resolved Photoemission Electron Microscopy TR-PEEM. Reprinted with permission from [63] 35
Figure 31 – Time-Resolved PEEM images, plot d, and e shows the intensity of the signal over the rectangular area highlighted in the image acquired for a delay equal to 0.0 ps. Reprinted with permission from [63].......... 36
Figure 32 - Experimental setup of RHEED (on the left) and change in lattice constant during growth of lithium bromide on sodium bromide (on the right). Reprinted with permission from [93].......... 38
Figure 33 – Sketch of the Ultrafast Electron Diffraction setup: on the left diffraction from gold nanoparticles in transmission mode and on the right diffraction from gallium arsenide quantum dots in reflection mode. Reprinted with permission from [97] and [24].......... 39

Figure 34 – EBSD diffraction pattern on InAs: reference frame and time-resolved differential spectra. Reprinted with permission from [9] 39
Figure 35 - Sketch of the experimental setup of Ultrafast Transmission Microscope. It is possible to collect the magnified electron beam on a detector (on the left) or the diffracted electrons and the energy-loss spectrum (on the right). Reprinted with permission from [73] 41
Figure 36 - Energy spectrum of the PE beam after interacting with the near electric field induced by an optical pulse on a carbon nanotube. If the electron and optical beam overlap temporally on the nanotube (red plot) the electron exchange quanta of energy with the electric field. Reprinted with permission from *[18]* 41
Figure 37 – Absorption coefficient (on the left) and absorption depth (on the right) for the 1st, 2nd and 3rd harmonics of the laser. Data from [110] 44
Figure 38 – Comparison of experimental setups of SEM and ultrafast SEM 47
Figure 39 – The Scanning Auger Microscope model 660 by Physical Electronics before the upgrade 49
Figure 40 – Picture of the electronic column before the upgrade (on the left) and cross-section sketch (on the right) 50
Figure 41 – From the left to the right: sketch of path of the electron beam in maximum current mode, path of the electron beam in the minimum spot size mode 51
Figure 42– Astigmatism compensation with an electrostatic octupole on the left and raster scan path on the right 51
Figure 43 – Scheme of an Everhart-Thornley SE detector 52
Figure 44 – Sketch of the SE detector installed on the Phi 660 scanning electron microscope 53
Figure 45 – Sketch of the amplification and processing chain of the SE current signal. Input parameters defined by the user are Multiplier, and DC offset and output is a digital signal 54
Figure 46 – Sketch of the project of an UHV compatible Everhart- Thornley detector 55
Figure 47 – Peaks of germanium and silicon in different position on the surface of the sample. Reprinted with permission from [51] 55
Figure 48 – Scheme of the movement allowed by the sample stage (from user manual of Phi660) and a sample holder ready to be installed into the SEM chamber 56
Figure 49– The lanthanum hexaboride source removed (on the left) and the new Schottky field emission gun with optical access installed (on the right) 57
Figure 50 – Cross-section view of the Schottky field emission electron gun on the plane of the electron beam (on the left) and on the plane of the laser beam (on the right) 58
Figure 51 – Cross-section view of the original electronic column of the Phi660 electron microscope (on the right) and of the modified column (on the left). The LaB_6 filament, the beam blanker, steering plates, and part of the magnetic shield were removed to install the new Schottky field emission source with optical access 59
Figure 52 – The new mechanical 5 axis positioning stage designed to improve the alignment of the electron gun and to allow insertion of a screen for magnetic noise 60
Figure 54 – High magnification SEM images of a grain of dust 61
Figure 55 – High magnification SEM images of a grain of dust 61
Figure 55 – Diagram of the main components of the laser system 62
Figure 56 – Comparison between ultrafast Schottky field emission gun powered by a laser of wavelength 257 nm and 343 nm in efficiency (left) and stability (right). In Plot C it is shown that 257 nm is able to create more electrons per pulse with respect to 343 nm. In plot D it is shown that the emission obtained with 257 nm is constant over 3 hours while 343 nm decays linearly and becomes negligible in few hours. Reprinted with permission from [26] 63
Figure 57 – Optical scheme of the harmonic generator 64
Figure 58 – Optical path from the laser to sample 65

Figure 59 – Detail of the delay stage 65
Figure 60 – Path of the optical beam through the delay stage with optical beam parallel to the movement direction of the linear stage and with the optical beam tilted by 2° 66
Figure 61 – Path of the optical beam from the last mirror to the sample. On the right an optical view of the sample from the window............ 67
Figure 62 – Optical path from the laser to the ultrafast electron source............ 67
Figure 63 – Path of the optical beam from the last mirror to the ultrafast electron source. In the inset on the left the diffraction figure generated by the tip............ 68
Figure 64 - Comparison of the experimental setup used for testing pulsed beam emission with SEM and USEM 69
Figure 65 – Shadow of the tip in dependence on the position with respect to the focal point............ 69
Figure 66 – Plot of the extractor current versus the power absorbed by the chamber............ 70
Figure 67 – SEM images of the same area of a resolution test sample, made by tin spheres over carbon, with continuous electron beam (8 nA) on the left and with pulsed electron beam (40 pA) on the right............ 71
Figure 68 - Comparison of the experimental setup of SEM with optically excited sample with SEM and USEM ... 71
Figure 69 - Phosphorescence due to the laser beam on the sample of phosphors powder detected by an optical camera 72
Figure 70 - SEM images of the phosphors: from the right to the left laser on, laser off and difference image. The white dashed ellipse indicate the footprint of the laser spot on the sample............ 73
Figure 71 – Cross-section SEM image of the aluminum oxide thin film on silicon (on the left) and top image of the surface, uniform and flat except for contamination 73
Figure 72 - Classical SEM image of the morphology of alumina (left) and effect of the laser pump on the SEM image of alumina, showing a bright zone mainly in the laser spot area (right) 74
Figure 73 – From left to right surface of silicon, surface of silicon after 12 minutes of laser exposure at a fluence of 1 $\boldsymbol{mJ/cm2}$ per pulse, and difference image. The white dashed ellipse indicates laser footprint 75
Figure 74 - From left to right surface of silicon, surface of silicon after 15 minutes of laser exposure at a fluence of 0.5 $\boldsymbol{mJ/cm2}$ per pulse, and difference image. The white dashed ellipse indicates laser footprint 75
Figure 75 - From left to right surface of silicon, surface of silicon after 30 minutes of laser exposure at a fluence of 0.1 $\boldsymbol{mJ/cm2}$ per pulse, and difference image. The white dashed ellipse indicates laser footprint 76
Figure 76– Time-resolved SEM images acquired on highly p-doped 001 silicon. From left to right the extra path added by the delay stage is equal to 562.50 mm, 581.25 mm and 600.00 mm. Dashed ellipse is centered on the laser-induced contrast, with double size. The zero is set at the extremum of the delay stage. 77
Figure 77 – Processing of time-resolved image acquired with extra path added by the delay stage is equal to 562.50 mm. From left to right: raw image, outlier removal, outlier and horizontal bar removal 78
Figure 78 – Processing of time-resolved image acquired with extra path added by the delay stage equal to 581.25 mm. From left to right: raw image, outlier removal, outlier and horizontal bar removal 78
Figure 79 – Processing of time-resolved image acquired with extra path added by the delay stage equal to 600.00 mm. From left to right: raw image, outlier removal, outlier and horizontal bar removal 78
Figure 80 – Equalization of contrast of time-resolved SEM images. In the first line from left to right images acquired with an extra path added by the delay stage equal to 562.50 mm, 581.25 mm and 600.00 mm after removal of outliers and horizontal bars. In the second line the corresponding images after histogram equalization. 79
Figure 81 - From left to right images acquired with an extra path added by the delay stage equal to 562.50 mm (0 ps), 581.25 mm (63 ps) and 600.00 mm (125 ps) after contrast enhancement and noise compensation. The white dashed ellipse is centered on the optically-excited area, with double size 79
Figure 82 – Position of the area of the spot and of the background............ 80

Figure 83 - Plots of the average gray over the area of the spot, on a nearby area called background, and the difference of the two signal versus the electrons to photons delay. Forward scan on the left and backward scan on the right. 81
The average gray evaluated only on the area of the spot, shown in Figure 83, is not exactly the same in the forward and backward scan; the same happens for the background. This observation suggests that a systematic error contribution adds to the SE contrast while the acquisition time increases, independent on the delay time between pulses. This contribution may result from several drifts in the apparatus, probably more than one at the same time. The most probable cases include thermal and electronics drifts. The average gray of the spot and the background are very near to the corresponding value of the spot for each delay and in both scans and are almost equal for negative delays. The differential SE contrast, also reported in Figure 84, is defined as the difference between the average gray on the area on the spot and on the background. The adoption of the differential SE contrast is necessary to compensate unpredictable drifts in the average mean luminosity of the image. The choice of the position of the reference area on the background, which is horizontally aligned to the photon beam spot, allows to compensate the external electromagnetic noise visible as horizontal stripes, that will be discussed in paragraph 3.6.4 Discussion of the horizontal stripe noise in the SE images. A comparison of the differential contrast in the forward and backward scan is reported in Figure 85........ 81
Figure 85 – Contrast, evaluated as spot-background, versus electrons to photons delay. Points corresponding to the images shown in Figure 81 are highlighted by red arrows........ 82
Figure 86 – Phantom images showing the effect of a sinusoidal noise on the PE current........ 83
Figure 87 – Attenuation of the effect of a noise on the PE current obtained when comparing spot and background areas, horizontally aligned, versus the frequency of noise with respect to spot area alone........ 84
Figure 88 - Contrast, evaluated as spot-background, versus electrons to photons delay on (001) surface p-doped (10^{19} cm^{-3}) silicon. Forward and backward scans on the entire delay stage with delay steps of 500 ps were acquired........ 85
Figure 89 - Contrast, evaluated as spot-background, versus electrons to photons delay on (001) surface p-doped (10^{19} cm^{-3}) silicon. Forward and backward scans in the delay region near time zero with delay steps of 83 ps were acquired........ 86
Figure 90 - Contrast, evaluated as spot-background, versus electrons to photons delay on (001) surface p-doped (10^{19} cm^{-3}) silicon. Forward and backward scans in the delay region near time zero with delay steps of 20 ps were acquired........ 86
Figure 91 – Comparison of average contrast of Figure 88, Figure 89, and Figure 90........ 87
Figure 92 - Superposition of the plot of time-resolved scans acquired on silicon p-doped with different probe current........ 88
Figure 93 – Amplitude and offset versus PE current........ 89
Figure 94 – Rise time from 20% to 80% versus the number of electrons per pulse........ 90
Figure 95 – Energy-momentum band dispersion for silicon. Electrons are optically excited (blue arrows), then thermalize to conduction band minimum (red arrows) and finally recombine (green arrow). Adapted from [120] 93
Figure 96 – Energy bands versus depth for a p-doped semiconductor. Without light (a) and with light (b). Reprinted with permission from [129]........ 94
Figure 97 – Oxygen and carbon Auger KLL peaks on silicon p++ cleaned in HF exposed or to air or to nitrogen for few minutes........ 95
Figure 98 – Experimental setup for measurements on silicon........ 96
Figure 99 - Comparison of dynamics on silicon samples with different doping exposed to air versus delay........ 98
Figure 100 - Comparison of dynamics on silicon samples with different doping exposed to nitrogen versus delay 99

Figure 101 – SE differential contrast on silicon exposed to air (on the left) and exposed to nitrogen (on the right) after constant offset subtraction 101
Figure 102 – Fitting of the data on highly n-doped silicon $n = 1019cm - 3$ 103
Figure 103 – Fitting of the data on n-doped silicon $n = 1015cm - 3$ 103
Figure 104 – Fitting of the data on intrinsic silicon $n = 1010cm - 3$ 104
Figure 105 – Fitting of the data on lightly p-doped silicon $p = 1015cm - 3$ 104
Figure 106 – Fitting of the data on intermediately p-doped silicon $p = 1017cm - 3$ 105
Figure 107 – Fitting of the data on highly p-doped silicon $p = 1019cm - 3$ 106
Figure 108 – Amplitude of the slowest component of the fitting as a function of doping parameter 106
Figure 109 – Optical picture of a magnesium oxide bulk sample optically excited with photons of 3.6 eV 109
Figure 110 – Optical absorption spectrum of aluminum oxide in its virgin status (1) and after exposure to a neutron flux of $4.4 \cdot 1016$ n/cm2 (2), $1.3 \cdot 1017$ n/cm2 (3), $7.5 \cdot 1017$ n/cm2 (4) , $9.2 \cdot 1017$ n/cm2 (5), and $1.4 \cdot 1018$ n/cm2 (6). Reprinted from [140] 110
Figure 111 - Possible lattice defects in a crystal of aluminum oxide. Drawing a shows the crystalline structure without defects, drawing b shows the vacancies with a single atom missing and drawing c the double vacancies. Letters F and V indicate vacancies of oxygen and aluminum atoms, respectively. Reprinted from [142] 111
Figure 112 - Band diagram of alumina summarizing the main electronic processes for single (F type) and double (F_2 type) oxygen vacancy [39,139]. The numbers written vertically refers to the energy values expressed in eV. Reprinted from [134] 111
Figure 113 - Excitation-emission spectroscopy on aluminum oxide with oxygen vacancy. Reprinted from [111]. The blue line indicates the excitation wavelength used in the Ultrafast Scanning Electron Microscopy presented in this thesis 113
Figure 114 - Cross-section scanning electron microscope image of the sample 114
Figure 115 – Comparison of USEM images acquired oh highly doped p-silicon and on aluminum oxide 115
Figure 116 – USEM on the left and the experimental setup used for measurements on alumina on the right ... 115
Figure 117 - SEM image of aluminum oxide excited by pump laser. Yellow rectangle highlights the averaging area 116
Figure 118 – Time-resolved demodulated SE intensity versus electrons to photons delay on the surface of aluminum oxide. Green, red and blue curve highlight the main dynamics 117
FIGURE 119 – ULTRAFAST DYNAMIC OF SE EMISSION FITTED WITH THE MODEL (ON THE LEFT) INCLUDING: 119
Figure 120 - Root mean square error (RMSE) of the fit versus the value of τ_1 on the left and τ_2 on the right 120
Figure 121 – Crystal of magnetite (from Italian Alps) 125
Figure 122 – Experimental UED setup with integrated optical pulse tilting system, adapted from [88] 126
Figure 123 – Group velocity mismatch and tilting principle, reprinted from [88] 127
Figure 124 - Transverse size and the temporal spread of the electron pulses while propagating through the beamline. Reprinted from [22] 127
Figure 125 – Comparison of monoclinic cell, double line, with cubic cell, dashed line. Reprint from [153] 128
Figure 126 – Diffraction pattern of magnetite in dependence on temperature, arrow points at Bragg diffraction spot corresponding to lattice planes (440) 129
Figure 127 – Intensity and lattice strain versus electrons to photons delay at room temperature. Reprinted from [159,160] 130
Figure 128 – Intensity and lattice strain versus optical pump fluence at room temperature. Reprinted from [159,160] 131
Figure 129 - Intensity, lattice strain, and amplitude versus electrons to photons delay. Sample temperature was below Verwey transition threshold before optical excitation. Reprinted from [159,160] 131

Figure 130 - Lattice strain versus optical pump fluence at room temperature. Sample temperature was below Verwey transition threshold before optical excitation. Reprinted from [159,160] 132
Figure 131 - SE emission intensity from the optically excited area of silicon highly n-doped ($\mathbf{1019cm} - \mathbf{3}$) versus delay 133
Figure 132 - SE emission intensity from the optically excited area of silicon n-doped ($\mathbf{1015cm} - \mathbf{3}$) versus delay 134
Figure 133 - SE emission intensity from the optically excited area of silicon intrinsic ($\mathbf{1012cm} - \mathbf{3}$) versus delay 134
Figure 134 - SE emission intensity from the optically excited area of silicon p-doped ($\mathbf{1015cm} - \mathbf{3}$) versus delay 135
Figure 135 – Average SE emission intensity from the optically excited area of silicon p-doped ($\mathbf{1015cm} - \mathbf{3}$) versus delay 135
Figure 136 - SE emission intensity from the optically excited area of silicon p-doped ($\mathbf{1017cm} - \mathbf{3}$) versus delay 136
Figure 137 - SE emission intensity from the optically excited area of silicon p-doped ($\mathbf{1019cm} - \mathbf{3}$) versus delay 137
Figure 138 - SE emission intensity from the optically excited area of silicon n-doped ($\mathbf{1019cm} - \mathbf{3}$) exposed to air versus delay 138
Figure 139 - SE emission intensity from the optically excited area of silicon n-doped ($\mathbf{1015cm} - \mathbf{3}$) exposed to air versus delay 138
Figure 140 - SE emission intensity from the optically excited area of silicon intrinsic ($\mathbf{1012cm} - \mathbf{3}$) exposed to air versus delay 139
Figure 141 - SE emission intensity from the optically excited area of silicon p-doped ($\mathbf{1015cm} - \mathbf{3}$) exposed to air versus delay 139
Figure 142 - SE emission intensity from the optically excited area of silicon p-doped ($\mathbf{1017cm} - \mathbf{3}$) exposed to air versus delay 140
Figure 143 - SE emission intensity from the optically excited area of silicon p-doped ($\mathbf{1019cm} - \mathbf{3}$) exposed to air versus delay 141

List of tables

Table 1 – Comparison of time-resolved techniques for time-resolved dynamics of optically excited carriers in semiconductors 43
Table 2 – Result of the fitting on the scans in dependence on pulsed PE beam current 88
Table 3 - Result of the fitting on SE contrast on silicon in dependence on pulsed PE beam current, offset on the delay was fixed 89
Table 4 – Processing of data to obtain rise time versus the number of electrons per pulse 90
Table 5 – Resistivity and doping concentration of the samples measured. 95
Table 6 - Statistic of the experimental data 97
Table 7 – Review of the energy, wavelength and time constant of the decay of excited states of oxygen vacancies of aluminum oxide according to the report available 112
Table 8 – List of the free parameters used in the fitting 118
Table 9 - Results estimated by the fitting model for the free parameters and the confidence bounds at 95% ... 120
Table 10 – Size of the monoclinic and the cubic cell 128
Table 11 – Results of the fitting for silicon exposed to air 142
Table 12 – Results of the fitting for silicon exposed to nitrogen 143

Acknowledgements

Undertaking this Ph.D. has been a truly life change experience for me and it would not have been possible to do without the support that I received from many people.

First, I would like to thank my PhD supervisor Prof. Alberto Tagliaferri, for supporting and guiding my Ph.D. and the implementation of the Ultrafast Scanning Electron Microscope (USEM) at Politecnico di Milano. His guidance, continuous support, patience, good mood, commitment and passion for experimental physics where fundamental for the success of the project. His extensive personal and professional guidance taught me a great deal about both scientific research and life in general. I would like to thank him also for his useful comments on this thesis.

I would like also to thank the other members of electron microscopy group that were not only mentors but also friends. I would like to thank Prof. Silvia Maria Pietralunga not only for her help on the alignment of the laser and the discussions about semiconductors, but also for her advice on life and physics. I would like to thank Prof. Maurizio Zani, who supported me during the measurements on aluminum oxide, in data analysis and paper production.

Besides my advisors, I would like to thank the members of my supervisory committee.

I would like to thank also Gabriele Irde, my lab mate in Milano that shared with me the burden and the happiness of scanning electron microscopy.

I would like to thank Prof. Ezio Puppin, not only for his advice and cooperation in my work but also for being always able to find something funny also in the most difficult moments.

I would like to thank Prof. Giovanni Isella and Dr. Jacopo Frigerio for providing me the silicon samples and Prof. Francesca Bragheri and Dr. Petra Paiè for cleaning them in hydrofluoric acid.

Thanks also to all the members of the Physics Department of Politecnico di Milano and thanks to all the people from Center of Nanoscience and Technology of the Italian Institute of Technology for providing such a good atmosphere and being always kind to me.

I would like to thank Prof. Fabrizio Carbone for accepting me in the LUMES research group at EPFL in Lausanne. I would like to thank Prof. Giovanni Maria Vanacore for his guidance and support and Dr. Francesco Pennacchio, not only for accepting me in his lab and teaching me how to use proficiently the Ultrafast Electron Diffraction Setup but also for not let me alone in Switzerland. I cannot forget the other member of the group Enrico Pomarico, Guil Berruto, Ivan Madan and Leonor Camporeale for their help and support. I am in debt to all my friends who opened their homes to me during my time at EPFL in Lausanne and made me feel like I was at home.

More in general my thanks goes to all of those with whom I have had the pleasure to work during this and other related projects.

Of course, I also want to thank all my family for believing in me, supporting me in pursuing of this project and encouraging me to follow my dreams. Especially, I want to thank my parents for giving me life, the guidance and doing whatever they could for practical support in all those things of life beyond and including doing a Ph.D..

I would like also to thank my sister: her unconditional support, sense of humor, patience, optimism, and advice is more valuable than she could ever imagine.

My thanks go also to my friend Matteo D'Achille for reminding me about the beauty of the mathematical equation applied to physics and for reminding me that my research should always be useful and serve good purposes for all mankind. More in general I would like to thank to all the friends from Albatros for their genuine support to my interest in physics and in science.

Thanks to the friends of the group of Monday and Friday evening for providing a much-needed form of escape from my studies, also deserve thanks for helping me keep things in perspective.

Finally, my thanks go to all the people who have supported me to complete the research work directly or indirectly.